Elsevier Editorial System(tm) for Advances in Colloid and Interface Science
Manuscript Draft

Manuscript Number: CIS-D-12-00042R1

Title: Cryogels: morphological, structural and adsorption characterisation

Article Type: Review Article

Keywords: Cryogel; Structural characteristics; Microscopic image treatment; Cryoporometry; Thermoporometry; Adsorption; Diffusion; Interfacial phenomena

Corresponding Author: Prof. Vlad Gun'ko, Doctor of Science

Corresponding Author's Institution: Institute of Surface Chemistry

First Author: Vlad Gun'ko, Doctor of Science

Order of Authors: Vlad Gun'ko, Doctor of Science; Irina N Savina, PhD; Sergey V Mikhalovsky, Professor

***Suggested Reviewers**

F. E. Du Prez
Polymer Chemistry Research Group, Department of Organic Chemistry, Ghent University, Krijgslaan 281, S4, 9000 Ghent, Belgium
E-mail: filip.duprez@ugent.be

Kejian Yao
Zhejiang University of Technology, Hangzhou 310032, China
E-mail address: yaokj@zjut.edu.cn

A. Lazaridou
School of Agriculture, Aristotle University, Thessaloniki GR-541 24, Greece
E-mail address: biliader@agro.auth.gr

V. Samouillan
Laboratoire de Physique des Polymeres, CIRIMAT UMR 5085, Bat 3R1B2 118, route de Narbonne, Universite Paul Sabatier, 31062 Toulouse Cedex 04, France
E-mail address: vsamou@cict.fr.

Tatiana V. Burova
A. N. Nesmeyanov Institute of Organoelement Compounds of the Russian Academy of Sciences, Vavilov St. 28, 119991 Moscow, Russian Federation
E-mail: burova@ineos.ac.ru

A. Denizli
Department of Chemistry, Biochemistry Division, Hacettepe University, 06532 Beytepe, Ankara, Turkey
E-mail: denizli@hacettepe.edu.tr

***Graphical Abstract (for review)**

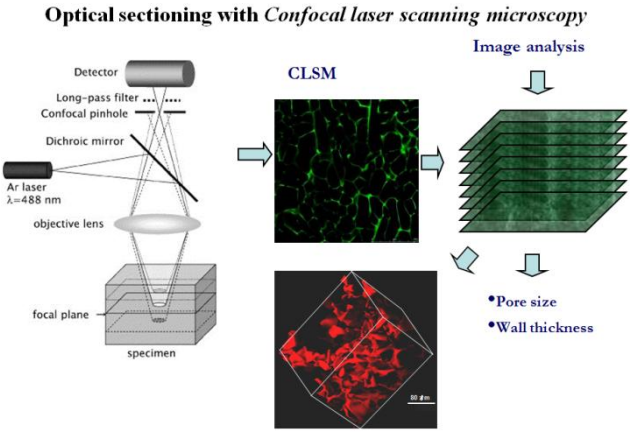

***Highlights (for review)**

- Cryotripic gelation technique allows the synthesis of solid and soft macroporous gels
- Textural characterisation of cryogel in native superhydrated state with noninvasive methods
- Adsorption and diffusion characteristics of macroporous cryogels with respect to macromolecules and cells
- Theoretical modelling of adsorption from aqueous media

National Academy of Sciences of Ukraine
Chuiko Institute of Surface Chemistry
17 General Naumov Street, Kiev 03164, Ukraine
Tel: +38044-4229627; Fax: +38044-4243567; E-mail: vlad_gunko@ukr.net

September 28, 2012

Prof. R. Miller
Editor
Advances in Colloid and Interface Science
Science Park Golm,
Max Planck Institut (MPI) für Kolloid und Grenzflächenforschung,
Am Mühlenberg 1, 14424 Potsdam, Germany

Dear Professor Miller,

Please find the revised manuscript entitled "Cryogels: morphological, structural and adsorption characterisation" by Vladimir M. Gun'ko, Irina N. Savina, Sergey V. Mikhalovsky to re-consider for publication in the "Advances in Colloid and Interface Science**"**

The paper was completely edited and changed according to reviewers comments.

Sincerely yours,

Prof. V. M. Gun'ko

Cryogels: morphological, structural and adsorption characterisation

Vladimir M. Gun'ko[a*], Irina N. Savina[b], Sergey V. Mikhalovsky[b,c]

[a] *Chuiko Institute of Surface Chemistry, 17 General Naumov Street, Kiev 03164, Ukraine*
[b] *School of Pharmacy & Biomolecular Sciences, University of Brighton, Lewes Road, Brighton BN2 4GJ, United Kingdom*
[c] *School of Engineering, Nazarbayev University, 53 Kabanbay Batyr Ave., Astana 010000, Kazakhstan*

ABSTRACT

Experimental results on polymer, protein, and composite cryogels and data treatment methods used for morphological, textural, structural, adsorption and diffusion characterisation of the materials are analysed and compared. Treatment of microscopic images with specific software gives quantitative structural information on both native cryogels and freeze-dried materials that is useful to analyse the drying effects on their structure. A combination of cryoporometry, relaxometry, thermoporometry, small angle X-ray scattering (SAXS), equilibrium and kinetic adsorption of low and high-molecular weight compounds, diffusion breakthrough of macromolecules within macroporous cryogel membranes, studying interactions of cells with cryogels provides a consistent and comprehensive picture of textural, structural and adsorption properties of a variety of cryogels. This analysis allows us to establish certain regularities in the cryogel properties related to narrow (diameter $0.4 < d < 2$ nm), middle ($2 < d < 50$ nm) and broad ($50 < d < 100$ nm) nanopores, micropores (100 nm $< d <$ 100 μm) and macropores ($d > 100$ μm) with boundary sizes within modified life science pore classification. Particular attention is paid to water bound in cryogels in native superhydrated or freeze-dried states. At least, five states of water - free unbound, weakly bound (changes in the Gibbs free energy $-\Delta G < 0.5$-0.8 kJ/mol) and strongly bound ($-\Delta G > 0.8$ kJ/mol), and weakly associated (chemical shift of the proton resonance δ_H = 1-2 ppm) and strongly associated (δ_H = 3-6 ppm) waters can be distinguished in hydrated cryogels using ^{1}H NMR, DSC, TSDC, TG and other methods. Different software for image treatment or developed to analyse the data obtained with the adsorption, diffusion, SAXS, cryoporometry and thermoporometry methods and based on regularisation algorithms is analysed and used for the quantitative morphological, structural and adsorption characterisation of individual and composite cryogels, including polymers filled with solid nano- or microparticles.

Keywords: Cryogel; Structural characteristics; Microscopic image treatment; Cryoporometry; Thermoporometry; Adsorption; Diffusion; Interfacial phenomena

*Corresponding author.
E-mail address: vlad_gunko@ukr.net (V.M. Gun'ko)

Content

1. Introduction
2. Cryotropic gelation features and the nature of freezing process
3. Types of cryogel based composite and hybrid materials
4. Structural and adsorption characterisation of cryogels
   4.1. Microscopy of native hydrated and freeze-dried cryogels and models for the porosity analysis
   4.2. SAXS
   4.3. Thermogravimetry, DSC and thermoporometry
   4.4. Low-temperature ^{1}H NMR spectroscopy, TSDC and quantum chemistry in structural and energetic characterisation of cryogels
   4.5. Adsorption equilibrium and kinetics
   4.6. Diffusion of molecules and cells within macropores of cryogels
5. Conclusions

   References

1. Introduction

What is the difference in the structure of the same hydrated materials obtained by fast and slow freezing? Why fast freezing results in less destructed materials? A simple answer to these questions is based on the common view that fast or slow freezing of water results in the formation of smaller (less ordered) or larger (more ordered) ice crystallites, respectively. Therefore, the structure of the frozen hydrated materials depends both on the amount of water and freezing rate. The slower the freezing rate, the larger the ice crystallites formed, which can destroy pore walls, cellular membranes, whole cells, *etc*. These effects are due to a larger volume of ice crystallites than related water droplets, nanodomains and clusters. Firstly, ice has a larger specific volume than water. Additionally, water domains and droplets are more compacted due to their spherical shape *vs*. non-spherical ice crystallites. There is also a cryoconcentration effect responsible for the displacement of dissolved compounds into residual liquid water during freezing of a solution. Ice crystallites are much more pure and homogeneous than the original aqueous solution. For instance, sea ice is not salty but some brine saline droplets become trapped in pockets between the ice crystals. Concentrating of the saline solution residue between the ice crystallites leads to a depression in its freezing point because of colligative properties of the solutions [1]. This difference in solubility in liquid and solid (ice) water causes the effect of cryoconcentration, *i.e*. “pushing out” the dissolved compounds into the liquid aqueous phase, with gradually decreasing freezing temperature [2-4].

Additionally, the freezing temperature of water and other liquids located in narrow pores decreases below the normal freezing point in a bulk volume. This effect is described by the Gibbs-Thomson relation for the freezing point depression of pore-confined liquids. It is due to the influence of the surface fields extending from the pore walls on the liquid structures contained inside pores, which are dependent on the pore size and shape and surface structure. The surface chemistry (polarity, presence of O-containing and other polar or charged functionalities) affects the hydrogen bond network and ion distribution at a surface and in the adsorption layer [1,5]. The mentioned effects, formation of ice microcrystallites, and cryoconcentration are the base of a cryogelation technique [2-4]. At low water content (up to several percent) it is strongly bound (SBW) and cannot form ice crystallites. For such systems, differential scanning calorimetry (DSC) shows the absence of both crystallisation exotherm and melting endotherm [6,7]. Therefore, the cryogelation can be carried out only in the systems containing a significant amount of a solvent with unbound major fraction.

Thus, the freezing point of a residual concentrated solution decreases due to both colligative properties and confined space effects caused by ice crystallites and/or other solid surfaces surrounding droplets or thin layers of this solution. These effects are used in synthesis of organic or inorganic materials in aqueous media (or other liquids) at temperatures lower than the freezing point of a pure liquid. This technique was named “cryogelation” or “cryotropic gelation”. The synthesised materials were named “cryogels” (κριοσ from the Greek meaning ice) [2-4]. Thus, cryotropic gelation or cryostructuration is the formation of polymeric, protein, solid or composite gels at temperatures below the normal freezing point of a bulk solvent. It starts from freezing an initial solution, keeping it frozen for certain time to allow for the pore formation with a precursor cryoconcentrated in residual liquid layers, influenced by microcrystallites of frozen bulk solvent, with physical or chemical cross-linking of the compounds forming macropore walls and then defrosting (Fig. 1). Changes in the amounts of water and organic co-solvents, ionic strength, pH, cooling rate, gradients of temperature and solute concentrations, precursor composition, and other conditions of polymerisation of monomers or oligomers or cross-linking of polymers allow significant variations in the structural characteristics of cryogels, such as distributions of pore size and pore wall thickness, as well as in other properties of the materials [2-4]. Typically, cryogels are micro/macroporous materials (average pore diameter in the range $1 < d < 300$ μm) with pore walls of several micrometers in thickness. Notice that according to the life science classification [8], pore sizes at diameter $d_{nano} < 0.1$ μm, $0.1 < d_{micro} < 100$ μm, and $d_{macro} > 100$ μm correspond to nano-, micro-, and macropores, respectively. This pore classification is more appropriate for macroporous cryogels than the IUPAC pore classification because in the latter all pores at $d > 50$ nm are defined as macropores. For a more detailed classification of nanopores, they can be divided into three types,

namely, narrow ($0.4 < d_{nn} < 2$ nm), middle ($2 < d_{mn} < 50$ nm) and broad ($50 < d_{bn} < 100$ nm) nanopores which correspond to micro- (nano-), meso- and macropores of the IUPAC pore classification [9]. This classification aspect is of importance for non-contradictory description of the pore size distributions (PSD) over the 0.4 nm - 300 μm range of pore sizes. There are only a few published papers, which provide insight into the texture of cryogels over the whole pore size range (*vide infra*). Typically, in the literature only micro/macroporous structure of cryogels at $d > 1$ μm has been analysed but frequently only qualitatively using microscopic images without their quantitative treatment [2,3]. Therefore, one of the aims of this paper is to show in detail possible ways of quantitative description of pores over the total size range. This is of importance for understanding interactions of small molecules, ions, macromolecules, and cells with cryogels and their behaviour (*e.g.* diffusion and adsorption of solutes, cell proliferation and attachment) within pores of different sizes [2,3].

Various polymeric, protein and complex polymer/protein systems are named "hydrogels" due to large water content in the native materials. If hydrogels are synthesised at subzero temperatures they can be named "cryogels". They can be pure polymeric or filled with solid nano/microparticles. These materials are used in numerous biomedical, cosmetic and pharmaceutical applications because of their high biocompatibility and rubbery nature similar to that of natural soft tissues [2,3,10]. Micro/macroporous hydrogels at $d > 1$ μm are widely used in tissue scaffold engineering [2,3,11], as separation matrices [12-15], in bioreactors [16] and other applications [2-4]. To a large extent, the applications of cryogels are defined by their macroporous structure allowing effective mass transport of macromolecular solutes and migration of cells, high biocompatibility, good mechanical properties and water state in the interior of these highly hydrated systems similar to the state of bulk water, *i.e.* strongly associated water (SAW). Water located in macropores of cryogels is characterised by much higher activity as a solvent than water bound in nanopores of such typical adsorbents as activated carbons or silica gels or in nanopores in pore walls of cryogels.

Information on the structural properties of polymeric cryogels can be obtained using microscopy, water uptake (swelling), equilibrium and kinetic adsorption and breakthrough of low- and high-molecular weight compounds, X-ray diffraction (XRD, both small, SAXS, and wide, WAXS, angle X-ray scattering), nuclear magnetic resonance (NMR), thermally stimulated depolarisation current (TSDC), dielectric relaxation spectroscopy (DRS), DSC, thermogravimetry (TG), cryoporometry, relaxometry, and thermoporometry. Therefore, the main aim of this paper is to analyse the literature to show the relationship between the structures of pristine and dried cryogels and the interfacial behaviour of bound water and aqueous solutions within pores in these materials, and connections to their adsorption and other

characteristics using the above mentioned methods. It is of importance to describe in detail the analysis methods of the cryogel structure using invasive methods, which can be applied to both intact and dried soft cryogels. Additionally, certain features of the treatment techniques (mathematical models, software) applied to the corresponding experimental data are analysed here. These techniques include quantitative analysis of microscopic images giving the textural characteristics (specific surface area, S, pore volume, V_p, pore size distributions, PSD, pore wall thickness distribution, PWTD, pore connectivity and tortuosity). Secondly, different versions of cryoporometry, thermoporometry and relaxometry based on the temperature behaviour of probe liquids can be used for comparative structural characterisation of cryogels in different hydration states. Thirdly, regularisation procedures can be applied to the experimental data to determine the PSD, particle size distributions, adsorption energy, free adsorption energy, diffusion rate distributions, *etc*. based on measurement results with various adsorption and diffusion methods (including quartz crystal microbalance, QCM). Relaxation (NMR, DRS, TSDC) and absorption/transmittance (infrared (IR), Raman, ultraviolet/visible, UV/vis) spectroscopies give very useful information upon deep analysis of the spectra of cryogels in different states, especially with comparative analysis of adsorption and SAXS data. Finally, modelling of gels and interfacial phenomena with quantum chemistry with consideration of the solvation effects, as well as molecular mechanics (MM) and molecular dynamics (MD) methods applied to relatively large realistic models, gives structural, electronic, and energetic characteristics of the materials.

2. Cryotropic gelation features and the nature of freezing process

Cryogelation used to synthesise cryogels at temperatures below the freezing point of a bulk solvent has attracted considerable attention because it allows the production of micro/macroporous materials from almost any organic or inorganic precursors without using toxic organic solvents and with controlled textural, structural and adsorption characteristics [2-4,17-19]. It should be noted that controlled cross-linking of polymers or proteins forming nano/microporous walls of macroporous cryogels could be chemical, with the formation of chemical bonds between macromolecules, or physical, due to intermolecular interactions between macromolecules. The number of cross-links can be varied in a wide range that allows the alternation of the mechanical and other properties of the materials. Additionally, in contrast to directional freezing in liquid dispersion media during preparation of cryogels in the form of monolith macrostructures (Fig. 1), spray freezing in gaseous dispersion media can be used to prepare small porous particles of varied sizes and porosity. Clearly, cryogelation conditions in the different dispersion media influence pore formation and whole

structure of cryogels, which to a large extent define their textural and adsorption features and other important characteristics. Therefore, it is of importance to understand regularities in the freezing processes occurred in different conditions and affecting the cryogel texture.

Qian and Zhang [20] reviewed the basis of freeze-drying and the theory of freezing which can be applied to describe morphological and structural features of cryogels. As it was mentioned above, impurities (organics, salts and other solutes) have low solubility in ice crystals in contrast to the bulk aqueous solutions. Therefore, a concentration gradient of solutes is arisen at the solution-ice interface. These processes play an important role in the synthesis of cryogels in both liquid and gaseous dispersion media. The concentration of solutes (*i.e.* pore wall precursors) increases ahead of the ice front [21]. The cryoconcentration and the confined space effects lead to the freezing/melting point depression of the solution near the ice surface (*i.e.* in pores, voids between ice crystallites), and the supercooling zones can form there [1,20]. This can result in breakage of the planar interface [22,23], which is of importance in destruction of biological objects and other systems during their freezing/thawing. This phenomenon is known as Mullins–Sekerka instability [20]. The following equation was obtained by linear stability analysis for the growth rate of a perturbation (δ) to the planar interface, of magnitude $\dot{\delta}$ as a function of the instability [20]

$$\dot{\delta}/\delta = v\omega\left\{-2\left[\omega^*-\gamma\right]\left(Tm\Gamma w^2+G\right)+2mG_c\left[\omega^*-v/D\right]\right\}\left\{2G\left(k_s-k_l\right)/\left(k_s+k_l\right)\left[\omega^*-\gamma\right]+2\omega mG_c\right\}^{-1} \quad (1)$$

where $\omega^* = v/2D+\left[\left(v/2D\right)^2+\omega^2\right]^{1/2}$, ω is the frequency and m is the slope of the liquidus line on the phase diagram, v the growth velocity, T_m the equilibrium melting point, Γ the ratio of the surface energy and the latent heat of fusion, D the diffusion coefficient, k is the partition coefficient, G the temperature gradient, G_c the solute concentration gradient at the interface, and k_s and k_l the thermal conductivities of the ice and solution phases. Eq. (1) can be used to describe the pore spacing of aligned porous cryogels formed by directional freezing [20,24].

Clearly, for multicomponent systems used in the cryogel synthesis, a similar analysis is more complicated. To simplify the description of interparticle and intermolecular interactions, a theoretical study of the freezing process can consider freezing of a suspension of hard spheres [20,25,26]. Notice that the hard sphere approach is effectively used in molecular density functional theory (DFT). A balance of attractive and repulsive forces yields the critical ice growth velocity (v_c) at which particles theoretically are rejected or encapsulated by the ice [20]:

$$v_c = \Delta\sigma d\left(a_0/d\right)^n/(3\eta r), \quad (2)$$

where a_0 is the average intermolecular distance, d the distance between the particle and the ice front, r the particle radius, η the viscosity of the liquid suspension, n a parameter with a value

ranged from 1 to 4, and $\Delta\sigma$ the balance of the surface forces at the ice-solution-particle boundary (this affects pore and pore walls structures and interconnectivity of pores). The $(a_0/d)^n$ term is a correction to the disjoining force on the particle [20]. Peppin *et al.* [27,28] developed mathematical models for the unidirectional solidification of the colloidal suspensions with hard spheres. The investigations were focused on the planar interfaces moving at low velocities (0.1–1 μm/s) by optical observation of the systems, which reach equilibrium by Brownian diffusion [20,27,28]. To understand the critical parameters controlling the stability of solidification interfaces in colloidal suspensions, where the freezing velocities were in the range 10–100 μm/s, X-ray radiography and tomography were used to investigate the stability of a cellular interface [29]. The constitutional supercooling and interface instabilities can be explained by Brownian diffusion [20].

Thus, when water as a solvent freezes out, the ice crystallites (forming micro/macropores of 0.1-300 μm in size in cryogels) expel the gel precursors (monomers, polymer, cross-linker and reaction initiator) into the inter-crystallite space where the concentrated solution remains unfrozen even at -10^oC to -30^oC due to the above mentioned effects. Polymerisation or cross-linking of a precursor in these liquid inter-crystallite layers results in the formation of relatively thin nano/microporous walls of macropores [2-4,30-39]. The growth of ice crystallites can cause a significant pressure on the formed pore walls. Therefore, these macropore walls are typically relatively thin and have relatively low nano/microporosity. If the amount of water is much greater than that of a precursor, the resulting cryogel can be macroporous or supermacroporous (porosity up to ~99%). This is due to the formation of relatively large ice crystallites as pore-forming microparticles and relatively thin pore walls. The latter are thinner (smaller) by one-two orders of magnitude than the size of macropores. Therefore, the total pore volume of native cryogels can be huge, up to 20-40 cm^3/g [2-4,30-39]. The macropore walls (typically 1-10μm, rarely 15-50 μm in thickness) can include both nanopores ($d_{nano} < 0.1$ μm) and micropores ($d_{micro} > 0.1$ μm). The inner structure of macropore walls has been less studied than the structural characteristics of the main micro/macropores in cryogels [2-4]. In this paper, methods appropriate for the structural characterisation of the macropore walls in cryogels are described.

Cryogels as macroporous materials are attractive as matrices for tissue scaffolding as they allow unhindered diffusion of not only low-molecular solutes but also macromolecules and cells. This is due to the interconnected system of macropores, and the spongy and elastic morphology of the cryogels as a whole [2-4,30-40]. These features, in combination with a molecular-imprinting polymer (MIP) technique, provide a new approach for various biotechnological and environmental applications [2,3]. The MIP technique offers a simple way

to increase significantly the selectivity of cryogels used as adsorbents for specific compounds. The MIPs are removed during a post-cross-linking stage of the cryogel synthesis. In many applications, cryogels can be used as an alternative to functionalised sol-gel materials. Additionally, cryogels can be filled with solid porous micro- or nanoparticles to change their structural, mechanical, textural and adsorption characteristics. The particles of a whole cryogel can be functionalised to control their interactions with solutes. Besides organic cryogels, inorganic cryogels can be synthesised with oxides, carbons, and other materials.

There are several pathways of cryogel functionalisation: (i) direct formation of a polymeric cryogel from monomers or polymers with a required functionality; (ii) introducing of chemical functionality into a cryogel after its formation; (iii) making cryogel composites with functionalised components (co-polymers or nanofillers). Cryogels could be prepared with biodegradable, ionic, stimuli-responsive polymers or biopolymers with properties dependent on their applications [2-4,15,36]. Copolymerisation of a bulk monomer with another monomer bearing a functional group is often used to functionalise cryogels without compromising their mechanical and osmotic properties and reducing the material cost. Changing the ratio of the functional monomer to the bulk monomer allows one to control the number of functional groups introduced and their accessibility for target adsorbate molecules. For example, co-polymerisation with allyl glycidyl ether (AGE) is often used to introduce the epoxy functionality for further conversion into anion-exchange or chelating group or immobilisation of a bio-ligand. However, an increase in the allyl glycidyl ether content results in the formation of brittle and non-elastic cryogels [41]. Co(polyacrylamide-allyl glycidyl ether) cryogels become brittle when concentration of AGE exceeds 20%. Moreover, most of the functional groups in such a material are in the bulk of the cryogel (*i.e*. in pore walls) rather than exposed on the surface, which lowers their accessibility for interaction with solutes or further modification. Post-modification is often used for introducing bio-ligands, which require special conditions for immobilisation without losing their bio-activity.

Thus, the content of functional groups at a surface of cryogels depends on the modification type and technique, and in the case of surface modification, it is limited to the surface area available for interaction depending on the molecular size of a modifier. An increase in the number of functional groups enhances the adsorption capacity of a cryogel until it reaches a limiting value determined by the surface area available for interaction and type of grafting of a modifier (*e.g.* with or without cross-linking, mono- or polydentate binding, the size and chemical structure of the modifier). For instance, macroporous cryogels can have the adsorption capacity for proteins of 3-7 mg/mL [42]. Grafting of such ion-exchange polymers as poly(2-dimethylamino-ethyl methacrylate), polyacrylic acid and poly(2-methacryloyl-oxyethyl-trimethylammonium chloride) to

the cryogel surface considerably increases the number of the ion-exchange groups introduced into the cryogel [32]. The ion-exchange capacity of such cryogels does not depend on the matrix surface area anymore as ion-exchange groups are located on the flexible polymer chains attached by one end to the surface of pore walls to form brushes in macropores. Unless they are strongly cross-linked, the effective surface area *S* of the attached polymer brushes can be higher by one or two orders of magnitude than the *S* value of the initial macroporous cryogel. The number of ion-exchange groups depends on the number of the polymer chains attached, the length of a polymer chain and the density of ion-exchange groups per polymer chain, as well as the textural characteristics of the matrix. Thus, grafted macromolecules form polymer brushes with a great surface area and highly accessible for solvents and solutes. Ion-exchange groups introduced into flexible polymer brushes are accessible for interactions with solutes thus enhancing the binding capacity of the cryogel columns, especially for large molecules such as proteins [42]. The protein binding to cryogels modified with polymer brushes can be ten-fold higher comparing to the conventional surface modification. However, the accessibility of the ion-exchange groups for interaction with proteins remains an important issue. When the dense population of polymer brushes is formed, this effect being similar to physical cross-linking of the polymers, it hinders the ion-exchange groups inside a more strongly compacted grafted polymer layer, making them inaccessible for large biomolecules. In this case, the adsorption becomes independent of the ion-exchange group capacity but depends on the surface area accessible for macromolecules [32,42].

Another interesting approach used to modify cryogels is based on the application of the second freezing-gelation cycle on the top of a cryogel matrix already formed. For instance, agarose was gelled in the interior of polyacrylamide cryogel, PAAm [43]. The PAAm cryogel was used as a scaffold/support for the second polymer, agarose. It is interesting that adding agarose to PAAm had almost no effect on the macroporous structure of the cryogel. The second layer was formed on the top of the existing 3D polymer structure or in the interior of the matrix creating an interpenetrating network without blocking the macropores, which remain open. This technique opens perspectives for creating materials with unique properties but dependent on a combination of the properties of each polymer component. It can be particularly useful when the second polymer is unable by itself to form a mechanically stable matrix with large interconnected pores and the 3D cryogel matrix provides a scaffold to fix its porous structure. This method was used for preparation of different macroporous systems that can be used as chromatographic media or scaffolds for cell culture applications [43]. Clearly, the cryogelation process within the macropores of a matrix differs from that at the top of the matrix. This can influence the pore size distribution and other characteristics of the whole material.

The main effects in cryogelation such as cryoconcentration, cryotropic polymerisation and ice crystal formation, in the case of preparation of cryogels with thin pore walls filled with nano- or microparticles are influenced by the filler. These hybrid materials can combine the excellent flow-through properties of macroporous cryogels with high adsorption properties of added fillers. The latter can possess a very large specific surface area (such as activated carbons with S_{BET} up to 3500 m^2/g), great nanopore volume (1-3 cm^3/g), surface functionalities specific with respect to target compounds, *etc*. However, filler particles can be uniformly or nonuniformly distributed inside the pore walls, covered by polymers or attached to these walls directly or by polymeric brushes. The cryogels can be used as a 3D matrix to hold fine filler particles with carbon, metal oxides, polymers, *etc.* For instance, cryogel composites with iron oxide nanoparticles were developed for environmental applications [44]. Iron oxide nanoparticles are well known for effective adsorption or breaking down of a number of contaminants. However, their direct application for water purification faces a problem of high flow resistance during filtration. The minute size of nanoparticles leads to a very dense column packing creating high back pressure and making the flow through such a column impracticable. Moreover, concerns have been raised about the release of free nanoparticles to environment, which (especially with transition metals) could itself present a major environment problem. Embedding nanoparticles into a polymer matrix or polymer brushes in macropores of cryogels can significantly reduce the environmental risk, while retaining the bulk of the particle activity. A nanoparticle-cryogel composite can be prepared by dispersing nanoparticles in the reaction solution followed by cryogelation [44]. The composite cryogels with iron oxide nanoparticles synthesised by this rather straightforward method had high permeability and efficiency in removing arsenic from water. The adsorption capacity of nanoparticles was not significantly reduced by embedding into the cryogel, confirming that cryogels are a promising scaffold material for developing filtration/adsorption nanoparticle based devices for water purification [44].

Another example of composite cryogels was prepared with PVA and molecular-imprinted particles, selective for adsorption of endocrine disrupter compounds [45]. MIP was first synthesised with 17β-estradiol as a template, the template was removed by washing with methanol, and used for preparation of a macroporous PVA composite cryogel. The MIP composite cryogels could be operated at ten times higher flow rate (50 mL/min) comparing to MIP columns (1-5 mL/min). Additionally, it was possible to apply wastewater effluents containing the particles without clogging columns. Therefore, complete removal of 17β-estradiol as a probe compound by the MIP-cryogel composite from water was done at much shorter time [46].

Another challenge is to make cryogel composites with larger porous particles such as activated carbon (AC) and to preserve the adsorption properties based on the AC adsorbent porosity [47]. Nanoporosity of AC adsorbents is very important for adsorption of a range of organic compounds. However when it is incorporated in the interior of a polymeric cryogel, the AC particles could be covered with a polymer film reducing the pore accessibility for target compounds [2,3,36,47]. The negative polymer effects on the adsorption properties of cryogel/AC composites are discussed in detail below.

In the case of nonporous nanoparticles (NPNP) used as fillers, the task is simpler since there is no problem of blocking of nanopores. Xu *et al.* [48] prepared cryogels with acrylamide (AAm) cross-linked by N,N-methylene-bis-acrylamide and containing silica NPNP (the mass ratio of nanoparticles to AAm was 0.01-0.08). Embedded silica NPNP affected the flow velocity in the chromatography tests. However, the detailed analysis of the relationships between the breakthrough data and the textural characteristics was not performed due to the difficulties in the analysis of the textural properties of soft hydrated cryogels and related composites.

To optimise the structure of cryogels they should be characterised in different aspects and in different hydration states. However, techniques frequently used for structural characterisation of materials, *e.g.* gas or vapour adsorption of low-molecular probe compounds (nitrogen, benzene, hexane, carbon dioxide, water, argon, *etc.*), mercury porosimetry, pycnometry and conventional scanning electron microscopy (SEM) can be applied only to dry materials frequently degassed in vacuum. However, drying cryogels, which are superhydrated in the native state, can result in very significant changes in their macropore structure up to complete collapse of the entire pore network [2,3,49]. Although use of the freeze-drying technique in sample preparation for analysis significantly reduces the pore structure damage, it does not guarantee preserving the identity of the structural characteristics of cryogels before and after the treatment. Thus, there are certain difficulties in the adequate structural characterisation of cryogels in their native superhydrated state with up to 99 wt.% of water. Therefore, some specific techniques had to be developed, *e.g.*, based on variations in the characteristics of water bound in neat cryogels, to obtain information on their structure in native, intact state. This aspect is analysed below.

It should be noted that there are several states of water that can be distinguished in cryogels and hydrogels. First, there is unbound water, UBW, or strongly associated water, SAW, located in broad micropores and macropores; it does not interact with the pore walls and behaves as pure bulk water (Table 1). Second, weakly bound water (WBW), which shows weak interaction with the cryogel surface and freezes at subzero temperatures but close to 0^{o}C. It

includes mainly SAW. Third, strongly bound water (SBW) strongly interacts with the cryogel surface through the hydrogen bonds or electrostatic interactions, especially with the participation of ions OH^-, H_3O^+, $H_5O_2^+$ present in water in concentrations dependent on pH. SBW remains unfrozen at $T < -15^oC$ [50-55]. In contrast to the unbound water which is comprised of only SAW, water in other two energetic states, WBW and SBW (Table 1), can include both SAW (large clusters, nanodomains [1]) and weakly associated water (WAW) with small 1D or 2D or strongly branched 3D clusters located at mosaic polar/nonpolar surfaces [50,51]. Contributions of different forms of water depend on the porous structure and surface chemistry of the pore walls, as well as on the composition of the solution. Detailed analysis of bound water, especially with application of low-temperature ^{1}H NMR, cryoporometry (NMR), relaxometry (NMR, TSDC, DRS) and thermoporometry (DSC, TG) methods [1,5,50-54], can give useful information on the structure of native and treated cryogels and their interactions with solvents and solutes. The low-temperature methods can also be used to study the kinetics and dynamics of the cryogelation processes.

The amounts of water in different states affect interactions of solutes, biomolecules and cells with cryogels within both nano/micropores in their pore walls and in the main textural network of broad micropores and macropores. Therefore, determination of the amounts of different types of water in cryogels [50,51,54] is of importance to understand the nature of adsorption/desorption and diffusion processes within the pore network in cryogels, as well as to estimate the biocompatibility and structural organisation of whole cryogels [2-4,10-20,30-49,54]. A variety of experimental methods sensitive to the water state can be used for these purposes [50-56]. Low-temperature ^{1}H NMR spectroscopy with layer-by-layer freezing-out of bulk and bound waters gives information on the temperature dependence of the amounts of all the above mentioned types of water (Table 1), allowing for the structural and thermodynamic properties of these waters to be calculated in any system including superhydrated cryogels [54]. NMR cryoporometry gives certain structural information on the surroundings of the structured bound water (due to confined space effects on bound water), and in particular on the structure of nanopores [50,51,54]. NMR and other spectral methods can be also used to study the kinetics of cryogel formation. NMR relaxometry with organic probe compounds has been used to estimate the pore sizes up to 1 μm or even larger [54]. From DSC calorimetry data the thermodynamic characteristics of water and hydrated materials, hydration and phase transition effects can be quantified, whereas thermoporometry is applicable mainly to nanopores at $d <$ 100 nm. Thermogravimetry gives information on the relationship between evaporation of water as a function of temperature and the pore structure, and thus TG data can be used to estimate the

pore sizes (mainly nanopores at d < 50-100 nm). Temperature-programmed desorption with mass-spectrometry (TPD-MS) technique allows the estimation of the parameters of activation processes of water desorption [50] that can be used for the analysis of strongly bound water and surface functionalities of the materials. Thermostimulated depolarisation current (TSDC) method and dielectric relaxation spectroscopy (DRS) provide information on the structural organisation of bound water, plasticising effects, glass transition and other relaxation processes within the polymer matrices, as well as polarisation/depolarisation characteristics, energy of the hydrogen bonding and certain structural information on the bulk materials [53,54]. DRS gives detailed information on a variety of relaxation processes involving water and polymers, mobility of hydrated polymer fragments (segmental dynamics) and water itself [50,53,54]. Spectral methods - infrared (IR), Raman and ultraviolet/visible (UV/vis) spectroscopies give information on both polymer surface functionalities and the character of their interactions with bound water or solid particles used as a cryogel filler. Theoretical modelling methods - quantum chemistry, molecular mechanics (MM) and molecular dynamics (MD) give useful information on structural and energetic characteristics of polymer/water and polymer/filler/water systems. Comprehensive characterisation of intact cryogels and related dried systems with the methods mentioned above and other methods is of importance to optimise the morphological, structural, adsorption, diffusion and other characteristics of cryogels as advanced materials for many practical applications.

It should be noted that the analysis of water structure located in macroporous cryogels cannot give detailed information on the structure of macropores because water located there has the properties very similar to the properties of bulk water. Therefore, the structural characteristics of macropores of hydrated cryogels should be determined using other techniques, *e.g.* microscopic methods applied to both hydrated and freeze-dried states of cryogels with a detailed quantitative analysis of images using specific software. Certain organic and inorganic compounds are more appropriate probe liquids than water in NMR cryoporometry and relaxometry of macroporous materials [54].

3. Types of cryogel based composite and hybrid materials

There are numerous publications describing a variety of cryogels, including not only laboratory samples but also commercial materials. Despite such a substantial information flow, there is no uniformly accepted definition of the term “cryogel”. There are, at least, four different types of materials named “cryogels”: (i) gelatinous precipitate forming during cryoprecipitation - blood plasma treatment upon cooling to *ca*. 4°C [57]; (ii) frozen polymeric or other hydrogels used

as antipyretic materials or materials for thermal energy storage [58]; (iii) polymeric and inorganic cryogels produced using sol-gel technology with subsequent freeze-drying including individual and mixed inorganic oxides, polymers, hybrids, composites, and carbon cryogels (the latter is prepared by carbonisation of polymeric cryogels) [59-67]; (iv) synthetic and natural polymer or protein cryogels produced in a frozen solvent, usually water, by the cryotropic gelation [2-4,10,12-49,68-80]. In the latter case, frozen water (in the form of ice microcrystallites) plays a role of a pore-forming agent (porogen). Thus, materials of very different origin have been named "cryogels" due to their action in a frozen state, the use of precursors prepared by the cryogelation technique or the use of the freeze-drying technique or final materials prepared with the cryotropic gelation technique. This paper is mainly focused on the last group of materials, organic polymer cryogels. Organic polymer cryogels have been synthesised by polymerisation of from hydrophilic and hydrophobic monomers or cross-linking polymeric precursors with small active molecules or polymers in the presence of a large quantity of water (up to 99 wt.%). Depending on subsequent application, cryogels can be made in different shapes such as monoliths, rods, sheets, discs, spherical particles, *etc.*, the shape being determined by the contours of reaction vessel, nature of the dispersion medium, and other conditions of synthesis [2-4,36,81]. However, for most applications the geometric shape of cryogels is less important than their inner porous structure.

There are many cryogels prepared from synthetic polymers such as poly(vinyl alcohol), PVA, which was one of the first polymers used in cryogel preparation [2-4,36,38,74,78,82]. PVA alone or in combination with other polymers or proteins is very popular material for the cryogel preparation because its structure containing the $(\text{-CH}_2\text{-C(OH)H-})_n$ chain allows various degrees of cross-linking with the participation of the active COH groups, different cross-linkers and co-polymers. The PVA structure can undergo both chemical and physical cross-linking. However, pure PVA cryogels are insufficiently functionalised for many practical applications. Therefore, PVA is used as a matrix polymer in composite cryogels.

Functionalised cryogels are popular due to enhancement and broadening of their properties, especially adsorption, and, therefore, widening of applications. For instance, Liu *et al.* [83] prepared a thermoresponsive monolithic cryogel using isopropylacrylamide as a functional monomer and poly(ethylene glycol) PEG-20000 as a pore-forming agent at -12^{o}C, the temperature frequently used in cryogelation. The morphology of the cryogel studied by SEM is characterised by a submicron skeleton structure. The rates of swelling/deswelling (determined by TG method) were higher for the thermoresponsive monolithic cryogel than for a hydrogel prepared by conventional method at 25^{o}C. According to Vrana *et al.* [84], PVA cryogels are characterised by a slow rate of endothelialisation, and the mode of cell attachment leaves the endothelium susceptible to removal

under physiological shear stress conditions. Therefore, PVA/gelatine cryogels were developed as more functionalised materials more suitable for endothelialisation [84]. In these cryogels, the application of a ramped shear stress had a profound effect on endothelial cell proliferation (22-fold increase), necrosis (eliminated) and overall facilitation of endothelialisation while concomitantly increasing nitric oxide synthesis [84].

Another family of cryogels is based on biocompatible polysaccharides and related compounds which have numerous hydroxyls (similar to PVA but with a more complex structure of cyclic monomers) and other functionalities with O and N atoms such as in chitosan or hyaluronic acid. Tripathi and Kumar [85] synthesised agarose–alginate cryogels of different shapes (monoliths, sheets, discs and beads). These degradable materials with a highly interconnected macroporous network had mechanical strength similar to soft natural tissues. Fibroblast (NIH-3T3) cells showed good adherence and proliferation within these scaffolds. It was concluded [85] that the synthesised materials have good potential for applications in soft tissue engineering. However, in this paper only qualitative structural characterisation of the materials was made. Physically cross-linked cryogels containing PVA and various amounts of microcrystalline cellulose prepared by freezing/thawing technique were characterised using SEM, FTIR, XRD, rheology, TG, and swelling methods [86]. However, the textural characteristics of the cryogels were not analysed in detail.

The next very popular group of cryogel precursors are proteins, especially collagen and gelatine, because of great biocompatibility and significant functionalisation of protein-based materials. Mu *et al.* [87] prepared a 3D spongy collagen cryogel using dialdehyde starch, DAS, with molecular weight m_w~3.5 MDa as a cross-linker. They used type I collagen with average radius of gyration $<r_g>$ = 125-100 nm and average hydrodynamic radius $<R_h>$ = 200-125 nm in acetic acid at 24-48^{o}C. Smaller structures at R_h = 20-30 nm were also observed. It was shown by FTIR and circular dichroism methods that cross-linking occurred *via* a reaction of aldehyde groups in DAS with free amino groups in collagen without affecting the triple helix of the protein [87]. This conservation of the protein structure could be of importance for biomedical applications of the material. SEM images demonstrated that the cryogel had a heteroporous structure with appropriate interconnectivity of macropores. DSC measurements revealed that the cryogel had improved thermal stability in comparison with pure collagen because starch is more thermally stable than proteins (*e.g.* TPD-MS measurements show that polysaccharides are effectively decomposed only at T > 200^{o}C). Moreover, depending on the composition, this collagen/DAS cryogel absorbed up to 28-32 grams of water per gram of dry material within one hour because of significant swelling. It decreased with increasing DAS content perhaps due to increased cross-linking degree and a higher swelling ability of collagen than cross-linked DAS. The high swelling degree was attributed to the

macroporosity of the collagen/DAS cryogel in aqueous media corresponding to the pore volume filled by water in the hydrogel up to $V_p \approx 30$ cm^3/g. The analysis of water evaporation showed that the cryogel could hold water for a long time meaning that this water is rather bound than bulk water. This collagen/DAS cryogel is haemocompatible because both collagen and DAS are nontoxic and it can be used as a wound dressing [87] similar to collagen-based INTEGRA^{TM} described in detail below.

Robert *et al.* [88] prepared cryoproteins using immunoglobulins (Ig). Similar cryogels are therefore named cryoglobulins. Using proteomic tools, a monoclonal IgM was identified as being the cause of the gel formation. Addition of water before incubation at 4^{o}C demonstrated that the monoclonal IgM was precipitable as a type I cryoglobulin (hypocryoglobulin) [88].

The synthesis of solid-based hard cryogel materials has also been reported. Mukai *et al.* [89] synthesised porous titania cryogel fibres using unidirectional freezing and subsequent freeze-drying of titania hydrogels, which were synthesised by sol−gel polymerisation of titanium tetraisopropoxide using dialysis. It is worth mentioning that the structural characterisation of solid inorganic cryogels is much easier than that of soft strongly hydrated organic cryogels because of a much higher stability of the texture of the former materials. Kraiwattanawong *et al.* [90] prepared a carbon/carbon composite cryogel by dispersing cotton fibres in a resorcinol-formaldehyde sol, followed by solvent exchange with *t*-butanol, freeze-drying and pyrolysis under inert atmosphere. Thus, the final material was not a cryogel, but the precursor could be attributed to the cryogel family. Pons *et al*. [91] synthesised silica cryogels with properties similar to those of silica aerogels, particularly in terms of monolithicity, density, porosity and specific surface area. This similarity can be explained by high pressure produced by ice crystallites onto thin residual liquid films between these crystallites that is similar to high-pressure condition used on synthesis of aerogels. The textural characterisation of silica cryogels was based on nitrogen adsorption isotherms appropriately analysed, SEM images (with no quantitative analysis), and the structure was also analysed using ^{29}Si MAS NMR and FTIR spectra [91]. Hybrid SBA-15/carbon cryogel composites were prepared by sol–gel polycondensation of resorcinol and formaldehyde followed by freeze drying, and subsequent pyrolysis [92], and characterised using nitrogen adsorption, XRD and SEM (images were not treated) methods. Highly conductive carbon cryogel based on graphene and prepared by the sol–gel polymerisation of resorcinol and formaldehyde in an aqueous surfactant stabilised suspension of graphene was characterised using nitrogen adsorption, XRD, FTIR and Raman spectroscopy, and SEM [93] but with no quantitative analysis of images. Carbon cryogels have been obtained by freeze-drying and pyrolysis of a family of tannin-formaldehyde organic gels prepared at different pHs [94]. The textural characteristics were analysed on the basis of nitrogen adsorption

isotherms. The materials were tested as electrodes for electric double-layer capacitors, specific capacitances as high as 100 F g^{-1}. Thus, the texture of dried solid cryogels was quantitatively characterised using standard adsorption methods. However, these methods cannot be applied to native superhydrated cryogels prepared with any materials, especially soft polymeric or protein cryogels.

Hybrid cryogels, reported in literature, include both soft and solid phases, *e.g.* polymers filled with activated carbons microparticles or other solids. Activated carbons are traditionally known as very effective adsorbents, especially for low-molecular weight organics [9,95-102]. However, when traditional AC materials were tested for use in haemoperfusion based medical applications their biocompatibility was not appropriate. The biocompatibility of AC can be improved by coating them with biocompatible polymers [103,104]. However, this coverage limited the adsorption characteristics (*S*, *V*, PSD) of the materials for the relevant biotoxins because of partial blocking of narrow pores of AC microparticles and a cut-off effect of the semipermeable membrane coatings. Using an improved technology and synthetic polymer precursors, highly biocompatible AC have been synthesised. Uncoated spherical AC were produced by MAST Carbon International Ltd, UK from phenolic resins and activated by CO_2 to different burn-off degrees (up to 86%) [101,102]. These AC could be used uncoated in direct contact with blood whilst retaining appropriate biocompatibility. It was found that a haemoperfusion column packed with carbon beads of 0.5-1.0 mm in diameter had satisfactory flow dynamics. However, in order to accelerate adsorption kinetics smaller AC particles would be preferred. To prevent microparticle release into the blood stream and reduce the pressure drop experienced in a microbeads packed bed system it is necessary to incorporate the AC microbeads into a structural "backbone" to fix the adsorbent microparticles in place and allow a free flow of fluid through the system. Cryogels with attached AC microparticles can be used for this purpose as a scaffold. The AC beads may be partially incorporated into thin polymer films, thin pore walls of macroporous cryogels or may be attached to the macropore walls of polymer gels by a small number of polymer links using loose polymer brushes attached in macropores. Cryotropic gelation technique can be used to prepare AC/polymer composites of the mentioned types. It is important that this process can be carried out without using organic solvents since it is difficult to remove them from AC nanopores. This technique allows the synthesis of macroporous matrices appropriate for the distribution of AC microparticles without blocking the macroporous channels of the cryogels and allows passage of blood cells during haemoperfusion. However, the narrow pores of the AC particles may still be partially blocked by a coating introduced during the cryogelation process. There are different ways to reduce these negative effects (*vide infra*).

In the case of preparation of AC filled cryogels [105-108], PVA as a matrix polymer and glutaraldehyde (GA) as a cross-linker were used at a varied ratio of their concentrations. The cryogel synthesis is relatively simple, which is an important advantage of this technique. The comparative structural and other characterisation of PVA and AC/PVA cryogels is described below using a variety of experimental and theoretical approaches. In this paper, which is mainly devoted to description of methods and approaches for morphological, structural and adsorption characterisation of cryogels, synthesis of cryogels is described only briefly, and the reader is referred to other review papers and books where the synthesis of cryogels is given in detail [2-4,36,38,74,78].

4. Structural and adsorption characterisation of cryogels

The structural characteristics of cryogels such as the pore volume, *V*, the specific surface area, *S*, the pore size distribution, PSD, the pore wall thickness distribution, PWTD, pore connectivity and tortuosity are of importance from the practical point of view [2-4,36,38,74,78]. A special interest is drawn to the detailed structure of pores and pore walls from nanoscale ($0.4 < d_{nano} < 100$ nm) to microscale ($0.1 < d_{micro} < 100$ μm) and macroscale ($d_{macro} > 100$ μm). However, there are some difficulties in quantitative characterisation of the texture of cryogels because of their soft nature and strong hydration in the native state. Therefore, in most published papers, the structural and textural characterisation cryogels was carried out only at qualitative or semi-quantitative level. Typical examples of this characterisation include microscopic images of dried or freeze-dried cryogels without determination of the mentioned parameters (*V*, *S*, PSD, and PWTD) or with estimation of the average size of pores and the porosity. However, in some papers, the PSD and other textural characteristics were determined in detail using mercury porosimetry [78] and analysis of images [3,76,105-108]. There are several papers describing the PSD of native polymer cryogels over the total range of pore sizes from narrow nanopores ($d_{nn} < 2$ nm) to macropores at $d_{macro} > 100$ μm [3,105-108]. In these papers, the structural characterisation was based on several techniques such as confocal laser scanning microscopy (CLSM), SEM, cryo-SEM, and other microscopic techniques with subsequent quantitative analysis of microscopic images of both native hydrated and freeze-dried cryogels. Additionally, narrow pores ($d_{nano} < 100$ nm) in the walls of macropores were analysed using DSC and TG thermoporometry, NMR cryoporometry and TSDC relaxometry. A comparative analysis of the approaches appropriate to obtain detailed structural and textural information on native hydrated and freeze-dried cryogels given below is of significant interest.

4.1. Microscopy of native hydrated and freeze-dried cryogels and models for porosity analysis

Microscopic methods are frequently used to study cryogels. For instance, Sur *et al.* [109] characterised nanofibers with collagen and amphiphile peptide using several microscopic methods (AFM, TEM, cryo-TEM, confocal reflection microscopy, and SEM). Despite a large number of used microscopic methods, quantitative analysis of microscopic images was done to estimate only the surface area. In most cases, the analysis of microscopic images has been done at qualitative or semi-quantitative level. Luan *et al.* [110] investigated the influence of acidification and salting effects on the properties of hyaluronan aqueous solutions and cryotropic weak gels using rheometry, polarising and optical microscopy, SEM, XRD, DSC and FTIR spectroscopy. However, the structural characteristics of gels were not quantitatively analysed.

A more advanced analysis of microscopic images was used by Autissier *et al.* [76]. They applied a combined freeze-drying/cross-linking process to prepare porous polysaccharide-based scaffolds using pullulan and dextran with sodium trimetaphosphate and showed that the degree of porosity of cryogels depends on freeze-drying pressure. Scaffolds treated at high freeze-drying pressure have pores of d = 55±4 μm in mean diameter and the porosity φ = 33±12%. The scaffolds treated at low freeze-drying pressure contained larger pores at d = 243±14 μm and φ = 68±3% (Fig. 2a). The porosity is an important parameter of performance of tissue scaffolds because the cells can penetrate deeper into scaffolds with larger pores [76]. However, the next step in deeper characterisation of the cryogel structures to obtain the PSD and other structural characteristics using image analysis of clear pictures (Fig. 2a) was not done [76]. We calculated the PSD (Fig. 2b) for two porous samples shown in Fig. 2a using ImageJ [111] with granulometry plugin (this is a simplified approach in comparison with the techniques described in papers [105-108], *vide infra*). In both samples PSD have complex shapes that are typical of similar materials. The nonuniformity of the texture increases in the case of the more porous sample (Fig. 2b).

One of the most advanced structural characterisation of cryogels was performed by Yun *et al.* [80]. They developed a capillary-based model to characterise the structure of monolithic cryogels applying such key parameters as the PSD, $f(d_i)$, determined from Eq. (3) (Fig. 3), the tortuosity (τ) and the skeleton thickness. The distribution function of the capillary diameter $f(d_i)$ can be expressed as a normal distribution [80]

$$f(d_i) = F(d_i) / \left(1 - \int_{-\infty}^{d_{\min}} F(d)\mathrm{d}d - \int_{d_{\max}}^{\infty} F(d)\mathrm{d}d \right) \quad (3)$$

$$F(d_i) = (2\pi\sigma^2)^{-0.5} \exp[(d_i - d_m)^2 / 2\sigma^2] \quad (4)$$

where σ is the standard deviation and d_m the mean diameter of capillaries in the cryogel column, d_i the capillary diameter in the range from the minimum pore diameter d_{min} to the maximum pore

diameter d_{max} within cryogels. Laminar flow, liquid dispersion and mass transfer in each capillary were considered but without taking into account the protein adsorption process. The model was solved numerically by the finite difference method applied to poly(hydroxyethyl methacrylate), PHEMA, cryogels prepared by radical cryo-copolymerisation. The authors analysed the axial dispersion behaviour, the pressure drop *vs*. flow rate performance, the non-adsorption breakthrough curves of lysozyme, bovine serum albumin, BSA, and concanavalin A, at various flow velocities in the cryogel beds [80]. The model developed was based on the structural characteristics (diameter, length, porosity, and permeability) and the analysis of the protein breakthrough curves gave detailed information on the textural and adsorption properties of the cryogels. Calculation results for the $f(d_i)$ distributions were in agreement with SEM images (Fig. 3). However, the direct calculations of the PSD with quantitative analysis of SEM images were not carried out in this paper [80]. Additionally, the $f(d_i)$ distributions with Eq. (3) can give a simplified picture because of the postulated shape of the distribution with Eq. (4). More accurate PSD based on improved quantitative treatment of images and adsorption data could be obtained using specific software (such as ImageJ, Fiji, Amira, VGStudioMax, Morpho+, *etc.*), regularisation procedures, maximum entropy method, interval arithmetic and other advanced methods of applied mathematics [2,3,54,105-108] (*vide infra*).

Jurga *et al.* [112] prepared bioactive scaffolds using cryogelation of dextran or gelatine linked to laminin. The textural characteristics of native cryogels were analysed using CLSM. The pore size and wall thickness distributions were calculated for one sample using quantitative analysis of CLSM images with ImageJ software [111]. However, a more detailed analysis of the structure-property relationships was not done. Bereli *et al.* [113] prepared PHEMA cryogel and estimated the average values of the specific surface area, pore volume, porosity and swelling degree. This PHEMA cryogel was modified by anti-human β-lipoprotein antibody molecules immobilised and oriented through protein A onto the cryogel to remove cholesterol from hypercholesterolaemic human blood plasma. Unfortunately, the relationships between the textural characteristics of the cryogel and its adsorption capability were not analysed.

According to our experience in the structural and adsorption characterisation of cryogels, the direct quantitative analysis of microscopic images can be the most appropriate procedure for PSD estimation but in the range of micro- and macropores only for both native hydrated and freeze-dried cryogels. HRTEM or HRSEM images of adsorbents can be used to determine the PSD of nanopores, which can be compared with the PSD determined with adsorption, SAXS, cryoporometry or thermoporometry methods [54]. To obtain microscopic images of cryogels, the freeze-drying procedure is frequently used. Therefore, there is a question about the influence of this procedure on the textural and structural characteristics of cryogels. For deeper

insight into this problem, these characteristics were studied in detail for both native hydrated and freeze-dried samples of the same cryogels [105-108]. The cryogel samples for SEM analysis were prepared by freeze-drying during relatively long time [105,106]. After drying, specimens were mounted on metal stubs fitted with adhesive carbon pads, sputter coated with palladium and examined using SEM. Cryo-imaging was carried out using SEM coupled to a cryo-unit (cryo-SEM) with a wet cryogel mounted onto a cryo-SEM holder, flash frozen by liquid nitrogen to -175^{o}C and freeze-fractured to produce a freshly cut surface. The frozen water was sublimed off at -65^{o}C for 30 min, and the sample was sputter-coated with palladium. Cryogel samples were also examined by confocal laser scanning microscopy with a Leica TCS SP5 CLSM [105,106]. A slice of approximately 1 mm in thickness was cut from the wet cryogel and stained with fluorescein isothiocyanate (FITC) solution (0.02 mg/mL in sodium phosphate buffer, pH 9.0) for 48 h in the case of (poly(2-hydroxyethyl methacrylate-allyl glycidyl ether, PHEMA-AGE gels) or 20 h in the case of gelatine, G, and gelatine-fibronectin, GF, gels. The samples were washed with buffer and water to remove non-bound FITC. The excitation and emission wavelengths used were 488 and 530 nm, respectively. Images were generated by optical sectioning in the XY-planes along the Z-axis with 50 optical sections with 1 μm intervals [3,105,106]. Multiphoton microscopy (MPM) with a Zeiss LSM520 Meta NLO microscope with a Coherent Chameleon XR Ti Sapphire pulsed laser at 800 nm was also used to study native hydrated cryogels [105]. Each sample was stained with FITC and prepared as for the CLSM study. MPM scanning was carried out in the Z-axis for 87 μm in depth with an image resolution 440×440 pixel. The image resolution depended on the laser beam penetration. Therefore, only stacks of 50 images were used to analyse the cryogel structure [105]. ImageJ [111] and Fiji [114] software was used to treat microscopic images with optical sectioning to determine the textural characteristics of the cryogels. With this software, fifty 2D images in each stack were transformed into 3D image. The porosity in the resulting image was calculated using Voxel counter plugin [115], and granulometry plugin [116] was used to estimate the PTWD. The surface area and pore interconnectivity was estimated using 3D objects counter plugin [111]. The morphology of PHEMA-AGE gel (Table 2, sample A) was studied using several imaging techniques such as SEM, cryo-SEM, MPM and CLSM (Fig. 4) [105]. Images of superhydrated cryogels were obtained using MPM and CLSM. These images were used to estimate the pore interconnectivity and PSD of 3D models reconstructed from the stacks of 2D images obtained by optical sample sectioning. The quantitative analysis of images was used to estimate the average values of the porosity, specific surface area, and pore size and wall thickness (Table 2). The MPM and CLSM techniques provided similar results but with

consideration of known limitation of image analysis with the mentioned software [111,114] (*vide infra*).

MPM (Fig. 4a) and CLSM (Fig. 4b) images represent the projections of fifty images in the stacks obtained along the Z-axis with 50 μm in depth. These projections show a 3D structure of native hydrated cryogels that is similar to the structure obtained with SEM (Fig. 4c) and cryo-SEM (Fig. 4d) of freeze-dried cryogels. Consequently, the morphology of cryogels was not strongly altered during drying. For image analysis with ImageJ software, a manual "by eye" approach was used to choose a proper threshold [111]. However, changes in the image threshold affect (Table 3) estimations of the porosity of PHEMA-AGE gel (Fig. 5). A number of options from fully automatic to a manual "by eye" approach is available in image analysis software for determining the 'best' threshold. Although seemingly more subjective, the latter method is actually quite consistent even between different individuals as it allows the user to explore different options with some software packages and see which areas of the image are affected by the changes. The methodologies used in automated routines are based on a statistical analysis, interpreting the histogram as two overlapping normal distributions of the tonalities associated with pores and walls, respectively. The increase in the porosity from 83.0 to 94.6% is accompanied by an increase in the mean pore size from 56 to 70 μm but the mean wall thickness decreases from 13 to 9 μm. Because of the subjective nature of this approach the results obtained from the image analysis can have certain deviations which are not too large (±5-10%). Additionally, the wall thickness calculated using the granulation plugin [116] could be overestimated because this program cannot distinguish the thickness of walls positioned perpendicular or parallel to the 2D image plane.

The analysis of PHEMA-AGE gels of a varied morphology examined with CLSM (Fig. 6) showed a distinguishable difference in the structure due to different polymerisation conditions [105]. Soft cryogels can display a different morphology in different layers. The cryogels produced in the form of small cylinders were characterised by uniform distribution along the sample. Three different regions (cross-sections) in the GF gel were analysed using CLSM. The pore size and wall thickness distributions were similar for all the areas analysed. The average porosity, surface area, average pore size and wall thickness were 87.4±2.5%, 0.049 $\mu m^2/\mu m^3$, 98±8.5 μm and 18.7±2.8 μm, respectively [105]. However, strongly different pictures were observed for larger samples.

The gelatine cryogel produced in the form of a thick sheet had different porosity in different layers with larger pores at the top (in contact with air during gel preparation) and smaller pores at the bottom (in contact with a glass substrate) (Fig. 7) [105]. The pore size in this gelatine gel gradually decreased from d = 76 μm at the top of the sheet (Fig. 7b), through 54 μm in the middle (Fig. 7c) and 30 μm at the bottom (Fig. 7d). The gradient porosity in different parts of the cryogel

sample was due to different regimes of heat exchange and hence freezing of the solution in the bulk and at the liquid-air and liquid-glass interfaces. Because of the temperature gradient the solution at the glass interface froze faster with formation of smaller ice crystals, while the solution at the liquid-air interface froze for longer time with formation of bigger ice crystallites, *i.e.* with larger pores in the cryogel [2-4]. Notice that the gelatine cryogel structure (Fig. 7) [105] strongly differs from the gelatine gel prepared at $T > 0^{o}$C [56] because the cryogelation resulted in less uniform and more macroporous structure of the gel.

The analysis of porous structure of cryogels in both native and freeze-dried states with the CLSM provided additional information on changes in the cryogel structure during and/or after drying. FITC stained PHEMA-AGE cryogel was freeze-dried and CLSM image of the dried sample was compared with that obtained for the hydrated intact cryogel (Fig. 8). This comparison showed that changes in the porous structure of the gel after freeze-drying were insignificant [105]. This result is in agreement with other observations with qualitative comparison of microscopic images of native hydrated and freeze-dried samples [34-39]. It should be noted that in the paper [105] the pore structure of freeze-dried and hydrated samples was compared quantitatively (Fig. 8). It was found that only a small diminution in the porosity, pore size and wall thickness of PHEMA-AGE gel occurred after careful drying (Fig. 8c,d). The observed changes could be attributed to some shrinkage of the polymer walls but with small changes in the textural characteristics of the whole gel determined mainly by micro/macropores (Figs. 4 and 8). These results confirmed that micro/macropores in both hydrated and freeze-dried cryogels have relatively thin walls. During drying the mean thickness of the walls decreased from 11.2 to 9.6 μm (Table 2). It can be concluded that most of the water in hydrated cryogels is located in micro/macropores (*i.e.* this water is mainly UBW/SAW with smaller contribution of WBW/SAW, Table 1) rather than in the swollen nano/microporous walls of the micro/macropores (*i.e.* with different combinations with SBW/WBW and SAW/WAW in nano/micropores of different sizes). A relatively small thickness of the walls provides the cryogel elasticity, sponge-like morphology and significant mechanical strength that are necessary for scaffold engineering.

The analysis of PHEMA-AGE gels of a varied morphology examined with CLSM (Tables 2 and 3, Fig. 6) [105] showed a distinguishable difference in their structure due to different polymerisation conditions. The porosity depended on the monomer concentration used and reaction conditions (Table 2). A higher monomer concentration resulted in smaller pores (samples B and D *vs.* A and C, respectively). A higher concentration of initiator in samples C and D enhanced the polymerisation rate resulting in the polymer formation prior to sample

freezing and it was already the polymer containing solution that froze rather than the monomer solution (samples A and B). Polymerisation then continued in the frozen sample and cryogels with aligned polymer walls and smaller pores compared to samples A and B were formed (Tables 2 and 3, Fig. 6).

All PHEMA-AGE gel samples [105] had relatively uniform pore size and wall thickness distributions (Fig. 9). The pore sizes of samples A, B and C were mainly in the range of 3-100 μm with mean pore sizes of 64, 47 and 41.4 μm, respectively (Table 2). Gel D displayed a more narrow pore size distribution (3-83 μm) with a mean pore size of 25.7 μm. The most narrow distribution of the wall thickness calculated using ImageJ with granulometry plugin was in gel B (2-14 μm) whilst gels A, C and D had broader wall thickness distributions (2-32, 2-23 and 2-32 μm, respectively) (Fig. 9b). Fiji software (local thickness plugin with auto-threshold) gave systematically smaller average wall thickness (t) values (Fig. 9a) than ImageJ with the granulometry plugin.

Dainiak *et al.* [35] synthesised and characterised macroporous sponge-like gelatine–fibrinogen (G–Fg) cryogels cross-linked with glutaraldehyde at different concentrations X (0.05–0.5%). These cryogels, G–Fg–GA(X) had a uniform interconnected open porous structure (porosity 90–92%) and pore sizes of 10–120 μm (Fig. 10a). Perhaps, the pore wall thickness was overestimated (Fig. 10b) because of the features of the image treatment software which cannot distinguish pore wall thickness for the walls differently oriented to the image plane. These cryogels were elastic and mechanically stable (with one exception for the gel at a minimal cross-linking degree at C_{GA} = 0.05%). Swelling kinetics (Fig. 10c) and degradation rate, but not the porous structure of the cryogels, were strongly dependent on the cross-linking degree (χ). A five-fold increase in χ resulted in ten-fold increase in the swelling degree for 2 min. A ten-fold increase in the χ value resulted in a very significant decrease in the degradation rate in a solution of protease [35].

Petrov *et al.* [117] synthesised polymer cryogels employing the UV irradiation technique and hydrogen peroxide as an initiator. Hydroxyethylcellulose and poly(N-isopropylacrylamide) (PNIPAAm) cryogels were characterised by a non-linear temperature dependence of the swelling degree (Fig. 11), which decreases with increasing temperature.

Wu *et al.* [118] prepared gelatine cryogels cross-linked with glutaraldehyde and characterised by great porosity (94-98.5%). Water adsorption (C_w) decreased with increasing content of gelatine (C_{gel}) during cryogelation from C_w = 25 g/g (C_{gel} = 1 %) to 6 g/g (C_{gel} = 5 %), as well as with increasing content of the cross-linker. Thus, there is no general regularity in the relationship between the water adsorption or swelling of cryogels and changes of the porosity, gel chemistry,

component contents because all these parameters differently affect the interaction of cryogels with water.

There are several simple equations for estimation of the textural characteristics of cryogels. The relative density (ρ^*/ρ_s) can be estimated from the wall thickness (t) and the average pore diameter (d) using a polyhedral unit cell model [119], such that

$$\rho^*/\rho_s = 8.19\left(t/d\right)^2. \quad (5)$$

For an open-cell tetrakaidecahedral unit cell with edges of circular cross-section, the surface area per unit volume (S_A/V) or specific surface area can be described by the relation

$$S_A/V = 3.65/l\left(\rho^*/\rho_s\right)^{1/2}, \quad (6)$$

where l is the edge length of the tetrakaidecahedral unit cell. The edge length can be related to the average pore diameter $d = 2.78l$, assuming that the internal volume of the tetrakaidecahedron is similar to that of a spherical pore with the same diameter d (or radius R) [120]

$$\rho^*/\rho_s = 3.33\left(R/l\right)^2. \quad (7)$$

Instead of Eq. (6) for S_A/V, it is possible to estimate this value from the d value only [121]

$$S_A/V = 0.718/d. \quad (8)$$

It has been demonstrated that both d and S_A/V values affect cellular activity within the hydrogel matrix, and changes in the pore size can strongly influence cell adhesion within hydrogels. Cell-mediated tissue (or matrix) contraction, largely by myofibroblasts, plays a critical role in many physiological and pathological processes, notably the organised contraction observed during wound healing [122]. The S_A/V value as a function of the average pore size, d and pore wall thickness, t showed that it strongly diminishes with an increasing d value [105]. However, it depends weakly on the pore wall thickness, t (S_A/V increases with t). As a whole, the S_A/V value re-calculated in m^2/g is about 1 m^2/g or smaller at the macropore volume of 10 cm^3/g or higher. Form these values one can conclude that the availability of micro/macropores of a very large volume is the main structural feature of cryogels. However, this results in a small value of the specific surface area of macropores.

The scaffold permeability (K) can be used as an important characteristic when described in terms of percentage compression (ε) (essentially equivalent to contraction), mean pore diameter (d), scaffold relative density ρ^*/ρ_s and a dimensionless system constant (A'') [123]

$$K = A''\left(d/2.785\right)^2(1-\varepsilon)^2\left(1-\rho^*/\rho_s\right)^{3/2}. \quad (9)$$

And if compression of the scaffold is absent ($\varepsilon \approx 0$), then $(1-\varepsilon)^2 \approx 1$.

Understanding of the influence of microscale topography of scaffolds on fibroblast attachment and motility is essential [124]. The NMR cryoporometry technique was used to analyse nanopores (d < 100 nm) in collagen hydrogels, but without detailed analysis of micro/macropores [52]. More detailed structural characterisation of glycosaminoglycan-cross-linked collagen hydrogel INTEGRA^{TM} was carried out using a combined CLSM–NMR-cryoporometry approach [106]. The whole hierarchy of the porous structure of this hydrogel is of interest because it is commonly used for wound healing, chiefly for burns and ulcers [125-130]. Additionally, analysis of interactions of proteins (bovine pancreatic tripsin inhibitor (BPTI), bovine serum albumin (BSA), and human serum fibrinogen (Fg)), normal primary human skin fibroblasts, and 3T3 mouse fibroblast cells with the collagen hydrogel was carried out using diffusional analysis, confocal laser scanning microscopy, and quartz crystal microbalance (QCM) methods [106] (*vide infra*).

The structure of freeze-dried PVA and PVA/AC cryogels was studied using SEM imaging [107,108]. For porosimetry analysis of PVA or PVA/AC, the cryogels were dried in *vacuo* at 40^{o}C for 24 h until a constant weight was achieved. Nitrogen adsorption-desorption isotherms were used to compute the PSD using two models of mixed pore structures with (i) slit-shaped and cylindrical pores for carbons using the non-local DFT (NLDFT) method [131] (Quantachrome software, version 2.02) and (ii) slit-shaped (carbon) and cylindrical (carbon or polymer) pores and voids between spherical carbon particles, SCV (modified Nguyen-Do, MND, method) [132-140]. The differential PSDs $f(R) \sim \mathrm{d}V/\mathrm{d}R$ ($\int f(R)\mathrm{d}R \sim V_p$, where R is the pore radius or half-width, were converted into incremental PSDs ($\Sigma\Phi(R_i) \sim V_p$) for a better view of the PSDs over the total pore range. The errors of the pore model were calculated as in [134]

$$\Delta w = S_{BET}/S_{NLDFT} - 1. \quad (10)$$

Mercury porosimetry was used to determine the micropore and macropore size distributions of the samples (differential PSD $f(d) \sim \mathrm{d}V/\mathrm{d}(\log d)$, where d is the pore diameter) [107,108].

For SEM analysis, the freeze-dried gel samples were sputter coated with a 50 nm thick layer of gold [107,108].

The freeze-dried PVA gel alone (Fig. 12a) or that containing AC microparticles (Fig. 12b) included broad pores (micro- and macropores) with pore walls of 1-10 μm in thickness [107,108]. The micro/macropore walls also have nano- and micropores. However, the volume of these pores was much smaller (0.1 to 0.14 cm^3/g, Table 4) than the macropore volume in the PVA gels (3.8-5.7 cm^3/g, Table 5) or the nanopore volume in the ACs (0.8-2.1 cm^3/g, Table 4). The hybrid classification mentioned above includes five types of pores which is sufficient to analyse the pore size distributions over the total range of pores of materials studied here (Fig. 13) [107,108].

The carbonised material (Table 4, C-1) produced from porous phenol-formaldehyde resin and ACs (C-2 – C-7, burn-off degree 32-52%), produced by activation of C-1 with carbon dioxide (MAST Carbon International Ltd) (or by activation of other similar two carbonisates at S_{BET} = 581 and 631 m^2/g prepared with the same precursor) have different porosity. Their PSDs have some similarities such as the similar shape of the narrow nanopores but larger differences in the shapes of the middle and broad nanopores (Fig. 13a). AC sample C-7 was additionally heated in air at 300^oC for 15 h. This treatment did not strongly change the porous characteristics of the AC but added oxygen containing surface functional groups. Therefore, the sample C-7 was selected for preparation of the PVA/AC composites [107]. The textural, adsorption, electronic and other characteristics of similar AC were described in detail [135-140].

All tested carbons have broad PSDs over the total range of nanopores (Fig. 13a) and include voids between nanoparticles forming microglobules and granules (Fig. 12b, C-7) [133-140]. An increase in the burn-off degree of ACs can cause an increase in the contribution of narrow nanopores (Table 4) and a PSD peak of broad nanopores shifted towards narrower pores (Fig. 13a) due to compaction of the secondary particles (aggregates of nanoporous nanoparticles). There is a tendency of an increase in the volume of all types of nanopores with increasing burn-off degree because the bulk density of AC typically decreased (*e.g.* from 0.53 g/cm^3 for carbonisate to 0.21 g/cm^3 for AC at 49% burn-off) [136]. The presence of broad nanopores provided good transport properties for the ACs studied [107,108,135-140]. However, these properties can be changed during preparation of PVA/AC composites. Freeze-dried PVA cryogels typically have middle nanopores at R_{mn} = 1-10 nm, broad nanopores at R_{bn} = 40-100 nm (based on nitrogen adsorption) (Fig. 13c,d), micropores and macropores (based on mercury porosimetry) (Fig. 13b). The porosity of PVA gels in the nanopore range is much smaller than that of ACs (Fig. 13c, Table 4) and it is due to the presence of pores in the nano/microporous walls of micro/macropores [2-4,105-108]. On the contrary, the macroporosity (based on the mercury porosimetry) of PVA gels was greater than that of AC (Table 5, Fig. 12). In the case of freeze-dried PVA and PVA/AC samples, the contribution of narrow nanopores was much smaller (Fig. 13c,d) than that of ACs alone. However, the influence of AC on the PSD of PVA/C-7 samples can be observed, especially for PVA7/C-7 demonstrating certain contribution of narrow nanopores (Fig. 13c,d). According to the mercury porosimetry data, the specific surface area of PVA7/C-7 was S_{Hg} = 143 m^2/g (Table 5), which was greater than S_{BET} (Table 4) [107]. Notice that the PSDs calculated from the nitrogen adsorption-desorption isotherms and mercury porosimetry are complementary (Fig. 14) because nitrogen cannot completely fill pores at d > 100 nm and mercury poorly penetrates into narrow nanopores. The total pore volume of PVA and PVA/AC samples was between V_{Hg} = 3.8 (PVA3) and 5.7 (PVA2) cm^3/g (Table 5). These

values were much greater than $V_{p,}$ measured with N_2 adsorption (because nitrogen was adsorbed mainly in the porous walls of micro/macropores), due to the micro/macroporous nature of the PVA gel materials (Fig. 12) [107].

In the case of another set of hybrid AC/PVA cryogels [108], prior to their incorporation into PVA/GA cryogels, the microspherical AC samples (beads of 10-30 μm in diameter) were shown to contain different internal porosity (V_p) and specific surface area (S_{BET}) with significant contributions from narrow to broad nanopores (Table 6 and Fig. 15 show representative samples of ACs, PVA/GA and PVA/GA/AC). ACs are characterised by broad PSD of a complex shape as seen in Fig. 15 [108] and similar to the PSD shown in Fig. 13. In contrast to description of the first series of PVA/AC samples (Tables 4 and 5, Figs. 12-14) [107], the analysis of the second series of samples (Table 6) was improved using a self-consistent regularisation (SCR) procedure with the model of slit-shaped and cylindrical pores and voids between spherical nanoparticles (SCV), *i.e*. SCV/SCR method, as well as the textural characteristics of certain composites [108]. Therefore, the analysis of the second series of PVA/AC samples is described here in detail. The shapes of carbon nanoparticles, which are strongly aggregated, and voids between them are complex (Fig. 16). However, motifs of slit-shaped pores in AC nanoparticles and cylindrical pores and voids between nanoparticles can be found in the SEM image. According to calculations with the SCV/SCR model, slit-shaped pores provide the main contribution to the carbon porosity (Table 6, c_{slit}), and the contribution of cylindrical pores (c_{cyl}) is larger than that of voids between spherical particles (c_{void}). The small c_{void} values are in agreement with small Δw_{NLDFT} values for the SC model (NLDFT) (Table 6) showing a small deviation of the pore shape from the model [108].

The mercury porosimetry data (Fig. 17) showed [108] a significant contribution of broad nanopores and micropores in the same range of pore size as the MND PSDs showed (Fig. 15). These pores can be attributed to voids between both nanoparticles in microparticles (Fig. 16) and microparticles *per se* [108]. The main peak of the carbon PSDs at $d \sim 0.1$ μm (Fig. 17) corresponds to the broad nanopore peak obtained from the nitrogen adsorption with the complex pore model (Fig. 15). Consequently, one can assume that AC particles maintain their integrity throughout measurements at high Hg pressures [108]. However, during similar measurements of PVA/GA and PVA/GA/AC composites, a significant loss of the macroporosity was observed (by an order of magnitude, compare the PSD intensity for AC and PVA/GA, PVA/GA/AC in Fig. 17) due to the high Hg pressure used and the softness of the polymeric materials [108]. Comparison of the PSDs based on mercury porosimetry and SEM image analysis of a PVA/GA sample (Fig. 18) showed a clear shift of the former PSD towards smaller pore sizes. According to SCV/SCR calculations [108], the contribution of slit-shaped pores (Table 6, c_{slit}) decreased but the contribution of

cylindrical pores (c_{cyl}) and voids (c_{void}) increased in PVA/GA/AC composites in comparison with ACs alone. The broad PSDs, that are important for the adsorption of both small and large molecules and thus for the practical application of ACs as medicinal adsorbents, can be adversely affected by the interaction of the carbon micro-particles with PVA (Fig. 19).

GA cross-linked PVA can cover the outer surface of AC beads by continuous or fragmentary films. PVA/GA totally blocked or filled the narrow nanopores (R < 1-2 nm) since linear polymers, GA, monomers and oligomers can penetrate into narrow pores and be cross-linked there. AC surface hydroxyls can participate in cross-linking reactions with GA/PVA. Additionally, GA can penetrate into nanopores of AC and polymerise there. These effects significantly reduced accessibility to middle nanopores at 1 < R < 25 nm. There was a shift of the PSD of PVA/GA/AC in comparison with PVA/GA at R = 1-2 nm (NLDFT for all samples and MND/SCV/SCR for certain samples) [108]. This result can be explained by the strong interactions that exist between the PVA/GA and AC surface (Fig. 20). Pores at 1 < R < 10 nm gave the main contribution to the nanoporosity of PVA/GA/AC samples. However, the random structure of micro/macropores in PVA and nanopores in both AC particles and PVA/GA films did not allow detailed analysis of the features of pores and their assignment to PVA/GA or AC. SEM image (Fig. 16) showed the inner texture of AC consisting of aggregates of nanoparticles (20-50 nm) with voids between them constituting transport broad nanopores, micropores and macropores. However, in the case of PVA/GA/AC composites (Figs. 19 and 20), multilayer PVA/GA coverage can block this inner texture from adsorbates [108].

The pore wall thickness of the PVA/GA gel (~1-3 μm for dried samples) was smaller than the AC microparticle size (Figs. 19 and 20) [108]. The pore walls in PVA/GA cryogel are soft and flexible. Therefore, during mercury porosimetry measurements at high pressures, the contribution of pores at 0.03 < d < 0.3 μm was larger for PVA/GA/C-1 than for GA/PVA alone (Fig. 17a). This can be due to the pore contribution of AC (Fig. 20) [108].

Thus, synthesis of PVA/GA cryogel in the presence of the carbon microparticles resulted in a considerable diminution of the accessibility of AC surface and pores even for small nitrogen molecules [108]. Macropores visible in SEM images of AC particles (Fig. 20) are not the main adsorption space for nitrogen (Fig. 15) but mercury can completely fill them during the porosity measurements (Figs. 17 and 18). Therefore, a mechanical mixture of ACs with PVA/GA cryogel in the cross-linker GA solution was prepared to attach AC microparticles to the PVA macropore walls. However, the flexibility of the PVA pore walls and the presence of GA monomers and oligomers as well as mobile PVA tails and trains caused too strong an attachment of AC microparticles to the PVA structures by GA (or blocking of AC pores by GA oligomers). A relatively low specific

surface area of these samples (at maximal AC content C_C = 62.4 wt.% S_{BET} = 119 m^2/g) can be considered as evidence of cross-linking of AC surface hydroxyls with PVA by GA and GA polymerisation in AC pores. Therefore, the AC surface blocking by PVA/GA was significant but incomplete in contrast to the initial series of PVA/GA/AC samples (compare PSDs in Figs. 15 and 21) [108]. An increase in the AC content in PVA/GA/AC resulted in an increase in the contribution of narrow nanopores (Fig. 21) and the accessible AC pore volume increased (compare the PSD intensity in Figs. 15 and 21) [108]. One can assume that better results can be obtained at $C_{PVA} < 10$ wt.% in PVA/AC and smaller amounts of a cross-linker because both components can block/fill pores of AC particles. However, an increase in the AC content to 45.4-62.4 wt.% could cause a decrease in the composite material elasticity [108]. A six-fold decrease in the C_{GA}/C_{AC} ratio results in the PVA/AC composite with much higher S_{BET} value (499 m^2/g) (Fig. 21, Table 6, PVA/C-3). This S_{BET} value is close to the contribution of AC in the composite. In other words, practically total AC surface in this composite is accessible for nitrogen molecules.

The AC surface includes different oxygen-containing functionalities (-COOH, ≡COH, ≡C-O-C≡, >C=O, ≡C-O-C=O) [95,99,141-144], which can strongly interact with PVA through hydrogen bonds ($>O_{AC}\cdots HO_{PVA}$ or $\equiv COH_{AC}\cdots O(H)C_{PVA}\equiv$) and dispersion forces or be cross-linked (COH, COOH) by GA. In order to model these interactions, quantum chemical calculations of complexes of a PVA fragment (four units) with different AC functionalities were carried out with consideration for solvation effects using the IEFPCM method (DFT B3LYP with the 6-31G(d,p) basis set) and the geometry optimisation using the HF/6-31G(d,p) method [108].

Changes in the free energy (ΔG) upon PVA complex formation were in the range of −14 ÷ −30 kJ/mol and −30 ÷ −55 kJ/mol (per a bond or a hydrogen bond) for hydrophobic (without O-containing groups) and hydrophilic O-containing functionalities of the AC models, respectively [108]. These values are close to that for complexes between water molecules and both PVA and AC. However, PVA having many contact points with the carbon surface, can displace a portion of water molecules from both the pores and outer surface of AC particles as it is shown in a large model (Fig. 22) calculated using PM6 method [108]. A similar displacement of interfacial water occurs during interactions of macromolecules with a surface of different adsorbents [50,51,53,54]. This effect is stronger in the case of nanooxides with open surface of nonporous nanoparticles well accessible for macromolecules in contrast to narrow nanopores of AC. Therefore, a significant portion of water remains in narrow pores of the AC particle interacting with PVA (Fig. 22).

The initial AC particle model [108] (Fig. 22) was developed according the Monte Carlo modelling results [145-147] using the CharMM force field [148] and then its geometry was optimised using semiempirical PM6 quantum chemical method with the MOZIME algorithm [149].

Then, water molecules (~1100H_2O) were added to this AC particle using the solvation box algorithm with VEGA ZZ 2.4 [148] and the geometry was optimised by the PM6/MOZYME method. A polymer shell fragment with GA (~5 wt.%) cross-linked PVA (~2000 atoms) was formed at the hydrated AC particle and the geometry of the system was optimised using the CharMM force field and then the PM6/MOZIME. The PVA/GA shell fragment with two-three monolayers has mobile tails and trains that allow it to form relatively dense coverage of the hydrated AC particle from one side (Fig. 22a). The PVA/GA displaces only a certain portion of water from AC particle in the contact zone (Fig. 22). Calculations (with PM6) of the interaction energy gave ΔE = −10 kJ/mol (per a water molecule or a PVA-AC bond) for PVA/GA-water interactions, −24 kJ/mol for PVA/GA-AC, −32 kJ/mol for AC-water, and −41 kJ/mol for PVA/GA-AC-water [108]. These values are in agreement with other results on interactions of AC with water [144]. The interactions between PVA and AC are weaker than that between AC and water but stronger than interactions between PVA and water. Despite this, PVA can displace water molecules from AC because of kinetic/statistic effects since the number of intermolecular bonds between PVA and AC is much greater than the number of bonds between a water molecule and the AC surface [108]. To model the opposite effects such as the displacement of a small PVA fragment by water molecules from narrow pores (~0.7 nm in size), the pore size was fixed by the GA-cross-linking of corners of two carbon sheets with several O-containing functionalities [108]. The ΔG values for the PVA fragment (four units) and water complexes in this pore were similar (~ −30 kJ/mol). However, out of five water molecules placed in the pore around the PVA fragment three escaped in contrast to the PVA fragment [108]. Despite the positive ΔG value for this complex, the PVA fragment was not removed from the pore due to high energetic barrier of this motion. Additionally, PVA can form relatively tight complexes with the AC surface in the presence of water (Fig. 22). Strong retention of PVA (both tails and trains), as well as GA oligomers and polymers, within narrow pores and at the outer surface (*i.e.* macropores, Fig. 20) of AC particles explains textural features of PVA/GA/AC composites with PVA/GA-blocked narrow pores of AC particles (*e.g.* for N_2 molecules during the adsorption measurements shown above). Notice that PVA tails and trains have a high mobility in cryogels. Consequently, to maintain the AC porosity, carbon particles should be attached to the surface of PVA/GA macropores after cryogelation or AC pores should be filled by an inert compound (*e.g.* paraffin) which can be removed after preparation of PVA/GA/AC composites by fast heating to partially destroy the PVA/GA shells. AC microparticles can be distributed in macropores by shaking AC with macroporous PVA/GA cryogel (with pores of 30-100 μm in size) as it has been used to prepare the mechanical mixture with ACs and PVA/GA; however, the amounts of the cross-linker should be lower than 1 wt.% (Fig. 21, the best result was obtained at

C_{GA} = 0.5 wt.%, C_{AC} = 3 wt.% and C_{PVA} = 5 wt.% in the reaction medium).AC particles can be fixed at the macropore walls due to intermolecular bonds or weakly cross-linked to PVA by GA (*i.e.* with loose polymer brushes as described above). To prevent the removal of AC particles by a liquid flow through the PVA membranes (*e.g.* in haemoperfusion or filtration), they can be attached to the pore walls by covalent bonds using low amounts of PVA and/or GA to avoid significant blocking of pores by PVA/GA (Figs. 21 and 22). The oxidation of the carbon surface can be used to increase interactions between the hydrophilic polymer and hydrophilic segments of the AC surface. The formation of covalent bonds is possible (*e.g.* –C(O)OH of carbon + C(H)(OH)= of polymer → -C(O)OC(H)= + H_2O) but unlikely without coupling agents. If free aldehyde groups of cross-linked PVA/GA are blocked with ethylenediamine there is a possibility to form a link to the surface COOH group via ion-pair formation. However, the chemical modification of ACs by oxidation in air did not practically affect the textural characteristics of the PVA/GA/AC composites because of the high amounts of PVA/GA forming multilayer coverage on the AC microparticles [108].

Changes in the free energy in the cross-linking reactions calculated with consideration of the solvation effects using the IEFPCM/B3LYP/6-31G(d,p)//HF/6-31G(d,p) method showed [108] that the reactions can more easily occur according to the mechanism described in the works [150,151] with the participation of PVA (a four-unit fragment used) rather than AC (modelled by a two-ring fragment). For instance, ΔG = –80.1 kJ/mol (cross-linking PVA-GA-PVA with the formation of four C-O-C bonds and elimination of two H_2O molecules), –7.6 kJ/mol (AC(OH)-GA-(HO)AC), 4.3 kJ/mol (AC(COOH)-GA-(HOOC)AC), –41.4 kJ/mol (AC(COOH)-GA-PVA) and –12.9 kJ/mol (AC(OH)-GA-PVA). These differences in the ΔG values can be explained by a higher flexibility of the PVA chain in comparison with the O-containing functionalities attached to the aromatic structures in ACs. There is an additional aspect of the influence of these AC functionalities since the carboxylic groups can catalyse the oligomerisation and polymerisation of GA in pores of AC particles. These larger molecules can more effectively block the AC nanopores during the preparation of the mechanical mixture with GA-cross-linked PVA and ACs in the GA solution. A significant loss of the porosity and accessible AC surface was observed for the samples prepared at relatively high content of GA [107,108]. Therefore, the GA amounts should be reduced (see Fig. 21) to decrease the negative effects of blocking the AC surface.

Thus, PVA/GA/AC composites prepared at high content of GA using the cryogelation technique with the addition of carbon particles before PVA cross-linking by GA had by porosity similar to the GA/PVA cryogel porosity due to the pore blocking in AC particles by the polymer/GA coverage [107,108]. An increase in the AC content in composites, prepared as a mechanical mixture with subsequent attachment of ACs to the PVA macropore walls by the cross-

linker, increased the contribution of nanopores, which became more accessible. Apparently, the flexibility of mobile PVA tails and trains and the availability of GA oligomers resulted in a strong blocking of ACs pores due to the reactions of PVA/AC with GA. However, the porosity and specific surface area of PVA/GA/AC samples increased with increasing AC content. The five-fold increase in the AC content in PVA/GA/AC composites, resulted in a strong increase of the initial adsorption rate of low (*e.g.* dyes) and high (*e.g.* proteins) molecular weight compounds, which was similar to that for pure AC. A much stronger increase in the textural characteristics of the composites was observed in the case of diminution of the cross-linker GA content by an order of magnitude [108]. Quantum-chemical calculations showed that despite the fact that the values of energy of each of the hydrogen bonds between PVA or water molecules with O-containing functionalities of AC were similar, PVA macromolecules could displace water molecules from the carbon particle surface. However, water cannot displace polymer from the AC surface, especially from narrow pores. This resulted in the formation of a tight PVA/GA shell covering the AC microparticles [108]. Loose polymer brush coverage of the surface of cryogel macropores can be used for binding AC microparticles without a significant loss of the accessible surface and nanoporosity of these particles.

4.2.SAXS

X-ray diffraction methods can be used to characterise not only crystalline but also amorphous and soft materials such as cryogels, especially filled by solid nanoparticles or microparticles. Liu *et al.* [152,153] prepared freeze-dried cryogels using an aqueous suspension of chitosan/xanthan gum without or with Na^+-montmorillonite nanoclay filler (MF). The cryogels were freeze-dried to produce macroporous clay-filled foams with improved mechanical properties. The authors used two freezing methods such as contact freezing with a heat exchanger and immersion freezing in a cryo-bath. SEM images showed that rapid and slow contact freezing produced materials with the mean pore size of 40 μm and 68 μm, respectively. This is due to the formation of larger ice crystallites during slower freezing. Immersion freezing samples had bamboo-like straight structures with pore layer spacing of 22 μm. Small angle X-ray scattering (SAXS) data showed that the polymeric networks were modified by the exfoliated nanoclay. Some of these data are analysed below.

Pore size distribution can be estimated from the SAXS data using integral equation [154]

$$I(q) = A \int_{R_{\min}}^{R_{\max}} \frac{(\sin qr - qr\cos qr)^2}{(qr)^6} v(r) f(r) dr \qquad (11)$$

where $I(q)$ is the scattering intensity, $q = 4\pi\sin(\theta)/\lambda)$ the scattering vector value, θ the scattering angle, and λ the wavelength of incident X-ray, A a normalisation constant, $v(r)$ the volume of a

pore with radius r (proportional to r^3) and $f(r)\mathrm{d}r$ represents the probability of having pores with radius r to $r + \mathrm{d}r$; R_{min} (= π/q_{max}) and R_{max} (= π/q_{min}) correspond to lower and upper limit of the resolvable real space due to instrument resolution. For calculations of the PSD for MF materials using SAXS data [152], we used here two SAXS curves (Fig.23a) for MF1 and MF2 cryogels (freezing rate of 2 and 0.25°C/min, respectively) as representative samples. The PSD were calculated over very broad pore size range (Fig. 23b). Therefore, the differential PSD $f(d) \sim \mathrm{d}V/\mathrm{d}d$ ($\int f(d)\mathrm{d}d \sim V_p$, where d is the pore diameter) were converted into incremental PSD, IPSD $\Phi(d_i) = (f(d_{i+1})+f(d_i))(d_{i+1}-d_i)/2$ giving the sum $\Sigma\Phi(d_i) \sim V_p$, for better view of the PSD over the total range of pore sizes. This is useful especially at large d values where $\mathrm{d}V/\mathrm{d}d$ typically has very low intensity. The average value $<d>$ of the distribution function $f(d)$ was calculated as the ratio of the first and zero moments of the distribution functions using equation

$$< d >= \int_{d_{min}}^{d_{max}} df(d)\mathrm{d}d \Big/ \int_{d_{min}}^{d_{max}} f(d)\mathrm{d}d \qquad (12)$$

The $<d>$ values equal to 70.1 and 95.8 μm for MF1 and MF2 cryogels, respectively, show that these materials are micro/macroporous. These values are in agreement with SEM images [152]. The $\Phi(d)$ distributions (Fig. 23b) demonstrate the presence of narrow pores which can be attributed to inner pores in clay particles and voids between clay particles as well as pores in the walls of gel macropores. Thus, SAXS based PSD show a complex structure of the cryogel pore walls.

Ehrburger-Dolle *et al.* [155] and Perez *et al.* [156] used SAXS to characterise thermo-responsive macroporous cryogels with poly(*N*-isopropylacrylamide), pNIPA, cross-linked by *N*,*N*´-methylenebisacrylamide (MBAAm)synthesised in aqueous or dioxane/water (70:30 v/v) media. According to SEM images (Fig. 24) these materials are characterised by very different porosity and PWTD. The SAXS data [157] showed the formation of well-defined nanodomains in cryogels related to fluctuations in cross-link density of the materials. Treatment of SEM images here (Fig. 24) using Fiji software (local thickness plugin [114]) shows that the cryogel synthesised in the aqueous medium has much broader pores (Fig. 25a) than the cryogel synthesised in organic/water medium (Fig. 25b). The significant difference in the pore wall thickness (t_w) of cryogels prepared in aqueous (t_w = 1-2 μm) or dioxane-water (t_w = 10-40 μm) media [149] can be explained by the colligative properties of the organic/water mixture [1,50,54] that forms thicker unfrozen layers between ice crystallites in which the cross-linking occurs. Additionally, the water amount was lower in the latter case. Therefore, the d-MBAAm/pNIPA cryogel porosity decreases in comparison with w-MBAAm/pNIPA. The PSD based on SEM images (Fig. 25) and SAXS based PSD (Fig. 26) are in agreement but rather qualitatively. The observed differences in the PSD shapes can be

explained by features of both experimental (SEM and SAXS) and computational (Fiji and regularisation procedure) treatment methods, as well as by a difference in the amounts of samples used in these measurements. This can affect the average values because of a certain nonuniformity of the cryogels studied (*e.g.* compare left and right parts of image shown in Fig. 24a).

4.3. Thermogravimetry, DSC and thermoporometry

Thermogravimetry (TG) method can be used to estimate the amounts of water and the temperature profile of water desorption, which depends on both textural and chemical features of the materials, in native and dried cryogels. The TG/DTG data can be used in thermoporometric calculations of the PSD because desorption of water from narrower pores occurs at higher temperatures.

Bai *et al.* [157] compared properties of epichlorhydrin cross-linked PVA (CPVA) (with calcium carbonate used as a pore-forming agent) and PVA prepared by a more traditional freeze–thawing method, TPVA. The TG data (Fig. 27) showed that the amounts of water and thermal stability of the materials depend significantly on the methods of synthesis. From these data, one can conclude that the TPVA sample is more macroporous and thermostable than the CPVA sample.

The weight loss during TG desorption of water from the collagen hydrogel (type I bovine tendon collagen cross-linked by glycosaminoglycan, GAG), an inner collagen/GAG, CG, layer from INTEGRA^{TM} bilayer matrix wound dressing (Integra Life Science Corp., Plainsboro, NJ, USA) [106] corresponds to approximately 98 wt.% (aqueous medium) and 96 wt.% (PBS) at 220^{o}C (Fig. 28a). The main desorption of water occurs at $T < 100^{o}$C (aqueous medium, Fig. 28a, curve 3) or $T < 105^{o}$C (PBS, curve 1). Such large amounts of water in swollen collagen hydrogels are typical. This small difference in water content is due to water binding by salt and residual salt weight. However, in both cases desorption of water occurs mainly at $T < 100^{o}$C. The relatively low temperature of water desorption from collagen hydrogel suggests that most of it is unbound, UBW, bulk or weakly bound water, WBW (Table 1).

The TG plot $\Delta m(T)$ (Fig. 28a) [106] may be converted into a plot where adsorbate volume loss is placed versus pore radius, $\Delta V(R)$ using the Kelvin equation $\ln p/p_0 = -2\gamma V_M/(R_k R_g T)$ [158]. This equation gives the relationship between the vapour pressure of a liquid over curved (in pore) and flat liquid surfaces, p and p_0, respectively, R_k is the radius of the liquid meniscus, γ the surface tension, and V_M the molar volume of the liquid. In our experiments, p is an external pressure equal to the atmospheric pressure and p_0 is the vapour pressure of the liquid at a given temperature.

The PSD of the CG hydrogel calculated here using the TG thermoporometry, which is described in detail elsewhere [158], corresponds to nanopores at 3-6 < R < 50 nm. These pores can

be assigned to pores in the walls of macropores. The PSD depends (especially at $R < 10$ nm) on the type of dispersion medium (PBS or water). These results can be compared with the DSC and NMR spectroscopy data (*vide infra*) obtained for different temperature ranges to get a more comprehensive picture of the interfacial behaviour of water in the hydrogels [50,54,106]. Water located in the micro- and macropores can be assigned to NBW and it desorbs mainly at $T < 100^{o}$C [50,54]. The TG weight loss during water desorption is consistent with the ρ^*/ρ_s value (CLSM) and the very low contribution of bound water registered by the ^{1}H NMR spectroscopy and cryoporometry [54,106]. This result is also in agreement with other ^{1}H NMR measurements of hydrogels [50,54] showing that the volume of weakly bound water (located in broad nanopores and frozen at temperature close to 0^{o}C) is much greater (by more than an order of magnitude) than the volume of strongly bound water (located in narrow and middle nanopores and frozen at $T < -10^{o}$C). The results (Fig. 28a) show that most of TG desorbed water corresponds to non-bound water (*i.e.* frozen at 0^{o}C) located in micro- and macropores of hydrogels. This type of water located in the CG hydrogel is of importance for diffusion of nutrients and proteins, and cell transport within the macropore network in this material used as the inner layer in INTEGRA^{TM} bilayer matrix wound dressing (Integra Life Science Corp., USA). Strongly bound water is characterised by a very low activity as a solvent [1,50,54]. Therefore, many processes (dissolution, diffusion) in broad macropores and narrow micropores and nanopores can be very different. Additional information on these features of water bound in cryogels can be obtained using DSC and NMR methods [50,54].

Differential scanning calorimetry gives the thermodynamic characteristics of hydrated or dried materials and processes of freezing-melting, glass transition, desorption, phase transition, decomposition, *etc.*), and provides information for the textural characterisation with thermoporometry. The latter is possible because melting and freezing processes depend on confined space effects [54]. During freezing liquid water transforms into ice along the pores from their open end where the liquid is in contact with bulk ice. Melting of ice is initiated from the liquid film at a surface of narrow nanopores and propagates towards broader pores and the bulk. Certain DSC results are analysed here with respect to the interfacial phenomena in cryogels.

Burova *et al.* [159] prepared an imprinted thermoresponsive cryogel with N-isopropylacrylamide and N-[3-(N,N-dimethylamino)propyl]acrylamide in the presence of ibuprofen as a molecular template. A reversible volume phase transition upon heating, which causes thermotropic collapse, of the swollen cryogel was studied by the DSC method over a broad temperature range. In the absence of small-molecular ligands, the transition temperature, enthalpy, and transition temperature width were 82.5^{o}C, 9.8 J/g and 32.2^{o}C, respectively. Significant changes in these parameters were observed in the presence of ibuprofen as the template ligand. With

ibuprofen concentration increasing, the transition temperature decreased to 30°C, the enthalpy passed through a minimum, and the transition temperature width reduced. The binding constants of ibuprofen by the cryogel in the collapsed and swollen states were 119 and $5M^{-1}$, respectively. This showed preferential binding of ibuprofen by the shrunken cryogel. This result can be explained by the typical behaviour of adsorbate molecules with nonpolar and polar fragments adsorbed in broader (poor adsorption because of low adsorption potential) and more narrow (good adsorption due to high adsorption potential) pores of a polar adsorbent, such as the cryogels studied, being in aqueous media [50]. The excess absorption of ibuprofen by the cryogel due to its collapse amounted to 0.327 mmol/g, while for all other ligands (structural analogues of ibuprofen) this parameter did not exceed 0.016 mmol/g. These data confirm that the imprinted cryogel possessed a selective molecular memory toward the template ligand. Thermodynamically this result can be explained by larger changes in the free energy upon the adsorption of the ligand into a cavity of appropriate size and geometry because it increases the adsorption energy but weakly affects the desolvation energy. However, in this paper [159] the DSC data were not used to estimate any textural characteristic of cryogels.

DSC measurements of PHEMA cryogels were carried out using samples in both hydrated and dried states [105]. The DSC data relating to the melting of frozen water confined in hydrogels as a function of temperature at a certain heating rate were used to determine the size of water clusters, nano- and microdomains bound to/in the gel pore walls using the thermoporometry method [1,50,51,54]. Water or other liquids can be frozen (or melted) in narrow pores at temperatures below normal freezing point. The relationship between the freezing temperature depression of water confined inside a cylindrical pore of radius R_p can be described by the Gibbs-Thomson equation:

$$R_p(nm) = 0.68 - \frac{k}{T_m - T_{m0}}, \qquad (16)$$

where T_m and T_{m0} are the melting temperatures of confined and bulk water, respectively, and k = 32.33 K nm [160]. The k value depends on the nature of the materials by analogy to NMR cryoporometry [54,55]. For simplicity, T_{m0} = 0°C can be used here. The equation constants were determined for the DSC melting thermograms of bound water [160]. The differential pore size distribution dV/dR can be calculated from the DSC melting thermograms using equation [161-163]

$$\frac{dV}{dR}(cm^3nm^{-1}g^{-1}) = \frac{\frac{dq}{dt}(T_m - T_{m0})^2}{k\rho\beta m\Delta H(T)}, \qquad (17)$$

where dq/dt, ρ, β, m and $\Delta H(T)$ are the DSC heat flow, the water density, the heating rate, the

sample mass and the melting enthalpy of water, respectively. The ΔH values as a function of temperature can be estimated as follows [161-163]

$$\Delta H(T)(\mathrm{J\,g^{-1}}) = 332 + 11.39(T_m - T_{m0}) + 0.155(T_m - T_{m0})^2, \quad (18)$$

at T_{m0} = 0°C. Notice that the position of melting endotherm depends slightly on the hydration degree and the heating rate (Fig. 29a-c). It was assumed that the pore wall surface is smooth (therefore S< 1 m^2/g for micro/macropores). However, the DSC thermoporometry calculations of the specific surface area gave S ~ 80-90 m^2/g for A-D samples (Table 2) because of the presence of nanopores in the micro/macropore walls [105]. Water analysed with DSC thermoporometry can be bound in these nanopores (1-30 nm in radius, Fig. 29d-f) located in the micro/macropore walls of several μm in thickness (Fig. 9) [105].

The left peak or a shoulder of the main PSD peak (Fig. 29d) [105] corresponds to nanopores with the size close to that of icosahedral nanodomains (~3 nm in size) of water [1,50,54]. Other water structures observed are of larger sizes (Fig. 29d-f). The freezing temperature of bound water was above –10°C; *i.e.* this water can be assigned to WBW (Table 1). Water with icosahedral nanodomain or larger domain structures (*i.e.* SAW) and frozen close to 0°C can be attributed to weakly bound water, WBW [50-54]. The main fraction of water in macropores corresponds to unbound, effectively bulk water. Bound water accounts for less than 1 % of the total amount of water in the native hydrated cryogel but it accounts for almost 100% of water in freeze-dried gels. Practically all bound water is weakly bound (WBW) within the cryogel pore network. This is due to the absence of narrow nanopores in the micro/macropore walls (PSD > 0 at R > 1 nm, Fig. 29d-f). The weak binding of water in hydrogels was confirmed by the thermogravimetric measurements on heating at a constant rate. These measurements showed that water started desorbing gradually from 30°C and desorption was practically complete at 87-103°C depending on the cryogel type [51,97]. In the case of nanoporous materials this process is completed at higher temperatures (~150°C) at the same heating rate [50]. A decrease in hydration of poly(2-hydroxyethyl methacrylate - allyl glycidyl ether), PHEMA-AGE, or gelatine (G) gels caused diminution of the PSD peaks of nanopores with the displacement towards smaller R values (Fig. 29e). Similar effects are observed for other cryogels studied (Fig. 29f). These results are in agreement with the CLSM data on shrunken walls of dried cryogels (Fig. 8).

PHEMA cryogels with the synthetic clay Laponite and Fe_3O_4 nanoparticles (Fig. 30) were prepared at –12°C. An increase of Laponite content resulted in an increase in the reaction solution viscosity that reduces the amount of embedded Fe_3O_4 nanoparticles and at Laponite concentration of 1-2 wt.% the embedding of Fe_3O_4 nanoparticles was considerably reduced. Cryogelation involves freezing of the solution before gel formed. The deposition of Fe_3O_4 nanoparticles was lesser

compared to the gel prepared at room temperature. This result is due to the effects described in Chapter 2 (see Eq. (2)) and dependent on the critical ice growth velocity determining conditions of rejecting or encapsulating of the oxide particles by the ice [20]. Therefore, in the case of effective encapsulation of the iron oxide particles by the ice their amount in the pore walls of the cryogel can be low. DSC analysis was carried out for hydrated (50 wt.% water) and dried gels. Samples were cooled from 25°C to –60°C and then heated to 200°C at a cooling/heating rate of 5°C/min. PHEMA-poly(ethylene glycol)diacrylate (PEGA, M_n ~ 258) (7.5% w/w) cryogels with 0.5, 1.5 and 3 w/w% of Laponite with or without addition of Fe_3O_4 (9 wt.%) were analysed. The shape of the DSC thermograms depended strongly on the water amount (Fig. 30). At low hydration h = 0.072 and 0.05 g/g water does not form large structures since crystallisation exotherm and melting endotherm are absent (Fig. 30c). DSC thermoporometry results show that water structures (estimated by subtraction of the baseline in the endotherm) are smaller than 4 nm in size. At high hydration, bound water structures are of a larger size (up to 10 nm) and the melting temperature approaches 0°C.

The total water amount in hydrated samples is by two orders of magnitude larger than in dry samples. Therefore, the main amount of water in strongly hydrated cryogels filled by oxide nanoparticles (20-30 nm in size) can be attributed to UBW (Table 1) similar to cryogels without solid nanoparticles (*vide supra*). Thus, the oxide filler nanoparticles distributed in the micrometer walls of micro/macropores gels weakly affect the behaviour of water located in the cryogels. This can be explained by the formation of relatively dense polymer shells around each oxide nanoparticle similar to PVA/GA/AC at high GA content discussed above. Thus, these nanofillers can change some properties of cryogels such as cohesion, mechanical strength, thermal and electrical conductivity, but they cannot strongly affect the adsorption characteristics of cryogels if these nanoparticles are covered by a relatively thick polymer layer due to inaccessibility of the surface of nanoparticles for adsorbate molecules. In other words, for the modification of surface properties of cryogels, surface functionalisation can be the most effective method, and nanoparticles can be bound in loose polymer brushes attached to the walls of micro/macropores.

4.4. Low-temperature ^{1}H NMR spectroscopy, TSDC and quantum chemistry in structural and energetic characterisation of cryogels

Low-temperature ^{1}H NMR spectroscopy and TSDC method are more sensitive to changes in state of local water structures than DSC which detects averaged thermal flows in the whole sample. Therefore, the ^{1}H NMR spectroscopy is more sensitive than DSC to the structure of bound water [50,54,105]. However, low-temperature ^{1}H NMR spectroscopy and especially NMR cryoporometry

have been rarely applied to superhydrated cryogels. NMR spectroscopy has been more frequently used as an analytical tool to analyse the chemical structure of dried materials or to control chemical reactions occurring during cryogel preparation. Van Camp *et al.* [164] studied chemical modification of alkyne containing PHEMA-based macroporous network of cryogels by Cu(I) catalysed azide-alkyne 'click' cycloaddition reactions using high-resolution magic angle spinning (MAS) NMR spectroscopy. The authors observed complete conversion when benzylazide molecules reacted with the grafted alkyne functions, but only partial conversion was observed when they used azide-modified poly(ethylene glycol) [164]. Subsequent addition of benzylazide consumed all remaining alkyne groups. All chemical modifications were easily monitored at each stage using the MAS NMR spectroscopy. The alkyne functionality and the resulting triazole ring gave well resolved ^{1}H resonances to monitor and quantify the progress of such 'click' reactions in general [164]. However, the authors did not use the NMR method to study the textural characteristics of the synthesised cryogels.

Goharian *et al.* [70] used magnetic resonance imaging (MRI) method to study the γ-irradiation effects on PVA cryogel. The measurements of the spin–lattice relaxation time, T_1 and the spin–spin relaxation time, T_2 showed that the γ-irradiation of PVA cryogel resulted in a decrease in the T_1 value but the T_2 value decreased only at field strengths of 1 T [70]. Additionally, the γ-irradiation enhanced the electrical conductivity of PVA cryogels because of induced chemical reactions with elimination of mobile ions.

Shapiro *et al.* [165] studied the self-diffusion of water in the presence of PVA cryogel using the NMR-PGSE (pulsed-gradient spin-echo) method and found that the value of the self-diffusion coefficient for water in 10 wt.% PVA cryogel was lower by approximately one order of magnitude than in bulk water. Shapiro [166] applied the NMR method to estimate dimensions of the PVA cryogel compartments using the effects of the restricted diffusion in a *q*-space. The significant decrease of the compartment dimensions, pores, and channels as well as filaments was observed after the introduction of DMSO. The entrapment of BSA into the PVA cryogel matrix enhanced the average diameter of the water-filled pores and partially destroyed molecular packing of the cryogel. In recent review paper [55], Shapiro described in detail the use of the NMR spectroscopy for investigation of structural, diffusion, thermodynamic and other properties of a variety of polymeric systems including hydrogels and cryogels.

Kirsebom *et al.* [167] studied free radical polymerisation of dimethylacrylamide-co-PEG diacrylate in a semi-frozen aqueous solution using ^{1}H NMR spectroscopy. They concluded that the ^{1}H NMR spectroscopy is an appropriate method to study the formation of cryogels, changes in the

amounts of unfrozen water and the progress of the polymerisation reaction. However, the authors [167] did not undertake quantitative structural characterisation of cryogels using the NMR data.

To study the textural features of gelatine (G) cryogel (described in Chapter 4.4), the ^{1}H NMR spectra were recorded for static samples at 200-280 K using a high resolution spectrometer with 90^o probe pulses of 2 μs duration [105]. To prevent supercooling of the gelatine cryogel studied, the temperature dependence of the concentration of unfrozen water was determined upon heating of samples pre-cooled to 200 K [54]. The signals of water molecules from ice did not contribute to the ^{1}H NMR spectra of static samples because of features of the measurement technique (narrow bandwidth) and a significant difference in the relaxation time T_2 of mobile and immobile phases [50-54,168]. Before the measurements, samples (placed in sealed NMR ampoules) were equilibrated for 15 min (at each fixed temperature). Changes in the Gibbs free energy (ΔG) of bound water and free surface energy (γ_S), as the modulus of integrated changes of the ΔG values in the bound water layers, were determined from the temperature dependence of the amount of unfrozen water, C_{uw} in mg of water per gram of dry gelatine gel at T = 200-273 K [50,54,105]. Prior to NMR measurements, samples were wetted by the addition of a certain amount of water (h = 0.1 or 1 g per gram of freeze-dried gel) and equilibrated. Several solvents (acetonitrile, chloroform, benzene) miscible or immiscible with water were used in the deuterated form to avoid their contribution to the ^{1}H NMR signals of adsorbed water unfrozen at T < 273 K [105].

Water can be frozen in narrower pores at lower temperatures as described by the Gibbs-Thomson relation for the freezing point depression for liquids confined in cylindrical pores of radius R [5,50,54]

$$\Delta T_m = T_{m,\infty} - T_m(R) = -\frac{2\sigma_{sl}T_{m,\infty}}{\Delta H_f \rho R} = \frac{k}{R}, \qquad (19)$$

where $T_m(R)$ is the melting temperature of ice in cylindrical pores of radius R, $T_{m,\infty}$ the bulk melting temperature, ΔH_f the bulk enthalpy of fusion, ρ the density of the solid, σ_{sl} the energy of solid-liquid interaction, and k is a constant. Eq. (19) is similar to Eq. (16); however, the k value can be different. For instance, for bound water it was varied from 21 to 87 K nm depending on the adsorbents characteristics [54]. Eq. (19) was used to determine the differential distribution function $f_V(R) = dV_{uw}(R)/dR$ of the size of water structures unfrozen at T < 273 K [50,54,133]:

$$\frac{dV_{uw}(R)}{dR} = \frac{A}{k}(T_m(R) - T_{m,\infty})^2 \frac{dC_{uw}(T)}{dT}, \qquad (20)$$

where $V_{uw}(R)$ is the volume of unfrozen water in pores of radius R, C_{uw} the amount of unfrozen water per gram of a dry material as a function of temperature, and A is a constant. The $f_V(R)$

function can be used to determine the distribution function in respect to the specific surface area of the water structures [50,54,133]

$$f_S(R) = \frac{w}{R}\left(\frac{\mathrm{d}V_{uw}(R)}{\mathrm{d}R} - \frac{V_{uw}(R)}{R} \right) \quad (21)$$

where w is the form-factor equal to 2 for cylindrical pores. Integration of the $f_S(R)$ function gives the specific surface area of the contact area between unfrozen water and a surface [50,54]. Notice that application of the NMR cryoporometry to a variety of solid and soft materials gave reliable structural characteristics compared with those based on the data of the standard adsorption methods [50-54,133,168,169].

To study the PSD of gelatine cryogel with different amounts of water, low-temperature ^{1}H NMR spectroscopy was applied to freeze-dried and then re-hydrated samples. A freeze-dried gelatine cryogel contained low amount of water that gave low intensity of water signal (Fig. 31a). Signals at the chemical shift of proton resonance δ_H = 7.2 and 0 ppm (Fig. 31a) were due to residual $CHCl_3$ in chloroform-d and tetramethylsilane (TMS) added as a standard, respectively. Weak signals at δ_H = 4.8 and 1.3 ppm can be attributed to strongly (SAW) and weakly (WAW) associated water [50-54]. Strongly associated water was not observed at T < 250 K, but the signal of weakly associated water, whose intensity decreased with lowering temperature, was observed even at 210 K. Consequently, all strongly associated water was WBW but a portion of weakly associated water corresponded to SBW [105]. The addition of polar acetonitrile to weakly polar chloroform (Fig. 31b) resulted in the appearance of the signal of methyl groups of CH_3CN (as an impurity in CD_3CN) at δ_H = 2 ppm. This signal can overlap with a signal of water associated (ASW) with molecules of organic solvents. The main portion of this water was bound in complexes with acetonitrile HO–H···NCCD_3, ASW at δ_H = 2-2.5 ppm. Signal of weakly associated water was observed on the right wing of signal of the CH_3 groups of acetonitrile. An increase in water concentration to 10 wt.% (Fig. 31c) caused appearance of broad signal of SAW at δ_H = 4.8 ppm. Its intensity sharply decreased with decreasing temperature but the ASW intensity increased. Notice that glutaraldehyde cross-linked gelatine cryogel (G gel) is characterised by diminished water bonding in comparison with unmodified gelatine described in the monographs [50,54].

For a more strongly hydrated gelatine cryogel (h = 1 g/g which corresponds to ca. 10% of the total volume of macropores, Table 7) exposed to the air, broad asymmetrical signal of SAW was observed (Fig. 32) [105]. This signal tended to split into two peaks because of the presence of several forms of bound water and spatial heterogeneity of the sample (Fig. 7) with different magnetic susceptibility in different local structures. A sample in the C_6D_6 medium (Fig. 32b) was spatially more uniform (with respect to bound water) because of the filling of macropores by

benzene and changes in water location in pores. Therefore, only one broad signal of SAW was observed [105]. For a mixture of solvents (C_6D_6 + CD_3CN, Fig. 32c, or $CDCl_3$ + CD_3CN, Fig. 32d), signals of WAW (δ_H = 1.3 ppm), water associated with acetonitrile ASW (δ_H = 2-2.5 ppm), and CH_3 groups in CH_3CN (δ_H = 2 ppm) were observed. Consequently, water structure and location in or out pores depends on the presence of organic co-solvents, their polarity (hydrophilicity/hydrophobicity) and concentration.

Water can be considered as weakly bound if its freezing temperature T > 250-260 K, which corresponds to changes in the Gibbs free energy ΔG > –0.8 - –0.5 kJ/mol due to water binding [50,54]. Therefore, the main fraction of water bound in gelatine gel was weakly bound [105], which is in agreement with the DSC data discussed above. The main reason of this effect is the micro/macroporosity of the cryogels. The amount of water strongly bound in hydrated gelatine cryogel at h = 1 g/g correspond to the volume of 0.2-0.3 cm^3/g (Table 7, V_{nn}). The main portion of this water is located in a confined space between adjacent and cross-linked macromolecules. Organic solvents can displace strongly bound water which appears as diminution of S_{nn} and V_{nn} values of narrow nanopores (Table 7) and changes in the size distribution of pores filled by bound water unfrozen at T < 273 K (Fig. 33). Water located in macropores of gelatine cryogel can be attributed to bulk water (UBW) which is not registered by low-temperature ^{1}H NMR spectroscopy at T < 273 K. Therefore, the main portion of bound water (V_{nn} + V_{mn}) is probably located in swollen pore walls or at their surface. The displacement of water from narrow nanopores by organic solvents [54] can play an important role in practical applications of cryogels. The PSD based on the NMR (Fig. 33c) and DSC data for hydrated gelatine cryogel is close to that for PHEMA-AGE gel (Fig. 29). This similarity for different hydrogels is due to the presence of great amount of bulk water which can mask fine details of the effects related to bound water, especially in the case of DSC thermoporometry.

In the native hydrated state, polymer- and protein-based cryogels produced by cryogelation are characterised by a large micro/macropore volume, small specific surface area of the micro/macropore walls, high pore interconnectivity and high hydrophilicity. The main portion of water in micro/macroporous cryogels can be attributed to bulk water located in micro/macropores at d > 1 μm. The amount of mainly weakly rather than strongly bound water located in nanopores in the swollen micro/macropore walls is smaller by one-two orders of magnitude. This makes micro/macroporous cryogels an attractive biomaterial for medical applications because strongly bound water is characterised by a low activity as a solvent and hence can affects adversely a variety of bioprocesses within the cryogel matrix. These structural features of the macropores in the collagen hydrogel are important for cell accommodation, migration and growth. Whether

preparation of samples according to the procedure described above damages their intact porous structure is a subject for discussion. in general, critical point drying is considered to be a gentle procedure preserving the structural integrity of the cryogels analysed here, and structures similar to SEM images were also observed in CLSM micrographs taken of native, hydrated and freeze-dried gels (Figs. 4 and 8).

The total PSD of collagen gel constructed from the NMR-cryoporometry and CLSM data (Fig. 34) revealed a certain hierarchy of pores from narrow (< 2 nm) and broad (2-50 nm) nanopores to macropores at 200-250 μm [106]. The incremental PSD_{NMR} function (Fig. 34, left) was renormalised with respect to the PSD_{CLSM} (Fig. 34, right) to obtain a smooth total PSD curve. From this log-scale distribution, it is clear that micro/macropores at d > 20 μm provide the main contribution to the overall porosity of the hydrogel.

This result is in agreement with microscopic images and thermally stimulated depolarisation current, TSDC relaxometry (Fig. 35c) and other data [52,105,106]. The TSD current method can be effectively used to analyse the associativity and the mobility of the interfacial water because the measured temperature dependence of depolarisation relaxation characterises the environment of water molecules [53,54]. It can be used to study the interaction of these molecules with their neighbours and to estimate the number of hydrogen bonds per molecule; their strength, mobility of bound charges (water dipoles) and free charges (protons) and the size of water clusters [53]. The activation energy of depolarisation (E) on dipole re-orientation was calculated using Eq. (22) for the TSD current [53]:

$$I(T) = S_{el} P_0 \int_{E_{\min}}^{E_{\max}} f(E) \sum_{i=1}^{N} w_0^i \exp\left[-\frac{E}{k_B T} - \frac{w_0^i k_B T^3}{hE} \exp\left(-\frac{E}{k_B T} \right) + \frac{w_0^i k_B T_0^3}{hE} \exp\left(-\frac{E}{k_B T_0} \right) \right] dE \,, \quad (22)$$

where

$$w_0^i = \frac{h}{k_B T_i^3} (E + k_B T_i) \exp\left(\frac{E}{k_B T_i} \right),$$

S_{el} is the surface area of the electrodes, P_0 the frozen polarisation, k_B the Boltzmann constant, h the heating rate, T_0 the initial temperature, and T_i is the temperature of the ith TSD current maximum. Eq. (22) was solved using a regularisation method with a non-negativity condition ($f(E) \geq 0$ at any E) and a fixed value for the regularisation parameter [53].

Low-temperature TSDC peaks at T < 160 K (Fig. 35a) and low-energy activation $f(E)$ peak (Fig. 35b) correspond to relaxation of small water structures, which are attributed to WAW. High-temperature TSDC peaks and high-energy relaxation correspond to SAW with addition to the relaxation of the collagen matrix [50,53,54]. The TSDC results showed that water located in micro/macropores (*i.e.* UBW) in native superhydrated collagen hydrogel (~98% of water) has the

properties close to those of bulk water (Fig. 35a,b). However, water bound to collagen (WBW, SBW and WAW, Table 1) is more structured than bulk water. Therefore, the direct current (dc) relaxation is observed in the hydrated collagen gel at relatively high temperature $T > 250$ K (Fig. 35a) and the activation energy $E_{dc} = 62.3$ kJ/mol ($F_p = 350$ V/cm) and 71.6 kJ/mol ($F_p = 500$ V/cm). For water alone, the activation energy is higher $E_{dc} = 88.2$ kJ/mol but the dc relaxation begins at lower temperature (230 K). The activation energy of the dc relaxation increases with increasing intensity of the polarisation field. Two $f(E)$ peaks at E between 20 and 37 kJ/mol shift towards higher energy for the collagen gel-water system in comparison with water alone (Fig. 35b). However, the peak at $E = 42$ kJ/mol shifts in the opposite direction. The first two peaks can be assigned to WAW/WBW and WAW/SBW, and the high-energy peak can be mainly due to SAW/WBW in collagen gel-water [53,54,162]. In the case of water alone, the first peak at 22 kJ/mol can be assigned to re-orientation of interstitial water molecules or the molecules in small water clusters present in water structure [1,50,53,54]. The second peak is due to re-orientation of the molecules in larger clusters, and the third peak is due to the depolarisation processes in bulk water structures (domains) [53,54]. The displacement of the high-energy peak towards lower energy for CG/water (Fig. 35b) can be explained by diminution of the size of UBW/SAW structures located in micro/macropores of the collagen hydrogel in comparison with water alone (SAW).

Seven sets of CLSM images of different collagen gel sections were used for calculations of its structural characteristics [106]. The average relative density of the dried gel matrices was $\rho^*/\rho_s = 0.0533$. The average specific surface area was $S_A/V = 0.0274$ μm^{-1} (from Eq. (6)) and 0.0083 μm^{-1} (Eq. (8)). The average permeability was $K = 0.451\times10^{-10}$ m^4/Ns with Eq. (9) without compression of the initial gel. These values were calculated using the average pore diameter $d \approx 90$ μm (Fig. 34) and the average wall thickness $t \approx 7$ μm estimated from the CLSM data [106]. These values are in agreement with other published data on the structure of the collagen materials [50-52,106]. They show that the main contribution to the collagen gel porosity is due to pores at $d > 20$ μm (Fig. 34). The micro/macropore volume filled with a solvent (water or/and alcohol) in the collagen gel was approximately 95%, *i.e.* $V_p = 14.4$ cm^3/g calculated from ρ^*/ρ_s at $\rho_s = 1.3$ g/cm^3.

To model cryogels [105,106], hydrated fragments (up to 6000 atoms) of polymer and protein hydrogels were calculated using the PM6 method (MOPAC 2009) [149] with the geometry optimisation using a localised molecular orbital method (MOZYME). The initial structure of the polymer model systems was optimised using the CharMM forcefield (Vega ZZ 2.4.0) [148]. Initial structures of proteins collagen used instead of gelatine and fibronectin were taken from the Protein Data Bank [170].

Nanopores of 1-2 nm in radius were observed in the PHEMA-AGE model (Fig. 36) in

areas of both low and high hydration. The PM6/MOZYME calculations of the hydrated fragments of hydrogels (Fig. 36) were carried out to estimate the hydration energy of polymers and proteins and the macromolecule-macromolecule interactions. Hydrated two triple coils (*i.e.* six fragments) of collagen (Fig. 36b) are characterised by hydration energy E_h = –9.5 kJ/mol per water molecule. This value is not great as it is 3-4 times smaller than the energy of a strong hydrogen bond because a significant portion of water molecules does not have direct contact with the protein molecules (Fig. 36b). Protein-protein interaction energy in the triple coils is relatively high, E_{pp} = –19 kJ/mol per each amino acid residue. Taking into account the solvation effect the value of $E_{pp,h}$ = –106.7 kJ/mol per each amino acid residue because water molecules can act as bridges between protein functionalities of neighbouring chains enhancing their interactions. In the case of the hydrated fibronectin (8-9FnI) – collagen complex (Fig. 36c), the hydration energy E_h = –28.6 kJ/mol is greater than that for collagen alone because of more densely packed water layers. The E_h value is minimal (–8.6 kJ/mol per water molecule) for PHEMA-AGE gel (Fig. 36a), in which a significant portion of water molecules (larger than that for collagen model in Fig. 36b) is not located in the first layer directly contacting with the polymer. These results are in agreement with the DSC and NMR data showing that water is weakly bound in the PHEMA-AGE and gelatine cryogels. The NMR study gives changes in the Gibbs free energy of bound water $\Delta G > -3.5$ kJ/mol for the first layer, *i.e.* $\Delta G > E_h$ ($E_h \approx \Delta H_f$) due to an entropy decrease in the bound water layer. The properties of bound water such as activity, mobility, diffusivity, *etc*. differ from that of bulk water [50-52]. However, the relative amount of water bound in the cryogels is small (< 10 wt.% of bulk water) because the main contribution to the porosity of these materials is given by macropores, in which water is practically unbound (bulk). This factor is important for understanding the mechanism of biocompatibility of cryogels and normal functioning of cells in macropores since bulk water has much greater activity as a solvent than bound water has.

4.5. Equilibrium and kinetic adsorption

Despite the mainly micro/macroporous character of their porosity, cryogels can adsorb ions and small molecules because their pore walls are nano/microporous, and they can be swollen and include functionalities effective in the specific interactions with solutes. Arpa *et al.* [171] found that PHEMA/Reactive Green HE-4BD cryogel exhibited the following metal ion adsorption selectivity: Cu(II) > Cd(II) > Pb(II). This conclusion is too far fetching, because there are perhaps adsorbents which adsorb Cu better than Pb, for example, oxide adsorbents [50]. Bajpai and Saini [172] studied PVA/casein physically cross-linked cryogels. These cryogels strongly absorbed water and showed

significant swelling. This observation is in agreement with strong uptake of water by other protein-based cryogels [52,106,107]. The effects of salt and various model biological fluids on the cryogel swelling were studied [172]. The *in vitro* biocompatibility of the prepared cryogels was also evaluated by several methods such as BSA adsorption, blood clot formation and percentage haemolysis measurements.

The adsorption of dyes from an aqueous solution is frequently used to test the adsorption capability of various adsorbents towards toxic aromatic functionalised compounds, which is important for medical and environmental applications [173-186]. This capability is dependent on the accessibility of adsorbent pores, and it is particularly relevant for composite materials where polymer coverage of adsorbent particles occurs [107,108]. Dyes such as Congo red (CR) [173-177], methylene blue (MB) [178-183] and methyl orange (MO) [184-186] are frequently used to study the adsorption capability of adsorbents [187-189]. These investigations were focused on the removal or decomposition of toxic, harmful compounds from wastewater using adsorption, catalytic or photocatalytic methods. However, polymer/AC composites with macroporous matrices produced by cryogelation have not been practically studied using dye adsorption [107]. Papancea *et al.* [190] studied sorption and diffusion of three dyes: Congo red, methylthymol blue (MTB), and crystal violet (CV) through PVA membrane. After sorption, the dye-release kinetics (desorption) from the PVA membrane was monitored to evaluate regeneration of the membrane. The diffusion experiments revealed that CR and MTB do not permeate the PVA membrane making it a promising candidate in the advanced purification of wastewaters. The effect of the incorporation of dyes on chemical properties of PVA cryogels was studied using DSC, SEM, and FTIR spectroscopy [190].

However, polymer/AC composites with macroporous matrices produced by cryogelation have been seldom studied using dye adsorption. Sandeman *et al*. used adsorption of cationic (MB, molecular weight 319.85 Da) and anionic (MO, 327.33 Da and CR, 696.66 Da) dyes to study the porous characteristics and adsorption capability of poly(vinyl alcohol) (PVA) cryogels, AC and PVA/AC composite materials (Table 4), whose preparation was discussed above [107].

The adsorption experiments were carried out at 37^{o}C for 24 h. Three different PVA gels were studied. Samples 1 and 2 (PVA1 and PVA2) were prepared using a 5% solution of PVA and dried *in vacuo* (PVA1) or freeze-dried and evacuated (PVA2). Sample PVA3 was prepared using a 7% PVA solution and dried in the same way as PVA2. Two samples of PVA/C-7 were prepared using the 5% (PVA5/C7) and 7% (PVA7/C7) PVA solutions, GA cross-linked PVA, freeze-dried and evacuated as described above (Table 4) [107].

To calculate the free energy distributions $f(\Delta G)$ of dye adsorption, the Langmuir equation [90] was used to obtain the kernel of the Fredholm integral equation of the first kind [50,54]

$$\Theta = \int C_e \exp(-\Delta G / R_g T)(1 + C_e \exp(-\Delta G / R_g T))^{-1} f(\Delta G) \mathrm{d}(\Delta G), \quad (23)$$

where $\Theta = C_a/C_m$ is the relative adsorption, C_m is the monolayer capacity, C_e is the equilibrium concentration (g/mL or mM) in the solution, C_a is the current adsorption and R_g is the gas constant. Eq. (23) was solved to obtain the $f(\Delta G)$ functions using a regularisation procedure with an unfixed regularisation parameter determined on the basis of the F-test and confidence regions using the parsimony principle [191].

The dye molecules studied differ in their size (Fig. 37), chemical and electronic structures. The MB molecules (cations) can penetrate into the narrowest pores at $d \approx 0.7$ nm (Fig. 37a). For the MO and CR molecules (anions), this pore size threshold value is greater as 0.8 and 1 nm, respectively. The size difference, as well as the difference in charge and chemical structure, resulted in both maximal adsorption (Fig. 38) and removal (Fig. 39) of MB [107]. The maximum adsorption of MB and MO was observed for activated carbon C-3 possessing high S_{BET} and the largest S_{mn} (Table 4). The CR adsorption was maximal for activated carbon C-6 with a similar S_{BET} value to that of C-3. Atomic charges in CR, q, were calculated using the IEFPCM method with B3LYP/6-31G(d,p) [192] and a total charge $q = -2$ a.u. is derived mainly from two SO_3 groups with a q value of −1.59 a.u. The lower adsorptive gel capacity towards CR was due to several factors including its larger size, less planar geometry, and a greater value of free energy of solvation at $-\Delta G$ = 574 kJ/mol. MO and MB have $-\Delta G$ = 258 and 147 kJ/mol respectively. MB has the smallest size, planar geometry, and relatively low $-\Delta G$ values, which explain its greater adsorption among the three dyes studied. Additional oxidation of AC C-7, causing an increase in the amounts of negatively charged surface acidic COOH groups, led to a two-fold increase in the difference in adsorption of MB over MO and a five-fold increase over adsorption of CR (Fig. 38).

Percentage of dye removal from solution (Fig. 39) decreased with increasing equilibrium dye concentration in the solution for all systems studied [107]. It was close to 100% at $C_e < 0.1$ mM reducing to less than 50% at C_e = 10-20 mM. For PVA and PVA/C-7, the dye removal percentage was minimal (Fig. 39g).

The porosity and the surface functionality of the materials studied (AC, PVA and PVA/AC) were non-uniform, as were the properties of the selected dye molecules (Fig. 37) [107]. The calculation of the $f(\Delta G)$ distribution functions of the free energy of adsorption (Fig. 40) using Eq. (23) with unfixed regularisation parameter frequently gave from one to three peaks depending on the molecular structure and the concentration of the adsorbate (Fig. 37h). This is due to the presence of different active sites of different accessibility and enhanced lateral interaction effects with increasing adsorption value. For symmetrical CR molecules, at low concentration of the adsorbate

(*i.e*. dye adsorption onto more active and well accessible surface sites with no lateral effects), the $f(\Delta G)$ curves had only one peak. Asymmetrical MO molecules more strongly interact with a larger number of different surface functional groups than CR or MB, which resulted in a more complex $f(\Delta G)$ curve for MO. For MO, with q = –0.82 a.u. for SO_3 and q = –0.3 a.u. for NH_2 functional groups, the distribution function had two to three peaks. The $-\Delta G$ values were relatively large because of the adsorption of positively charged (MB) or negatively charged (MO, CR) molecular ions at the charged AC surface and possible binding of counterions. This was due to the presence of O-containing groups and such reactions as $COOH \rightarrow COO^- + H^+$ at pH > PZC (point of zero charge) [194]. Dyes have aromatic rings (weakly polar) and several polar active groups (Fig. 37). N, O, S, and H atoms provide dispersion, electrostatic, and hydrogen bonding in the adsorption complexes at heterogeneous carbon surface [50-54]. Each dye molecule can form several different intermolecular bonds with the functional groups and the basal planes of the carbons, especially in the narrow nanopores, where it is possible to form bonds with two opposite walls (Fig. 37). The major $f(\Delta G)$ peaks, indicating occurrence of strong bonding, were mainly between –20 and –30 kJ/mol (Fig. 40). There were additional peaks at $-\Delta G$ < 10 kJ/mol created by relatively weak adsorption complexes and high-energy tails at $-\Delta G$ = 40-60 kJ/mol created by very strong bonding of dyes in the narrow nanopores [107]. The difference in the adsorption of dyes on different carbons (Figs. 38 and 39) and the corresponding difference in the shape of the $f(\Delta G)$ functions (Fig. 40) was due to the difference in the PSDs (Fig. 13a), contribution of narrow and middle nanopores (Table 4), the concentration of active surface sites related to the burn-off degree [195] and additional activation of C-7 in air. These factors as well as the difference in the chemical structure and charge of dye molecules (Fig. 37) resulted in a complex shape of the $f(\Delta G)$ function for certain carbons, especially at higher dye concentrations when additional factors appear (lateral interaction of adsorbed dye ions, occupation of less active sites and adsorption in broader pores). A complex dependence of the $f(\Delta G)$ function on the textural and structural characteristics of adsorbents was reflected in relationships between the ratio of the first and zero moments of the $f(\Delta G)$ distributions $\langle \Delta G \rangle = \int \Delta G f(\Delta G) d(\Delta G) / \int f(\Delta G) d(\Delta G)$ and the S_{nn}, D_{FHH} and Δw values (Fig. 41). The $\langle \Delta G \rangle$ dependences on the specific surface area of narrow nanopores (as the main adsorption places for dye ions), fractality D_{FHH} as a measure of the surface roughness, and the deviation of pore shape from the slit-shaped pore model are not smooth. There are certain trends such as an increase in the $\langle \Delta G \rangle$ value (*i.e.* diminution of the complex strength) with an increase in the deviation of the pore shape from slit-shaped pore model (Fig. 41c) or with an increase in the fractality. These results can be explained by a stronger binding of dye ions in narrow pores with the shape closer to the ideal slit

shape where the dispersive interactions were stronger and the adsorbed dye ions can simultaneously interact with both pore walls. The high-energy tails were absent when dyes adsorb onto PVA and PVA5/C-7 because of the absence of accessible narrow nanopores (Fig. 13). The above mentioned tails were observed more frequently for smaller MB and MO ions, because CR ions can penetrate primarily into the broader pores, unlike the MB or MO ions. In the case of the PVA/AC composite, the polymer molecules can block pores and the dye ions can be adsorbed to the PVA films covering the carbon particles (Fig. 42). Figure 42 models the way in which the dyes interacted with the hydrated PVA, which covered and blocked the narrow pores of the AC particles within the AC/PVA composite. Water molecules are much smaller than dyes and can fill the narrow pores of the AC particle, despite its PVA coating. The displacement of the water molecules located in the pores of embedded ACs by organic molecules, even those smaller than the studied dyes, was more difficult, in comparison with the displacement of water from the pores of uncoated ACs by different organics [50,54]. These structural and adsorption characteristics should be taken into account when considering applications for polymer-coated AC adsorbents or composite cryogels.

Thus, differently charged dye ions of different size and symmetry (totally symmetrical CR, partially symmetrical MB and asymmetrical MO) were effectively adsorbed by ACs with a high specific surface area, with practically 100% removal achieved, expressed in g/g. However, re-calculation of the dye adsorption in mM/m^2 or g/m^2 units gave higher adsorption figures for PVA/AC or PVA alone rather than for AC alone [107]. This result was due to monolayer adsorption of dye ions controlled by the specific surface area accessible for the adsorbate. The S_{BET} value determined from nitrogen adsorption was larger than the surface area accessible for dye molecules since they are much larger than the N_2 molecule. However, this difference in the accessible surface area decreases for adsorbents without narrow nanopores because the surface area of the broader pores is more accessible for larger molecules. Additionally, when larger amounts of dye were adsorbed onto the ACs, the lateral repulsive interactions of the adsorbed dye ions were stronger than those at lower adsorption concentrations of dyes bound onto PVA or PVA/AC. Therefore, the overall dye adsorption in g/m^2 can be larger for PVA/AC than for the ACs alone [107].

The charge of adsorbate molecules and functionalisation of the adsorbent surfaces are the second important factor affecting dye adsorption. The changes in the Gibbs free energy of dye adsorption are relatively large (up to $-\Delta G$ = 50-60 kJ/mol) because of the interaction of charged structures contained within the dye ions and on the AC surface, including the interaction of counter ions in the narrow and middle nanopores [107]. This occurs despite the high solvation energy values for the dye ions and, therefore, the great desolvation energy values. The latter provide a barrier to adsorption because a significant portion of water strongly bound to ions must be displaced during

adsorption especially in narrow nanopores, and the narrow the pore, the stronger the desolvation effects. Partial blocking of the AC surface by PVA polymer significantly reduced its specific surface area and adsorption capacity of PVA/AC per gram of composite.

In summary, dye interactions with the ACs or AC/PVA cryogel composites depend on the properties of the dyes themselves (size, symmetry and charge) and on the nature of the AC or PVA/AC surface available for adsorption, its structural and textural characteristics. The influence of several factors affecting the dye adsorption resulted in complex, non-smooth shapes of the relationships between the textural characteristics of the adsorbents and the dye adsorption characteristics (adsorption amount, removal percentage, free energy of adsorption). Quantum chemical modelling allowed for a detailed description of the adsorbent-adsorbate interactions. Not only it revealed the strong interactions between PVA and AC resulting in pore blocking but also the displacement of adsorbed water by PVA that led to hindering of the diffusion of dye ions [107].

Cryogels as macroporous materials can adsorb high-molecular compounds such as proteins. These macromolecules having the radius of gyration of several nanometres easily penetrate into broad pores of micrometer range. Macromolecule breakthrough effects can be observed for solutions flowed through cryogel membranes because of high interconnectivity of macropores in cryogels.

Derazshamshir *et al.* [196] synthesised molecular-imprinted macroporous cryogels for depletion of hemoglobin (Hb) from human blood (Hb-PHEMAH gel) with gel fraction yields up to 90%. The morphology and porosity of the cryogels were characterised by FTIR, SEM, swelling studies, flow dynamics and surface area measurements. Selectivity of Hb binding was tested in the presence of such competitive proteins as myoglobin (Myb) and BSA. Hb-PHEMAH cryogel exhibited a high binding capacity and selectivity for Hb in the presence of the other proteins. The selectivity of Hb-PHEMAH cryogel for Hb was confirmed by HPLC. Selective depletion of Hb from the blood haemolysate was also confirmed using sodium dodecyl sulfate polyacrylamide gel electrophoresis, SDS-PAGE. Hb-PHEMAH cryogel was reused many times with no apparent decrease in Hb adsorption capacity. Figure 43 shows the Hb adsorption isotherm and fitting with standard [196] and integral [50,54] Langmuir equations.

In comparison with Eq. (23), the improved integral Langmuir equation is [50,54]:

$$C_a / C_m = \int_{\Delta G_{\min}}^{\Delta G_{\max}} aC_e \exp(-(\Delta G + z)/R_g T)(1 + aC_e \exp(-(\Delta G + z)/R_g T))^{-1} f(\Delta G)\mathrm{d}(\Delta G) \qquad (24)$$

where $f(\Delta G)$ is the distribution function of the free energy of protein interaction with a cryogel surface, a is an equation parameter, z depends on the presence of pre-adsorbed protein (at $z = 0$ corresponding to a pure surface, Eq. (24) corresponds to Eq. (23)), and R_g is the universal gas

constant. The z value was estimated as $2R_gT$ corresponding to relatively weak lateral interactions between protein molecules in the term of Gibbs free energy (< 5 kJ/mol). Eq. (24) can be solved using a regularisation procedure based on the CONTIN algorithm [191] after minimisation of the functional of discrepancies to estimate the equation parameter a. The deviation of the standard Langmuir isotherm from the experimental isotherm (Fig. 43) is due to the use by the authors [196] of larger adsorption values than monolayer because the Langmuir equation works well only at coverage smaller than a monolayer [98]. The integral equation (24) gives exact fitting (Fig. 43).

Myoglobin from horse skeletal muscle (16.7 kDa) was used as a model protein to evaluate protein adsorption on AC and AC/GA/PVA cryogel composites (Table 4) from 10 mM sodium phosphate buffer containing 0.15 M NaCl at pH 7 and 22°C [108]. The myoglobin adsorption was as high as 667 mg/g (Fig. 44a) [108]. Similarly high protein adsorption is characteristic of fumed silica composed of nonporous nanoparticles [50]. Despite this, changes in the free energy due to myoglobin adsorption to AC are relatively small since $-\Delta G < 6$ kJ/mol (Fig. 44b). Two peaks in the $f(\Delta G)$ function are due to stronger adsorption at lower $C_{e,Myb}$ values (peak at $\Delta G = -4.5$ kJ/mol) and weaker adsorption at greater $C_{e,Myb}$ values ($f(\Delta G)$ peak at –1 kJ/mol). These results can be explained by confined space effects resulting in slow diffusion of protein molecules within nanopores of AC (Fig. 45) and low accessibility of the surface area in narrow pores. The adsorbed amounts of myoglobin on AC are high (200-250 mg/g) at low equilibrium concentrations of the protein (Fig. 45a) [108] because of a great affinity of AC possessing a broad PSD (*i.e.* a small effect of pore blocking by protein) towards relatively small protein molecules. Accessibility of broad pores of AC exhibiting relatively large specific surface area for myoglobin (hydrodynamic radius 2.1 nm [76]) could be a probable reason for the high capacity but slow kinetics of adsorption due slow penetration of macromolecules into pores. The average value $\langle D \rangle \approx 6.0\times10^{-8}$ cm^2/s of the distribution of the diffusion coefficient for Myb interacting with AC (Fig. 45b) is much smaller than the diffusion coefficient of myoglobin in water $D_0 \sim10^{-6}$ cm^2/s [197]. Although the diffusion of myoglobin at/within AC particles is much slower than in water [108], its adsorption onto the outer surface of AC microparticles is relatively fast as the right $f(D)$ peak (Fig. 45b) is located at $D \approx 0.2\times10^{-6}$ cm^2/s, which is close to D_0. The adsorption becomes much slower when myoglobin molecules penetrate into broad and middle nanopores of AC microparticles, which is reflected by a D value dropping down to 10^{-8} - 10^{-9} cm^2/s. The initial adsorption rate of myoglobin onto composite AC/GA/PVA cryogel was several times lower than that for Myb interacting with individual ACs (Fig. 45a). The difference in the adsorption rate of myoglobin is clearly observed in the first 10 h of the adsorption (Fig. 45a). Subsequent curve courses are close [108]. This multi-step process is described by the distribution functions of the diffusion coefficient, which have two peaks

(Fig. 45b) due to slow and fast adsorption depending on the pore sizes where this adsorption occurs. An increase in the AC content in PVA/GA/AC composite by an order of magnitude gave a significant increase in the efficiency of the adsorption kinetics of myoglobin (Fig. 46) which became closer to that for pure ACs (Fig. 45) [108]. Fig. 47 shows the structure of PVA/AC composites. In the presence of embedded carbon particles the pore walls of PVA cryogel become thinner. The cryogel adheres to the particles and binds them together (Fig. 47) [108]. After drying, the particles seem to have shells, which look partially empty inside, because in the superhydrated cryogels these shells were strongly swollen. Textural features of PVA/AC cryogels ensure their lower flow resistance than the PVA cryogels (Fig. 48).

Odabas *et al.* [198] studied DNA adsorption on Zn^{2+}–chelated supermacroporous poly(2-hydroxyethyl methacrylate-N-methacryloyl-(L)-histidine methyl ester) [poly(HEMA-MAH)] monolithic cryogel column. The DNA adsorption was much lower in the case of poly(HEMA-MAH) without Zn^{2+} (Fig. 49). These results show the importance of cryogel functionalisation and filling by nano/microparticles to control the adsorption and other properties of the materials.

4.6. Diffusion of small molecules, polymers, proteins and cells within macropores of cryogels

Different applications of cryogels deal with the diffusion and breakthrough of both small and large molecules as solutes in diluted or concentrated solutions within the macropore network of a different thickness. Therefore, many authors investigated these phenomena mainly in aqueous media.

Wang *et al.* [199] developed a separation method to isolate directly cytidine triphosphate (CTP) from fermentation broth of yeast cells using an anion-exchange supermacroporous cryogel. The anion-exchange cryogel with tertiary amine groups was prepared by graft polymerisation. The breakthrough characteristics and elution performance of pure CTP in the cryogel bed were investigated and the CTP binding capacity was determined. Then the CTP separation from crude fermentation broth of yeast cells was carried out on the cryogel column using deionised water and 0.01 M HCl as washing buffer, respectively. The purity and concentration of CTP were determined by HPLC. The maximal purity of CTP obtained using 0.01 M HCl as washing buffer and 0.5 M NaCl in 0.01 M HCl as elution buffer was as high as 93% [199]. In this paper, the quantitative structure-property analysis of the cryogels was not done.

Erzengin *et al.* [200] synthesised cryogels with poly(2-hydroxyethyl methacrylate) cross-linked by N,N-methylene-bis-acrylamide and embedded with Cu^{2+}-attached sporopollenin particles. The adsorption kinetics of HSA was modelled with the kinetic equations of the pseudo-first and second order. However, the authors did not quantitatively analyse the relationships between the

structural characteristics of the cryogels and their adsorption capacity because only the porosity was estimated from the amounts of bound water.

Three proteins different in size and shape: BSA (67 kDa), human serum fibrinogen, Fg (340 kDa), and aprotinin (basic (bovine) pancreatic tripsin inhibitor, BPTI, 6.7 kDa) were used in the diffusion experiments with collagen hydrogel membranes (type I bovine tendon collagen cross-linked by glycosaminoglycan, GAG), an inner layer from INTEGRA^{TM} bilayer matrix wound dressing [106,195]. Both BPTI and BSA are globular proteins, but of different sizes, whilst Fg is a much larger rod-like protein (Fig. 50).

The collagen hydrogel was characterised by the ability of these different molecular markers to pass through a thin collagen membrane (~1 mm in thickness) [106]. Protein diffusion was studied using both fresh collagen samples and hydrogels that had already been exposed to a first run through with BPTI, BSA, Fg or Fg/BSA. A diffusion cell included two compartments separated by the collagen membrane. The protein solution was added into compartment 1 and the protein molecules diffused through the membrane into compartment 2 [106].

To gain more information from the diffusion kinetics data (*i.e.* measured $c(t)$ in the second diffusion cell), the distribution function of the diffusion coefficient $f(D)$ was calculated using an integral equation [201]

$$c(x,t) = 0.5 c_0 \pi^{-0.5} \int_{D_{\min}}^{D_{\max}} (Dt)^{-1/2} \exp(-x^2/(4Dt))\, f(D) dD\,, \qquad (25)$$

where c_0 is the initial concentration in the feeder cell, x the collagen membrane thickness, and $D_{\min}$ and $D_{\max}$ the minimal and maximal values of the diffusion coefficient, respectively, used on integration. This equation was solved using a regularisation procedure with unfixed regularisation parameter [191]. The value of specific surface area S_A/V = 0.0274 μm^{-1} (calculated with Eq. (6)) corresponding to 0.4 m^2/g is much smaller than the specific surface area of narrow pores in the collagen hydrogel. Notice that the average thickness of the pore walls at $t \approx 7$ μm corresponds to a smooth film with the surface area of 0.12 m^2/g. A portion of the pore walls can be thinner than the average thickness and the surface can be rough. Both these attributes can result in an increase in the surface area of the macropores. According to the NMR cryoporometry calculations, the specific surface area of nanopores at d < 50 nm was equal to 119 m^2/g. However, the pore volume at d < 50 nm was relatively small ~0.2 cm^3/g. Thus, there were opposing relationships between the pore volume and the specific surface area of nanopores at d < 50 nm and micro/macropores at d > 1 μm. The latter, despite being the main contributor to the overall macropore volume ($V_m \approx$ 14.4 cm^3/g), provided only a small contribution to the total surface area of the pores ($S_m \approx$ 0.4 m^2/g), the converse

being true for the nanopores ($V_n \approx 0.2$ cm^3/g and $S_n \approx 119$ m^2/g, respectively). This feature of collagen gel provided adsorption of small polar molecules in nanopores because these molecules can be poorly adsorbed in micro- and macropores due to significant desolvation effects for polar adsorbates in the aqueous medium, as well as for a polar surface of collagen occupied by adsorbed molecules. Based on purely dimensional considerations it could be expected that macromolecules were adsorbed in nanopores at d = 10-100 nm and cells were located in micro- and macropores at d > 20 μm. Whilst this may well be true, both cells and macromolecules can potentially anchor in the more narrow pores which would strengthen their attachment to the matrix. The large micro/macroporosity and interconnectivity of pores in the collagen material can provide good conditions for diffusion of macromolecules such as proteins through a collagen membrane. The results of measurements of the diffusion kinetics of BPTI, BSA and Fg [106] that are different in size and shape (Fig. 50) are shown in Figure 51.

Using the twin-chambered diffusion cell, with a protein solution on one side of a sample and PBS on the other, the experiments showed that within 60-65 minutes from the start of the diffusion of relatively small BPTI molecules, the system reached equilibrium [106]. This observation was made for two initial concentrations of BPTI (1.3 and 2.6 mg/mL) (Fig. 51). The larger BSA molecules needed about 75 minutes to reach the equilibrium, and Fg molecules equilibrated within 90 minutes (Fig. 51). This pattern was characteristic of the relationship between the diffusion coefficient and the hydrodynamic radius of solutes: the larger the molecules, the slower their motion (diffusion). For example, the diffusion coefficients D_0 of BPTI, BSA and Fg molecules in the aqueous solution are equal to $(0.8\text{-}1.9)\times10^{-6}$, $(0.6\text{-}1.0)\times10^{-6}$ and $(1.9\text{-}3.1)\times10^{-7}$ cm^2/s [205-208], respectively.

The D_0 values also depend on the amount of dissolved compounds (due to intermolecular interactions and changes in the medium properties with increasing solute concentration), pH (affecting charge of molecules, their shape and size) and ionic strength (influencing aggregation of protein molecules) [50,209]. These effects and protein interactions with the collagen gel membrane resulted in broadening of the D value range. This range corresponds to certain monomodal, bi- or trimodal $f(D)$ distributions that depend on individual protein types and surrounding conditions. The left $f(D)$ peak (Fig. 51d) or the left shoulder at $D < D_0$ of broad $f(D)$ curves in the case of monomodal distributions (Fig. 51b,d,f) indicated that the diffusion of a portion of protein molecules through the collagen membrane was much slower than in the free aqueous solution of the protein. This is due to their interactions with the pore walls and adsorption within the collagen gel. The adsorption reduced the membrane pore sizes that had a negative impact on diffusion rates. Diffusion of BPTI through the collagen membrane was slower after a pre-run of Fg, and particularly after a

pre-run of BSA and Fg (Fig. 51b). This effect is equivalent to the biofouling phenomenon. Due to more effective adsorption [50] and physical trapping, larger macromolecules from the previous run had a larger effect on membrane permeability than smaller BPTI molecules. A pre-run of BPTI itself did not have the negative effect on the second BPTI run as the main $f(D)$ peak remained in the same position. Additionally, a small $f(D)$ peak of BPTI appeared at $D > 10^{-5}$ cm^2/s due to diffusion of the protein molecules remained in the membrane after the first run. Retardation of the BSA diffusion was observed after the first run with the same protein (Fig. 51d) or Fg [106]. This could be due to the same effects as stated above for BPTI (Fig. 51b).

Protein molecules can form aggregates [209]. However, these structures must be smaller in size than the collagen macropores; therefore protein diffusion occurred despite the protein pre-runs, but at a lower rate (Fig. 51). In other words, complete blocking of the collagen pores by the proteins studied did not occur [106]. The appearance of several peaks on the $f(D)$ curves for certain samples (Fig. 51) can be explained by the mechanism of protein diffusion through the collagen hydrogel. However, the D values at the $f(D)$ maxima for all the proteins studied were close to the D_0 values in bulk solutions. Consequently, the diffusion of most of the protein molecules through the collagen membrane was as unhindered as their diffusion in aqueous solution without the hydrogel, in other words, $D_{por} \approx D_0$. This conclusion confirms that proteins of different molecular weight, shape and size such as the small globular polypeptide BPTI (size 2.9×1.9 nm), larger globular protein BSA (14×6×4 nm) and rod-like glycoprotein Fg (45×9×6 nm) penetrated through the collagen hydrogel membrane of 1 mm in thickness without significant retardation [106]. This result is of great importance from a practical point of view since the possibility of nearly free diffusion of macromolecules is important for the normal functioning of cells within any cryogel used as a dermal substitute. However, the broad shape of the $f(D)$ distributions showed that a certain portion of the proteins strongly interacted with the pore walls in the hydrogel and that the pore tortuosity factor could affect the measured D values.

There is an additional effect caused by the pre-adsorption of a protein which is related to the diminution of the contribution of very slow diffusion of BSA after its first run (Fig. 51d). This effect can be explained by two phenomena. Firstly, the number of strong adsorption sites at the collagen surface is reduced (as well as the pore tortuosity factor) in the second run due to the adsorption of the protein molecules during the first run. Secondly, pre-adsorbed macromolecules can block pores (especially narrow necks and bends of pores) but relatively weakly. The first effect results in weakening of interactions of the proteins with the collagen surfaces covered by pre-adsorbed protein molecules; *i.e.* the D value increases. Partial blocking of micropores gives the opposite but smaller changes in the D values because the diffusion occurs in macropores. The

overall effect can play an important role in cell migration and proliferation within the collagen hydrogel when used in practical applications [2-4,106].

Yao *et al.* [79] studied adsorption kinetics of BSA on supermacroporous polyacrylamide-based cryogels with embedded Fe_3O_4 nanoparticles. Breakthrough of BSA at different liquid flow rates revealed the effects of liquid velocity and pore structures. A typical BSA breakthrough curve is shown in Fig. 52. Kinetic behaviour of BSA interacting with cryogel was described by equation [79,210]

$$\mathrm{d}c_b / \mathrm{d}t = -K_L \left(c_b - (c_0 - c_b) V (q_m K_a m - K_a (c_0 - c_b) V)^{-1} \right) \quad (26)$$

where c_b is the protein concentration in the bulk phase at time t, c_0 the initial protein concentration of BSA, K_L the overall mass transfer coefficient for protein from liquid phase to pore surfaces, V the volume of the feed solution, and m is the mass of dried matrix used in the finite batch adsorption, respectively. The concentration at the out let of the cryogel bed was obtained by averaging the concentrations in capillaries based on their flow rates and written as [80]

$$C = Q^{-1} \sum_{i}^{N_g} C_i n_i Q_i \,, \quad (27)$$

where N_g is the total number of capillary groups with the same diameter, n_i the number of capillaries in group i, Q_i the flow rate [80]

$$Q_i = \pi d_i^4 \Delta p_i \,/(128 \mu_L L_i) \quad (28)$$

d_i the capillary diameter, Δp_i the pressure drop between the inlet and outlet of the capillary i, μ_L the liquid viscosity, and $L_i$the capillary length [80]. Yun *et al.* [80] obtained similar BSA breakthrough curves for PHEMA-based cryogels (Fig. 53a). We developed a model for estimation of the energetic characteristics from the breakthrough curves using the kernel as a kinetic analogue of the Langmuir equation [54,211]

$$\frac{C(t)}{C_0} = A \int_{\Delta G_{\min}}^{\Delta G_{\max}} \frac{\exp\left(v_L (t - t_b)/(\alpha L V_p)\right) \exp\left(-(\Delta G + z)/R_g T\right)}{1 + \exp\left(v_L (t - t_b)/(\alpha L V_p)\right) \exp\left(-(\Delta G + z)/R_g T\right)} f(\Delta G) d(\Delta G), \quad (29)$$

where A and α are equation constants; t_b the breakthrough time, L the thickness of a membrane, and V_p the pore volume. The calculations of the $f(\Delta G)$ functions with the regularisation procedure show (Fig. 53b) that interactions of BSA with cryogel decrease with increasing velocity of the flow through the membrane that correspond to shorter breakthrough time (Fig. 53a).

Cryogels prepared with synthetic and natural macromolecules (PVA, agar-agar, polyacrylamide, locust-bean gum, amylopectin, starch, chitosan, gelatine, *etc.*) are promising carriers for cell immobilisation [2-4,212-214]. Cell migration in tissue scaffolds was studied using 3T3 mouse fibroblast cells [106]. A suspension of 2.0×10^6 cells mL^{-1} was incubated with the

collagen hydrogel for 2 h. The collagen hydrogel with cells was stained with fluorescent 4',6-diamidino-2-phenylindole (DAPI) to stain the cell nuclei, and photographs taken using a fluorescent microscope at 488 nm [106].

Subsequently, normal primary human skin fibroblasts SKF276 (DBIS cell bank, University of Brighton, UK) were used to seed the collagen hydrogel [106]. Cells were maintained in fibroblast growth medium consisting of D-MEM supplemented with 10% foetal bovine serum, at 37^{o}C, in 5% CO_2 humidified incubator. Collagen hydrogel samples (1×1 cm^2) were placed into 6-well plates with the bottom surface facing upwards. Human fibroblasts were harvested (at passage 8 from isolation) and re-suspended in fibroblast growth medium at 10^5 cells/0.1 mL. Each collagen hydrogel was seeded dropwise with 10^5 fibroblasts. Plates with scaffolds were incubated at 37^{0}C in 5%CO_2 humidified incubator for 24 h. After cellular inoculation, hydrogels were rotated upside down so that the cell layer was now at the bottom, *i.e.* they had to migrate against gravity, and transferred into 24-well plates supplemented with fresh fibroblast growth media (2 mL/well) and incubated over a 28-day period [106].

After 28 days hydrogel samples with cells were fixed, stained with propidium iodide nuclear stain and photographs were taken using the CLSM [106]. ImageJ software was used to assess the depth of cell migration and cell numbers within collagen hydrogel by quantifying the cellular nuclei using an automatic particle analyser or manual cell counter plugins [106]. A micrograph of the distribution of 3T3 mouse fibroblast cells after two hours incubation of the cell suspension with collagen hydrogel demonstrates that the cells penetrated into the collagen gel relatively quickly, but this may be due to the cells simply sinking into the gel pores under gravity (Fig. 54a). However, human skin fibroblasts were able to attach to the collagen hydrogel, proliferate and migrate upwards, *i.e.* against gravity, through the scaffold during the 28-day incubation period (Fig. 54b). These results confirm that the macroporous collagen structure revealed by SEM and CLSM is suitable for cell migration (the average macropore size is larger than the cell size by almost an order in magnitude) and for cell growth within this material [106].

A more detailed analysis of migration (as an important desirable effect) of human fibroblast cells within these collagen hydrogels was performed using the ImageJ software package [111] to quantify the cell number (normal primary human skin fibroblasts) within a collagen sample over a range of time intervals [106].

The cell distribution was non-uniform across the collagen film (Fig. 55) because of a low migration rate and the structural characteristics of the material which in addition to macroporoses possessed a certain fraction of nano- and micropores, and pore bends and necks. The structural and textural non-uniformity of the material and its high biocompatibility may have caused relatively

strong attachment of cells in the layers located close to the material surface (Fig. 54b). This could have reduced the migration rate. It was also unclear whether the cells entered the gel by true migration, or by proliferation into the gel structure, or both processes. However, the cell distribution was relatively uniform within a 500 μm layer (Fig. 55). Some cell-mediated contraction was observed in this layer (Fig. 54b). A visual estimation gives about 50% contraction in a ¼ thickness of the film. This results in the diminution of the scaffold permeability, *i.e.*, K in Eq. (9), by four times to approximately 10^{-11} m^4/Ns [106].

To study cell – collagen gel interaction a quartz crystal microbalance (QCM) technique was used in [106]. Quartz crystals, 8.6 mm in diameter that had a resonance frequency of 10 MHz, were mounted in PEEK (polyether ether ketone) holders using a low viscosity elastomer (RS, Corby, UK), and 5 μm silver wires to yield a pressure-free cartridge crystal assembly. Introduction of the cell suspension was through a pulse-less injection valve fitted with 20 μl loops. Cartridges were held at 37±0.1ºC. The attachment of cells to collagen hydrogel layered onto a surface of a quartz crystal sensor reduced the resonant oscillation frequency by $\Delta f_1 = -75$ Hz after the first cell injection (Fig. 56, curve 1 at $t < 600$s).

The second cell injection led to the total $\Delta f_{12} \approx -105$ Hz, *i.e.* $|\Delta f_2| < |\Delta f_1|$. Both injections enhanced the auto-gain controller voltage (Fig. 56, curve 2) that indicated cell interactions with the collagen matrix. These frequency shifts can be interpreted in terms of mass addition of cells to the sensor surface according to the equation [215,216]

$$\Delta f = -f_0^{1.5}(\eta_l \rho_l /(\pi \mu_q \rho_q))^{0.5} - 2 f_0^2 \rho_f h_f (\mu_q \rho_q)^{-0.5}, \qquad (30)$$

where Δf is the measured frequency shift, f_0 is the resonant frequency of the unloaded crystal, ρ_l and η_l are the density and viscosity respectively of the liquid in contact with the coated crystal surface, ρ_q and μ_q refer to the specific density and the shear modulus of quartz. Treatment of the data shown in Fig. 56 with Eq. (30) [217] gives $h_f \approx 5$ nm. The use of this value and the cell size (~10 μm) allowed us to estimate the fraction of the collagen surface covered by cells. The cell covered area corresponds approximately to 0.05% of the total area of the collagen matrix. This small value can be explained by the short time (~20 min) of the QCM observation, which was too short for cell migration deeper into the collagen matrix. In other words, the observed small Δf value is due to cell attachment only to the outer surface of the collagen matrix without cell penetration into deeper layers of the material (as in Figs. 54 and 55) [106].

The response of the QCM sensor also reflects the dissipation of energy within the system and hence changes of viscoelastic properties of the collagen matrix and cellular overlayers. The QCM study showed that interactions of fibroblast cells with the collagen occurred relatively quickly since

the *f* minima were reached during first 3-5 min. Subsequent reduction of the $|\Delta f|$ value by 13 % after the second minimum was probably due to removal of a fraction of cells caused by several factors. The liquid flow could have washed off loosely attached cells from the outer surface of the collagen matrix which was possibly amplified by sensor vibration. The repulsive interaction of cells introduced with the second injection with pre-adsorbed cells, attached to the outer surface with the first injection without migration into deeper collagen layers, can result in weakening of the cell attachment. It should be noted that a kinetic analogue of the Langmuir equation was used to compare the changes in the Gibbs free energy on adsorption of proteins to different surfaces (including QCM measurements) [217], as well as in the case of diffusion of proteins through the hydrogel membrane [106].

The authors used kinetic analogue of the Langmuir equation to compare the changes in the Gibbs free energy on equilibrium and kinetic adsorption (including QCM measurements) of proteins to different surfaces [217]. The $h_f(t)$ function calculated from the $\Delta f(t)$ curve (Fig. 56a) has a sharp increase in the h_f value when $f(t)$ decreases due to the formation of an adsorbed cell layer. The $h_f(t)$ function can be re-calculated to extract the value of adsorption per surface unit of the sensor ($C_s(t)$). On this basis it is possible to write an overall equation [217]:

$$C_S(t)/C_p = \int_{\Delta G_{\min}}^{\Delta G_{\max}} aC_f(t)\exp(-(\Delta G+z)/R_gT)(1+aC_f(t)\exp(-(\Delta G+z)/R_gT))^{-1} f(\Delta G)\mathrm{d}(\Delta G), \quad (31)$$

where $f(\Delta G)$ is the distribution function of the free energy of cell interaction with a cryogel surface, *a* is an equation parameter, and *z* depends on the presence of pre-adsorbed cells ($z = 0$ for a pure gel surface). The $f(\Delta G)$ function for cells introduced with the second injection is located at smaller $-\Delta G$ values than that for the first injection (Fig. 56b). This shows that the most active surface sites were occupied by the cells from the first injection.

The photon correlation spectroscopy (PCS) allows the investigation of mobility of microorganisms [209]. This method could be used to study interactions of mobile (*e.g.* living *Proteus mirabilis,* PM) and immobile (inactivated PM) microorganisms with cryogel used as a membrane between two cells. Notice that the mobility of bacteria was studied using PCS in detail [209,218-222]. This ability of PCS is of importance in respect of elucidation of the influence of media or cryogel membrane or scaffolds on living microorganisms. The determination of the size distribution of mobile microorganisms by the standard PCS techniques gives a smaller hydrodynamic radius (R_h) than true *R* because of ignoring contribution of own mobility of microorganisms to their summary motion. The difference between the R_h (estimated with PCS) and R_e (measured with electron microscopy methods) values may be used to evaluate the microorganism mobility. However, this can be also done directly. The velocity ($\vec{v}$) distribution function ($f(v)$) can

be estimated using the diffusion coefficient ($D_{T,i}$) value for inactivated (i) microorganisms with equation for the autocorrelation function measured by the PSC method [209,223]:

$$g^{(2)}(\tau) = 1 + \exp(-2D_{T,i}q^2\tau)\left[\beta + (1-\beta)\int_0^\infty \sin(\vec{q}\vec{v}\tau)/(\vec{q}\vec{v}\tau)\, f(v)\mathrm{d}v\right]^2, \quad (32)$$

whereτ is the time shift ($\tau = t_2 - t_1$) between two time points (t_2 and t_1) of the observation, βa portion of inactivated microorganisms,

$$q = |\vec{q}| = |\vec{k}_f - \vec{k}_i| = 4\pi n/\lambda \sin(\theta/2), \quad (33)$$

q is the scalar of the wave scattering vector ($\vec{q}$) equal to the difference between the final wave vector ($\vec{k}_f$) and the incident ($\vec{k}_i$), n is the refraction index of the liquid, λ is the wavelength of the incident light in vacuum, and θ is the observation angle of the scattered light [209]. This method was applied to investigate the mobility of *Pseudomonas putida* [223], *Dunaliella viridis* [224] and *Escherichia coli* [225]. This approach was also used to study the influence of silica nanoparticles and poly(vinyl pyrrolidone) on the mobility of living flagellar microorganisms *Proteus mirabilis* 187 (*PM*187). Solution of Eq. (32) was obtained with the CONTIN algorithm [191] modified to compute not only the particle size distributions but also the velocity distribution [226]. It should be noted that the $D_{T,i}$ value in Eq. (32) can be easily determined, since the $f(D_T)$ distribution for living and partially inactivated microorganisms includes two separate peaks (Fig. 57) [209] corresponding to the motion of inactivated (participating only in Brownian motion) and living mobile (characterised by both own and Brownian motions) microorganisms *PM*187. A study of the mobility of microorganisms before and after interactions with the cryogel membranes can give information on the influence of the cryogel morphology (porosity, PSD, pore connectivity, tortuosity, *etc.*) and chemical composition (including drug delivery systems) on these interactions.

Recently, the dielectric behaviour of water-imbibed macroporous polymeric matrices with randomly oriented interconnected pores was investigated using DRS in the frequency range from 1 kHz to 2 GHz [227]. The confinement of an aqueous phase into mesoscopic regions (from 10 nm to 100 mm in size) inside the porous material resulted in the appearance of a new relaxation process due to the interfacial orientational polarisation of the aqueous phase at the polymer interface. The textural characteristics were analysed using the DRS data. This approach can be used to study strongly hydrated cryogels with attached cells and microorganisms because water organisation in macropores strongly differs from water in cells or bacteria.

In recently published papers, the characterisation of solid composite cryogels with silica [228], carbon [229,230], carbon/carbon [231] or carbon/silica composite [92] was carried out similarly to other adsorbents. It is typically based on nitrogen adsorption (with calculated PSD),

XRD, FTIR, Raman methods and microscopic images (but without quantitative image analysis) of dried materials. However, these solid cryogels were not studied in superhydrated state. Recent papers describing soft polymeric (PVA, PEG, PHEMA, chitosan, *etc.*), protein (fibronectin, lysozyme, gelatine) or polymer/protein composite cryogels used microscopic and adsorption methods [232-246] but without quantitative analysis of SEM, CLSM or other images. For instance, Yun *et al*. [247] synthesised polyacrylamide based supermacroporous cryogel beads with a narrow particle size distribution at average particle size around 1 mm with high porosity of 84-98%. However, the textural characteristics of these particulate cryogels were not analysed in detail. Berillo *et al*. [248] synthesised macroporous hydrogels formed with self-assembly of fluorenyl-9-methoxycarbonyl–diphenylalanine peptides induced using glucono-δ-lactone. However, CLMS and SEM images of cryogels were not treated to obtain quantitative structural information. Macroporous semi-interpenetrating polymer networks composite hydrogels were synthesised by cross-linking polymerisation of acrylamide with N,N'-methylenebisacrylamide in the presence of potato starch or an anionic polyelectrolyte at -18^{o}C. To give quantitative characteristics of cryogels, the sizes of macropores were shown directly on SEM images [249,250]. As a whole, this is useless presentation of the textural characteristics of the cryogels. Cryogels with molecular-imprinted polymers have attracted increased attention because of significant enhancement of the selectivity of the materials used as adsorbents [234,243]. Additionally, functionalisation of cryogels can be used for the same purposes. Unfortunately, in the major portion of published papers, which deal with structure, morphology and texture of hydrated or dried cryogels, the characterisation is rather qualitative or semi-quantitative since microscopic images and other data are not quantitatively analysed within the mentioned aspects. Standard adsorption methods cannot be used for these purposes with exception of cryogels with solid materials, which can be dried practically without structural changes. The textural changes affected by freezing (*i.e.* cryogelation) of aqueous suspensions of such solid materials as single (SLGO) and multi-layer (MLGO) graphene oxides in superhydrated state could be better studied by NMR cryoporometry [251] than by standard adsorption methods because these systems are very unstable during drying [252] similar to soft organic cryogels. Thus, structural, textural and adsorption characterisation of cryogels, especially with soft materials superhydrated in native state and unstable during drying, should be improved for deeper insight into the interfacial phenomena occurring at their surfaces or into the phenomena occurring in pores over the total size range ($2 < d < 3\times10^5$ nm).

5. Conclusions

Determination of the porous structure of intact soft cryogels in both superhydrated and dried states over the total range of pore sizes from narrow nanopores (d < 2 nm) to macropores (d > 100 μm) is a challenging task which is of extreme importance for predicting their performance and optimising their properties as tissue scaffolds, membranes, drug delivery systems, adsorbents, bioreactors, *etc.* No single analytical method can provide all the necessary information, however combining data obtained using modern experimental techniques such as NMR cryoporometry, DSC and TG thermoporometry, NMR, TSDC and DRS relaxometry, and mercury porosimetry, CLSM, adsorption-desorption, diffusion, breakthrough, *etc.* can help to solve this complex and challenging task. All the results obtained using the ^{1}H NMR, cryoporometry, thermoporometry, relaxometry, water desorption, CLSM, SEM, protein diffusion, cell attachment (analysed by QCM) and migration methods are in good agreement with each another. Combination of the PSD based on quantitative analysis of CLSM, SEM or other images (for micro/macropores) and NMR cryoporometry, TSDC relaxometry, DSC thermoporometry (for nanopores), and SAXS provides reliable description of pores over the whole diameter range from 2 nm to 300 μm and pore walls (0.5 nm < t < 30 μm). The investigations discussed above reveal the dominant role of pores at d > 1 μm contributing to the total porosity of cryogels, channels for protein diffusion, places for cell attachment and for cell migration and proliferation. The contribution of narrow (d < 2 nm) and middle (2 < d < 50 nm) nanopores into the total porosity is less than 2% because they are located in thin macropore walls (typically 1-10 μm in thickness). However, they contribute over 95% of the specific surface area of the material. In the native hydrated state, polymer- and protein-based cryogels are characterised by a large macropore volume (up to 20-40 cm^3/g) but a small specific surface area of the macropore walls (outer surface ~ 1 m^2/g, inner surface ~100 m^2/g for polymer and < 450 m^2/g for protein cryogels), high pore interconnectivity and high hydrophilicity. The main portion of water in macroporous cryogels can be attributed to bulk unbound water (frozen at T = 0^oC and desorbed at $T \leq 100^oC$) located in macropores. The amount of bound water located in nanopores in the swollen macropore walls is smaller, at least, by one order in magnitude. This water is weakly bound (frozen at temperatures close to 0^oC), which makes macroporous cryogels an attractive biomaterial for medical applications. Strongly bound water is characterised by a low activity as a solvent and hence affects adversely a variety of bioprocesses within the cryogel pore walls but it does not affect these processes in macropores of cryogels. This is of importance for dissolution and diffusion of nutrients, proteins, *etc.*, as well as migration of cells.

The developed approaches to calculate the distribution functions of changes in the free energy of equilibrium adsorption and adsorption kinetics, diffusion and breakthrough of small molecules,

macromolecules and cells interacting with cryogels in different dispersion media allow us to get a deeper insight in the structure-property relationships for a variety of soft materials such as cryogels.

Acknowledgements

This work was financially supported by FP7, projects MONACO-EXTRA (PIAP-GA-2008-218242) and Bio-Smart (PERG08-GA-2010-276954), and Marie Curie International Research Staff Exchange Scheme (COMPOSITUM, grant no. 230790). The authors thank Prof. V.I. Lozinsky (Russian Academy of Sciences), Dr. C.A. Howell, Dr. S.R. Sandeman, Dr. L.I. Mikhalovska, Dr. R.V. Shevchenko, Y. Zheng (University of Brighton, UK), Dr. O.P. Kozynchenko (MAST Carbon International Ltd, UK), Dr. A.E. Ivanov (Protista Biotechnology AB, Sweden), and Prof. V.V. Turov (CISC, Kiev, Ukraine) for their help in discussion of the results presented in this paper.

References

[1] Chaplin M. Water structure and behaviour. http://www.lsbu.ac.uk/water/, 2012.

[2] Mattiasson B, Kumar A, Galaev IYu (editors), Macroporous Polymers. Production Properties and Biotechnological/Biomedical Applications. CRC Press; 2009.

[3] Cui Zh (editor), Medical Biothechnology and Health Care. Vol. 5, Second edn., Elsevier; 2011.

[4] Lozinsky VI. Russ Chem Rev 2002;71:489.

[5] Mitchell J, Webber JBW, Strange JH. Physics Reports 2008;461:1.

[6] Bershtein VA, Yakushev PN. Adv Polym Sci 2010;230:73.

[7] Mikhalovsky SV, Gun'ko VM, Bershtein VA, Turov VV, Egorova LM, Morvan C, Mikhalovska LI. RSC Advances 2012;2:2868.

[8] Standard guide for assessing microstructure of polymeric scaffolds for use in tissue engineered medical products. Book of Standards, Vol. 13.01. http://www.astm.org/Standards/F2450.htm.

[9] Gregg SJ, Sing KSW. Adsorption, Surface Area and Porosity. Second edn., Academic Press, San Diego; 1982.

[10] Peppas NA, Bures P, Leobandung W, Ichikawa H. Eur J Pharm Biopharm 2000;50,27.

[11] Gomes ME, Holtorf HL, Reis RL, Mikos AG. Tissue Eng 2006;12:801.

[12] Kumar A, Plieva FM, Galaev IYu, Mattiasson B. J Immunol Method 2003;283:185.

[13] Arvidsson P, Plieva FM, Savina IN, Lozinsky VI, Fexby S, Bulow L, Galaev IYu, Mattiasson B. J Chromatogr A 2002;977:27.

[14] Hanora A, Savina I, Plieva FM, Izumrudov VA, Mattiasson B, Galaev IYu. J Biotech 2006;123:343.

[15] Plieva FM, Galaev IYu, Mattiasson B. J Sep Sci 2007;30:1657.

[16] Bansal V, Roychoudhury PK, Mattiasson B, Kumar A. J Mol Recogn 2006;19:332.

[17] Dubruel P, Unger R, Van Vlierberghe S, Cnudde V, Jacobs PJS, Schacht E, Kirkpatrick CJ. Biomacromolecules 2007;8:338.

[18] Hedberg EL, Shih CK, Lemoine JJ, Timmer MD, Liebschner MA, Jansen JA, Mikos AG. Biomaterials 2005;26:3215.

[19] Savina IN, Cnudde V, D'Hollander S, Van Hoorebeke L, Mattiasson B, Galaev IYu, Du Prez F. Soft Matter 2007;3:1176.

[20] Qian L, Zhang H. J Chem Technol Biotechnol 2011;86:172.

[21] Deville S, Saiz E, Tomsia AP. Acta Mater 2007;55:1965.

[22] Butler MF. Cryst Growth Des 2001;1:213. 2002;2:59.

[23] Butler MF. Cryst Growth Des 2002;2:541.

[24] Zhang H, Hussain I, Brust M, Butler MF, Rannard SP, Cooper AI. Nat Mater 2005;4:787.

[25] Uhlmann DR, Chalmers B, Jackson KA. J Appl Phys 1964;35:2986.
[26] Rempel AW, Worster MG. J Cryst Growth 1999;205:427.
[27] Peppin SSL, Elliot JAW, Worster MG. J Fluid Mech 2006;554:147.
[28] Peppin SSL,Wettlaufer JS, Worster MG. Phys Rev Lett 2008;100:238301.
[29] Deville S, Maire E, Bernard-Granger G, Lasalle A, Bogner A, Gauthier C, Leloup J, Guizard Ch. Nat Mater 2009;8:966.
[30] Partap S, Muthutantri A, Rehman IU, Davis GR, Darr JA. J Mater Sci 2007;42:3502.
[31] Van Vlierberghe S, Cnudde V, Dubruel P, Masschaele B, Cosijns A, Paepe ID, Jacobs PJS, Van Hoorebeke L, Remon JP, Schacht E. Biomacromolecules 2007;8:331.
[32] Savina IN, Mattiasson B, Galaev IYu. J Polym Sci Part A Polym Chem 2006;44:1952.
[33] Kim S-h, Chu C-C. J Biomed Mater Res Part B: Appl Biomater 2000;53:258.
[34] Plieva FM, Karlsson M, Aguilar M-R, Gomez D, Mikhalovsky S, Galaev IYu. Soft Matter 2005;1:303.
[35] Dainiak M, Allan I, Savina IN, Cornelio L, James L, James S, Mikhalovsky S, Jungvid H, Galaev IYu. Biomaterials 2010;31:67.
[36] Lozinsky VI, Galaev IY, Plieva FM, Savina IN, Jungvid H, Mattiasson B. Trend Biotech 2003;21:445.
[37] Bölgen N, Yang Y, Korkusuz P, Güzel E, Haj AJE, Pişkin E. Tissue Eng Part A 2008;14:1743.
[38] Dainiak M, Savina IN, Musolino I, Kumar A, Mattiasson B, Galaev IYu. Biotechnol Progr 2008;24:1373.
[39] Savina IN, Dainiak M, Jungvid H, Mikhalovsky SV, Galaev IYu. J Biomater Sci 2009;20:1781.
[40] Kumar A. 2008, http://www.scitopics.com/Supermacroporous_Cryogels.html.
[41] Plieva FM, Savina IN, Deraz S, Andersson J, Galaev IY, Mattiasson B. J Chromatography B 2004;807:129.
[42] Savina IN, Galaev IY, Mattiasson B. J Chromatography A 2005;1092:199.
[43] Plieva FM, Ekstrom P, Galaev IY, Mattiasson B. Soft Matter 2008;4:2418.
[44] Savina IN, English CJ, Whitby RLD, Zheng YS, Leistner A, Mikhalovsky SV, Cundy AB. J Hazard Mater 2011;192:1002.
[45] Le Noir M, Plieva F, Hey T, Guieysse B, Mattiasson B. J Chromatography A 2007;1154:158.
[46] Le Noir M, Plieva FM, Mattiasson B. J Sep Sci 2009;32:1471.
[47] Busquets R, Kozynchenko O, Ivanov AI, Savina IN, Whitby RLD, Jungvid H, Tennison S, Mikhalovsky SV, Cundy AB. Prog Environ Sci Technol 2011;3:589.
[48] Xu P, Yao Y, Shen S, Yun J, Yao K. Chinese J Chem Engin 2010;18:667.
[49] Spiller K, Laurencin S, Charlton D, Maher S, Lowman A. Acta Biomaterialia 2008;4:17.

[50] Gun'ko VM, Turov VV, Gorbik PP. Water at the Interfaces. Naukova Dumka, Kiev; 2009 (Russ).

[51] Gun'ko VM, Turov VV, Bogatyrev VM, Zarko VI, Leboda R, Goncharuk EV, Novza AA, Turov AV, Chuiko AA. Adv Colloid Interface Sci 2005;118:25.

[52] Mikhalovska LI, Gun'ko VM, Turov VV, Zarko VI, James SL, Vadgama P, Tomlins PE, Mikhalovsky SV. Biomaterials 2006;27:3599.

[53] Gun'ko VM, Zarko VI, Goncharuk EV, Andriyko LS, Turov VV, Nychiporuk YM, Leboda R, Skubiszewska-Zięba J, Gabchak AL, Osovskii VD, Ptushinskii YG, Yurchenko GR, Mishchuk OA, Gorbik PP, Pissis P, Blitz JP. Adv Colloid Interface Sci 2007;131:1.

[54] Gun'ko VM, Turov VV. Nuclear Magnetic Resonance Studies of Interfacial Phenomena, Taylor & Francis; 2013, in press.

[55] Shapiro YuE. Prog Polymer Sci 2011;36:1184.

[56] Djabourov M, Bonnet N, Kaplan H, Favard N, Favard P, Lechaire JP, Maillard M. J Phys II France 1993;3:611.

[57] Nosé Y, Horiuchi T, Malchesky PS, Smith JW, Matsubara S, Abe Y. Therapeutic Apheresis 2002;4:38.

[58] Ice Ball™ Thermal Storage, www.cryogel.com.

[59] Mukai ShR, Nishihara H, Shichi S, Tamon H. Chem. Mater 2004;16:4987.

[60] Szczurek A, Amaral-Labat G, Fierro V, Pizzi A, Celzard A. Carbon 2011;49:2785.

[61] Feaver A, Cao G. Carbon 2006;44:591.

[62] Tamon H, Ishizaka H, Yamamoto T, Suzuki T. Carbon 1999;379:2049.

[63] Babić B, Kaluđerović B, Vračar Lj, Krstajić N. Carbon 2004;42:2617.

[64] Yamamoto T, Endo A, Ohmori T, Nakaiwa M. Carbon 2005;43:1231.

[65] Soottitantawat A, Yamamoto T, Endo A, Ohmori T, Nakaiwa M. Amer Inst Chem Eng J 2007;53:228.

[66] ElKhatat AM, Al-Muhtaseb ShA. Adv Mater 2011;23:2887.

[67] Qian L, Zhang H. J Chem Technol Biotechnol 2011;86:172.

[68] Paranhos CM, Oliveira RN, Soares BG, Pessan LA. Mater Res 2007;10:43.

[69] Benoit DSW, Durney AR, Anseth KS. Biomaterials 2007;28:66.

[70] Goharian M, Moran GR, Wilson K, Seymour C, Jegatheesan A, Hill M, Thompson RT, Campbell G. Nuclear Instr Meth Phys Res B 2007;263:239.

[71] Bai X, Ye Z-f, LiY-f, Zhou L-c, Yang L-q. Process Biochem 2010;45:60.

[72] Pazos V, Mongrain R, Tardif JC. J Mechan Behavior Biomed Mater 2009;2:542.

[73] Kueseng P, Thammakhet Ch, Thavarungkul P, Kanatharana P. Microchem J 2010;96:317.

[74] Seal BL, Ortero TC, Panitch A. Mater Sci Eng R 2001;34:147.
[75] Patachia S, Florea C, Friedrich Chr, Thomann Y. eXPRESS Polym Lett 2009;3:320.
[76] Autissier A, Visage CL, Pouzet C, Chaubet F, Letourneur D. Acta Biomater 2010;6:3640.
[77] Noppe W, Plieva FM, Vanhoorelbeke K, Deckmyn H, Tuncel M, Tuncel A, Galaev IYu, Mattiasson B. J Biotechnol 2007;131:293.
[78] Svec F. J Chromatography A 2010;1217:902.
[79] Yao K, Shen Sh, Yun J, Wang L, Chen F, Yu X. Biochem Eng J 2007;36:139.
[80] Yun J, Jespersen GR, Kirsebom H, Gustavsson P-E, Mattiasson B, Galaev IYu. J Chromatography A 2011;1218:5487.
[81] Kumar A, Bansal V, Nandakumar KS, Galaev IYu, Roychoudhury PK, Holmdahl R, Mattiasson B. Biotech Bioeng 2006;93:636.
[82] Alves M-H, Jensen BEB, Smith AAA, Zelikin AN. Macromol Biosci 2011;11:1293.
[83] Liu H, Liu M, Bai L, Sun S, Liu Y, Yang G. Talanta 2011;85:1193.
[84] Vrana NE, Cahill PA, McGuinness GB. J Biomed Mat Res A 2010;94A:1080.
[85] Tripathi A, Kumar A. Macromol Biosci 2011;11:22.
[86] Păduraru OM, Ciolacu D, Darie RN, Vasile C. Mater Sci Eng C 2012;32:2508.
[87] Mu Ch, Liu F, Cheng Q, Li H, Wu B, Zhang G, Lin W. Macromol Mater Eng 2010;295:100.
[88] Robert D, Barelli S, Crettaz D, Bart P-A, Schifferli JA, Betticher D, Tissot J-D. Proteomics 2006;6:3958.
[89] Mukai ShR, Nishihara H, Shichi S, Tamon H. Chem Mater 2004;16:4987.
[90] Kraiwattanawong K, Sano N, Tamon H. Carbon 2011;49:3404.
[91] Pons A, Casas Ll, Estop E, Molins E, Harris KDM, Xu M. J Non-Crystal Solid 2012;358:461.
[92] Babić B, Kokunešoski M, Miljković M, Prekajski M, Matović B, Gulicovski J, Bučevac D. Ceramic Int 2012;38:4875.
[93] Marković ZM, Babić BM, Dramićanin MD, Holclajtner Antunović ID, Pavlović VB, Peruško DB, Todorović Marković BM. Synthetic Metals 2012;162:743.
[94] Amaral-Labat G, Szczurek A, Fierro V, Stein N, Boulanger C, Pizzi A, CelzardA. Biomass Bioenergy 2012;39:274.
[95] Bansal RC, Donnet JB, Stoeckli F. Active Carbon.Marcel Dekker, New York; 1988.
[96] Smisek M, Cerny S. Active Carbon. Elsevier, Amsterdam; 1970.
[97] Gregg SJ, Sing KSW, Stoeckli HF (editors), Characterization of Porous Solids. Soc Chem Industry, London; 1979.
[98] Adamson AW, Gast AP. Physical Chemistry of Surface. Sixth ed., Wiley, New York; 1997.
[99] Cooney DO. Activated Charcoal in Medical Applications. Marcel Dekker, New York; 1995.

[100] Rodriguez-Reinoso F, McEnaney B, Rouquerol J, Unger K (editors), Studies in Surface Science and Catalysis. Vol. 144, Characterisation of Porous Solids VI. Elsevier Science, Amsterdam; 2002.

[101] Tennison SR. Appl Cat A Gen 1998;173:289.

[102] Tennison SR, Kozynchenko OP, Strelko VV, Blackburn AJ. Porous carbons. US Patent 2004024074A1 (publ. 05 Feb 2004).

[103] Rahman MH, Haqqie SS, McGoldrick MD. Internat Sympos Home Hemodial 2006;10:256.

[104] Mikhalovsky SV. In Arshady R (editor), Microspheres, Microcapsules and Liposomes. Vol. 2, Citus Books, London; 1999, p. 133.

[105] Savina IN, Gun'ko VM, Turov VV, Dainiak M, Galaev IYu, Phillips GJ, Mikhalovsky SV. Soft Matter 2011;7:4276.

[106] Gun'ko VM, Mikhalovska LI, Savina IN, Shevchenko RV, James SL, Tomlins PE, Mikhalovsky SV. Soft Matter 2010;6:5351.

[107] Sandeman SR, Gun'ko VM, Bakalinska OM, Howell CA, Zheng Y, Kartel MT, Phillips GJ, Mikhalovsky SV. J Colloid Interface Sci 2011;358:582.

[108] Zheng Y, Gun'ko VM, Howell CA, Sandeman SR, Phillips GJ, Kozynchenko OP, Tennison SR, Ivanov AE, Mikhalovsky SV. ACS Appl Mater Interface, submitted for publication.

[109] Sur S, Pashuck ET, Guler MO, Ito M, Stupp SI, Launey T. Biomaterials 2012;33:545.

[110] Luan T, Wu L, Zhang H, Wang Y. Carbohydrate Polymers 2011;87:2076.

[111] http://rsbweb.nih.gov/ij/download.html, accessed July 2007.

[112] Jurga M, Dainiak MB, Sarnowska A, Jablonska A, Tripathi A, Plieva FM, Savina IN, Strojek L, Jungvid H, Kumar A, Lukomska B, Domanska-Janik K, Forraz N, McGuckin CP. Biomaterials 2011;32:3423.

[113] Bereli N, Yavuz H, Denizli A, Şener G. Mater Sci Engin C 2011;31:1078.

[114] http://pacific.mpi-cbg.de/wiki/index.php/Main_Page.

[115] Rasband W. http://rsb.info.nih.gov/ij/plugins/voxel-counter.html, accessed July 2007.

[116] Prodanov D. http://rsb.info.nih.gov/ij/plugins/granulometry.html, accessed August 2007.

[117] Petrov P, Petrova E, Tsvetanov ChB. Polymer 2009;50:1118.

[118] Wu X, Liu Y, Li X, Wen P, Zhang Y, Long Y, Wang X, Guo Y, Xing F, Gao J. Acta Biomaterialia 2010;6:1167.

[119] Kanungo BP, Gibson LJ. Acta Biomaterialia 2010;6:344.

[120] Corin KA, Gibson LJ. Biomaterials 2010;31:4835.

[121] Murphy CM, Haugh MG, O'Brien FJ. Biomaterials 2010;31:461.

[122] Harley BA, Freyman TM, Wong MQ, Gibson LJ. Biophys J 2007;93:2911.

[123] Tierney CM, Haugh MG, Liedl J, Mulcahy F, Hayes B, O'Brien FJ. J Mechanic Behavior Biomed Mater 2009;2:202.

[124] Berry CC, Campbell G, Spadiccino A, Robertson M, Curtis AS. Biomaterials 2004;25:5781.

[125] Yannas IV. Tissue and Organ Regeneration in Adults, Springer-Verlag, New York; 2001.

[126] Yannas IV, Burke JF. J Biomed Mater Res 1980;14:65.

[127] Yannas IV, Burke JF, Gordon PL, Huang C, Rubenstein RH. J Biomed Mater Res 1980;14:107.

[128] Michaeli D, McPherson M. J Burn Care Rehabil 1990;11:21.

[129] Jones I, Currie L, Martin R. Br J Plast Surg 2002;55:185.

[130] Seal BL, Otero TC, Panitch A. Materials Sci Eng Res 2001;34:147.

[131] Neimark AV, Ravikovitch PI. Micropor Mesopor Mater 2001;44/45:697.

[132] Do DD, Nguyen C, Do HD. Colloids Surf A Physicochem Eng Aspects 2001;187–188:51.

[133] Gun'ko VM, Turov VV, Leboda R, Zarko VI, Skubiszewska-Zięba J, Charmas B. Langmuir 2007;23:3184.

[134] Gun'ko VM, Mikhalovsky SV. Carbon 2004;42:843.

[135] Gun'ko VM, Turov VV, Kozynchenko OP, Palijczuk D, Szmigielski R, Kerus SV, Gorbik PP. Appl Surf Sci 2008;254:3220.

[136] Gun'ko VM, Turov VV, Kozynchenko OP, Nikolaev VG, Tennison SR, Meikle ST, Snezhkova EA, Sidorenko AS, Ehrburger-Dolle F, Morfin I, Klymchuk DO, Mikhalovsky SV. Adsorption 2011;17:453.

[137] Gun'ko VM, Meikle ST, Kozynchenko OP, Tennison SR, Ehrburger-Dolle F, Morfin I, Mikhalovsky SV. J Phys Chem C 2011;115:10727.

[138] Gun'ko VM, Zaulychnyy YaV, Ilkiv BI, Zarko VI, Nychiporuk YuM, Ptushinskii YuG, Pakhlov EM, Leboda R, Skubiszewska-Zięba J. Appl Surf Sci 2011;258:1115.

[139] Gun'ko VM, Kozynchenko OP, Tennison SR, Leboda R, Skubiszewska-Zięba J, Mikhalovsky SV. Carbon 2012;50:3146.

[140] Gun'ko VM, Leboda R, Skubiszewska-Zięba J, Zarko VI, Goncharuk EV, Mikhalovsky SV. Surface 2012;3:123.

[141] Fenelonov VB. Porous Carbon. Nauka, Novosibirsk; 1995.

[142] Marsh H, Rodríguez-Reinoso F. Activated carbon. Elsevier, London; 2006.

[143] McGuire MJ,Suffet IH. Treatment of Water by Granular Activated Carbon. Advances in Chemistry Series. N 202, Oxford University Press, Oxford; 1983.

[144] Brennan JK, Bandosz TJ, Thomson KT, Gubbins KE. Colloids Surf A Physicochem Eng Aspects 2001;187–188:539.

[145] Liu J-C, Monson PA. Adsorption 2005;11:5.

[146] Palmer JC, Brennan JK, Hurley MM, Balboa A, Gubbins KE. Carbon 2009;47:2904.

[147] Nguyen TX, Cohaut N, Bae J-S, Bhatia SK. Langmuir 2008;24:7912.

[148] Pedretti A, Villa L, Vistoli G. J Computer-Aided Mol Design 2004;18:167.

[149] Stewart JJP. MOPAC 2012. Stewart Computational Chemistry. Colorado Springs, CO, USA, http://openmopac.net/, 2012.

[150] Tashima T, Imai M, Kuroda Y, Yagi S, Nakagawa T. J Org Chem 1991;56:694.

[151] Kim K-J, Lee S-B, Han N-W. Korean J Chem Eng 1994;11:41.

[152] Liu H, Nakagawa K, Chaudhary D, Asakuma Yu, Tadé MO. Chem Eng Res Design 2011;89:2356.

[153] Liu H, Nakagawa K, Kato D-i, Chaudhary D, Tadé MO. Mater Chem Phys 2011;129:488.

[154] Pujari PK, Sen D, Amarendra G, Abhaya S, Pandey AK, Dutta D, Mazumder S. Nuclear Instr Method Phys Res B 2007;254:278.

[155] Ehrburger-Dolle F, Morfin I, Bley F, Anuilar MR, Gallardo A, Perez P, Roman JS, Plieva F, Galaev IYu, Mattiasson B, Mikhalovsky S. In: Magalhaes-Paniago R. Synchrotron Radiation in Materials Science: 6th International Conferences, American Institute of Physics; 2009.

[156] Perez P, Plieva F, Gallardo A, Roman JS, Anuilar MR, Morfin I, Ehrburger-Dolle F, Bley F, Mikhalovsky S, Galaev IYu, Mattiasson B. Biomacromolecules 2008;9:66.

[157] Bai X, Ye Zh-f, Li Y-f, Zhou L-ch, Yang L-q. Process Biochem 2010;45:60.

[158] Goworek J, Stefaniak W, Zgrajka W. Mater Chem Phys 1999;59:149.

[159] Burova TV, Grinberg NV, Kalinina EV, Ivanov RV, Lozinsky VI, Alvarez-Lorenzo C, Grinberg VY. Macromol Chem Phys 2011;212:72.

[160] Aksnes DW, Forland K, Kimtys L. Phys Chem Chem Phys 2001;3:3203.

[161] Landry MR. Thermochim Acta 2005;433:27.

[162] Rohman G, Lauprêtre F, Boileau S, GuérinP, Grande D. Polymer 2007;48:7017.

[163] Weber J, Bergström L. Langmuir 2010;26:10158.

[164] Van Camp W, Dispinar T, Dervaux B, Du Prez FE, Martins JC, Fritzinger B. Macromol Rapid Comm 2009;30,1328.

[165] Shapiro YuE, Pykhteeva EG, Levashov AV. J Colloid Interface Sci 1998;206:168.

[166] Shapiro YuE. J. Colloid Interface Sci 1999;212:453.

[167] Kirsebom H, Rata G, Topgaard D, Mattiasson B, Galaev IYu. Polymer 2008;49:3855.

[168] Turov VV, Gun'ko VM. Clustered Water and Ways of Its Applications. Naukova Dumka, Kiev; 2011 (Russ).

[169] Gun'ko VM, Turov VV, Zarko VI, Goncharuk EV, Turova AA. Colloids Surf A Physicochem Eng Aspects 2009;336:147.
[170] Protein Data Bank, http://www.rcsb.org/pdb/.
[171] Arpa Ç, Bereli N, Özdil E, Bektaş S, Denizli A. J Appl Polymer Sci 2010;118:2208.
[172] Bajpai A, Saini R. Polym Int 2005;54:796.
[173] Lorenc-Grabowska E, Gryglewicz G. Dyes Pigment 2007;74:34.
[174] Purkait MK, Maiti A, DasGupta S, De S. J Hazard Mater 2007;145:287.
[175] Namasivayam C, Kavitha D. Dyes Pigment 2002;54,47.
[176] Ahmad R, Kumar R. Appl Surf Sci 2010;257:1628.
[177] Mall ID, Srivastava VCh, Agarwal NK, Mishra IM. Chemosphere 2005;61,492.
[178] Hameed BH, Din ATM, Ahmad AL. J Hazard Mater 2007;141:819.
[179] Yang J, Qiu K. Chem Eng J 2010;165:209.
[180] Hameed BH, Ahmad AL, Latiff KNA. Dyes Pigment 2007;75,143.
[181] Wang Sh, Zhu ZH, Coomes A, Haghseresht F, Lu GQ. J Colloid Interface Sci 2005;284:440.
[182] Yener J, Kopac T, Dogu G, Dogu T. Chem Eng J 2008;144:400.
[183] El Qada EN, Allen SJ, Walker GM. Chem Eng J 2006;124:103.
[184] Li Y, Li X, Li J, Yin J. Water Res 2006;40:1119.
[185] Wang Sh, Gong Q, Liang J. Ultrason Sonochem 2009;16:205.
[186] Chen S, Zhang J, Zhang Ch, Yue Q, Li Y, Li Ch. Desalination 2010;252:149.
[187] Kim S-I, Yamamoto T, Endo A, Ohmori T, Nakaiwa M. Micropor Mesopor Mater 2006;96:191.
[188] Hao G-P, Li W-C, Wang S, Zhang S, Lu A-H. Carbon 2010;48:3330.
[189] Marangoni R, Pereira Ramos L, Wypych F. J Colloid Interface Sci 2009;330,303.
[190] Papancea A, Valente AJM, Patachia S. J Appl Pol Sci 2010;115:1445.
[191] Provencher SW. Comp Phys Comm 1982;27:213.
[192] Frisch MJ, Trucks GW, Schlegel HB, Scuseria GE, Robb MA, Cheeseman JR, et al. Gaussian 03 Revision E.01; Gaussian, Inc. Wallingford, CT, 2003.
[193] FieldView 2.0.2; http://www.cresset-group.com/.
[194] Hunter RJ. Zeta Potential in Colloid Sciences. Academic Press; London; 1981.
[195] Gun'ko VM, Kozynchenko OP, Turov VV, Tennison SR, Zarko VI, Nychiporuk YM, Kulik TV, Palyanytsya BB, Osovskii VD, Ptushinskii YG, Turov VA. Colloids Surf A Physicochem Eng Aspects 2008;317:377.

[196] Derazshamshir A, Baydemir G, Andac M, Say R, Galaev IYu, Denizli A. Macromol Chem Phys 2010;211:657.

[197] Longeville S, Doster W, Kali G. Chem Phys 2003;292:413.

[198] Odabaşı M, Baydemir G, Karataş M, Derazshamshir A. J Appl Polymer Sci 2010;116:1306.

[199] Wang L, Shen Sh, Yun J, Yao K, Yao Sh-J. J Sep Sci 2008;31,689.

[200] Erzengin M, Unlu N, Odabaşi M. J Chromatography A 2011; 1218:484–490.

[201] Mikhalovsky SV, Mikhalovska LI, James SL, Tomlins PE, Grant PV, Vadgama P, Gun'ko VM. In Loureiro JM, Kartel MT (editors), Combined and Hybrid Adsorbents, Fundamentals and Applications. NATO Security through Science, Series C: Environmental Security. Springer, Dordrecht, 2006, p. 309.

[202] Islam MM, Sohya S, Noguchi K, Kidokoro S, Yohda M, Kuroda Y. Proteins 2009;77:962.

[203] Yang F, Bian C, Zhu L, Zhao G, Huang Z, Huang M. J Struct Biol 2007;157:348.

[204] Kollman JM, Pandi L, Sawaya MR, Riley M, Doolittle RF. Biochemistry 2009;48:3877.

[205] Gottschalk M, Venu K, Halle B. Biophys J 2003;84:3941.

[206] Young ME, Carroad PA, Bell RL. Biotechnol Bioengin 1980;22:947.

[207] Hoffman R, Benz EJ, Shattil SJ, Furie B, Cohen HJ, Silberstein LE, McGlave P (editors), Hematology: Basic Principles and Practice. Third edn., Churchill Livingstone, Philadelphia, USA; 2000.

[208] Schmitz KS, Lu M. Proc Natl Acad Sci USA Biophys 1983;80:425.

[209] Gun'ko VM, Klyueva AV, Levchuk YuN, Leboda R. Adv Colloid Interface Sci 2003;105:201.

[210] Peng ZG, Hidajat K, Uddin MS. J Colloid Interface Sci 2004;271:277.

[211] Gun'ko VM, Palijczuk D, Leboda R, Skubiszewska-Zięba J, Ziętek S. J Colloid Interface Sci 2006;294:53.

[212] Kanazawa KK, Gordon JII. Anal Chem 1985;57:1770.

[213] Lucklum R, Hauptmann P. Electrochim Acta 2000;45:3907.

[214] Lozinsky VI, Plieva FM. Enzyme Microbial Technol 1998;23:227.

[215] Lozinsky VI, Plieva FM, Galaev IYu, Mattiasson B. Bioseparation 2002;10:163.

[216] Petrenko YuA, Ivanov RV, Petrenko AYu, Lozinsky VI. J Mater Sci: Mater Med 2011;22:1529.

[217] Gun'ko VM, Mikhalovska LI, Tomlins PE, Mikhalovsky SV. Phys Chem Chem Phys 2011;13:4476.

[218] Lebedev AD, Levchuk YuN, Lomakin AV, Noskin VA. Laser Correlation Spectroscopy in Biology. Naukova Dumka, Kiev; 1987 (Russ).

[219] Wu TY, Brokaw C, Brenan C (editors), Symposium on Swimming and Flying in Nature. Plenum Press, New York; 1975.

[220] Stock G. Biophys J 1978;22:79.

[221] Stock G, Krasner G, Holder N, Bryant S. J Exp Zool 1980;214:123.

[222] Wakeham WA., Nagashima A, Sengers JV (editors), Experimental Thermodynamics. Vol. 3, Blackwell Scientific, Oxford; 1991.

[223] Levchuk YuN, Mostovaya AV, Skripets EYu. Dopov NAN Ukr 1995;7:138.

[224] Levchuk YuN, Karachentseva AI, Andreev EI. Electron Obrabot Metal (Russ) 1990;154:53.

[225] Karachentseva AI, Levchuk YuN. Biopolym Cell (Russ) 1989;5:76.

[226] Gun'ko VM, Zarko VI, Voronin EF, Turov VV, Mironyuk IF, Gerashchenko II, Goncharuk EV, Pakhlov EM, Guzenko NV, Leboda R, Skubiszewska-Zięba J, Janusz W, Chibowski S, Levchuk YuN, Klyueva AV. Langmuir 2002;18:581.

[227] Barbetta A, Cametti C, Rizzitelli G, Dentini M. Soft Matter 2012;8:1120.

[228] Pons A, Casas Ll, Estop E, Molins E, Harris KDM, Xu M. J Non-Crystal Solid 2012;358:461.

[229] Marković ZM, Babić BM, Dramićanin MD, Holclajtner Antunović ID, Pavlović VB, Peruško DB, Todorović Marković BM. Synthetic Metals 2012;162:743.

[230] Amaral-Labat G, Szczurek A, Fierro V, Stein N, Boulanger C, Pizzi A, Celzard A. Biomass Bioenergy 2012;39:274.

[231] Kraiwattanawong K, Sano N, Tamon H. Micropor Mesopor Mater 2012;153:47.

[232] Ng KW, Torzilli PA, Warren RF, Maher SA. J Tissue Eng Regen Med 2012; doi:10.1002/term.1510.

[233] Aydoğan C, Andaç M, Bayram E, Say R, Denizli A. Biotechnol Progress 2012;28:459.

[234] Önnby L, Pakade V, Mattiasson B, Kirsebom H. Water Research 2012;46:4111.

[235] Tüzmen N, Kalburcu T, Denizli A. Process Biochemistry 2012;47:26.

[236] Sowasod N, Nakagawa K, Tanthapanichakoon W, Charinpanitkul T. Mater Sci Engin C 2012;32:790.

[237] Bereli N, Türkmen D, Köse K, Denizli A. Mater Sci Engin C 2012;32:2052.

[238] Gunasena DN, El Rassi Z. Electrophoresis 2012;33:251.

[239] Dispinar T, Van Camp W, De Cock LJ, De Geest BG, Du Prez FE. Macromol Biosci 2012;12:383.

[240] Petrov P, Jeleva D, Tsvetanov CB. Polym Int 2012;61:235.

[241] Millon LE, Padavan DT, Hamilton AM, Boughner DR, Wan W. J Biomed Mater Res Part B 2012;100B:1.

[242] Say R, Biçen Ö, Yılmaz F, Hür D, Öziç R, Denizli A, Ersöz A. J Appl Polymer Sci 2012;125:145.

[243] Ergün B, Baydemir G, Andaç M, Yavuz H, Denizli A. J Appl Polymer Sci 2012;125:254.

[244] Berillo D, Elowsson L, Kirsebom H. Macromol Biosci 2012;12:1090.

[245] Sun S, Tang Y, Fu Q, Liu X, Du W, Guo L, Zhao Y. J Sep Sci 2012;35:893.

[246] Andac M, Galaev I, Denizli A. J Sep Sci 2012;35:1173.

[247] Yun J, Tu C, Lin D-Q, Xu L, Guo Y, Shen S, Zhang S, Yao K, Guan Y-X, Yao S-J. J Chromatography A 2012;1247:81.

[248] Berillo D, Mattiasson B, Galaev IYu, Kirsebom H. J. Colloid Interface Sci 2012;368:226.

[249] Dragan ES, Apopei DF. Carbohydrate Polymers (2012), doi:10.1016/j.carbpol.2012.08.082.

[250] Dragan ES, Lazar MM, Dinu MV, Doroftei F. Chem Eng J 2012;204–206:198.

[251] Gun'ko VM, Turov VV, Whitby RLD, Prykhod'ko GP, Turov AV, Mikhalovsky SV. Carbon, submitted for publication.

[252] Whitby RLD, Korobeinyk A, Gun'ko VM, Busquets R, Cundy AB, Laszlo K, Skubiszewska-Zięba J, Leboda R, Tombacz E, Toth I, Kovacs K, Mikhalovsky SV. Chem Comm 2011;47:9645.

Figure Legends

Fig. 1. Cryogel preparation stages: (i) a solution of monomers or polymers with a cross-linker, (ii) frozen, (iii) stored at subzero temperature, and (iv) thawed to form (v) macroporous cryogel in native hydration state (then it can be freeze-dried).

Fig. 2. (a) CLSM images of fluorescein isothiocyanate (FITC) labelled scaffolds. Left to right: non-porous scaffold prepared without vacuum, porous scaffolds prepared under 6.5 mbar and under 0.1 mbar freeze-drying pressure. (Top) A typical single optical slice from a data set taken at a depth of 35 μm. Scale bar 200 μm. (Bottom) 3-D reconstructions generated from the same data set with Amira® software. Final size of the reconstructed image was 1 mm ×1mm ×92 μm (adapted from [76] with permission, Copyright 2010, Elsevier); and (b) PSD for weakly (pressure 6.5 mbar) and strongly (0.1 mbar) porous gels calculated here using ImageJ with granulometry plugin.

Fig. 3. Pore size distributions and SEM images of poly(hydroxyethyl methacrylate) cryogels (scale bar 50 μm) (re-designed from [80] with permission, Copyright 2011, Elsevier).

Fig. 4. PHEMA-AGE cryogel (sample A) morphology by (a) MPM (450×450 μm, scale bar 100 μm), (b) CLSM (750×750 μm, scale bar 250 μm), (c) SEM, and (d) cryo-SEM (scale bar 100 μm) (adapted from [105] with permission,Copyright2011, Royal Society of Chemistry).

Fig. 5. Effect of threshold selection (ImageJ) on porosity assessment for PHEMA-AGE cryogel (sample A) [105] (with permission, Copyright 2011, Royal Society of Chemistry); the hydrogel was scanned at 2.5 μm voxel resolution using a Photonic Science® XDI-VHR 16-bit CCD camera; sample area of 1224/1224/885 μm was analysed using VGStudioMax (www.volumegraphics.com/en/products/vgstudio-max.html) and Morpho+ (www.ugct.ugent.be/software.php) software.

Fig. 6. CLSM images of samples A, B, C and D (Table 2) [105] (with permission, Copyright 2011, Royal Society of Chemistry).

Fig. 7. CLSM image of gelatine sheet cross-sections and pore structure of cryogel for the top, middle and bottom layers [105] (with permission, Copyright 2011, Royal Society of Chemistry).

Fig. 8. CLSM images of PHEMA-AGE cryogel (sample A, Table 2) in (a) hydrated and (b) dried states with the pore (c) size and (d) wall thickness distributions [105] (with permission, Copyright 2011, Royal Society of Chemistry).

Fig. 9. Wall thickness distributions with (a) Fiji and (b) ImageJ, and (c) pore size distributions for PHEMA-AGE cryogels A, B, C and D (Tables 2 and 3) [105] (with permission, Copyright 2011, Royal Society of Chemistry).

Fig. 10. Pore size and wall thickness distribution of Gl–Fg–GA(0.1) (a) cryogels obtained by analysis of CLSM images by ImageJ software and (b) dependence of swelling on the cross-linking degree (adapted from [35] with permission, Copyright 2009, Elsevier).

Fig. 11. Temperature dependence of the swelling properties of HPC and PNIPAAm cryogels synthesised via UV irradiation (adapted from [117] with permission, Copyright 2009, Elsevier).

Fig. 12. SEM images of freeze-dried (a) PVA gel and (b) PVA/AC composite [107] (with permission, Copyright 2011, Elsevier).

Fig. 13. Pore size distributions of (a) activated carbons and (b, c, d) PVA, PVA/C-7 and C-7 samples based on (a, c, d) nitrogen adsorption/desorption isotherms and (b) mercury porosimetry. There are (a, c) incremental DFT PSDs (models of (a) slit-shaped and (c) cylindrical pores), (d) differential NLDFT PSDs (equilibrium model with cylindrical/slit-shaped pores) [107] (with permission, Copyright 2011, Elsevier).

Fig. 14.PSD of AC (C-7) from the nitrogen adsorption and mercury porosimetry [107] (with permission, Copyright 2011, Elsevier).

Fig. 15. Incremental PSD with the model of a mixture of (*) slit-shaped (carbon nanoporous nanoparticles) and cylindrical (carbon or polymer) pores and voids between spherical particles (carbon) (MND) and (**) slit-shaped and cylindrical pores for carbons (NLDFT) for PVA/GA and (a) carbon 1 and PVA/GA/carbon 1; (b) carbon 2 and PVA/GA/carbon 2 [108].

Fig. 16. SEM image of inner texture of AC composed of nanoporous nanoparticles (scale bar 20 nm) [108].

Fig. 17. Differential PSD based on the mercury porosimetry data for two PVA samples, and (a) carbon 1 and PVA/GA/carbon 1; (b) carbon 2 and PVA/GA/carbon 2; inserts show a portion of PSDs at large pore diameter [108].

Fig. 18. PSD based on the mercury porosimetry and SEM image analysis with Fiji software [114] for PVA/GA and PVA/GA/AC (AC has S_{BET} = 957 m^2/g, V_p = 1.33 cm^3/g) [108].

Fig. 19. SEM images of (a) freeze-dried PVA/GA cryogel and (b) PVA/GA/C-1 [108].

Fig. 20. Scanning electron micrographs of AC particles attached to freeze-dried PVA/GA gel surface for (a) carbon-1, (b) carbon-2 [108].

Fig. 21. Influence of the concentration of AC in PVA/GA/AC composite on the NLDFT PSD; *sample was heated at 80^{o}C, other samples were heated at 100^{o}C for 24 h prior to measurements; **C_{GA}/C_{AC} (AC with S_{BET} = 1109 m^2/g) was decreased by six times that gives S_{BET} = 499 m^2/g [108].

Fig. 22. Interaction of GA cross-linked PVA (~2000 atoms) with AC (~1700 atoms) in the presence of water (~1100 molecules) (the geometry was optimised by PM6/MOZYME), pictures show two sides of the same system [108].

Fig. 23. SAXS profiles for contact freezing samples: (a) 1D profiles exacted from *z*-axis direction [152] (with permission, Copyright 2011, Elsevier); (b) differential (curves 1 and 2) and incremental PSD (3, 4) calculated here for MF1 (curves 1 and 3) and MF2 (2, 4).

Fig. 24.SEM images of (a) w-MBAAm/pNIPA and (b) d-MBAAm/pNIPA cryogels synthesised in (a) water and (b) dioxane/water media (scale bar 100 μm, image size ~1 mm × 1 mm) [156] (with permission, Copyright 2008, American Chemical Society).

Fig. 25. Pore size distributions of (a) w-MBAAm/pNIPA and (b) d-MBAAm/pNIPA cryogels synthesised in (a) water and (b) dioxane/water media calculated using SEM images treated with Fiji software.

Fig. 26. PSD calculated here using the SAXS data [156] (with permission, Copyright 2008, American Chemical Society) for w-MBAAm/pNIPA and d-MBAAm/pNIPA cryogels with Eq. (11).

Fig. 27.Weight loss (1, 2) and differential TG curves (3, 4) for CPVA (1, 3) and TPVA (2, 4).

Fig. 28. (a) TG and differential TG curves of water desorption from collagen hydrogel being in (1, 2) PBS or (3, 4) water (heating rate 2^{o}C/min) [106] (with permission, Copyright2010, Royal Society of Chemistry); and (b) PSD calculated using the TG thermoporometry.

Fig. 29.DSC thermograms for representative samples (a) differently hydrated sample A at h = 6.6 to 0.03 g/g, (b) dry sample C (h = 0.11 g/g), and (c) hydrated sample G (h = 12.3 g/g), and (d-f) differential PSDs calculated from the DSC data for PHEMA-AGE (A, B, C, and D samples) and gelatine (G) gels (hydration $h = m_w/m_d$ where m_w is the weight of water evaporated on DSC measurements to 160^{o}C and m_d is the residual weight of heated sample) at (d) high and (e, f) low hydration [105] (with permission, Copyright 2011, Royal Society of Chemistry).

Fig. 30.DSC thermograms of differently hydrated PHEMA-PEGA (7.5 wt.%) with Laponite clay (1.5 wt.%) and without or with Fe_3O_4 (9 wt.%): (a) very strongly (hydration h = 12.2 and 3.6 g H_2O per gram of cryogel), (b) strongly (h = 0.94 and 0.76 g/g) and (c) weakly (h = 0.072 and 0.05 g/g) cryogels; (d) differential size distributions of narrow pores in the walls of macropores for very strongly and weakly hydrated samples.

Fig. 31.^{1}H NMR spectra, recorded at different temperatures, of water adsorbed by gelatine cryogel: (a) initial freeze-dried (0.3 wt.% H_2O) in $CDCl_3$; and in a mixture $CDCCl_3$: CD_3CN 3:1 at (b) 0.8 wt.% and (c) 10 wt.% of water [105] (with permission, Copyright 2011, Royal Society of Chemistry).

Fig. 32.^{1}H NMR spectra, recorded at different temperatures, of water bound in gelatine cryogel at hydration h = 1 g per gram of dried gel in different media: (a) air, (b) C_6D_6, (c) C_6D_6 : CD_3CN = 6:1 and (d) $CDCl_3$: CD_3CN = 3:1 [105] (with permission, Copyright 2011, Royal Society of Chemistry).

Fig. 33. (a) Amounts of unfrozen water (C_{uw}) as a function of temperature; (b) derivative $dC_{uw}/d(\Delta G)$, and (c) pore size distribution (NMR-cryoporometry) for gelatine cryogel in different media [105] (with permission, Copyright 2011, Royal Society of Chemistry).

Fig. 34. Pore size distribution calculated using the ^{1}H NMR-cryoporometry and CLSM methods for hydrated collagen gel INTEGRA^{TM} [106] (with permission, Copyright 2010, Royal Society of Chemistry).

Fig. 35.(a) Temperature dependence of the TSDC for the initial collagen hydrogel and 'free' (bulk) water; (b) distribution function of the activation energy of relaxation in these systems, (c) IPSD collagen hydrogel (died-wetted INTEGRA^{TM}) according to NMR and TSDC relaxometry [52] (with permission, Copyright 2006, Elsevier).

Fig. 36.Models of partially hydrated gels with (a) cross-linked PHEMA-AGE (2373 atoms) with 1192H_2O; (b) collagen (two triple coils (1639 atoms) and 1032H_2O); and (c) fibronectin (8-9FnI) – collagen (3200 atoms) with 827H_2O (PM6 geometry) [105] (with permission, Copyright 2011, Royal Society of Chemistry).

Fig. 37.Molecular models of (a, b) MB, (c, d) MO, and (e, f) CR in slit-shaped pores at minimum possible width of 0.7, 0.8 and 1.0 nm, respectively; (b, d, f) accessibility of dyes molecules for solvent molecules in narrow nanopores; and different types of fields around the molecular ions of (g) MB, (h) MO, and (i) CR calculated [107] (with permission, Copyright 2011, Elsevier)using the FieldView program [193].

Fig. 38.Adsorption isotherms of dyes (a, c, e) per gram and (b, d, f) m^2 of adsorbents for (a, b) CR, (c, d) MO, and (e, f) MB [107] (with permission, Copyright 2011, Elsevier).

Fig. 39. Removal of dyes (%) by ACs: (a) C-1, (b) C-2, (c) C-3, (d) C-4, (e) C-5, (f) C-6, and (g) C-7, PVA, and PVA/C-7 [107] (with permission, Copyright 2011, Elsevier).

Fig. 40. Distribution functions of Gibbs free energy of adsorption of dyes CR, MO, and MB onto ACs: (a) C-1, (b) C-2, (c) C-3, (d) C-4, (e) C-5, (f) C-6, and (g) C-7 and (h) PVA, PVA/C-7 [107] (with permission, Copyright 2011, Elsevier).

Fig. 41. Relationships between the first moment of the $f(\Delta G)$ distributions $<\Delta G>$ for the dye adsorption onto carbons C1-C7 and (a) S_{nn}, (b) D_{FHH} and (c) Δw values [107] (with permission, Copyright 2011, Elsevier).

Fig. 42. Model of interaction of MB, MO and CR ions with hydrated ($1084H_2O$) PVA coverage blocking narrow pores of AC particle (CharMM force field and PM6/MOZYME calculations) (energy of complex formation ΔE_t = –653 kJ/mol due to interaction mainly with water and PVA) [107] (with permission, Copyright 2011, Elsevier).

Fig. 43. Experimental data for Hb absorption onto Hb-PHEMAH cryogel fitted to standard Langmuir isotherm [196] and integral Langmuir equation (24) (experimental conditions: running buffer: 0.1 M phosphate buffer, pH.6.0, $T = 20^oC$, flow rate: 1.0mL/min, $m_{\text{dry cryogel}}$: 0.45 g [196]) calculated here.

Fig. 44. (a) Equilibrium adsorption of myoglobin (16.7 kDa) onto AC (particles of 40–80 μm in diameter, burn-off 55%, S_{BET} = 1939 m^2/g, V_p = 1.82 cm^3/g, bulk density = 0.16 g/cm^3) [108]; (b) distribution function of the Gibbs free energy of myoglobin adsorption.

Fig. 45.(a) Kinetics of myoglobin adsorption (shown as residual percentage) to AC and PVA/GA/AC (AC (6 mg) embedded into PVA/GA cryogel (1.2 mL)).Myoglobin solution (25 mL) is pumped through the gel within a closed circle. AC particles (6 mg) as a suspension in 0.1 mg/mL myoglobin solution (25 mL) [108]; (b) the distribution function of the Mb diffusion coefficient (assuming that the diffusion is limiting stage of adsorption).

Fig. 46. Adsorption kinetics of myoglobin to PVA cryogel (1.2 mL) with 6 and 56 mg of AC [108].

Fig. 47. SEM image of AC/PVA composites (from the middle of cryogels, transferred into aqueous ethyl alcohol of increasing concentrations, for drying, dried on air and under vacuum) [108].

Fig. 48.Flow rate through the PVA/GA cryogels (1, 2) and PVA/GA/AC with embedded carbon particles (0.8 × 2.5 cm, 1.2 mL) as a function of pressure at 15 (3) or 56 (4) mg of AC in cryogel [108].

Fig. 49.Effect of DNA concentration on adsorption. MAH content: 45.8 μmol/g; Zn^{2+} loading: 49.2 μmol/g; pH 7 (Tris buffer); flow rate 1 mL/min; $T = 25^oC$ (adapted from [198]).

Fig. 50.Molecular structures of (a) hydrated BPTI dimer [202], (b) HSA [203] (having a shape close to BSA) and (c) Fg [204] (H atoms are not shown here).

Fig. 51.Diffusion kinetics through a collagen hydrogel membrane (~1 mm in thickness) for (a) BPTI.Curve 1 is for an initial concentration of 1.23 mg/ml in the feeder cell (OD_{280} = 0.09), curves 2-4 are for an initial concentration of 2.46 mg/ml (OD_{280} =0.18); curve 2 - BPTI run after the first BPTI run; curve 3 – BPTI run after Fg; curve 4 - BPTI run after Fg and BSA; (c) BSA and BSA (with twice concentration) after the first BSA run, (e) Fg (initial concentration 1.7 mg/ml); curves (b), (d) and (f) show the corresponding distribution functions of the diffusion coefficient $f(D)$ for (b) BPTI, (d) BSA, and (f) Fg [106] (with permission, Copyright 2010, Royal Society of Chemistry).

Fig. 52. Breakthrough curve of BSA in cryogel with embedded Fe_3O_4 nanoparticles at various liquid superficial velocity U_L = 4.0 cm/min (sizes of bed were 26 mm in diameter and 88 mm in length) (adapted from [79], with permission, Copyright 2007, Elsevier).

Fig. 53.(a) Comparison of the predicted (lines) and experimental (symbols) breakthrough curves of BSA through PHEMA cryogel under non-adsorption condition at various liquid velocities: 8.25×10^{-5} (1), 1.65×10^{-4} (2), 2.48×10^{-4} (3) and 8.41×10^{-4} (4) m/s. The solid lines represent the calculation results by the model described in detail in [80]; (b) corresponding distribution functions of the Gibbs free energy of BSA interaction with PHEMA calculated here.

Fig. 54. Fibroblast cells (size ~10-20 μm) distribution in the collagen-GAG gel: (a) 3T3 mouse fibroblasts, ×400; (b) distribution of normal primary human skin fibroblasts (green nuclei) within collagen hydrogel scaffold (blue) after 28 days of *in vitro* incubation, the lower surface being the seeded surface (CG hydrogel cross-section, ×100) [106](with permission, Copyright 2010, Royal Society of Chemistry).

Fig. 55.Distribution function of cells. Graph shows the number of migrating human fibroblasts in 100 μm increments in a cross-section of a collagen hydrogel, as assessed with CLSM, after 28 days of *in vitro* incubation [106] (with permission, Copyright 2010, Royal Society of Chemistry).

Fig. 56. (a) Changes in frequency (1) and auto-gain controller voltage (2) on two injections (A and B) of 0.1 ml aliquot of 3T3 fibroblast suspension (2.0×10^6 cell ml^{-1}) upon an unsupported section of collagen hydrogel laid the surface of a 10 MHz gold coated crystal. Flow injection rate 0.01 ml min^{-1}, 37±0.1ºC, pH 7.2, PBS (adapted from [106] with permission, Copyright 2010, Royal Society of Chemistry); (b) the distribution functions of changes in the Gibbs free energy of interactions of cells with the collagen hydrogel calculated with Eq. (31).

Fig. 57.Distribution function of the diffusion coefficient of individual *PM*187 $10^6/cm^3$ in the physiological buffer. Two peaks correspond to inactivated (*i.e.* participating only in Brownian motion) and (2) living mobile (own + Brownian motion) microorganisms (adapted from [209] with permission, Copyright 2003, Elsevier).

Table 1

Classification of water types based on low-temperature ^{1}H NMR data.

Water type	Abbreviation	Boundary value of changes in the Gibbs free energy, ΔG (kJ/mol)	Chemical shift of the proton resonance, δ_H (ppm)	Note
Unbound water	UBW	0	4-5 (7 for ice)	Free bulk water (SAW)
Weakly associated water	WAW	< 0	1-2	It can be both SBW and WBW
Strongly associated water	SAW	< 0	4-6	SBW or WBW (typically WBW contribution is predominant)
Strongly bound water	SBW	<–0.5 - –0.8	1-2 (WAW) 4-6 (SAW)	Closer located to a surface or macromolecules
Weakly bound water	WBW	>–0.5 - –0.8	1-2 (WAW) 4-6 (SAW)	Distant from a surface or macromolecules
Water associated with co-solvents	ASW		2.0-3.5	Water dissolved in co-adsorbates such as DMSO or acetonitrile

Table 2
Textural characteristics of the porous structure of PHEMA-AGE gel samples A, B, C and D (see Table 3).

Sample	A*	A**	B*	C*	D*
Porosity, %	91	88	91	82	68
Surface area(S/V_A), $\mu m^2/\mu m^3$	0.045	0.10	0.06	0.095	0.186
Wall thickness (t), μm	9.6±0.8	10.9±1.6	5.7±0.5	8±1	9.5±1.3
Pore diameter(d), μm	64±2	56±1.5	47±2.8	41.4±6	25.7±1

Note. *CLSM and **MPM image analysis with ImageJ software [105].

Table 3
Threshold selection effect in ImageJ on quantification results (HEMA-AGE gel, sample A).

Gray-scale range, threshold	0-4	0-9	0-20
Porosity, %	83	90.4	94.6
Mean pore size, *d*, μm	55.8±8.2	64.0±2.0	69.6±5.6
Mean wall thickness, *t*, μm	13.3±2.1	11.2±0.83	8.9±2.3

Table 4
Textural characteristics of activated carbons (DFT with the model of slit-like pores for ACs and cylindrical pores for PVA and PVA/C-7) [107].

Sample (burn-off degree, %)	S_{BET} m^2/g	S_{nn} m^2/g	S_{mn} m^2/g	S_{bm} m^2/g	V_p cm^3/g	V_{nn} cm^3/g	V_{mn} cm^3/g	V_{bn} cm^3/g	Δw	D_{FHH}
C-1 (0)	549	496	45	7	0.831	0.265	0.219	0.346	0.035	2.8895
C-2 (32)	1236	1146	76	14	1.612	0.598	0.329	0.684	0.093	2.8921
C-3 (40)	1520	1395	118	7	1.260	0.588	0.389	0.283	0.360	2.8739
C-4 (43)	1484	1364	97	23	2.110	0.715	0.468	0.927	0.095	2.8867
C-5 (49)	1251	1209	40	2	0.687	0.527	0.061	0.099	0.288	2.9174
C-6 (49)	1549	1141	93	16	1.799	0.747	0.405	0.647	0.112	2.8886
C-7 (52)	740	639	97	5	0.991	0.356	0.483	0.152	0.017	2.8408
PVA1	61	2	59	0	0.109	0.001	0.105	0.003	0.142	2.5265
PVA2	56	1	55	0	0.100	0.0	0.100	0.0	0.153	2.4887
PVA3	55	4	51	1	0.141	0.002	0.119	0.020	0.199	2.5725
PVA5/C-7	66	10	55	1	0.164	0.006	0.114	0.044	0.284	2.3916
PVA7/C-7	65	35	28	2	0.149	0.018	0.048	0.083	0.220	2.1721

Table 5

Pore volume (V_{Hg}) and surface area (S_{Hg}) from the mercury porosimetry [107].

Parameter	C-7	PVA1	PVA2	PVA3	PVA5/C7	PVA7/C7
V_{Hg} (cm^3/g)	2.99	4.14	5.73	3.78	5.28	4.54
S_{Hg} (m^2/g)	44.6	1.7	4.6	142.8	36.1	23.4

Table 6
Structural characteristics of carbons, PVA/GA and PVA/GA (83.3%)/AC samples with SCV/SCR model (MND)* and of SC model (NLDFT) [108].

Sample	S_{BET} m^2/g	S_{nn}* (m^2/g)	S_{mn}* (m^2/g)	S_{bn}* (m^2/g)	V_p (cm^3/g)	V_{nn}* (cm^3/g)	V_{mn}* (cm^3/g)	V_{bn}* (cm^3/g)	S_{NLDFT} (m^2/g)	Δw_{NLDFT}	c_{slit}*	c_{cyl}*	c_{void}*
Carbon-1	724	448	266	11	0.955	0.147	0.578	0.230	675	0.073	0.648	0.255	0.097
Carbon-2	842	511	305	27	1.020	0.102	0.328	0.590	786	0.072	0.680	0.252	0.068
PVA	78	1	76	2	0.212	0.0	0.162	0.050	84	-0.063	0.684	0.124	0.192
PVA/C-1	69	0	64	5	0.210	0.0	0.107	0.103	70	-0.017	0.112	0.715	0.173
PVA/C-2	62	0	57	4	0.191	0.0	0.096	0.095	62	-0.006	0.387	0.440	0.174
PVA/C-3	499	264	233	2	0.634	0.076	0.497	0.061	467	0.042	0.328	0.575	0.097

Note. Contribution of narrow nanopores (S_{nn}, V_{nn}) at radius (half-width for slit-shaped pores) $R < 1$ nm, middle nanopores (S_{mn}, V_{mn}) at $1 < R < 25$ nm, and broad nanopores (S_{bn}, V_{bn}) at $25 < R < 100$ nm; Δw is the relative deviation of the pore shape from the SC model; c_{slit}, c_{cyl} and c_{void} are the weight coefficients of slit and cylindrical pores and voids between spherical particles, respectively, calculated using the MND method with the SCV/SCR model.

Table 7
Structural characteristics of gelatine gel calculated using NMR cryoporometry [105].

h, g/g	Medium	S (m^2/g)	S_{nn} (m^2/g)	S_{mn} (m^2/g)	S_{bn} (m^2/g)	V_{nn} (cm^3/g)	V_{mn} (cm^3/g)	V_{bn} (cm^3/g)	γ_S (J/g)
1	Air	465	423	43	0	0.157	0.431	0	34.4
1	C_6D_6	133	94	38	1	0.045	0.520	0.014	28.3
1	$C_6D_6 + CD_3CN$	176	88	87	1	0.042	0.928	0.010	37.6
1	$CDCl_3 + CD_3CN$	84	10	74	1	0.005	0.732	0.009	35.9
0.1	$CDCl_3 + CD_3CN$	8	0	8	0	0	0.031	0	1.3

***Response to Reviewers**

Reviewers' comments:

Reviewer #1: The manuscript entitled "Cryogels: morphological, structural and adsorption characterisation" by Gun'ko et al. discussed the textural, structural and adsorption characterisation of the cryogels and composite cryogels. The authors compare each of these polymeric materials and give valuable information on the production and the characterisation of these materials in detailed. They also give attractive examples for their application areas. This manuscript is original and well organized. In my opinion it can be published in Advances in Colloid and Interface Science. However, the authors should check the typing errors of references such as REF. 106, 185, 285.

Authors: The text and reference were corrected.

Reviewer #2: Review of Manuscript CIS-D-12-00042:

This long review describes the combination of different experimental methods and data treatment for the characterization of the porous structure of various organic cryogels over a maximum broad range size; the absorption behaviour (in peculiar small molecules and protein), protein diffusion and cell distribution of these cryogels are also discussed.
One of the original aims of this paper deals with the structural characterization of the macropore walls in cryogels, which contain nanopores, and it must be emphasized that there are only few papers with deep insight into the texture of cryogels over the whole (0.4 nm-300?m) pore size range; as a matter of fact the inner structure of macropore walls is little described in literature. Moreover, the adequate characterization of such materials in their native state is only accessible by specific techniques that are detailed in this review.

The cryogelation process is well described and detailed examples of different cryogels are listed including tissue scaffold engineering, separation matrices and bioreactors.
So this review is original and it is worth publishing. Nevertheless, several points must be clarified before publication in Advances in Colloid and Interface Science:

Part 1
Page 4, last paragraph: the structural analysis via different methods is described twice, it must be shortened.

Authors: The text was corrected.

Part 2
Page 11, last paragraph: the definition and description of the different states of water is a little unclear since different abbreviations correspond to similar definitions. A table including these different abbreviations would be useful to help the understanding.

Authors: The text was corrected and new Table was added.

Page 12, line 12 and line 31: information given by NMR experiments should be merged.

Authors: The text was corrected.

Part 3
Page 15, line 4: since there are 28 types of collagen please add the type used in this experiment. In my sense it should be acido-soluble collagen from type I since native type I collagen is cross-linked and no molecular weight can be associated.

Authors: The text was corrected. Additional information was added.

Page 16, last paragraph: too many experimental details are given concerning the preparation of AC filled cryogels in contrast with another cryogels; please summarize.

Authors: The text was corrected.

Part 4

In this part, the section 4.1. devoted to the structural and adsorption characterisation of cryogels is a very long chapter (very important when compared with the other sections. The description of micrographic images and the computation of structural parameters are detailed for lots of distinct cryogels, but in some cases too many details are given, disturbing a clear reading.
For example, the influence of AC content in narrow nanopores must be summarized.

Authors: The text was corrected. New results were added.

Section 4.2
Page 43: More explanation on incremental and differential PSD should be given, with a description of the Figure 23.

Authors: The text was corrected. Additional information was added.

Page 44, 45: Figures 24 and 25 should be got together for a better comparison. Curves 1 and 2 in Figure are not distinguishable.

Authors: Figures were corrected.

Section 4.3
Page 47, you assume that "a small amount of bound water desorbed at T>100°C"; it is not visible on the curves of Figure 28 a.
Since it is mentioned for other techniques, just a slight explanation would be necessary on the calculation of PSD from TG curves (even if the reference is given).
In this part on thermogravimetric measurements, use the term NBW instead of non-bound water to be homogenous with the rest of the text.

Authors: The text was corrected. Additional information was added.

Section 4.4. Since DSC is a part of thermal analysis as well as thermogravimetric experiments, these two sections could be merged. Moreover, DSC is mentioned in part 4.3.

Authors: The text was corrected.

Page 49, line 7: dV/dR corresponds to the differential pore size distribution (page 30), so the same definition must be used here.

Authors: The text was corrected. Additional information was added.

Page 49: it would be appreciable to show the DSC thermogram with the melting endotherm before presenting figure 29.
Which are the values of Tm and Tm0 in your example Page 50, line 23: where are presented data that allow maintaining that bound water structures are up to 10 nm?

Authors: The text was corrected. Additional information was added.

Figure 30d: is it PSD or differential PSD?

Authors: The text was corrected. Additional information was added.

Part 4.5
What is the relationship between eq (16) and (19)?
It would be appreciable to assign the different maxima of f(E) from TSDC experiments to the different kinds of water WBW, SBW, WAW directly on the figure

as it was performed in figure 31. I do not understand the terms WBW, SBW and WAW in the case of pure water.

Authors: The text was corrected. Additional information was added.

The last part of part 4.5. deals with prediction of structures; it must be added in the title of part 4.5.

Part 4.6
The presence of two peaks in the function of distribution of figure 44b must be explained.
Page 75, line 19: The type of collagen should be clarified.

Authors: The text was corrected. Additional information was added.

General remarks
An effort must be done to carefully check the ms. to remove grammatical mistakes. In a general way, some sentences are longer and must be cut into shorter sentences.

Minor points
Page 1, line 23: Replace by "TSDC"
Page 4, line 25: remove "can be"
Page 4, line 31: Replace "some other methods" by the name of these methods
Page 5, line 12: give the meaning of T0
Page 6, line 10: replace "destroy" by "destruction"
Page 8, line 16: "the most of the" should be replaced by "most of the"
Page 18, line 1: "amphiphile peptide"
Page 31, line 16: replace "was" by "were"
Page 31, line 21: replace "was" by "were"
Figures 39, 40: y-axis and x-axis titles are missing.
Page 73, line 2: remove "(Fig.47)".

Authors: The text was corrected.

Figure 1

Click here to download high resolution image

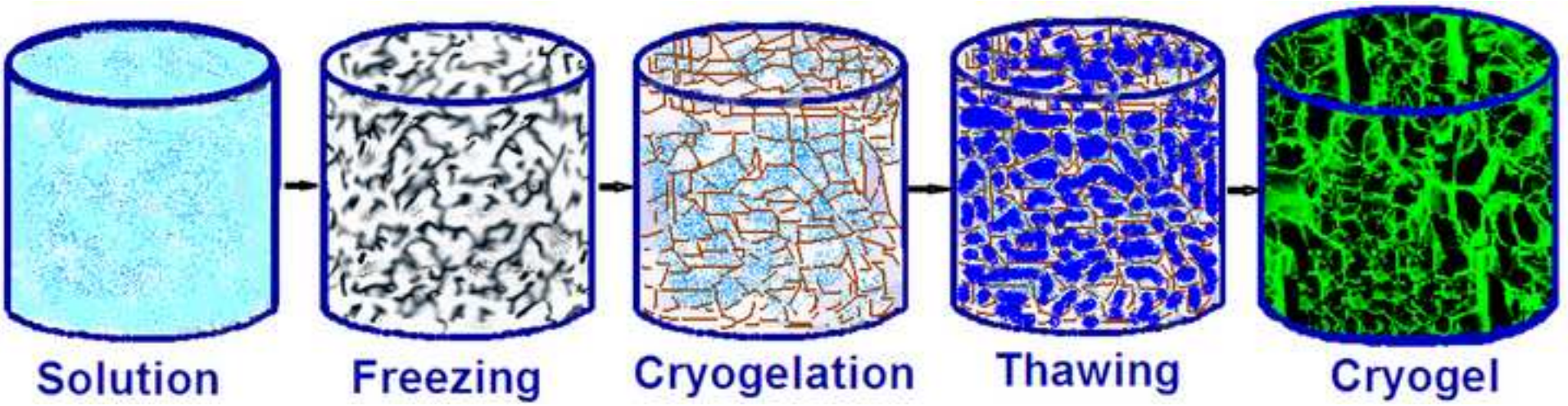

Figure 2

Click here to download high resolution image

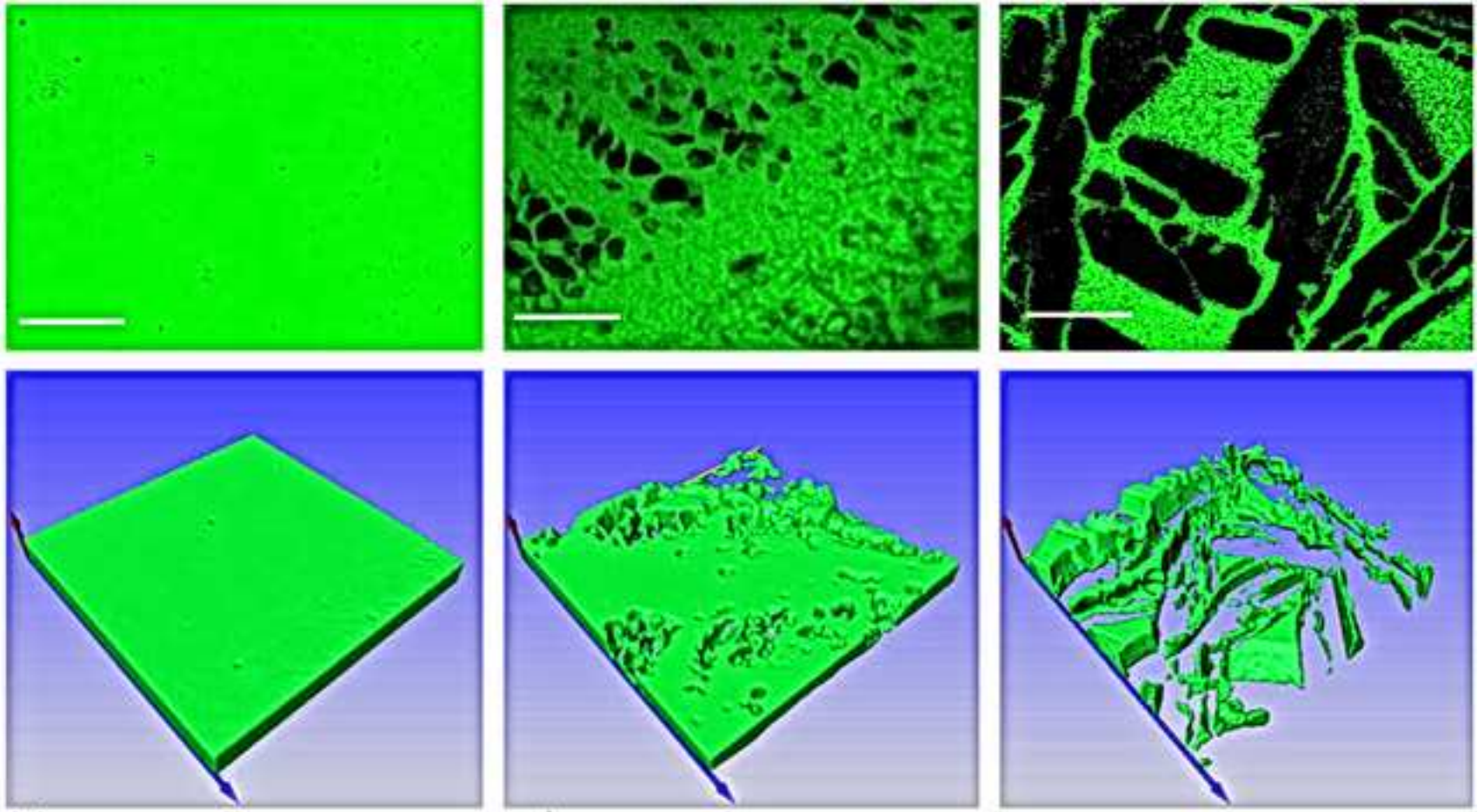

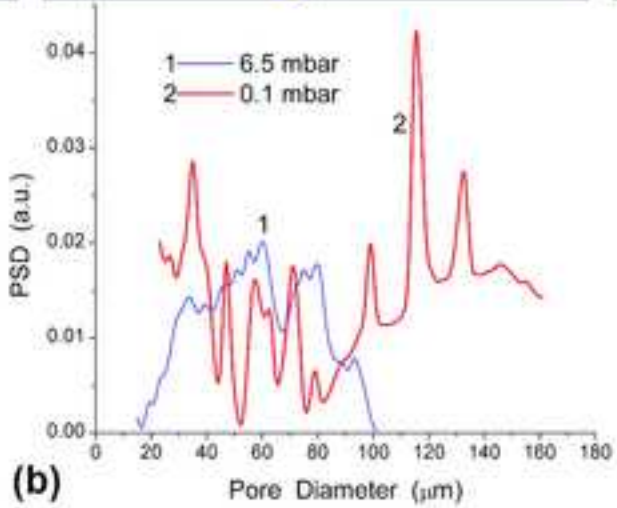

Figure 3

Click here to download high resolution image

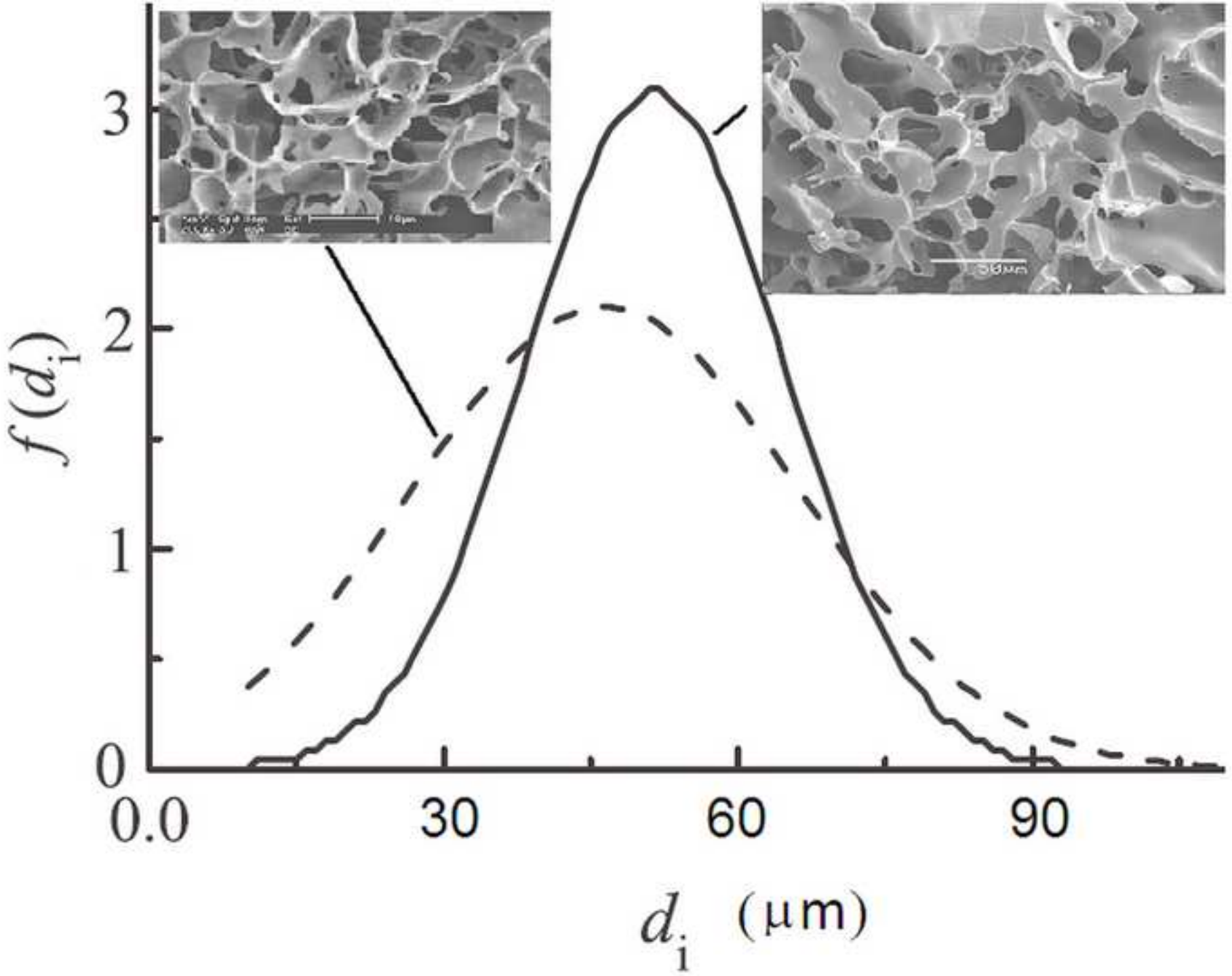

Figure 4

Click here to download high resolution image

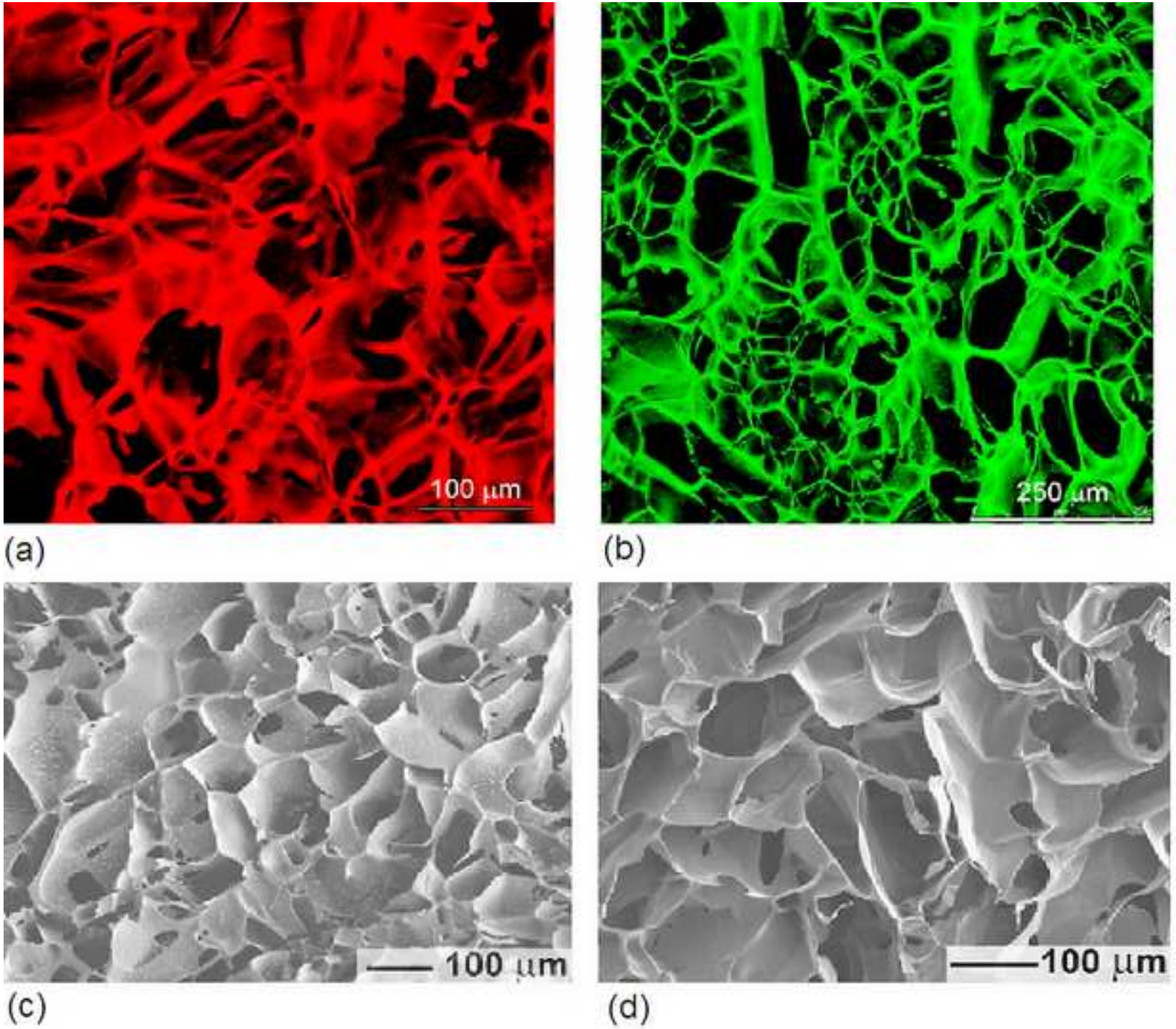

Figure 5
Click here to download high resolution image

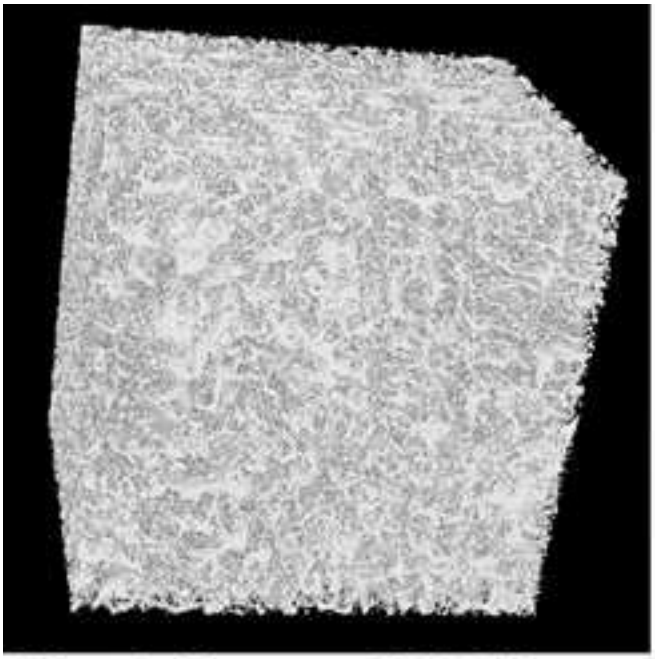

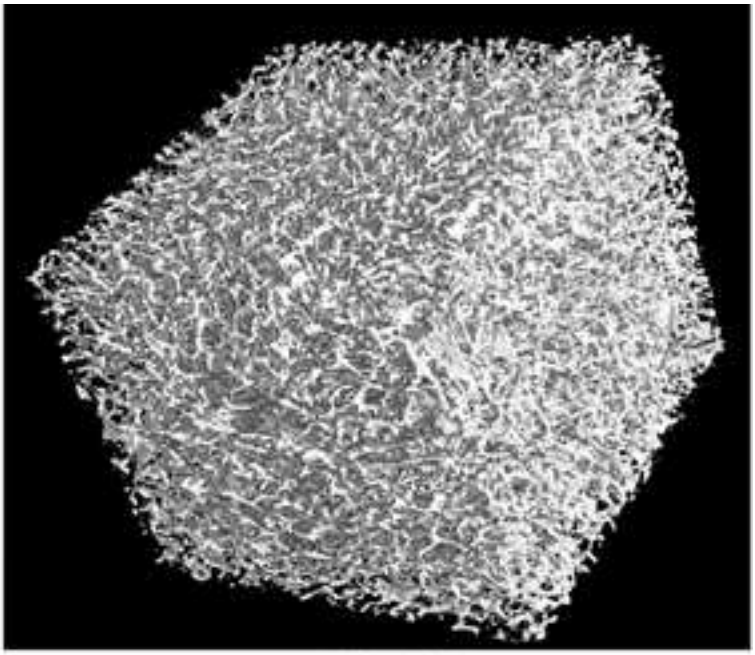

Threshold	220-240	190-235
Porosity	90 %	97 %
Max pore size	32.2 µm	81.8 µm

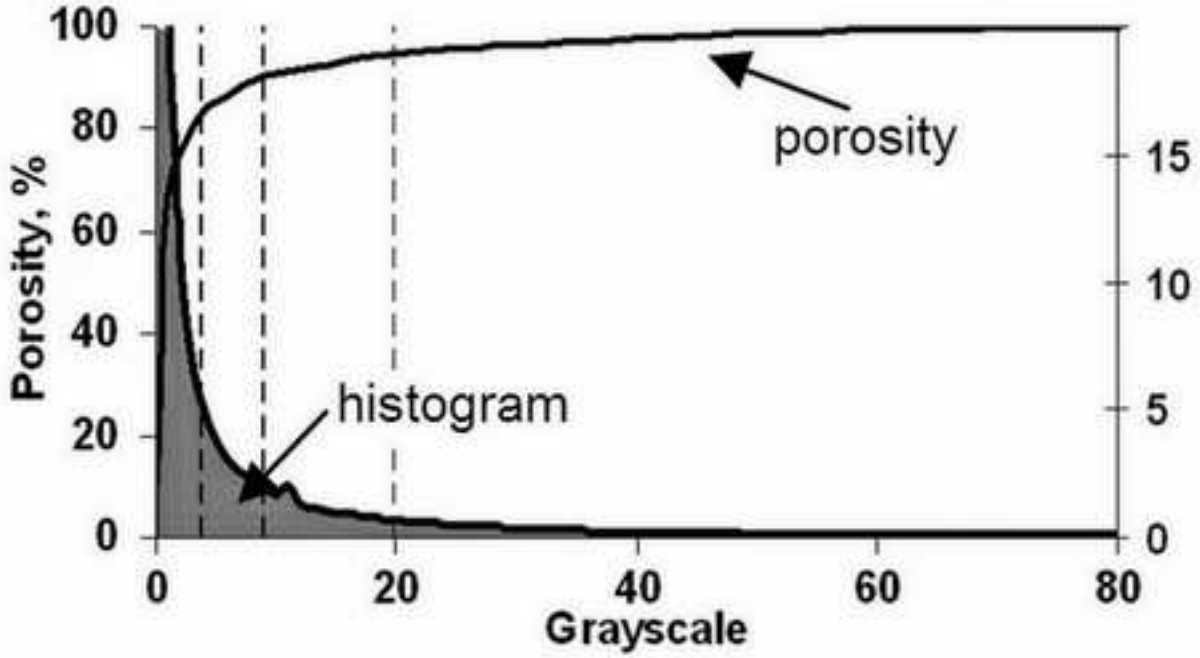

Figure 6

Click here to download high resolution image

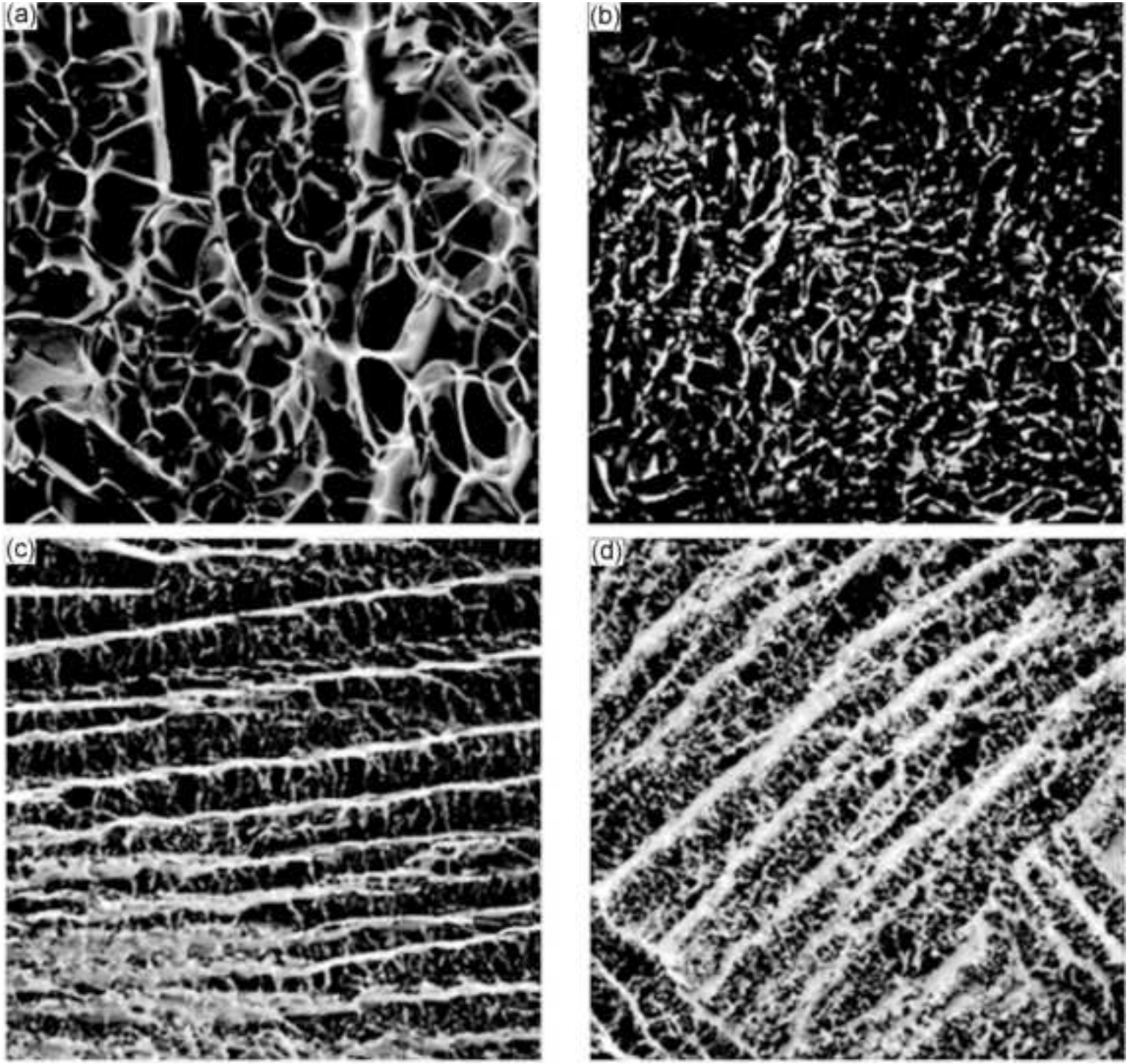

Figure 7
Click here to download high resolution image

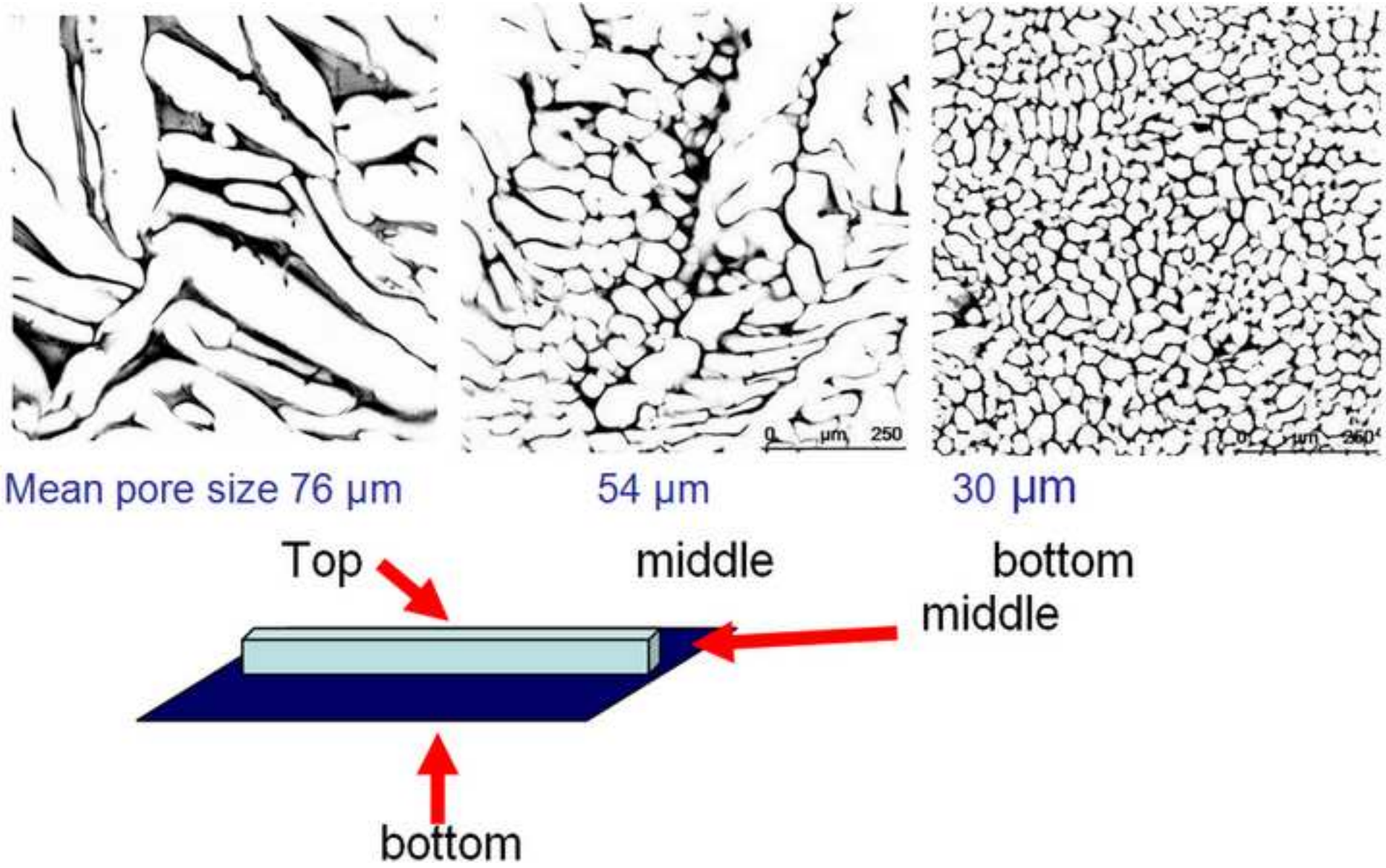

Figure 8

Click here to download high resolution image

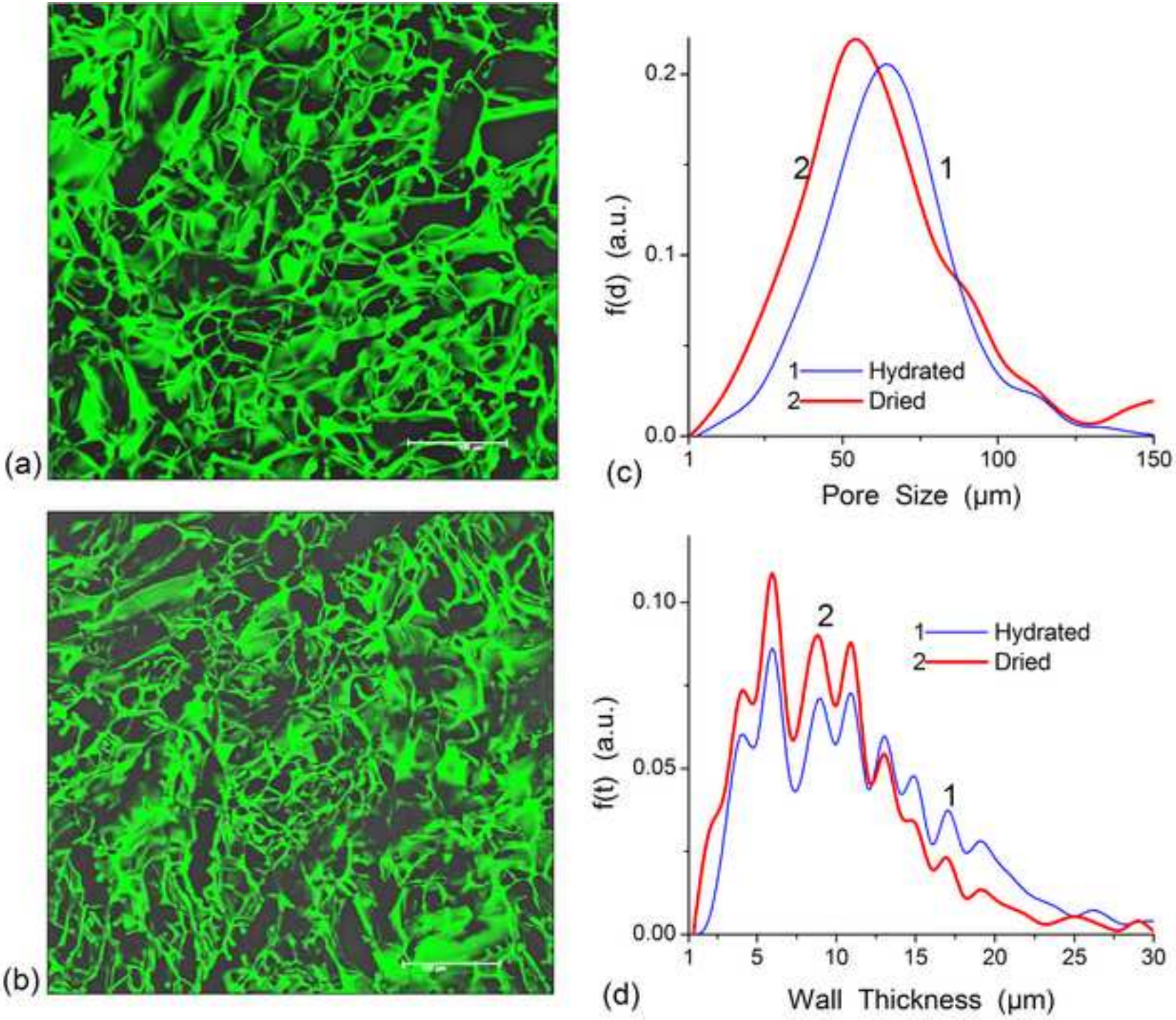

Figure 9

Click here to download high resolution image

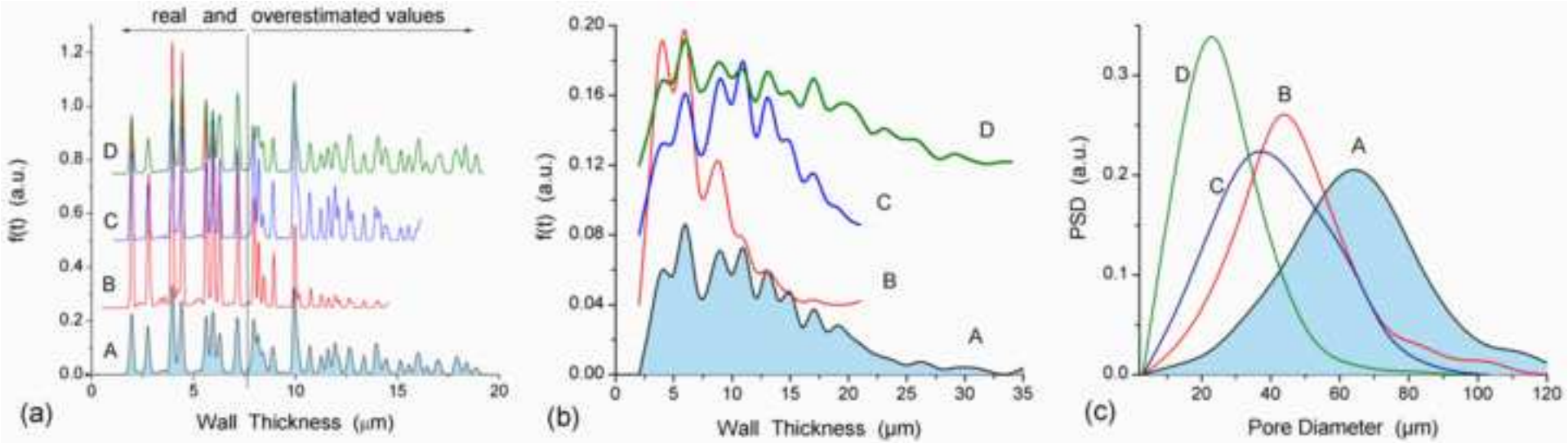

Figure 10

Click here to download high resolution image

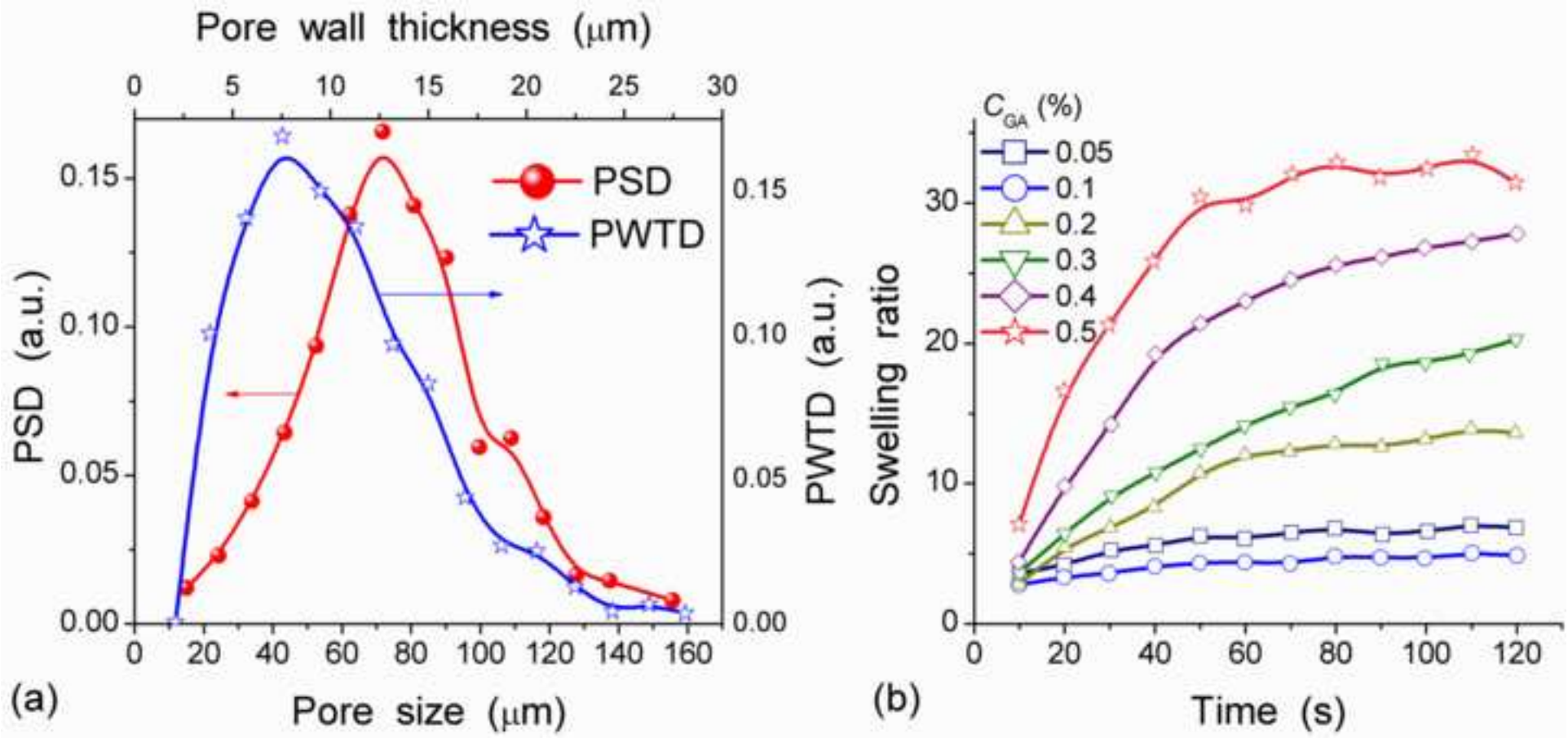

Figure 11

Click here to download high resolution image

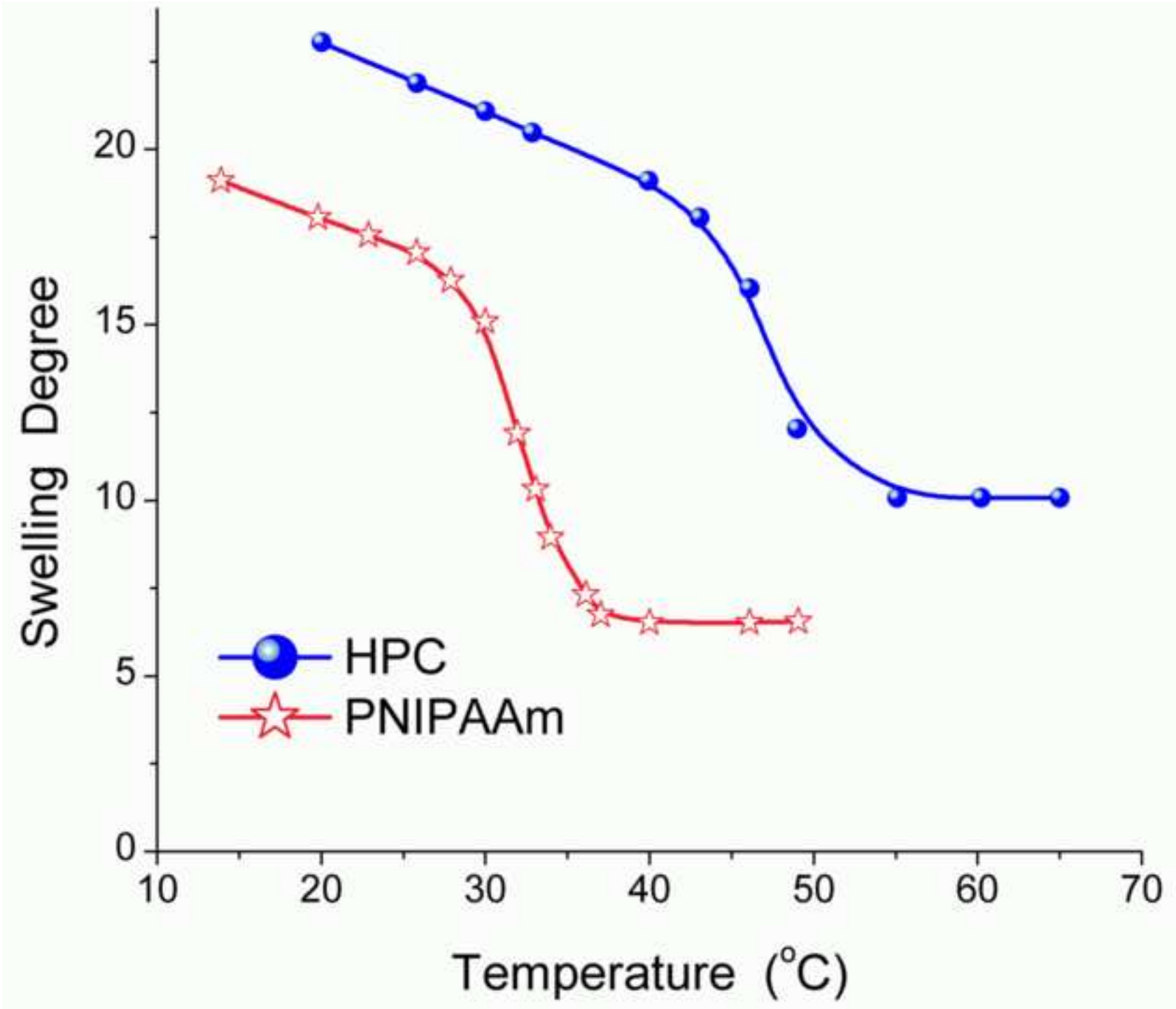

Figure 12
Click here to download high resolution image

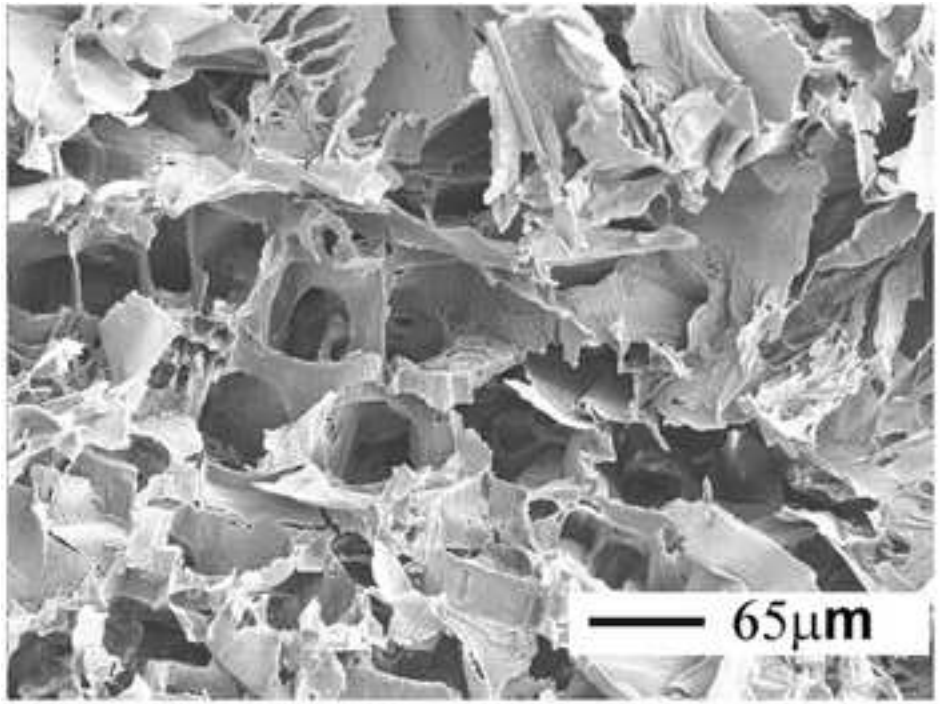

(a)

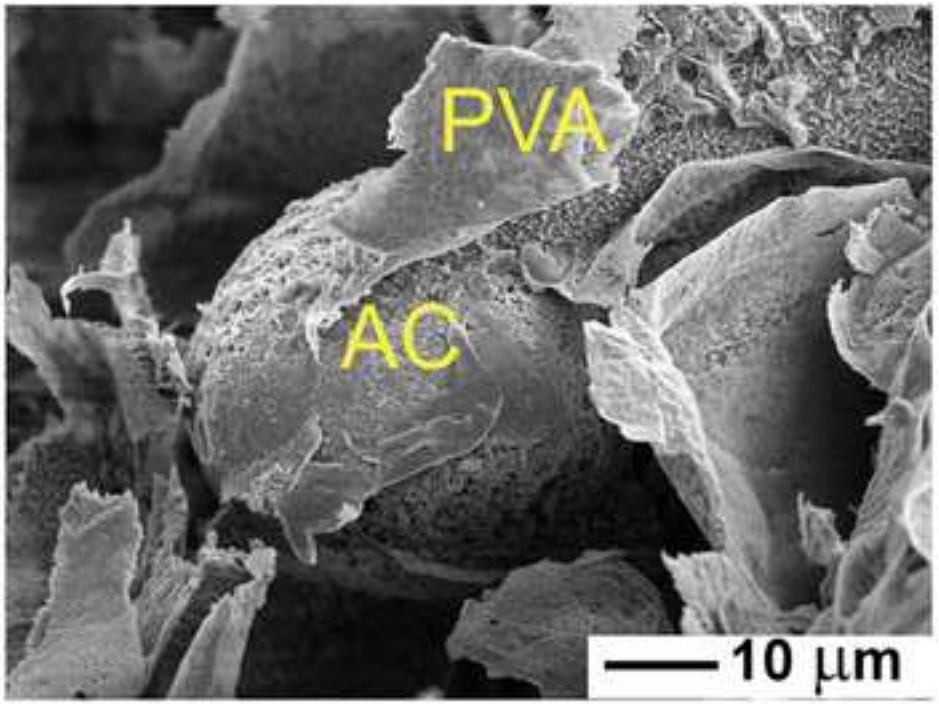

(b)

Figure 13

Click here to download high resolution image

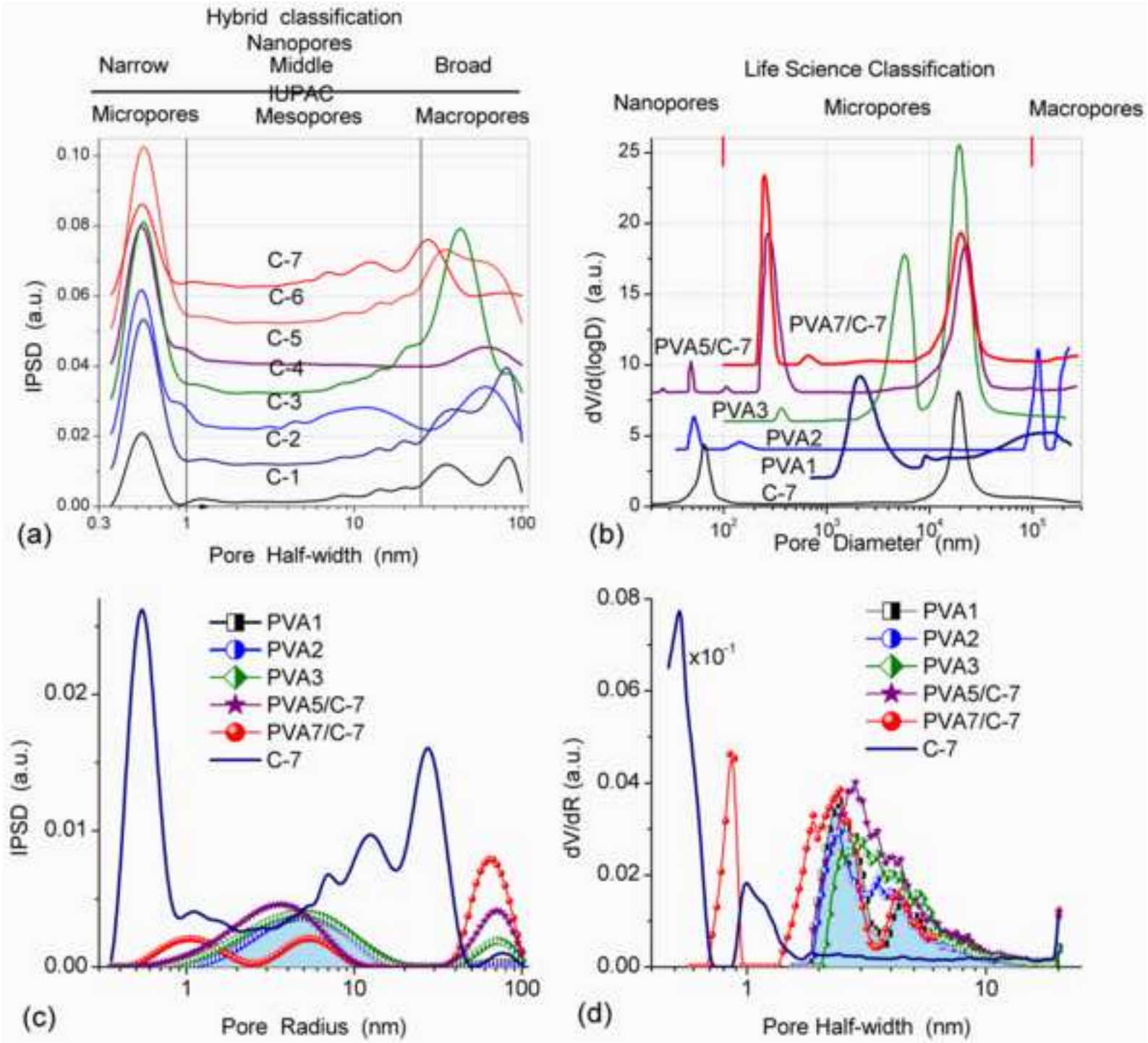

Figure 14

Click here to download high resolution image

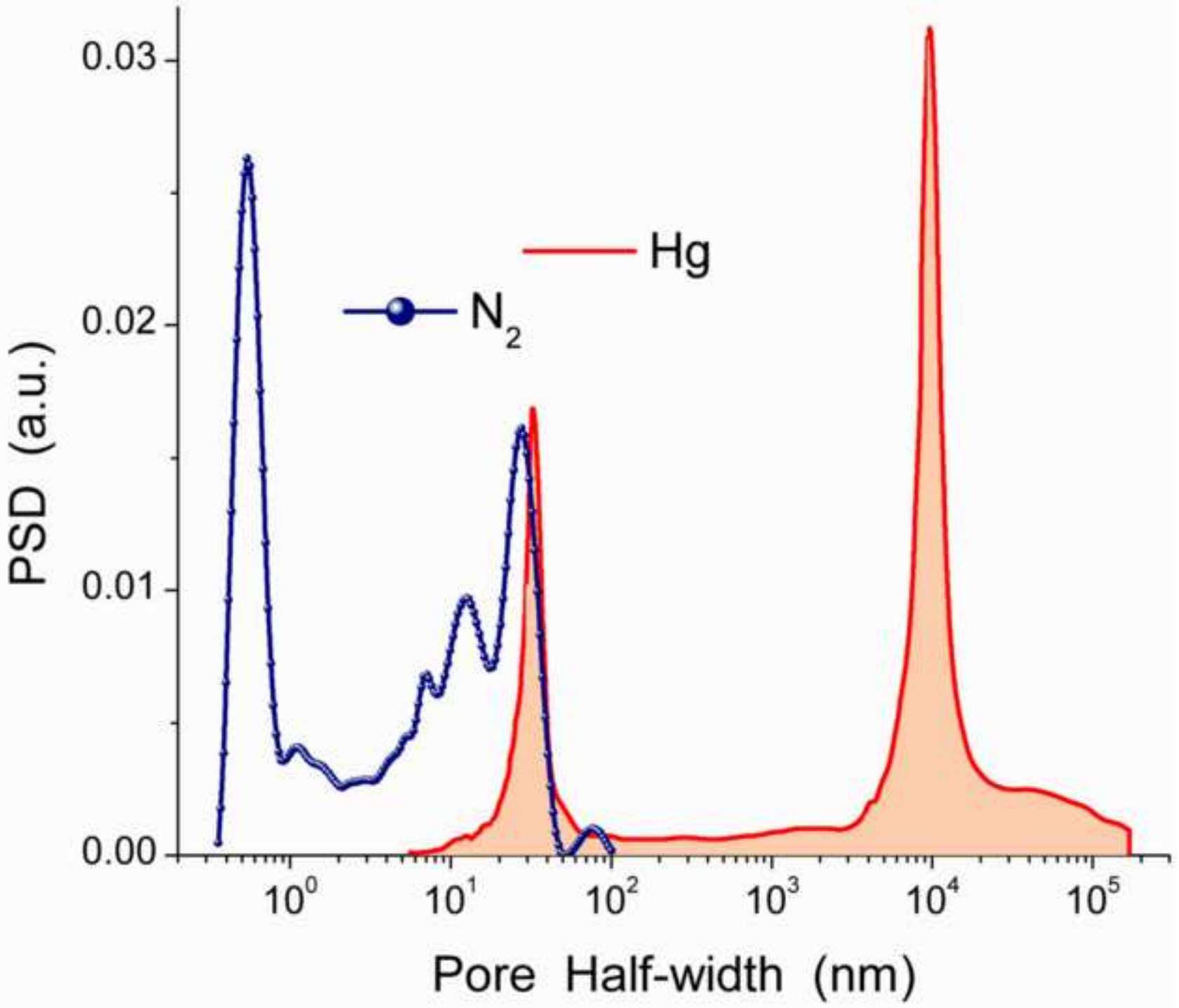

Figure 15

Click here to download high resolution image

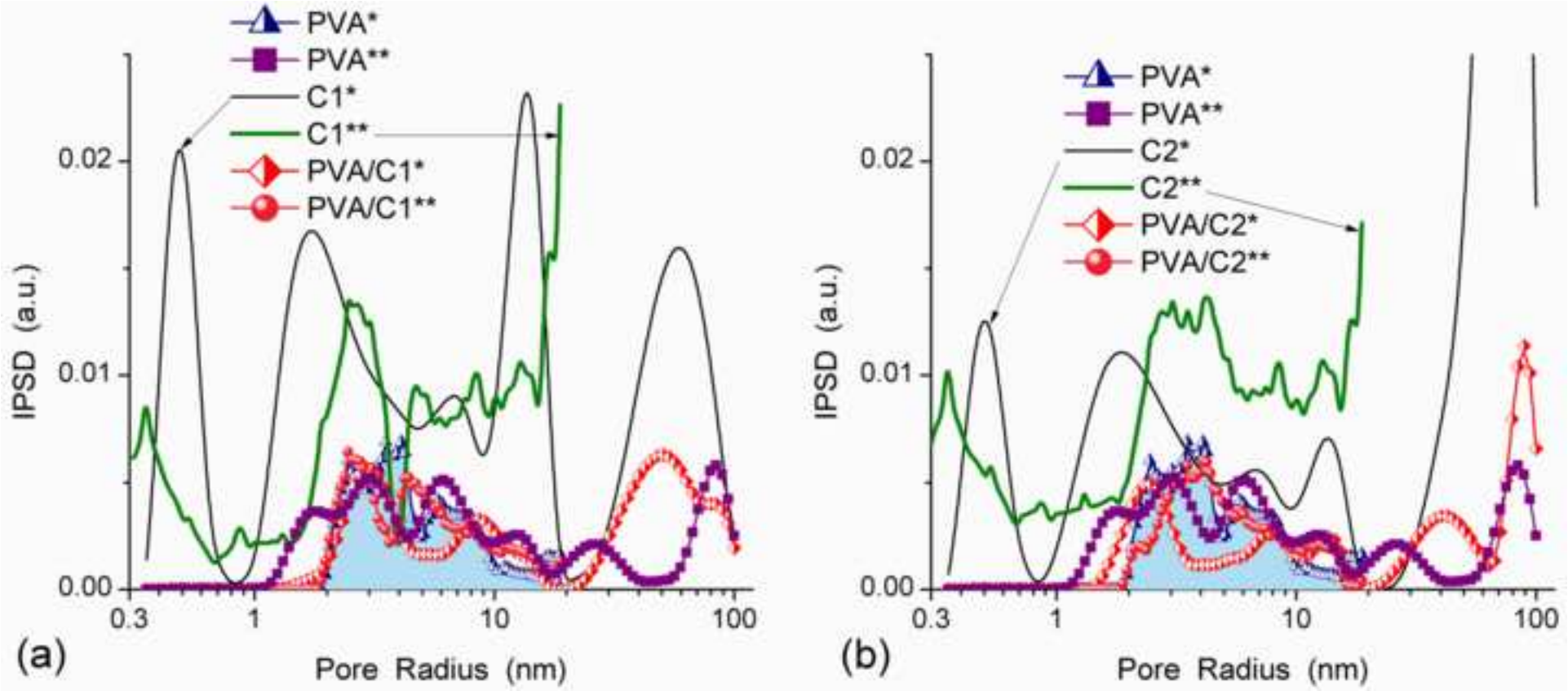

Figure 16

Click here to download high resolution image

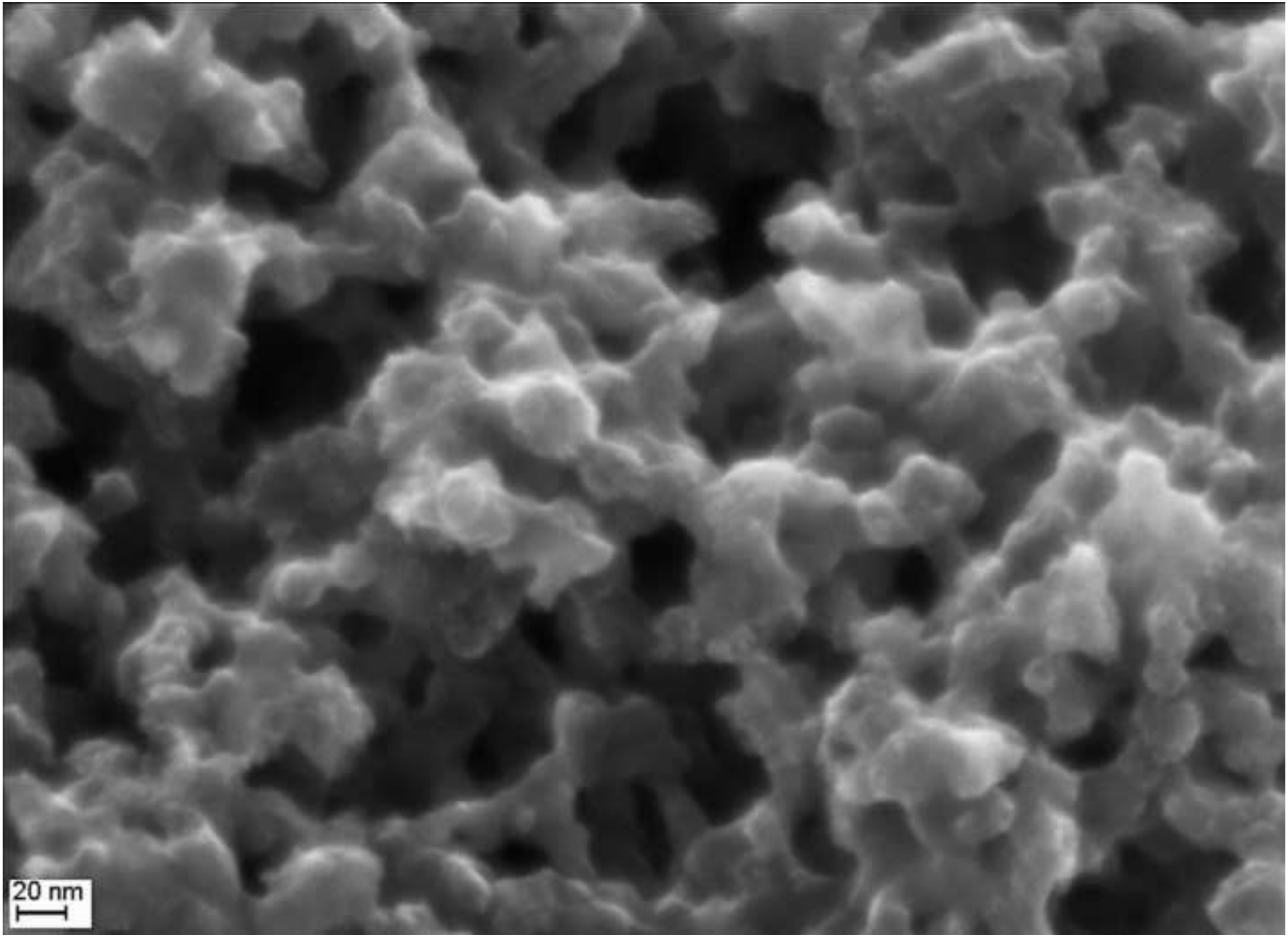

Figure 17

Click here to download high resolution image

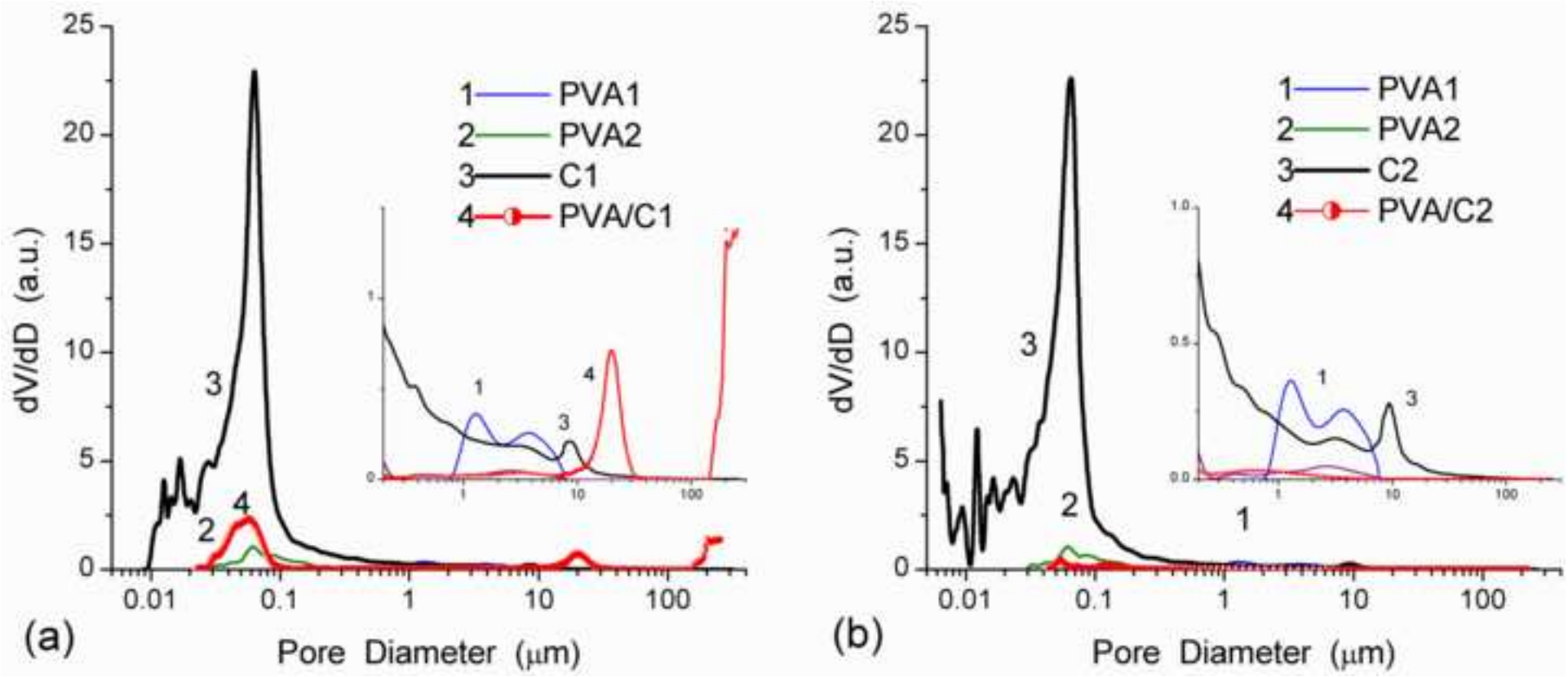

Figure 18

Click here to download high resolution image

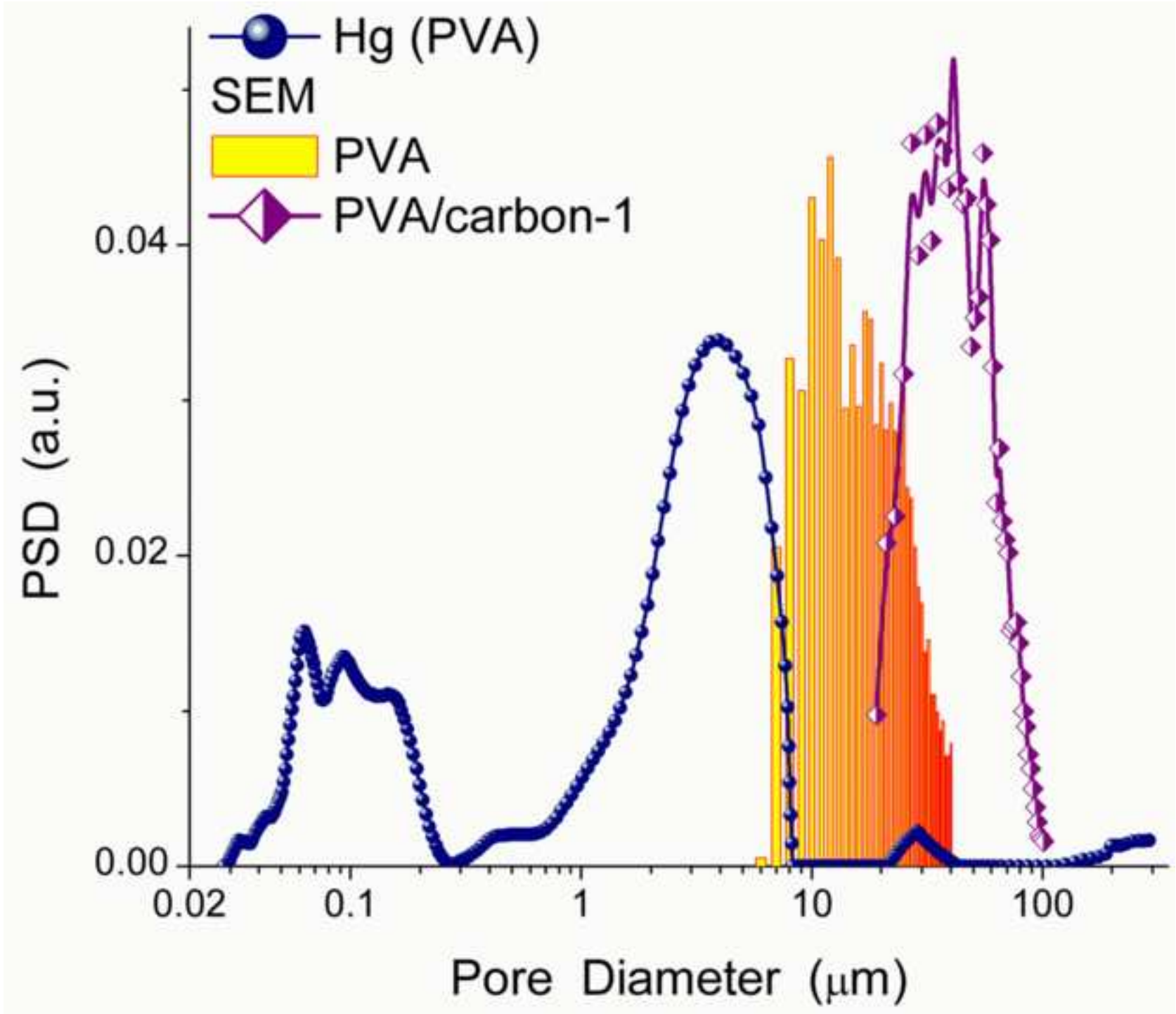

Figure 19

Click here to download high resolution image

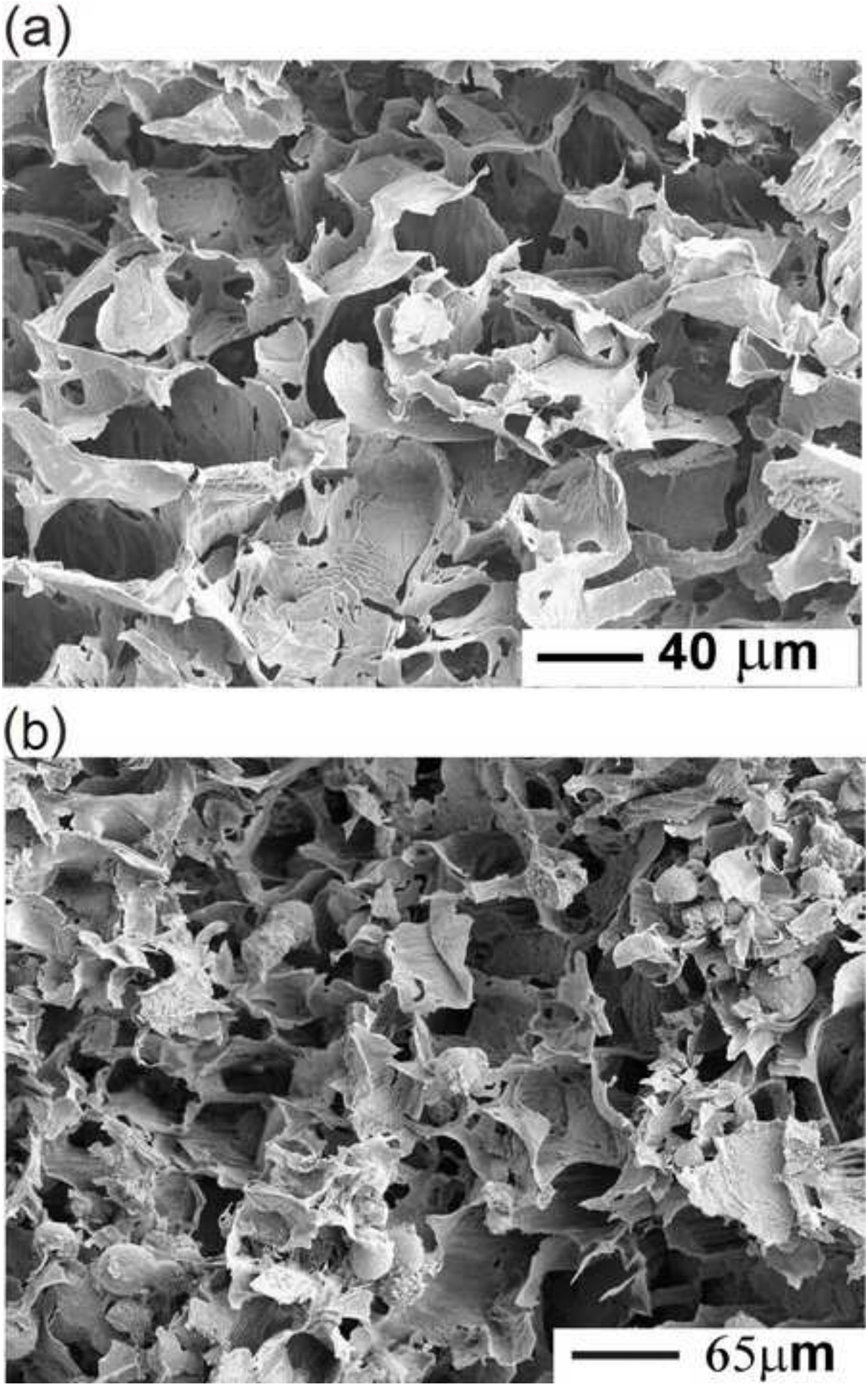

Figure 20
Click here to download high resolution image

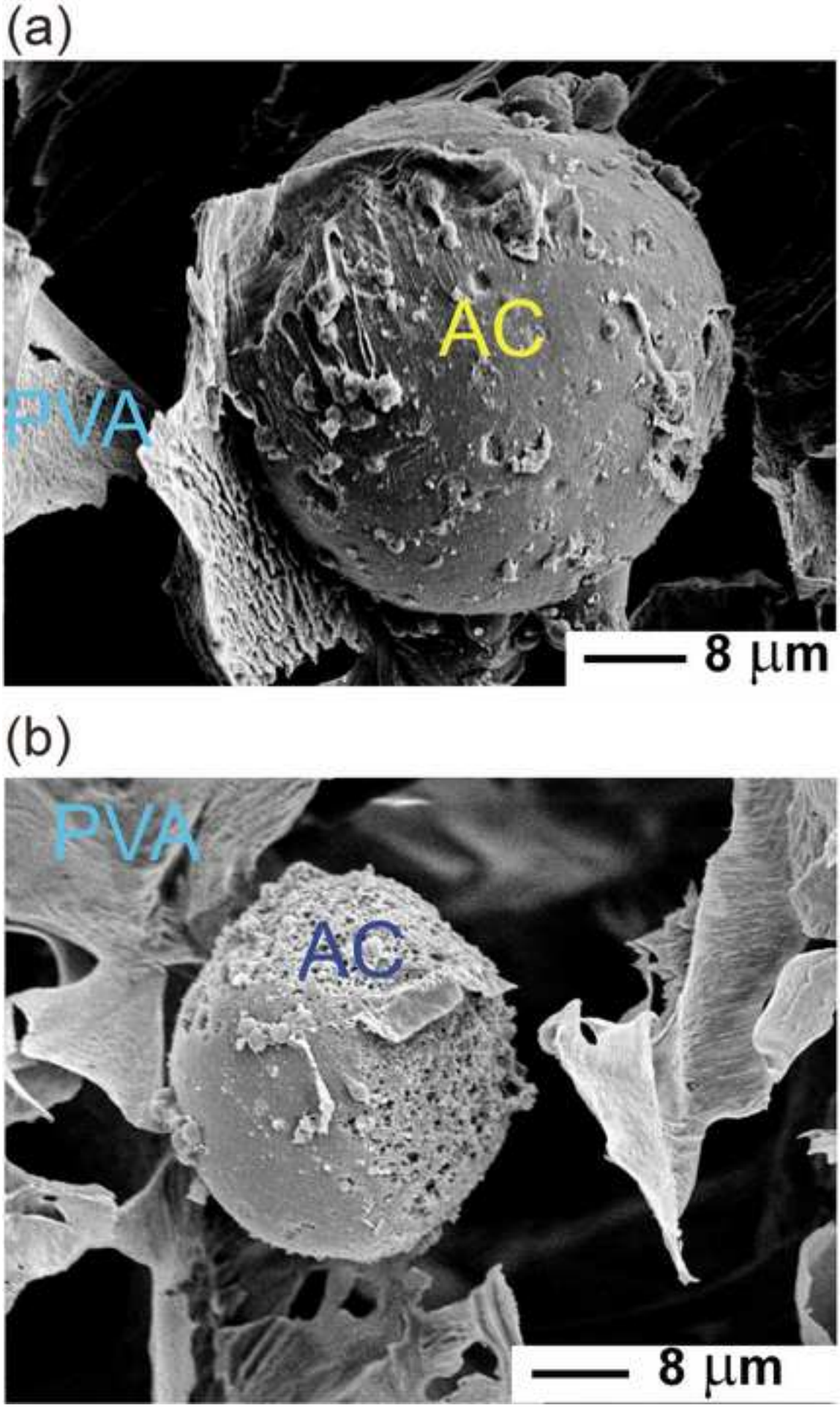

Figure 21

Click here to download high resolution image

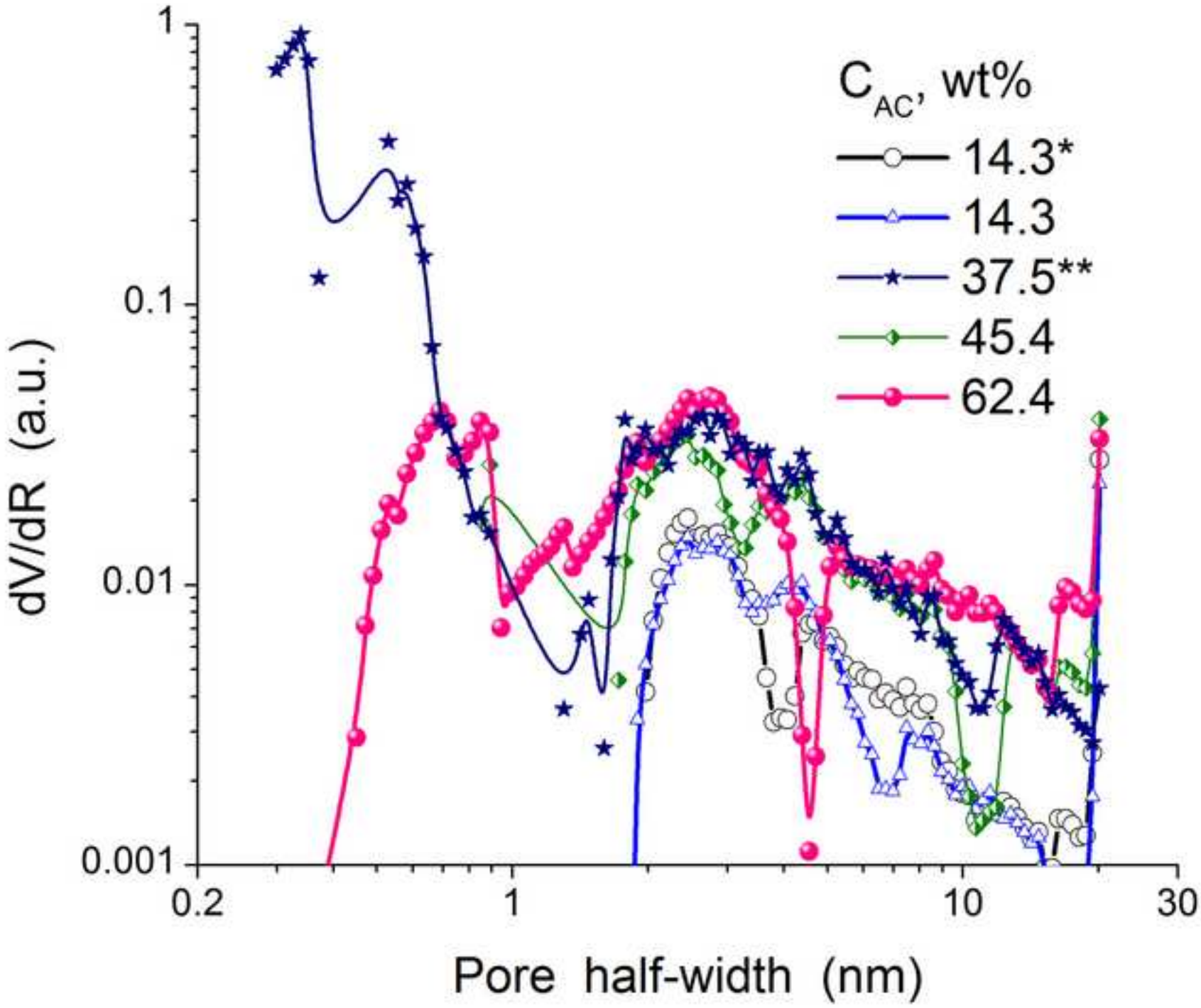

Figure 22

Click here to download high resolution image

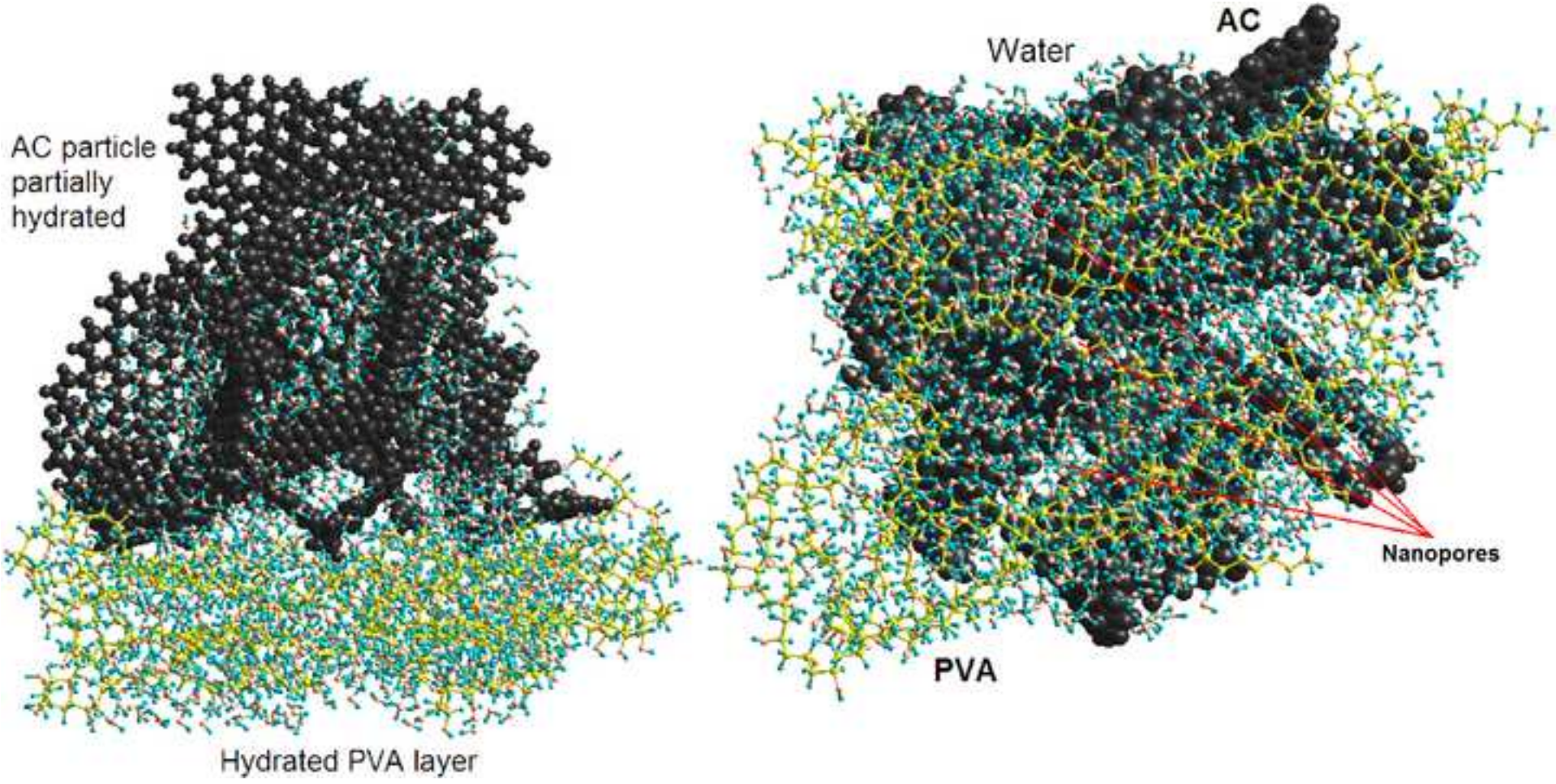

Figure 23

Click here to download high resolution image

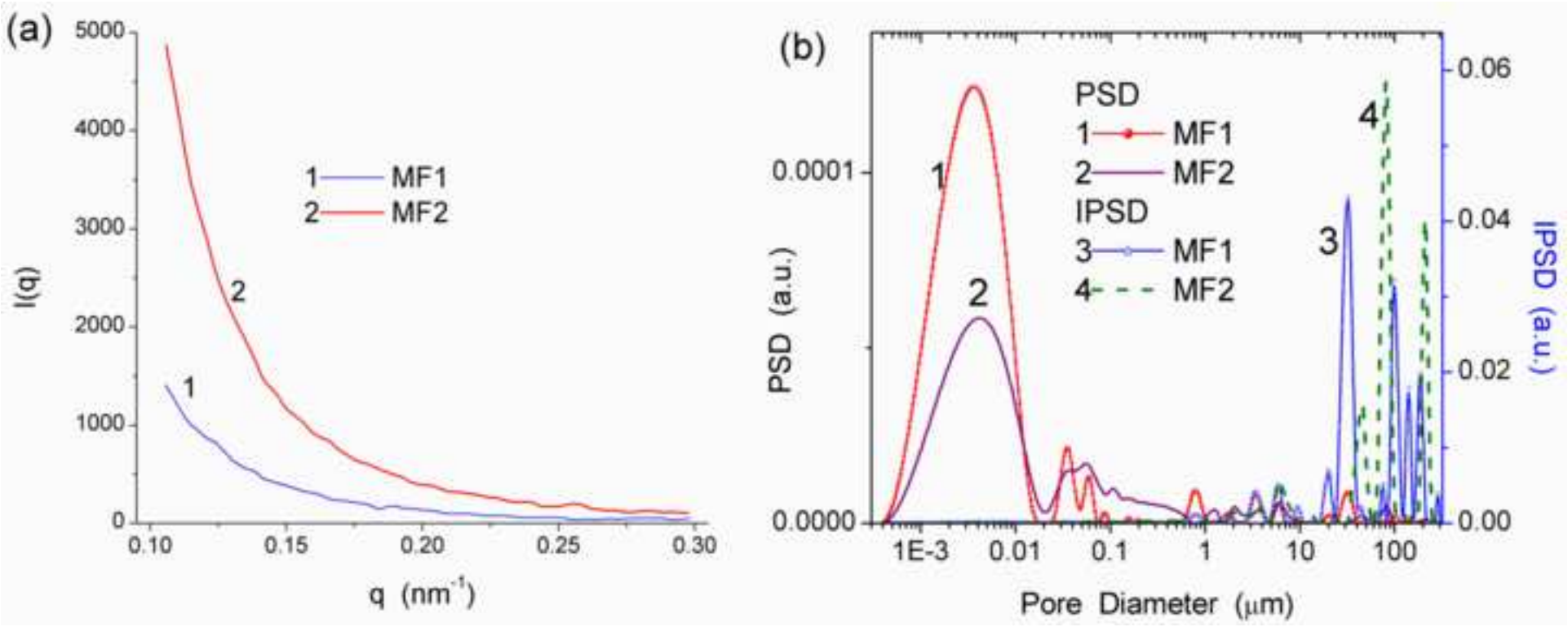

Figure 24

Click here to download high resolution image

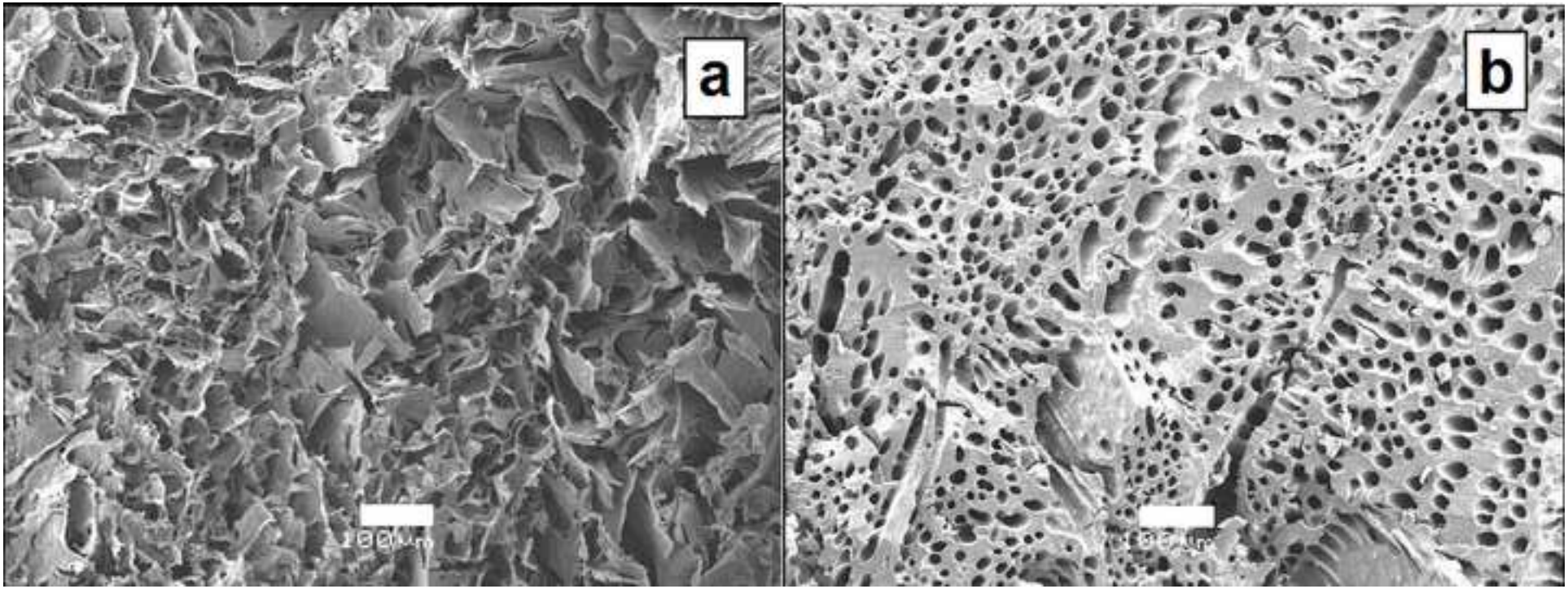

Figure 25

Click here to download high resolution image

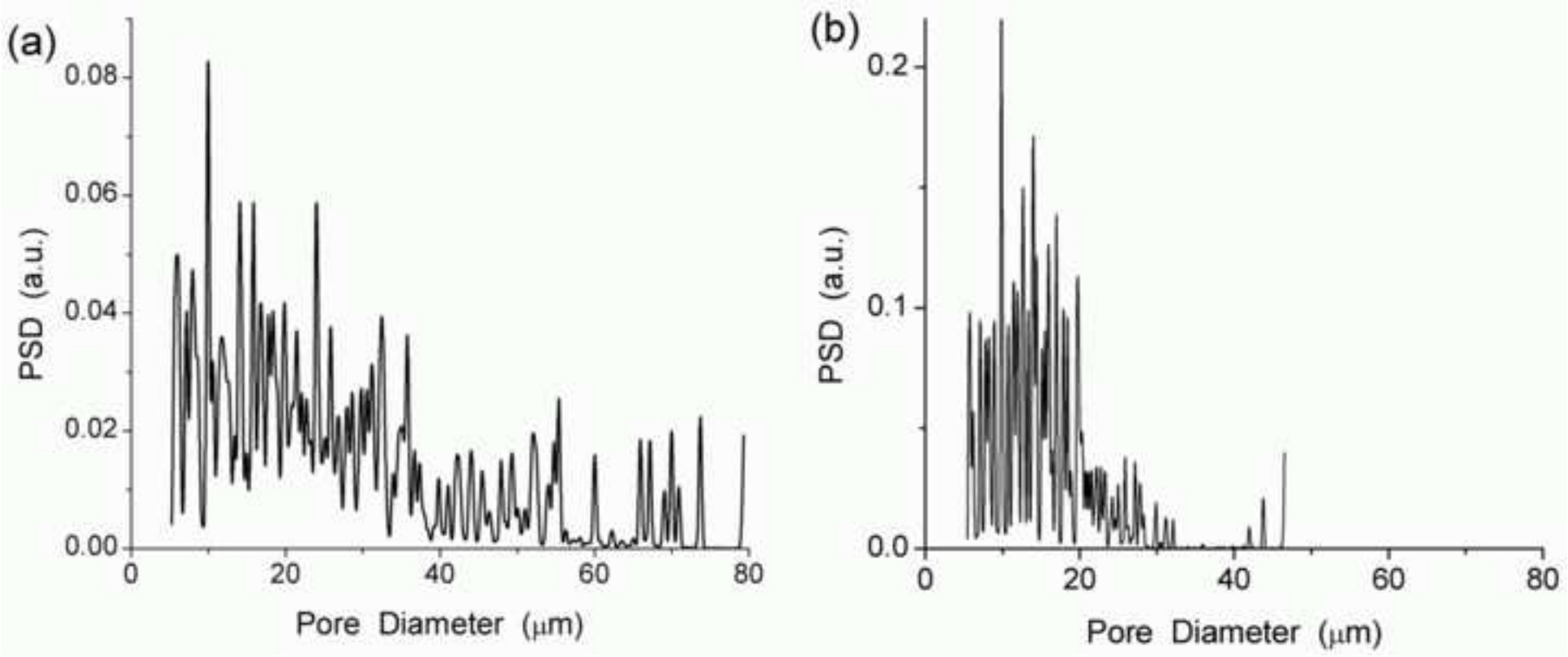

Figure 26

Click here to download high resolution image

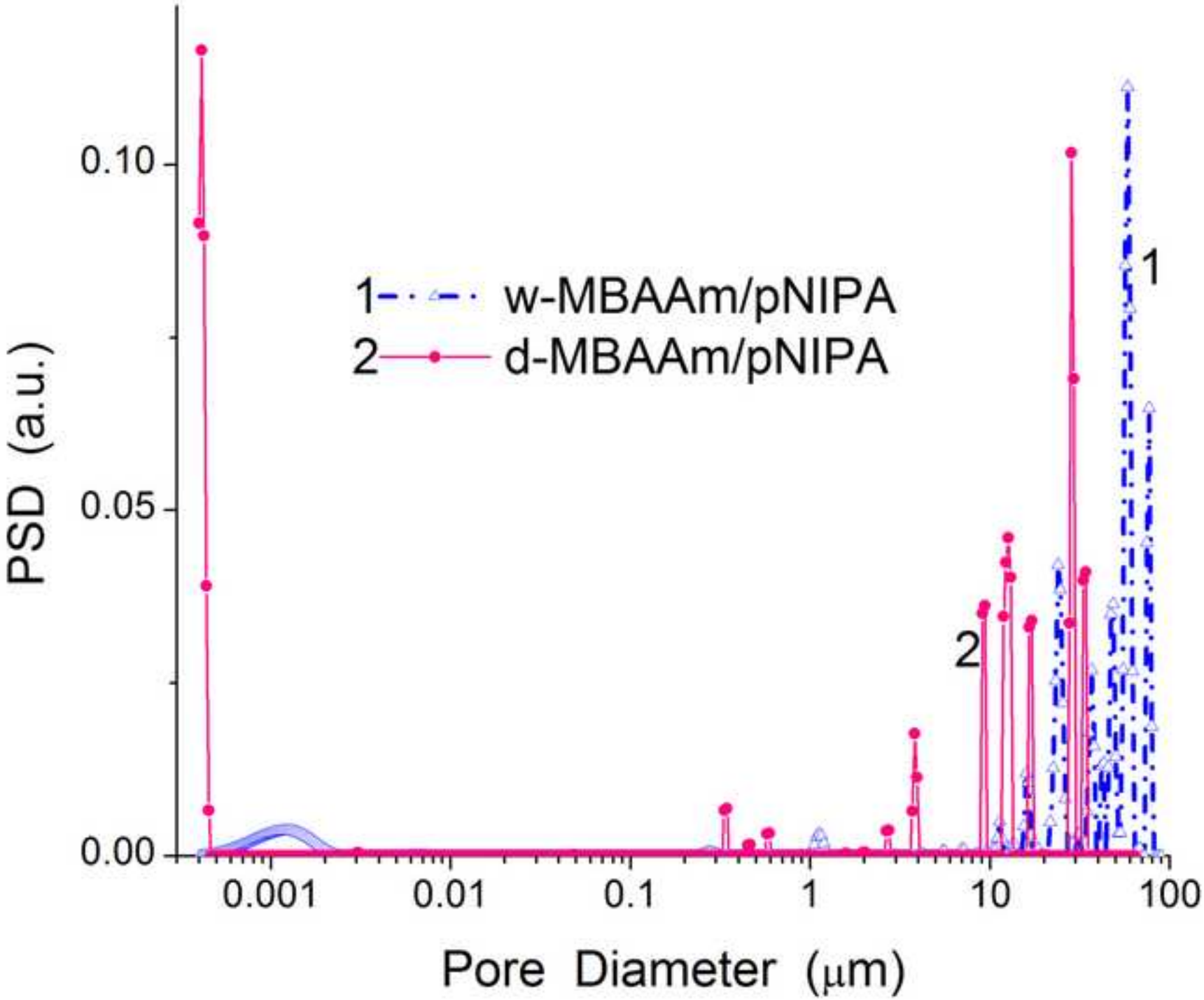

Figure 27

Click here to download high resolution image

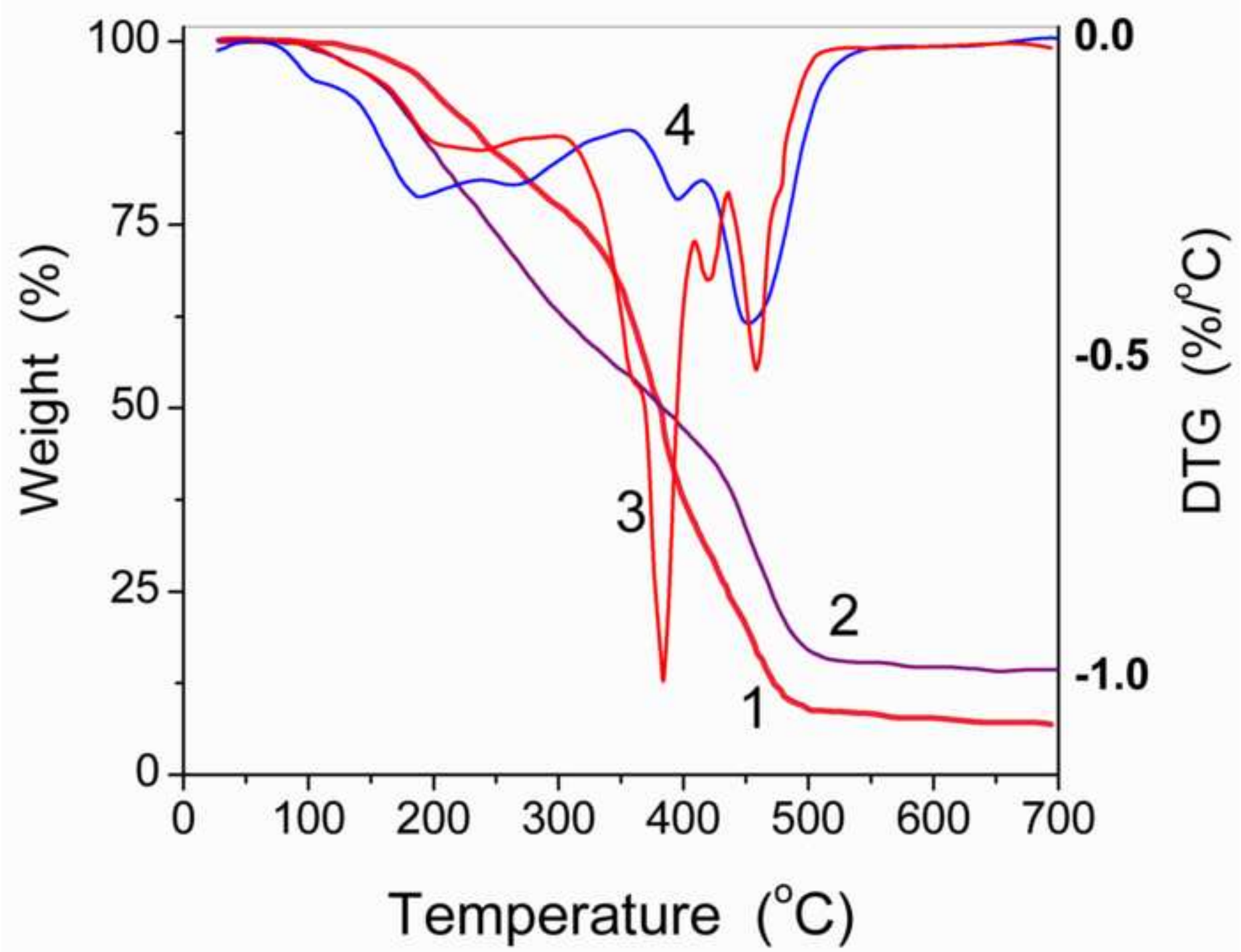

Figure 28
Click here to download high resolution image

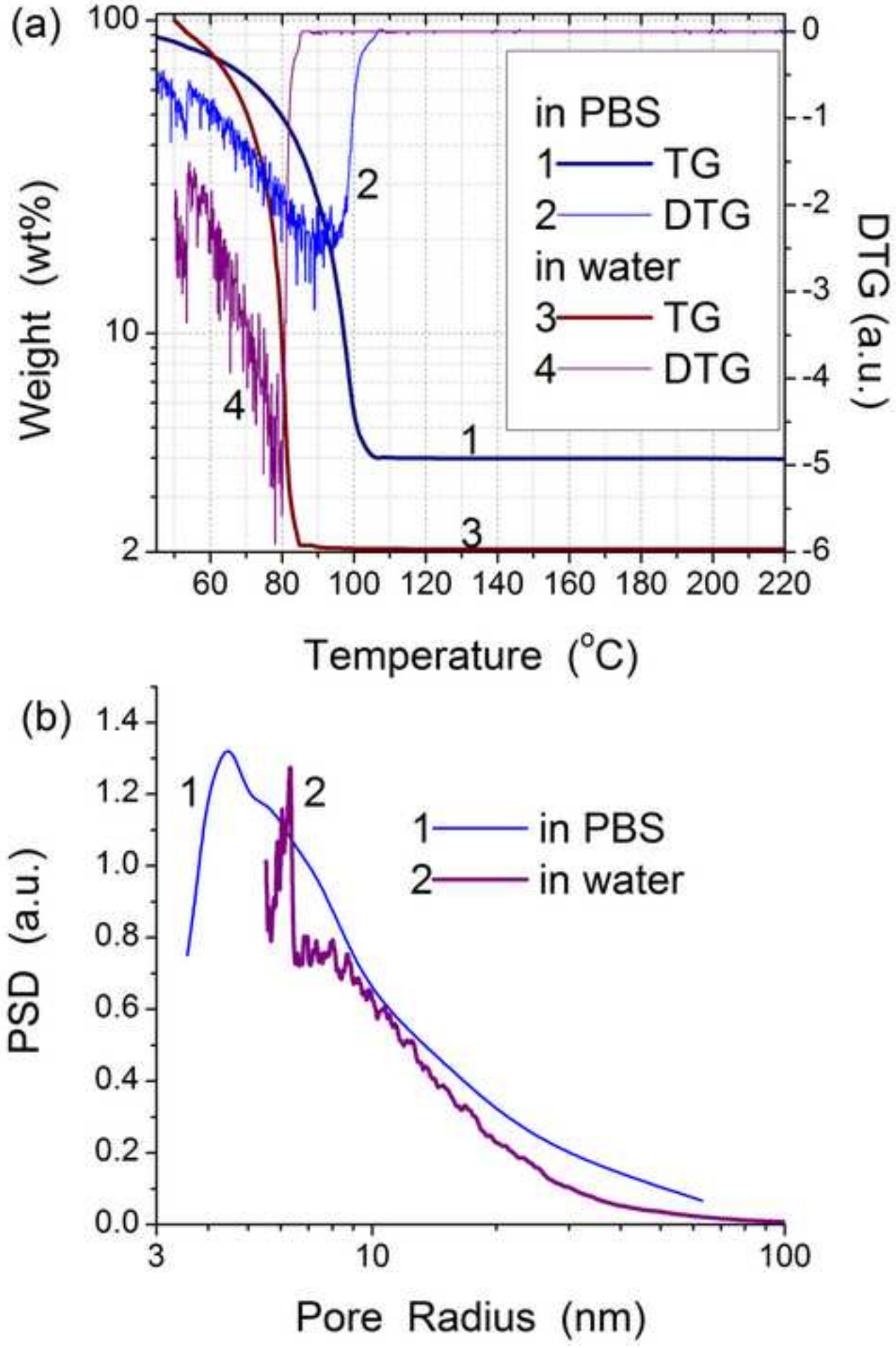

Figure 29

Click here to download high resolution image

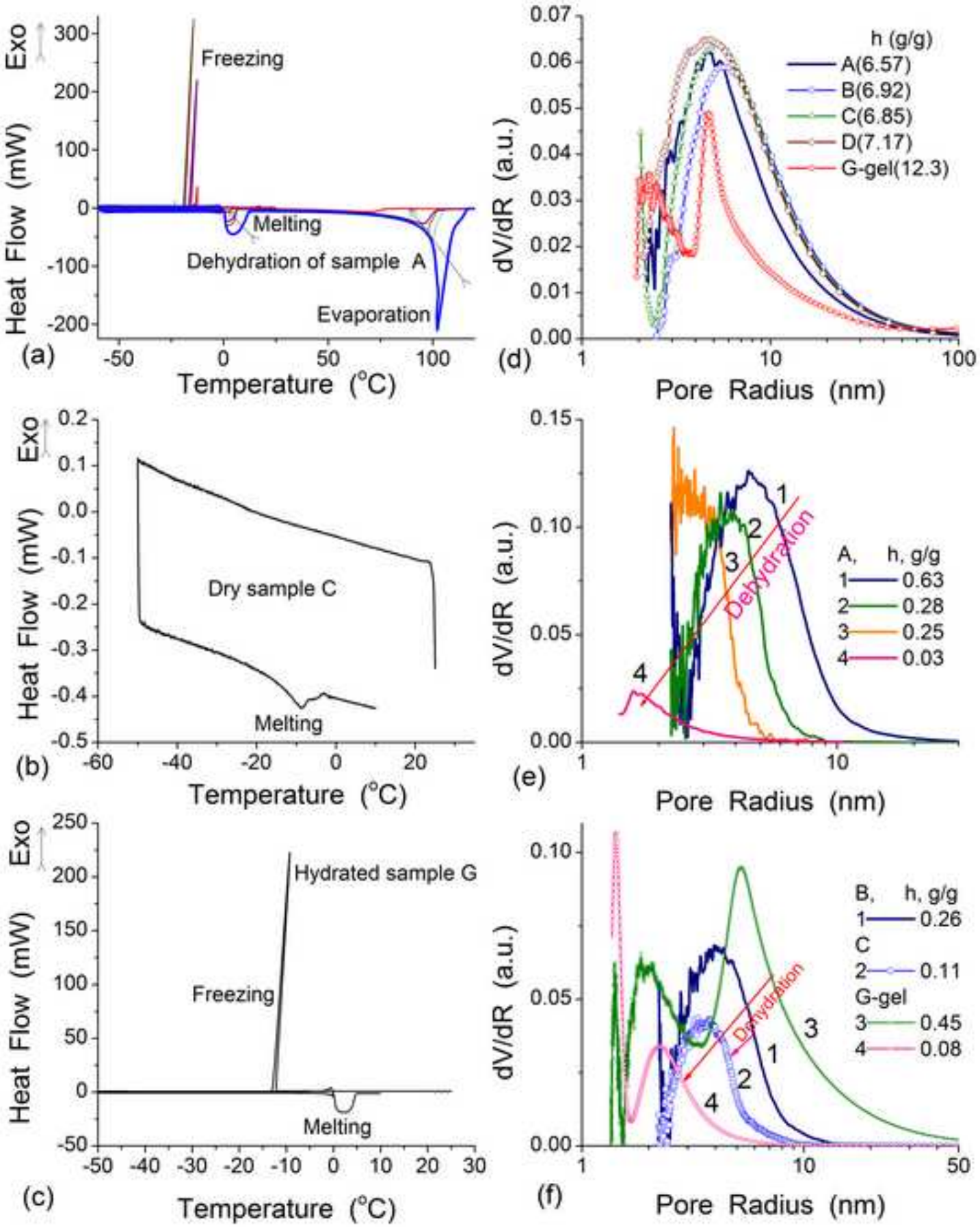

Figure 30

Click here to download high resolution image

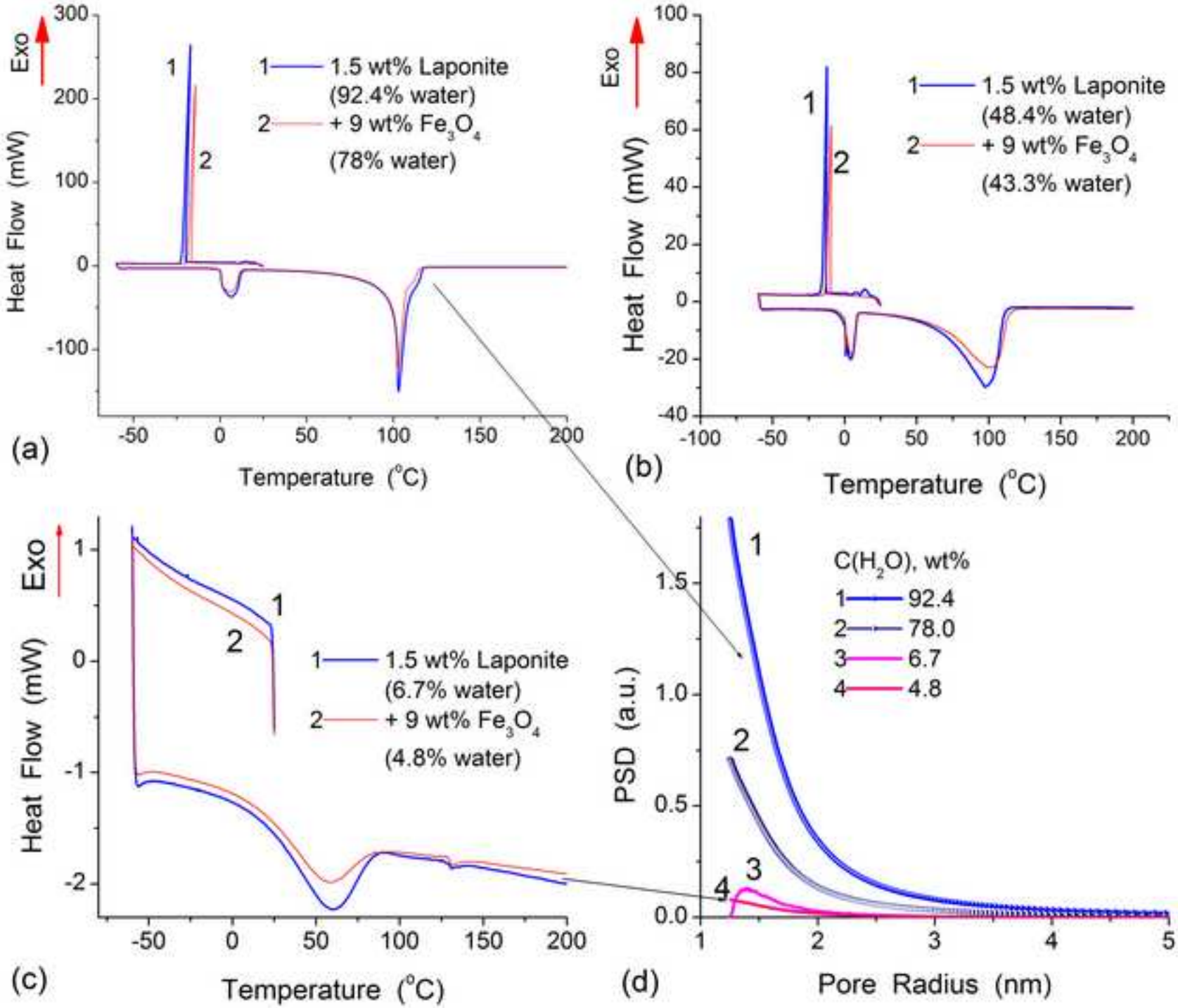

Figure 31

Click here to download high resolution image

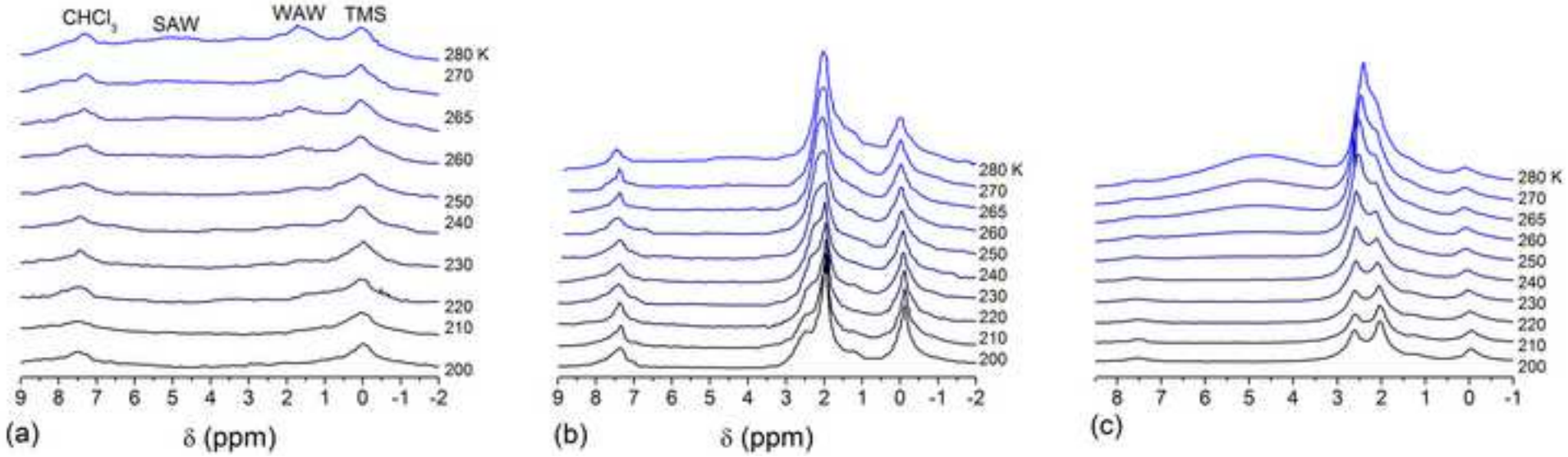

Figure 32

Click here to download high resolution image

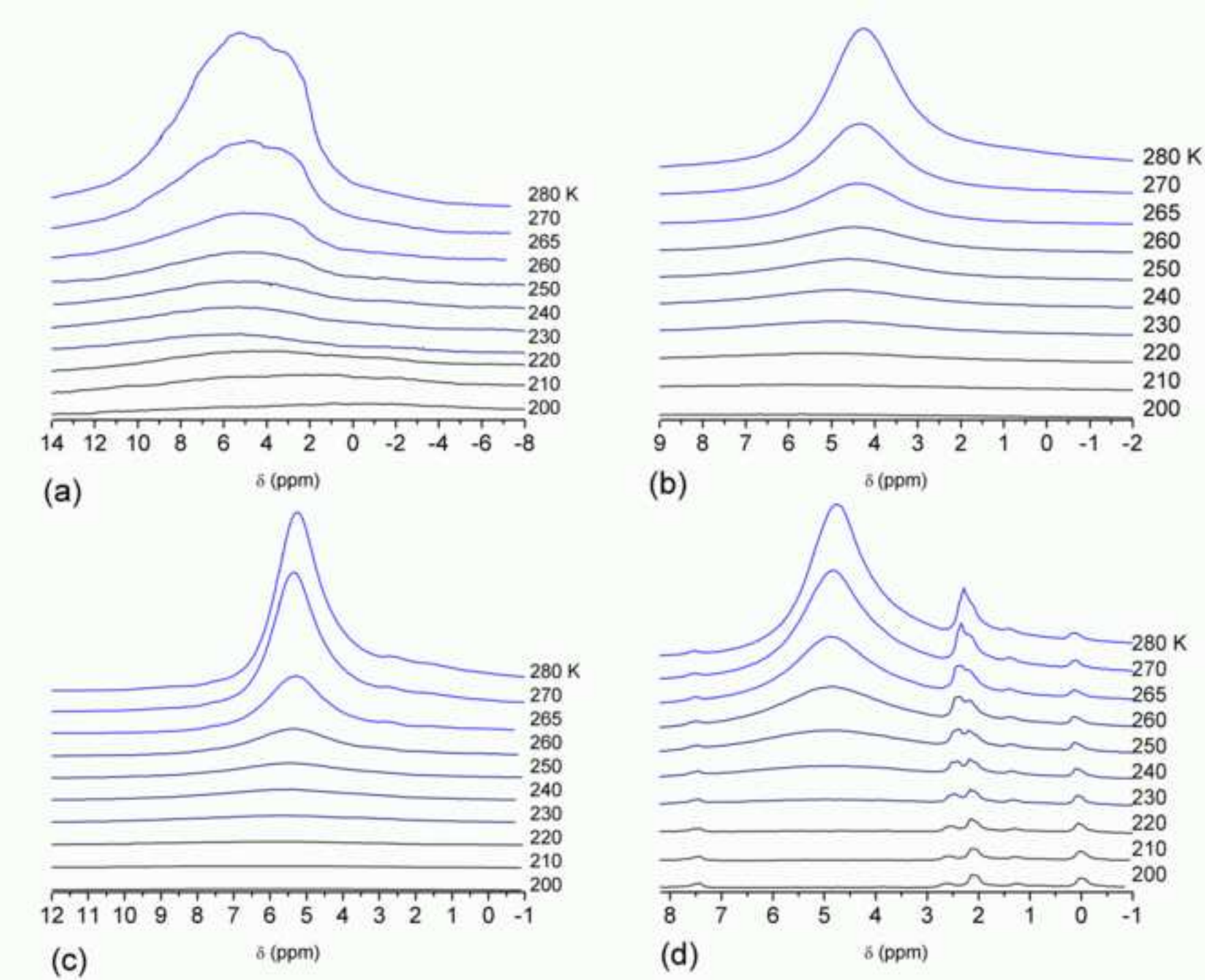

Figure 33

Click here to download high resolution image

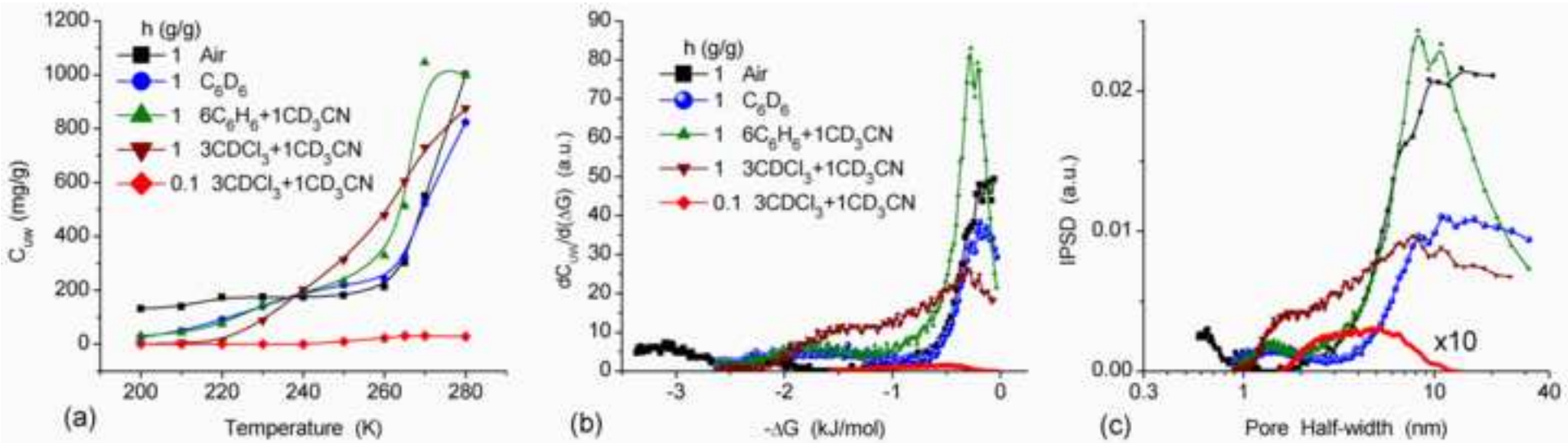

Figure 34

Click here to download high resolution image

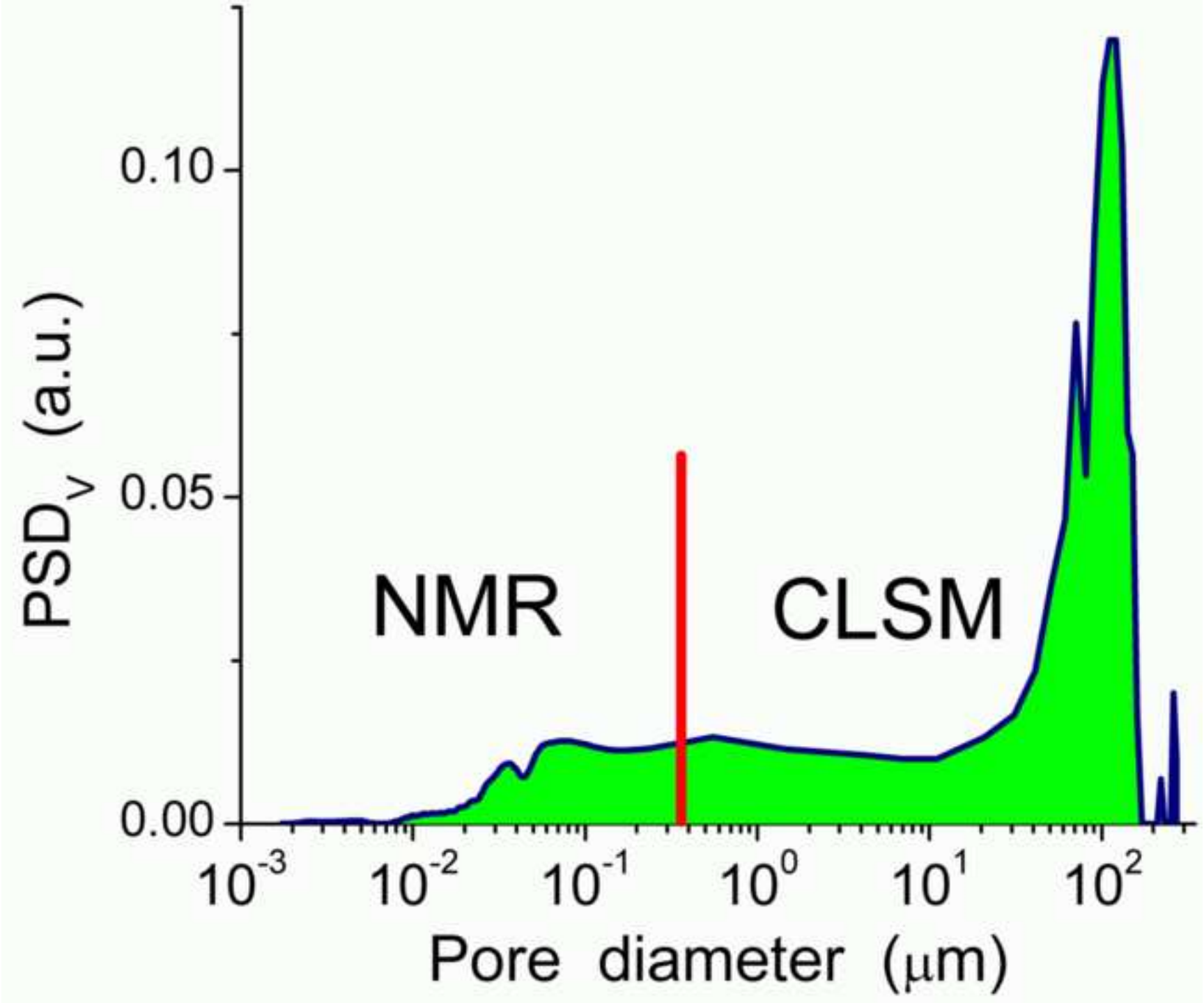

Figure 35

Click here to download high resolution image

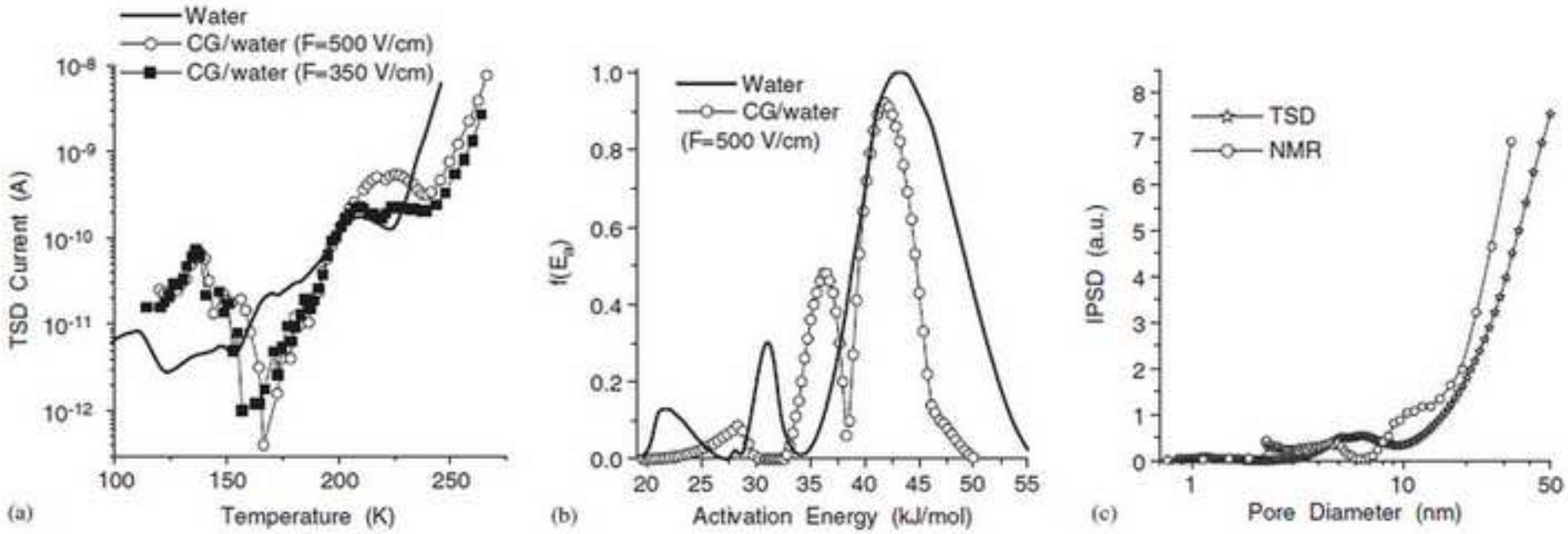

Figure 36

Click here to download high resolution image

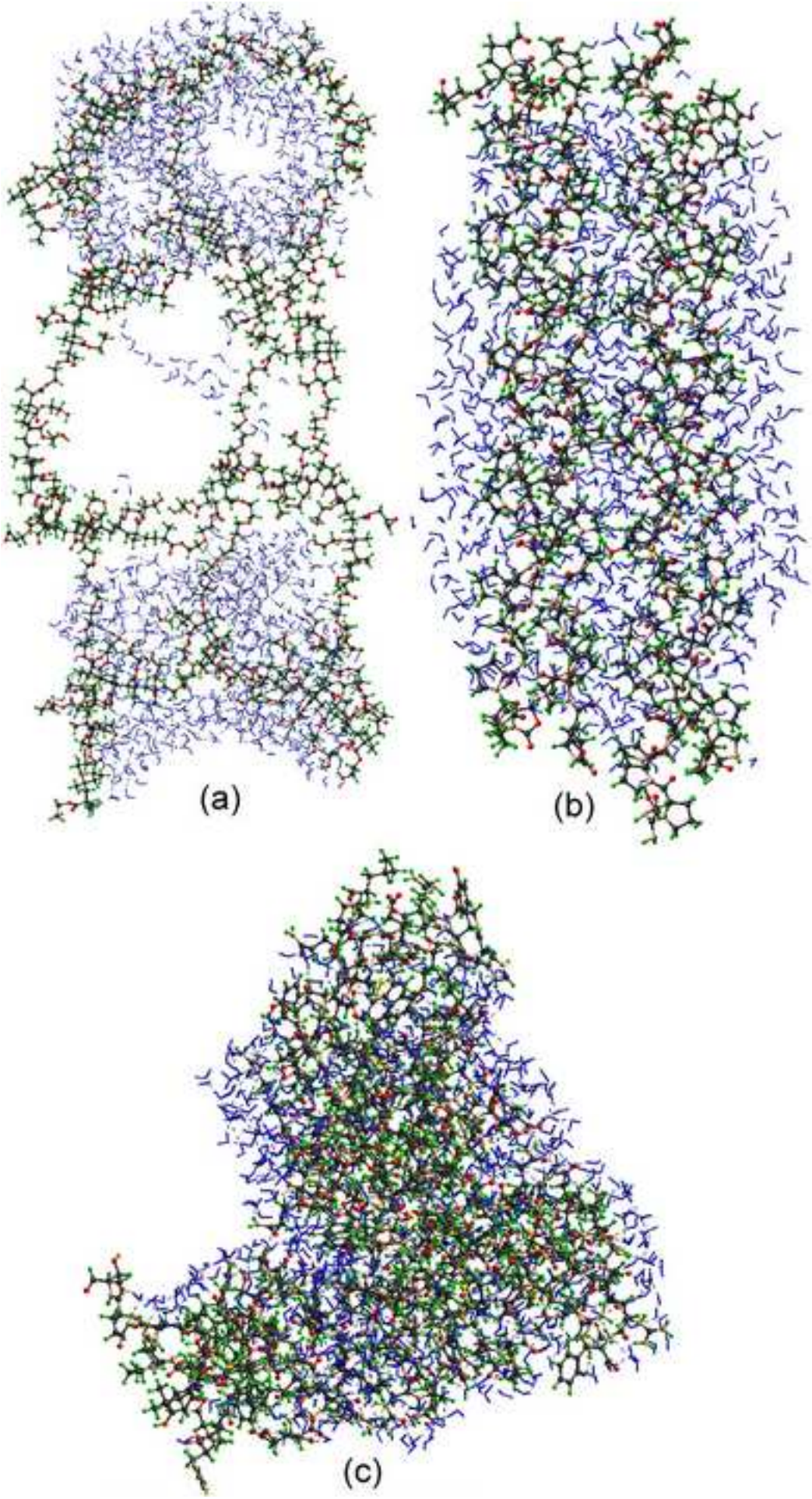

Figure 37

Click here to download high resolution image

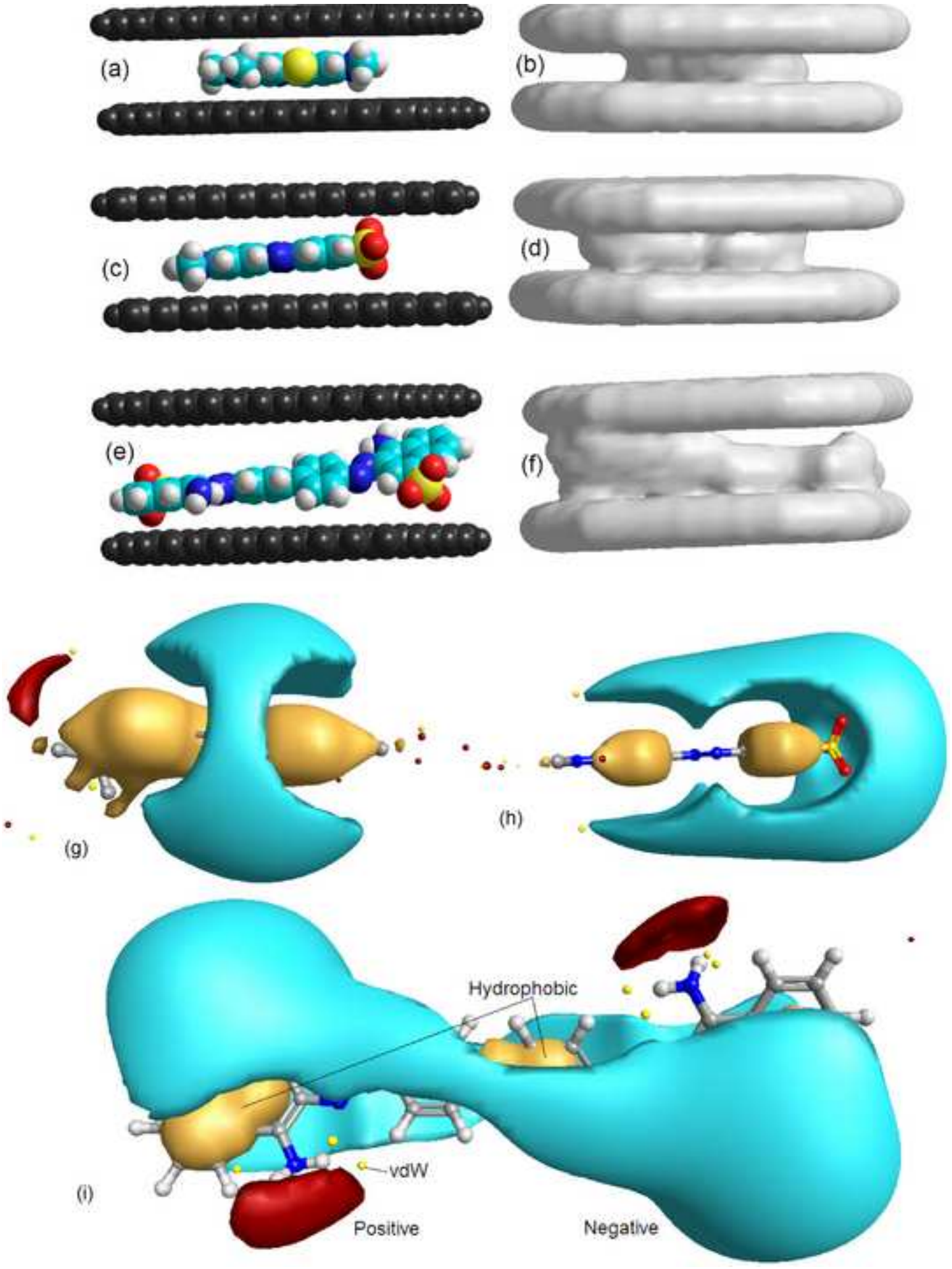

Figure 38

Click here to download high resolution image

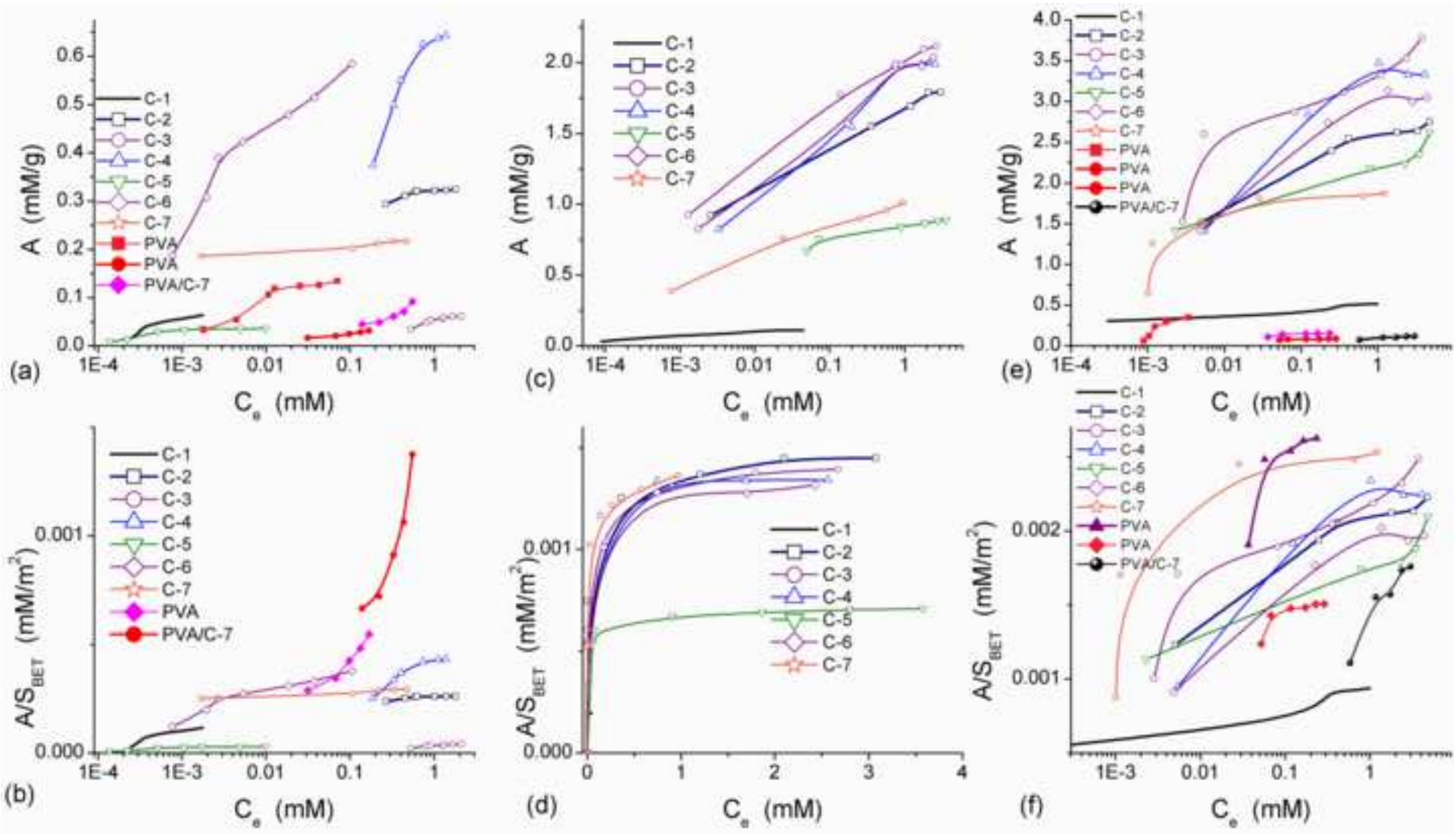

Figure 39

Click here to download high resolution image

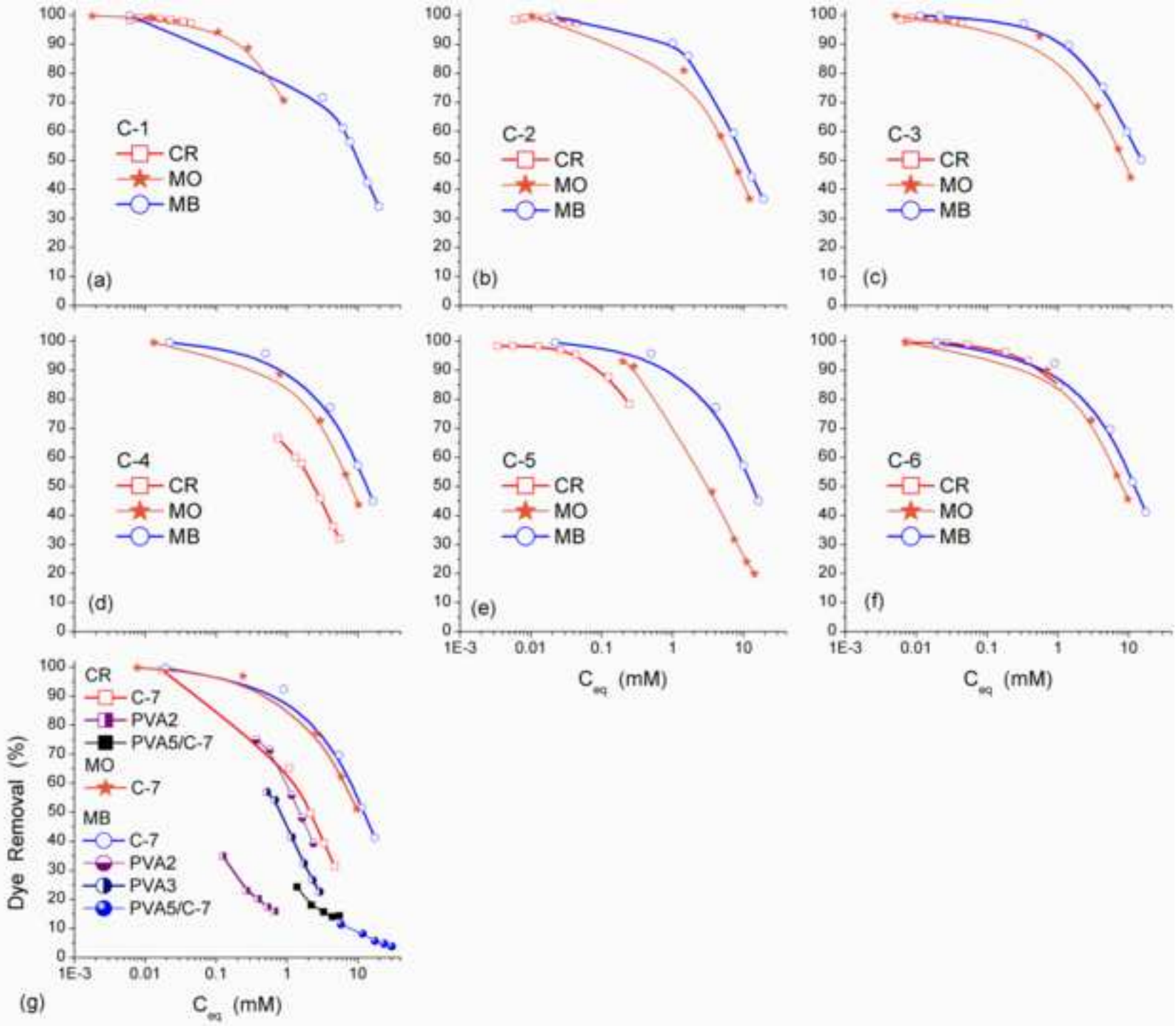

Figure 40

Click here to download high resolution image

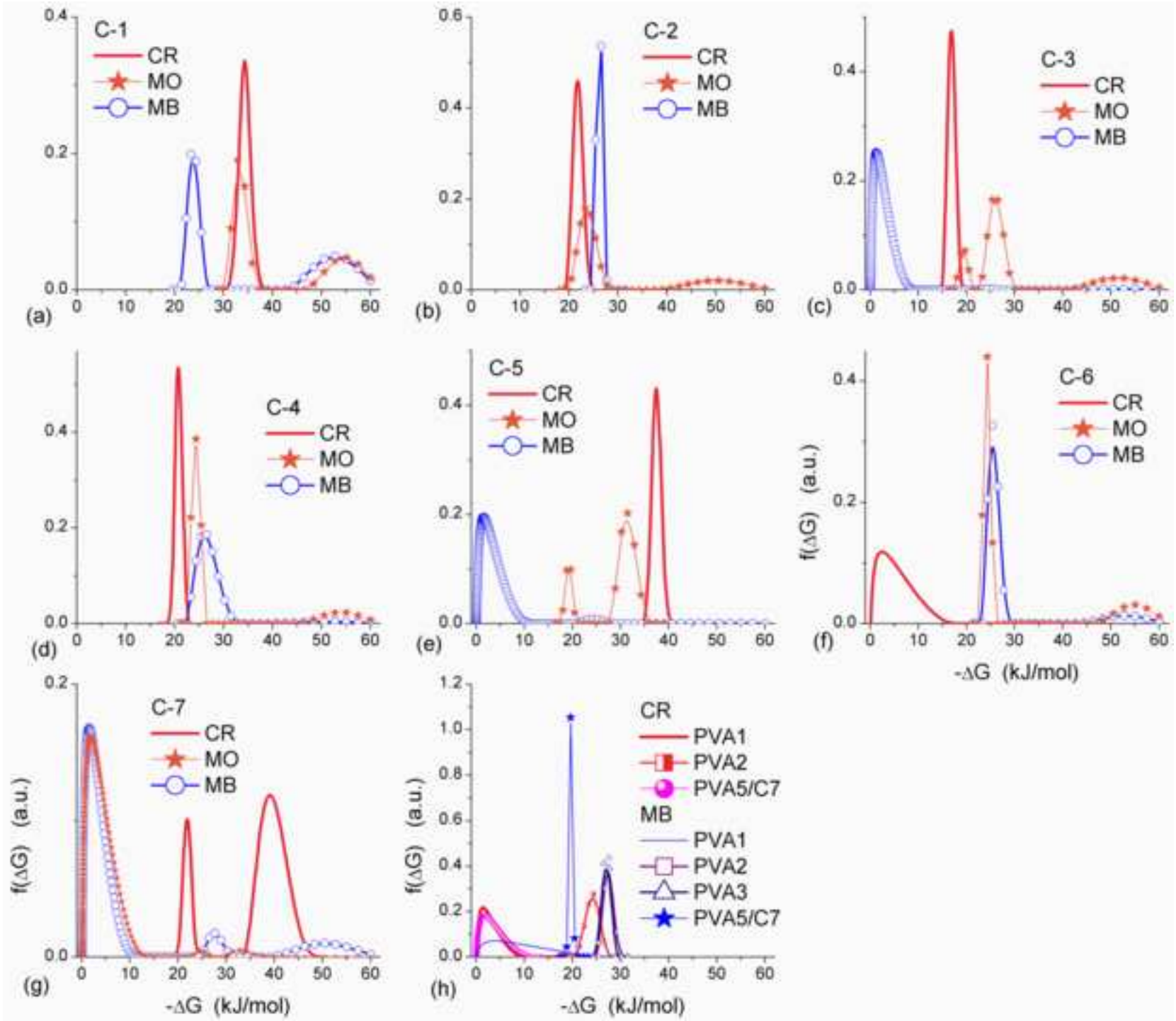

Figure 41

Click here to download high resolution image

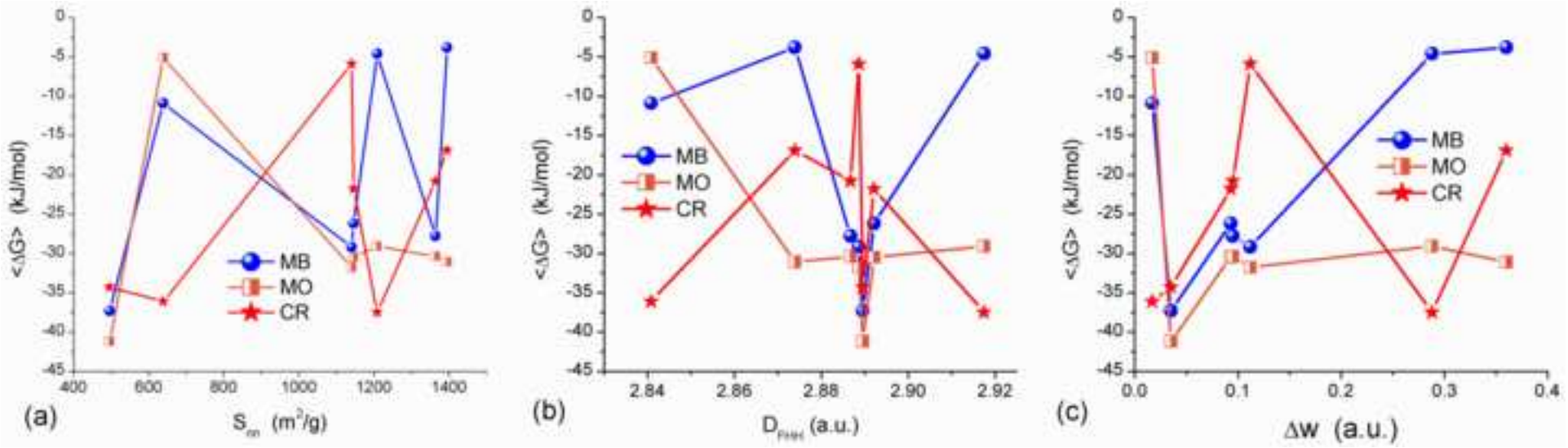

Figure 42

Click here to download high resolution image

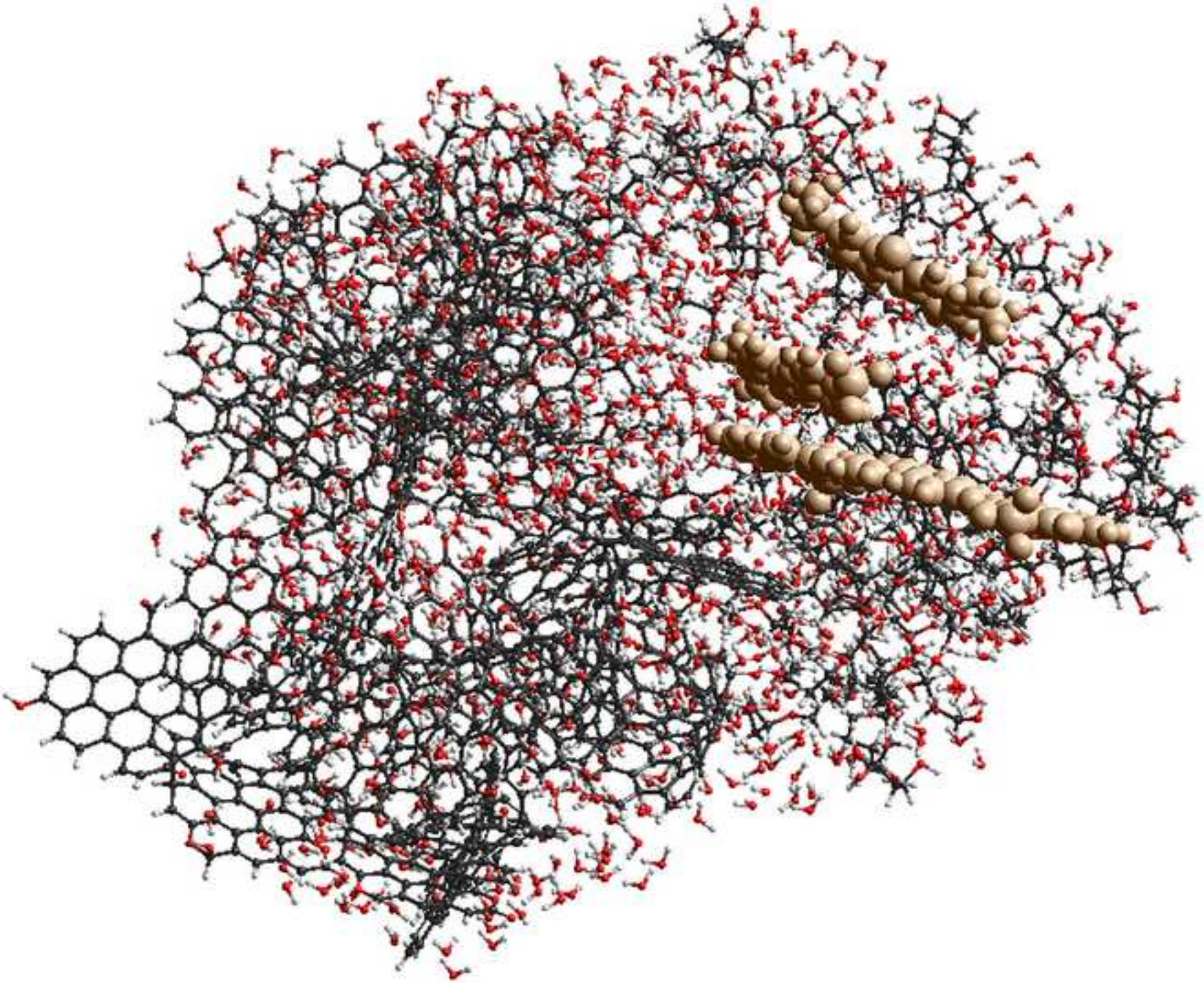

Figure 43

Click here to download high resolution image

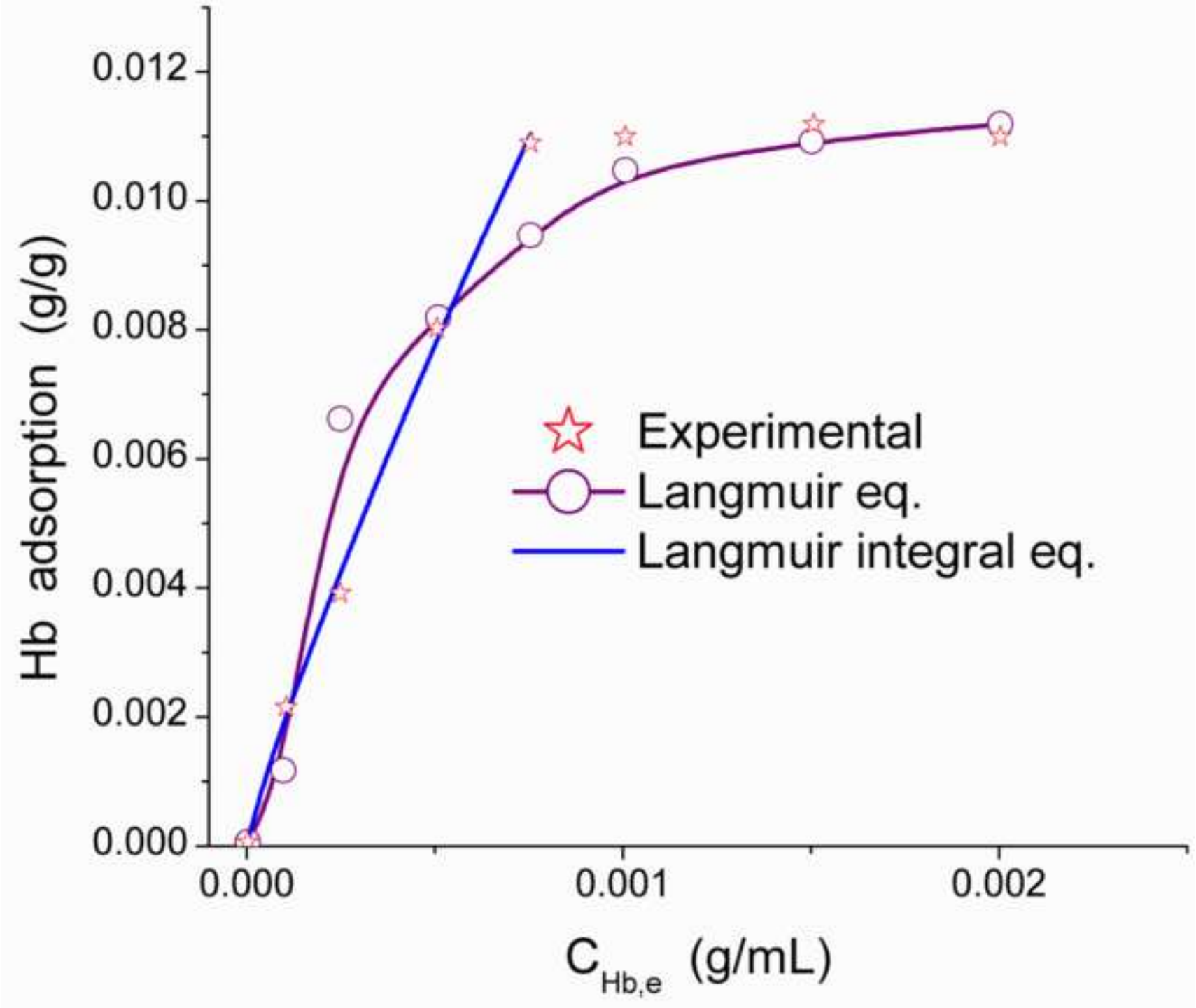

Figure 44
Click here to download high resolution image

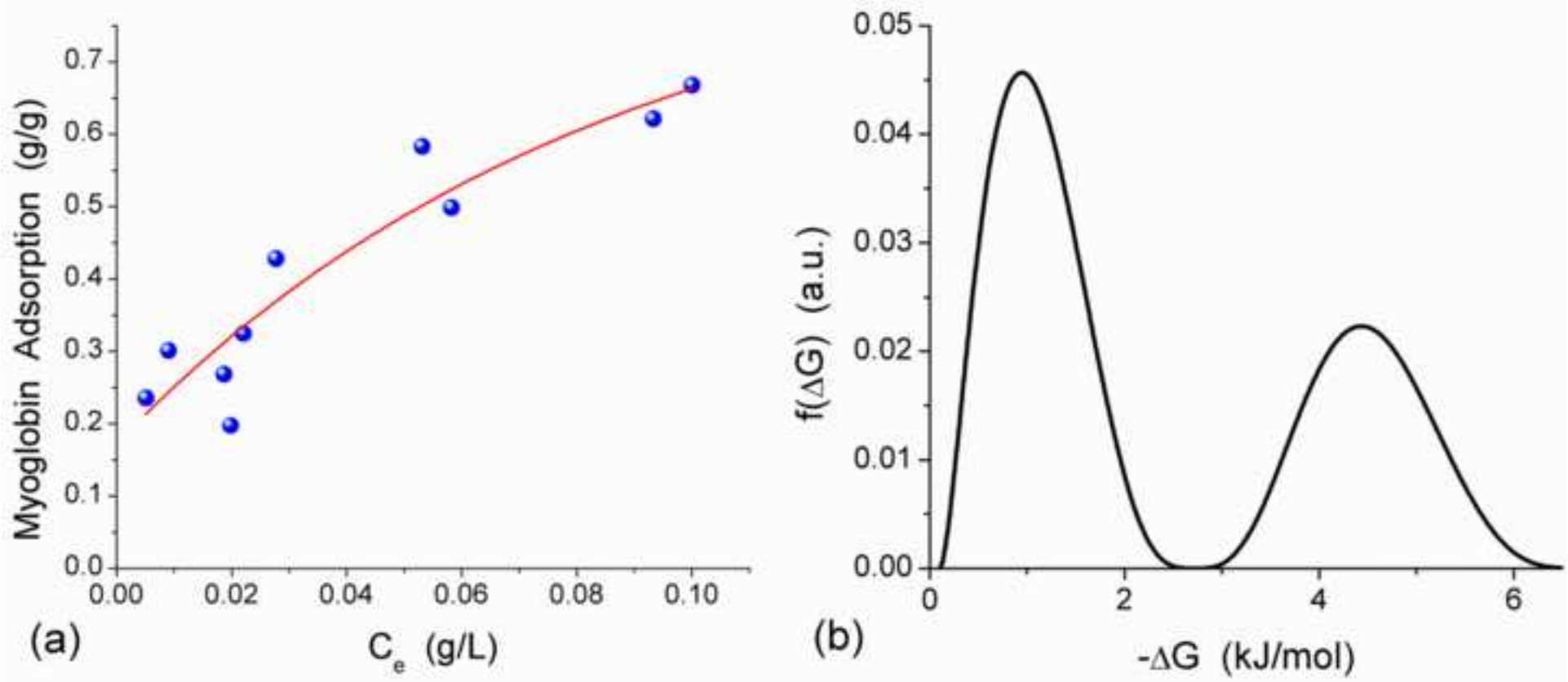

Figure 45
Click here to download high resolution image

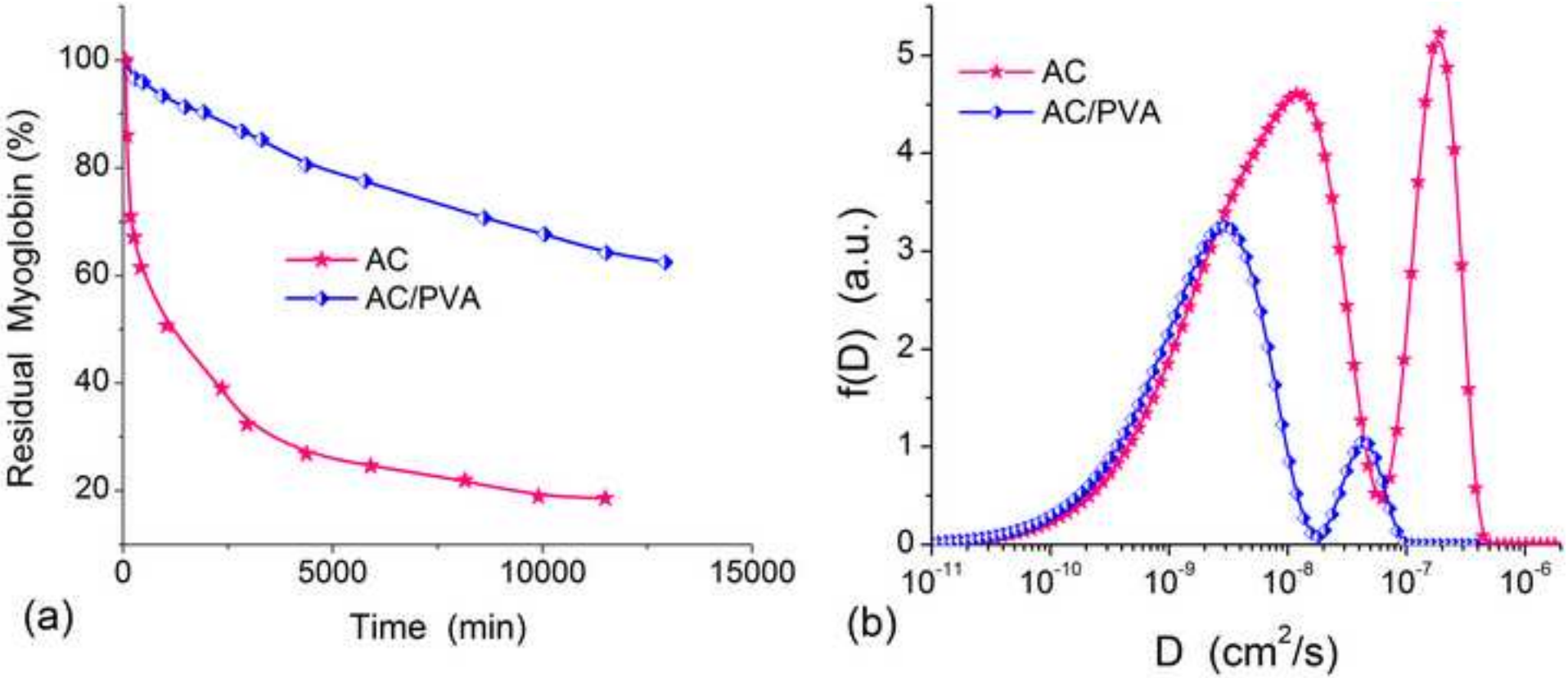

Figure 46

Click here to download high resolution image

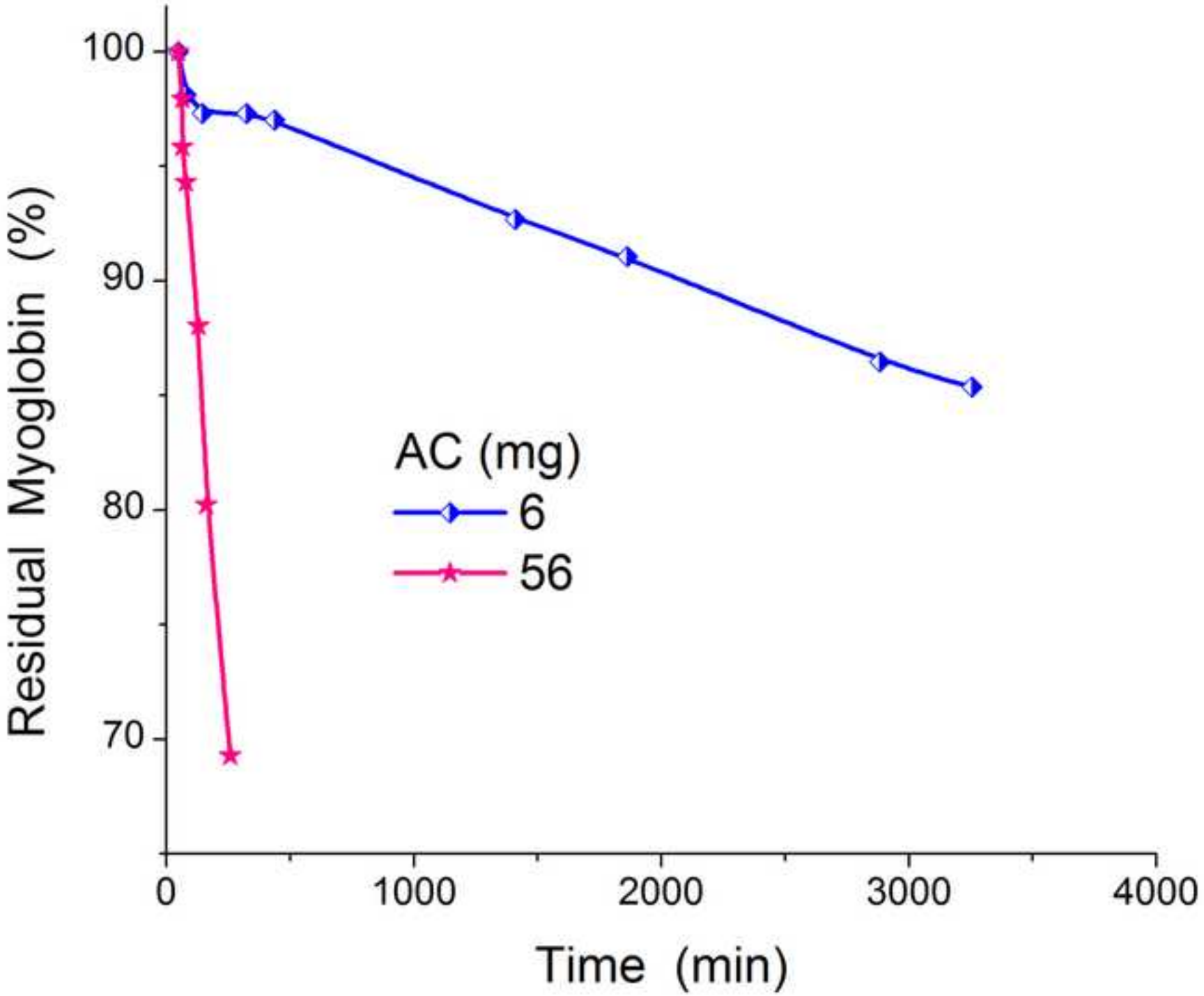

Figure 47

Click here to download high resolution image

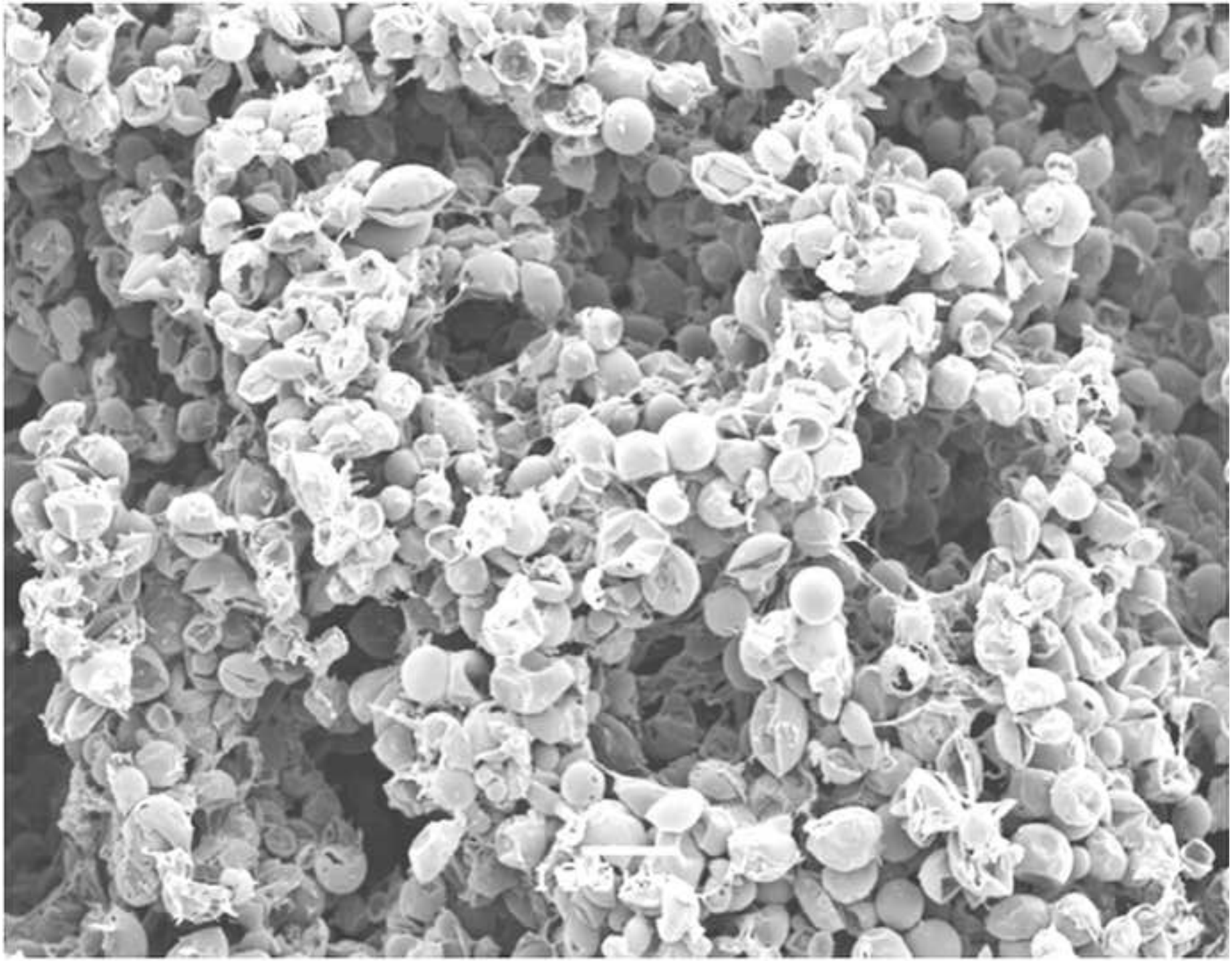

Figure 48

Click here to download high resolution image

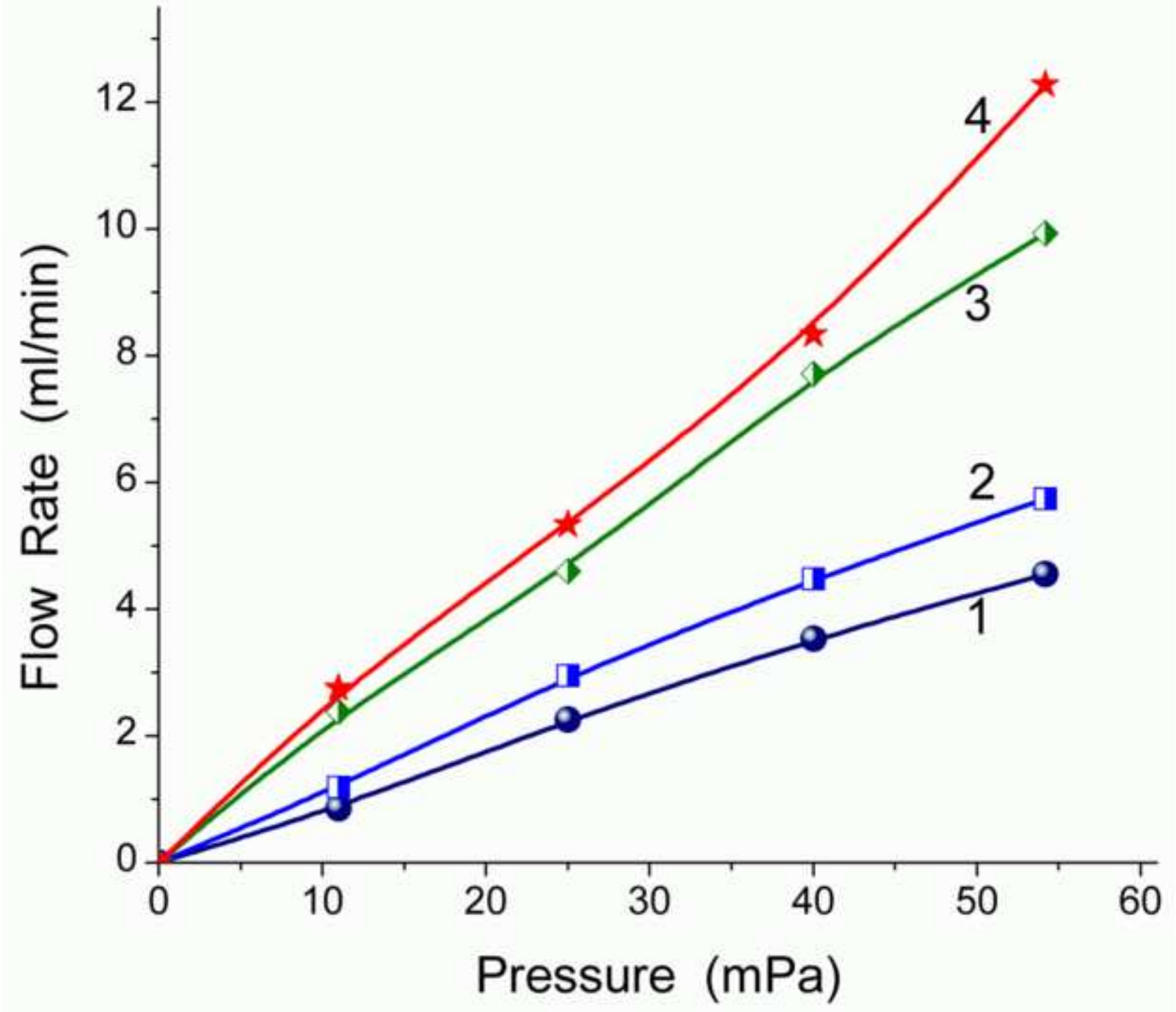

Figure 49

Click here to download high resolution image

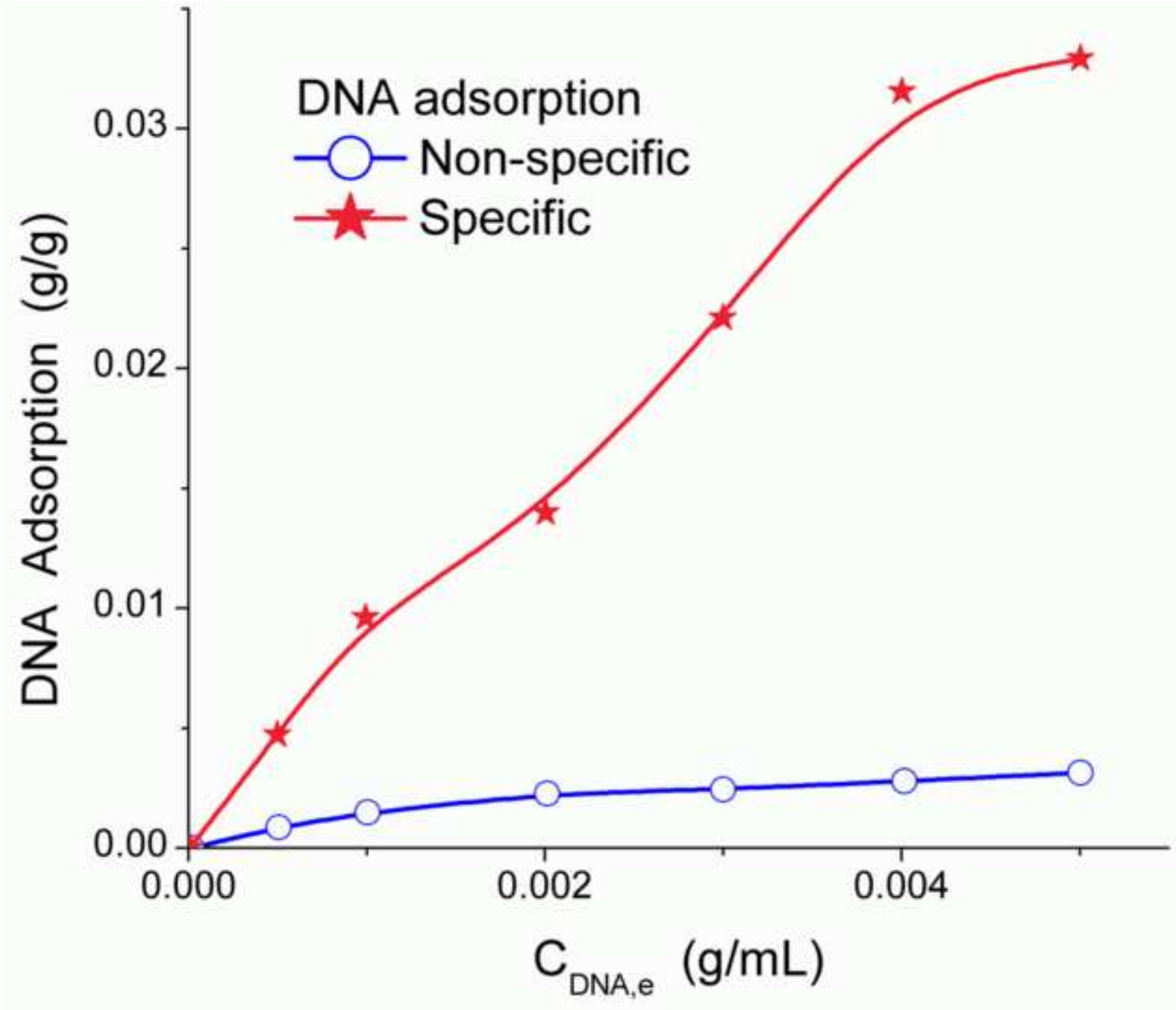

Figure 50
Click here to download high resolution image

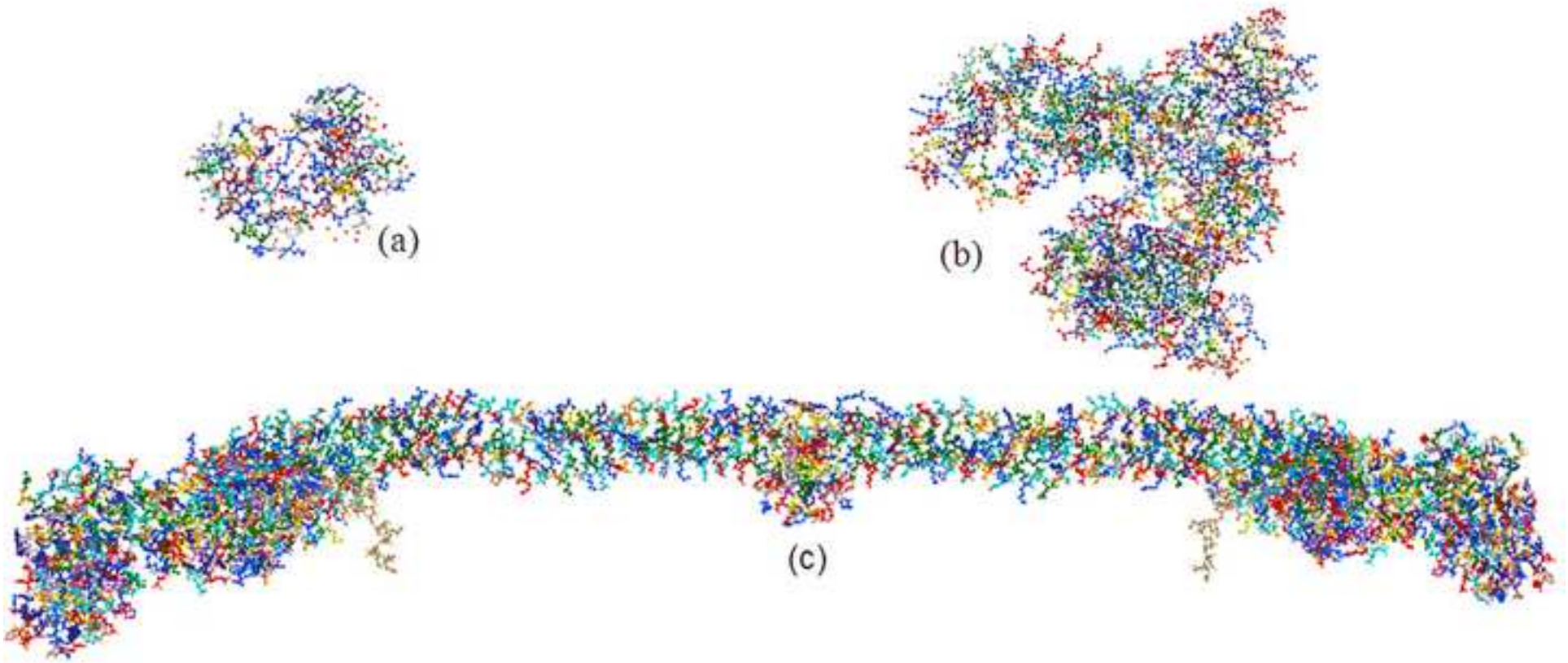

Figure 51

Click here to download high resolution image

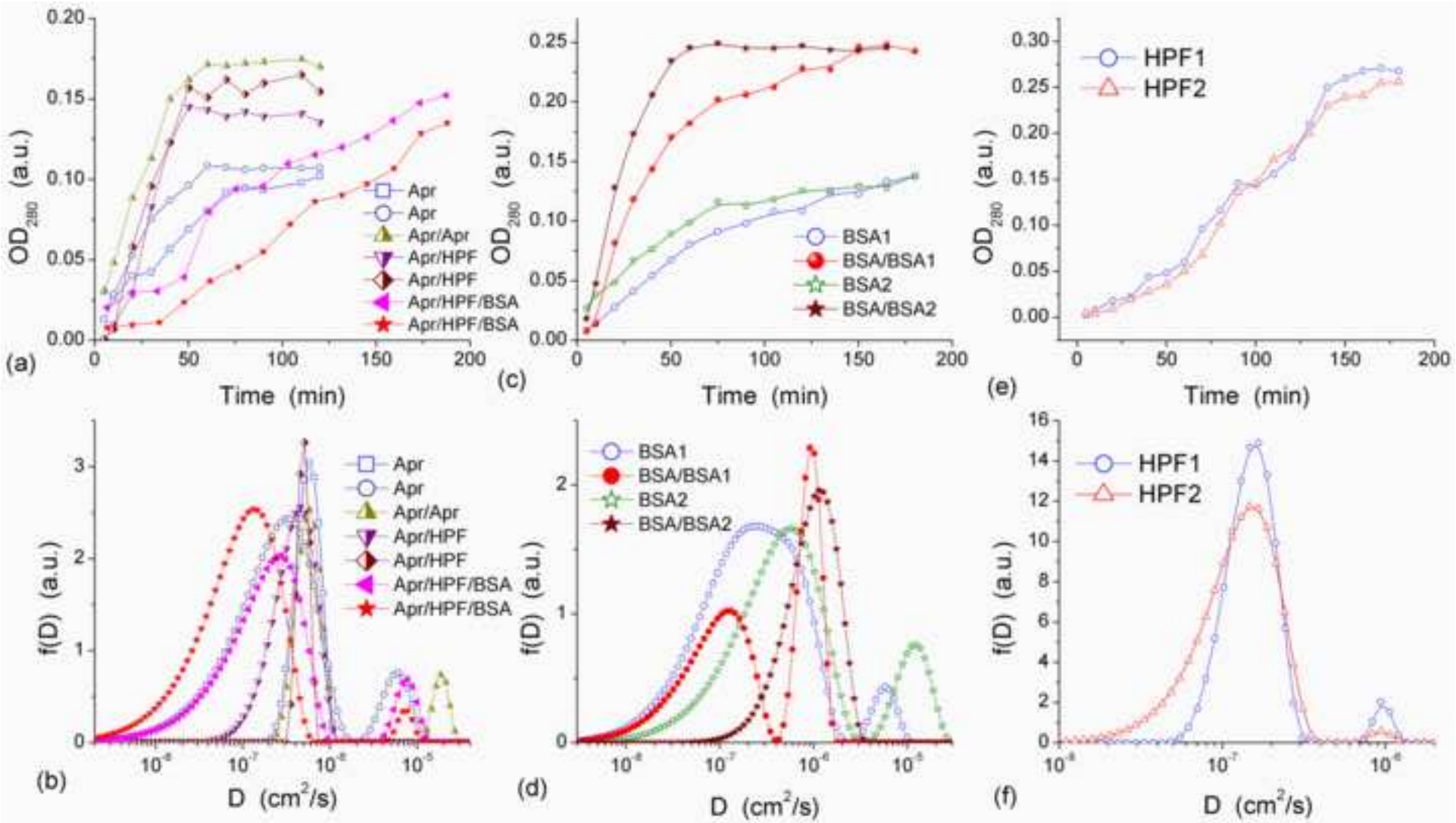

Figure 52
Click here to download high resolution image

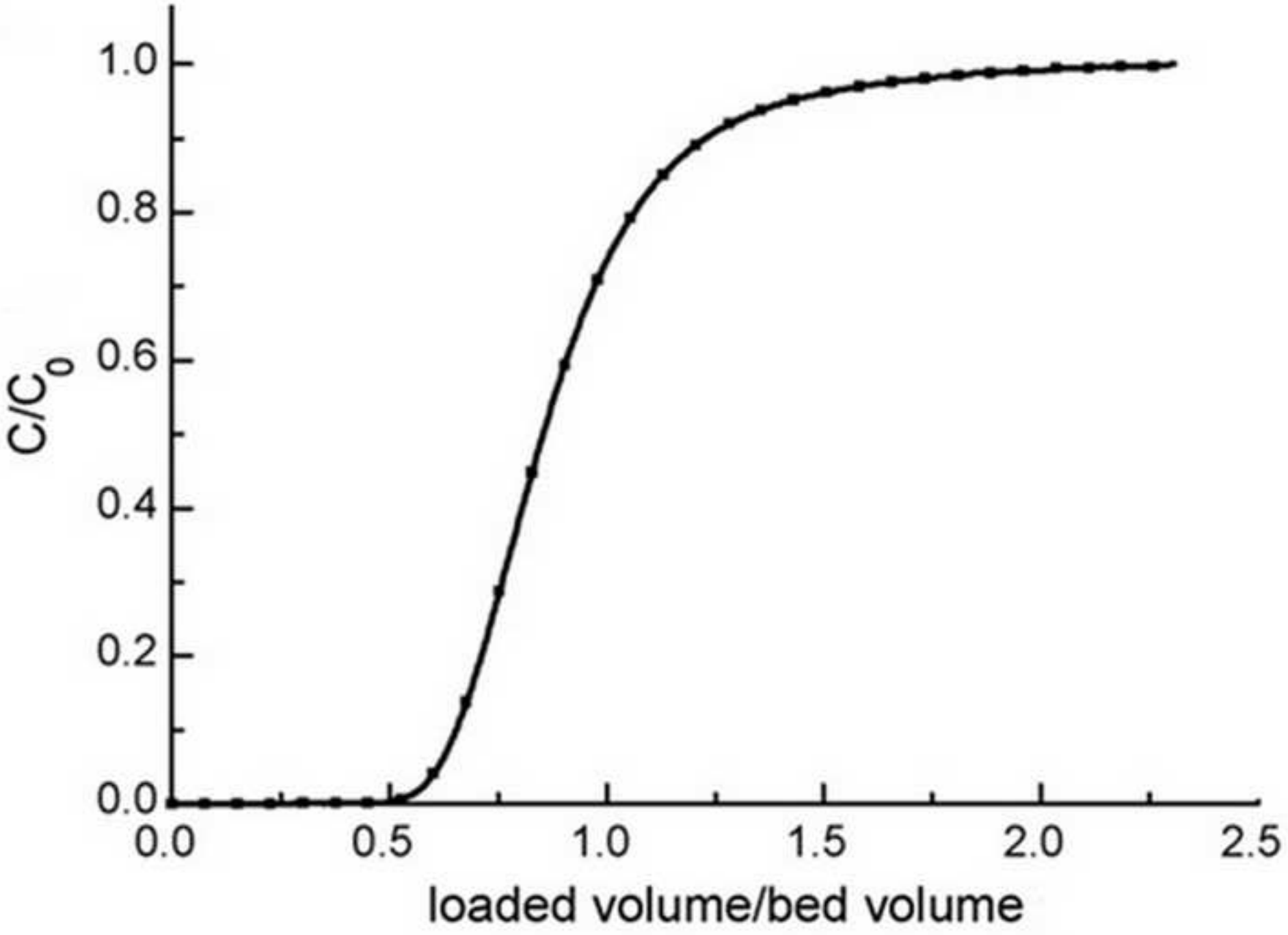

Figure 53

Click here to download high resolution image

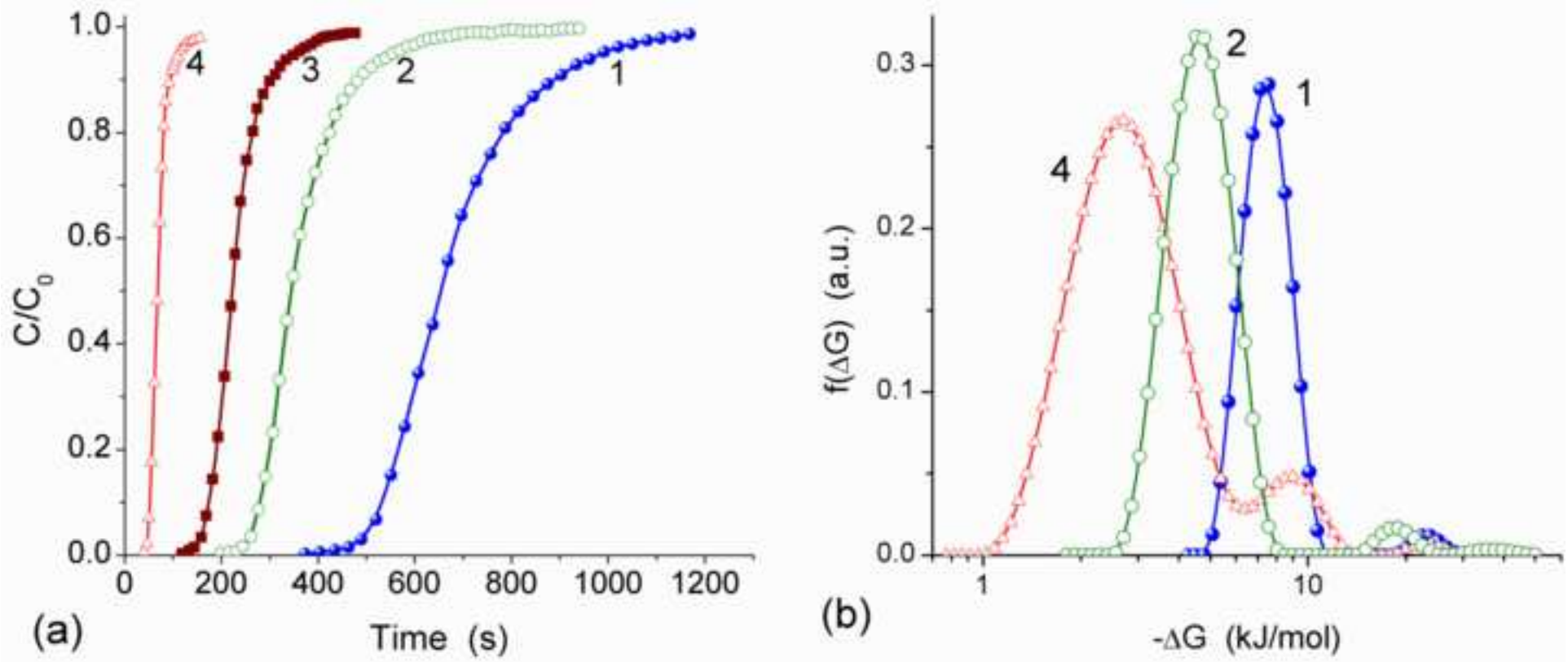

Figure 54
Click here to download high resolution image

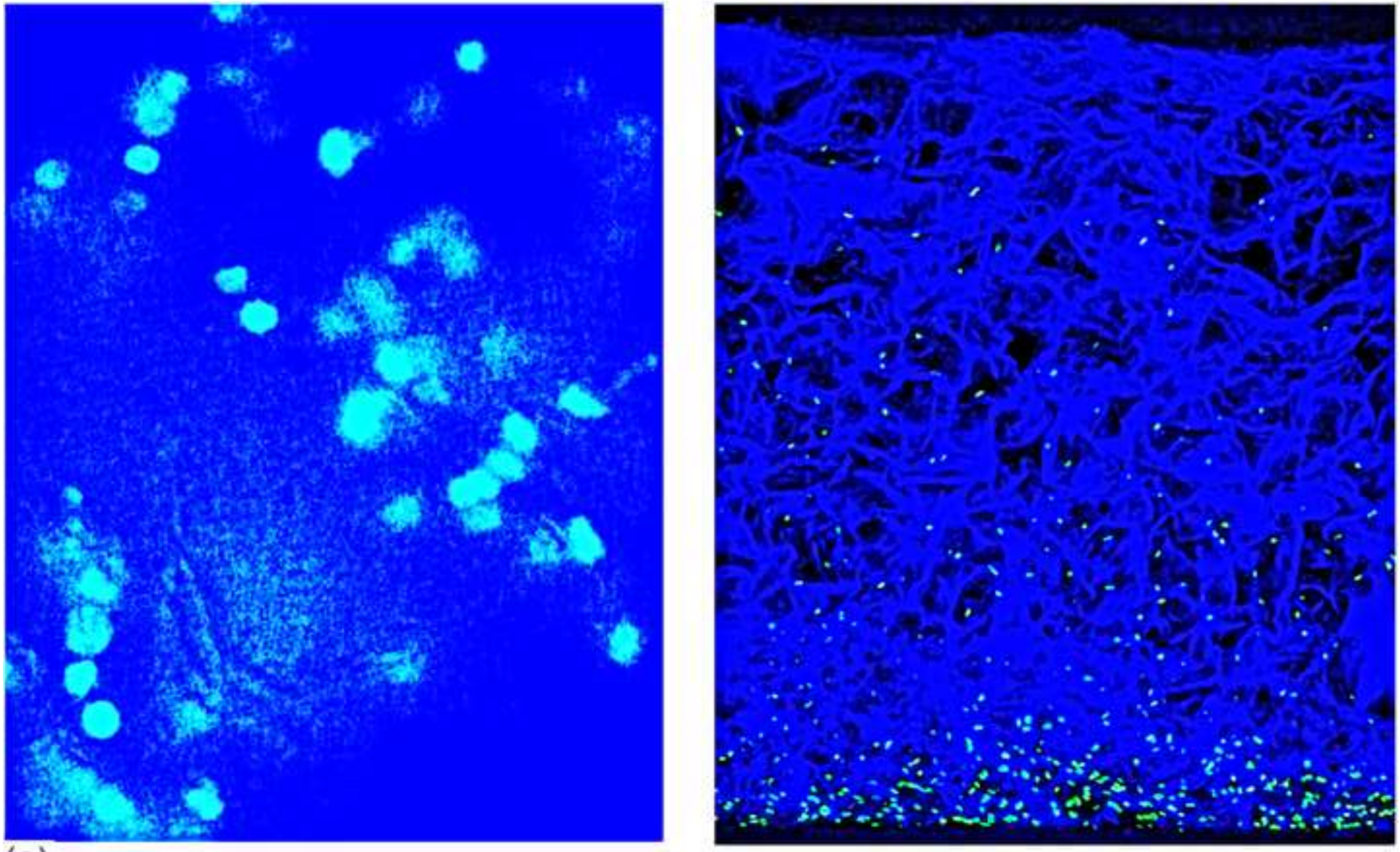

Figure 55

Click here to download high resolution image

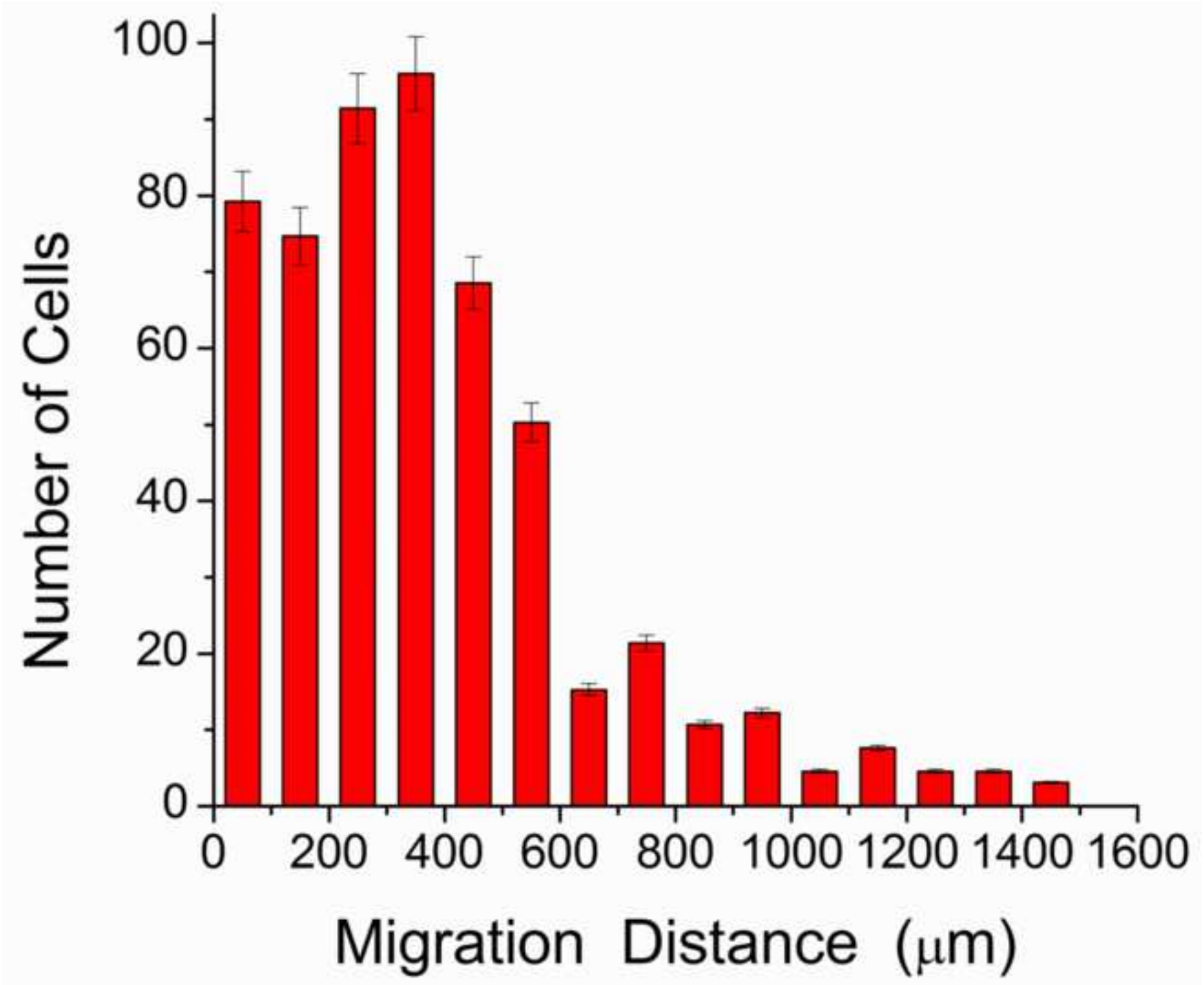

Figure 56

Click here to download high resolution image

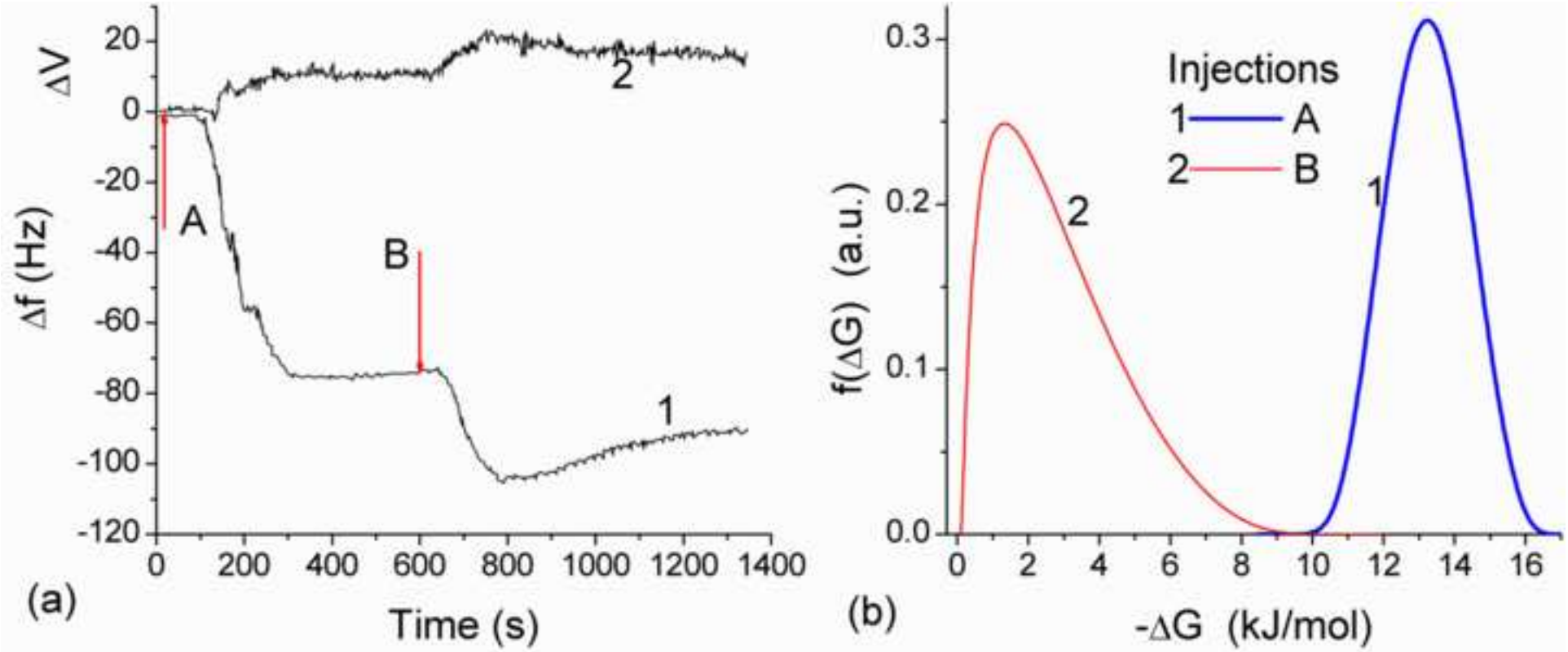

Figure 57
Click here to download high resolution image

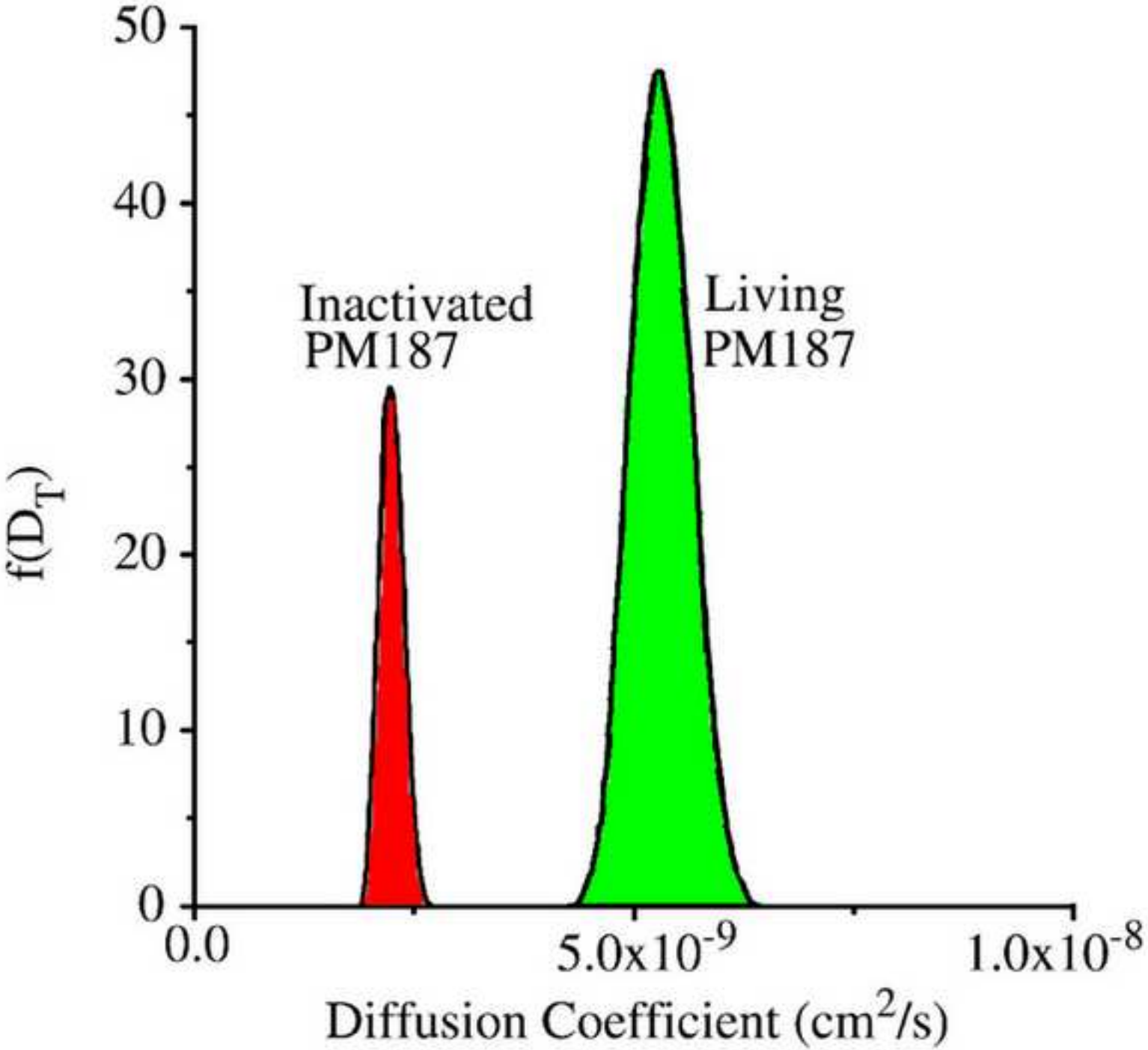

Publishers permissions

Click here to download Supplementary Material: all_permissions.docx